Synchrotron X-ray Analytical Techniques for Studying Materials Electrochemistry in Rechargeable Batteries

Feng Lin,*,[†] Yijin Liu,[‡] Xiqian Yu,[§,‖] Lei Cheng,[⊥] Andrej Singer,[#,△] Oleg G. Shpyrko,[#] Huolin L. Xin,[@] Nobumichi Tamura,[∇] Chixia Tian,[⊥] Tsu-Chien Weng,[□] Xiao-Qing Yang,[§] Ying Shirley Meng,[○] Dennis Nordlund,[‡] Wanli Yang,[∇] and Marca M. Doeff*,[⊥]

[†]Department of Chemistry, Virginia Tech, Blacksburg, Virginia 24061, United States

[‡]Stanford Synchrotron Radiation Lightsource, SLAC National Accelerator Laboratory, Menlo Park, California 94035, United States

[§]Chemistry Department, Brookhaven National Laboratory, Upton, New York 11973, United States

[‖]Beijing National Laboratory for Condensed Matter Physics, Institute of Physics, Chinese Academy of Sciences, Beijing 100190, China

[⊥]Energy Storage and Distributed Resources Division, Lawrence Berkeley National Laboratory, Berkeley, California 94720, United States

[#]Department of Physics, University of California San Diego, La Jolla, California 92093, United States

[@]Center for Functional Nanomaterials, Brookhaven National Laboratory, Upton, New York 11973, United States
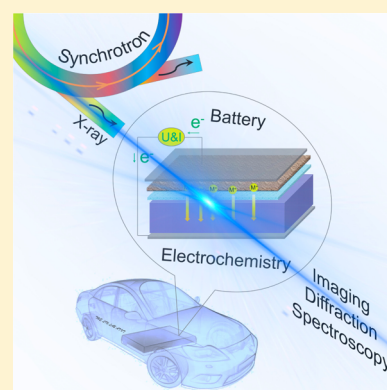
[∇]Advanced Light Source, Lawrence Berkeley National Laboratory, Berkeley, California 94720, United States

[□]Center for High Pressure Science & Technology Advanced Research, Shanghai 201203, China

[○]Department of NanoEngineering, University of California San Diego, La Jolla, California 92093, United States

S *Supporting Information*

ABSTRACT: Rechargeable battery technologies have ignited major breakthroughs in contemporary society, including but not limited to revolutions in transportation, electronics, and grid energy storage. The remarkable development of rechargeable batteries is largely attributed to in-depth efforts to improve battery electrode and electrolyte materials. There are, however, still intimidating challenges of lower cost, longer cycle and calendar life, higher energy density, and better safety for large scale energy storage and vehicular applications. Further progress with rechargeable batteries may require new chemistries (lithium ion batteries and beyond) and better understanding of materials electrochemistry in the various battery technologies. In the past decade, advancement of battery materials has been complemented by new analytical techniques that are capable of probing battery chemistries at various length and time scales. Synchrotron X-ray techniques stand out as one of the most effective methods that allow for nearly nondestructive probing of materials characteristics such as electronic and geometric structures with various depth sensitivities through spectroscopy, scattering, and imaging capabilities. This article begins with the discussion of various rechargeable batteries and associated important scientific questions in the field, followed by a review of synchrotron X-ray based analytical tools (scattering, spectroscopy, and imaging) and their successful applications (ex situ, in situ, and in operando) in gaining fundamental insights into these scientific questions. Furthermore, electron microscopy and spectroscopy complement the detection length scales of synchrotron X-ray tools and are also discussed toward the end. We highlight the importance of studying battery materials by combining analytical techniques with complementary length sensitivities, such as the combination of X-ray absorption spectroscopy and electron spectroscopy with spatial resolution, because a sole technique may lead to biased and inaccurate conclusions. We then discuss the current progress of experimental design for synchrotron experiments and methods to mitigate beam effects. Finally, a perspective is provided to elaborate how synchrotron techniques can impact the development of next-generation battery chemistries.

CONTENTS

1. INTRODUCTION

In 1991, Sony[1] announced the successful commercialization of the first lithium-ion batteries, now the devices of choice for consumer electronics as well as for emerging technologies such as transportation applications (electric vehicles) and grid energy storage. In the intervening years, the practical specific energy of cells has more than doubled (from <100 to ~240 Wh/kg) and costs have decreased from more than $1000/kWh to $300/kWh.[2] These remarkable advances are due not only to better engineering and cell design but also to improvements in materials, particularly, electrodes and electrolytes. Many of these improvements were enabled by improved understanding of electrochemical reactions that occur in the electrode materials and at the electrode−electrolyte interfaces. The development of nearly nondestructive synchrotron analytical techniques, capable of probing various length and time scales, in or ex situ, has coincided with the maturation of lithium-ion batteries, leading to significant insights into their functioning and what design principles are important for improvement. The investigation of batteries by synchrotron X-ray techniques started approximately 25 years ago (pioneered by McBreen and co-workers[3−10]) and has generated numerous publications. This is expected to grow as more scientists in battery research become familiar with the techniques and are eager to initiate studies making use of the ever-increasing capabilities at synchrotron light sources. This work reviews the application of synchrotron science to battery materials and device functionality. The emphasis is primarily on lithium-ion batteries but also includes some "beyond lithium-ion" chemistries, primarily those involving lithium metal anodes (e.g., solid state batteries, lithium/sulfur) and the closely related sodium-ion battery systems. A short summary of the relevant chemistries, cell designs, and grand challenges associated with these devices is given below, followed by descriptions of synchrotron techniques applicable to battery technologies and results and insights from these experiments. To conclude, we describe what the future may hold for the application of synchrotron science to batteries.

2. BATTERY DESIGN AND MATERIALS

2.1. Lithium-Ion Batteries

A schematic of a lithium-ion cell is shown in Figure 1.[11] The typical device is a dual intercalation system, consisting of two electrodes that can insert lithium ions at different potentials, where the insertion in the positive electrode (cathode) occurs at higher redox potentials than that of the negative electrode (anode). Lithium ions shuttle between the two electrodes during charge and discharge, and electrons from the external circuit compensate for the (dis)charge of the electrode materials. The electrodes are typically porous composites; in addition to the active materials, they contain polymeric binders and conductive additives such as carbon black. An aluminum current collector is used as the backing for the cathode and copper for the anode. A thin porous film separates the two electrodes,[12] and a liquid electrolytic solution consisting of a lithium salt dissolved in organic carbonates[13] wets the separator and electrodes. Various additives may also be used in the cell to improve the properties of the solid electrolyte interface (SEI) formed at the interface or to provide better oxidative stability and safety, among other functions.[14] Safety features such as shutdown separators, cell vents, or tear-away tabs may also be incorporated in cells.[15]
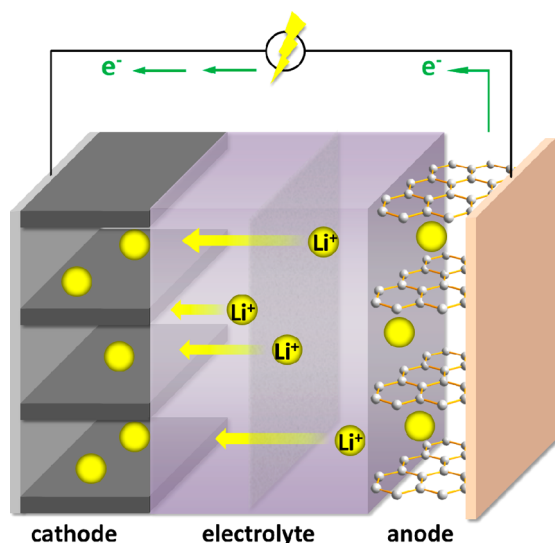
Figure 1. Schematic diagram of a lithium-ion cell consisting of (left) an intercalation cathode on an aluminum current collector, (middle) an electrolytic solution, and (right) a graphite anode on a copper current collector. Reproduced with permission from ref 11. Copyright 2012 Sigma-Aldrich Co. LLC.

Unlike many other batteries, lithium-ion system chemistry is not absolutely fixed. In principle, any of a number of redox active compounds, salts, and solvents may be used as electrode materials and in electrolytic solutions, resulting in variable performance characteristics such as average potential, energy density, rate capability, cycle life, safety, and cost. In actuality, rigorous requirements for specific applications have resulted in the commercialization of just a handful of materials. Graphite is the most commonly used anode, although small amounts of silicon are now often added to boost capacity.[16,17] For applications where high energy density is not mandated, such as hybrid electric vehicles (HEVs), the spinel titanate $Li_4Ti_5O_{12}$ is sometimes substituted. A variant of $LiCoO_2$, which was the first intercalating oxide cathode to be described,[18] is still the positive electrode of choice for small batteries intended for consumer electronics, although it is considered too expensive for electric vehicles. For electric vehicle applications, the olivine $LiFePO_4$, variants of $LiMn_2O_4$ (LMO) spinel, or layered transition metal oxides isostructural to $LiCoO_2$ containing multiple metals, are used. The latter are commonly referred to by their initials [e.g., NMC for $LiNi_xMn_yCo_zO_2$ (where $x + y + z = 1$) or NCA for $LiNi_{0.8}Co_{0.15}Al_{0.05}O_2$]. Because none of these materials alone meets all of the criteria necessary for transportation applications, such as high energy density, good thermal stability, high power, and long cycle life, materials are sometimes mixed together in the composite cathode to achieve the desired characteristics. For instance, NMC and LMO materials are blended as composite cathodes for the BMW i3 and Nissan Leaf.[19]

Likewise, the need for high conductivity, wide potential stability, and thermal operation windows and formation of the essential solid electrolyte interface (SEI) on the anode has led the battery industry to settle primarily on $LiPF_6$ in mixtures of organic carbonates containing ethylene carbonate (EC) as the basis for the electrolytic solution.

The consensus that has formed around these materials is the result of nearly 40 years of effort in intercalation chemistry and lithium battery research. Along the way, many initially attractive

candidates have been studied but then either modified or discarded outright because they failed on one performance metric or another. Nevertheless, the large and growing lithium-ion battery market (estimated in 2010 to be U.S. $10 billion[20]) provides strong incentives to continue development, especially as new opportunities in vehicular applications and large-scale energy storage emerge. In particular, there is a need for improved safety, lower cost, higher energy density, and more reliable cycling than currently available. For example, the EV Everywhere Blueprint, the umbrella effort of the U.S. Department of Energy to increase the adoption and use of plug-in hybrid electric vehicles, outlines goals for halving the weight and size of the battery and reducing cost from ∼ $500/kWh to $125/kWh by 2022 (see http://energy.gov/eere/vehicles/ev-everywhere-grand-challenge-does-10-year-vision-plug-electric-vehicles).

The push for higher energy density has driven interest in new anode materials based on alloying reactions.[21−23] Much attention in recent years has been directed toward silicon, in particular, because of the high gravimetric capacity for lithium (∼4200 mAh/g) and the existence of a manufacturing infrastructure for the semiconductor industry. Research efforts have been directed toward managing the large volume changes[24] and Coulombic inefficiencies associated with the lithium alloying reactions in silicon-based anode materials. These approaches include nanostructuring,[25,26] the use of composites, particularly with carbon,[27] and development of special binders[28] as well as electrolyte additives. As of this writing, silicon is used primarily to boost capacity of carbon anodes rather than as a stand-alone electrode material. Alloy anodes based on tin have also been intensively studied and have been used in composite form in the Sony Nexelion battery.[29,30] The energy density is 30% higher than that of conventional carbon anodes, although applications are limited to high-end video cameras.[31]

Conversion electrodes have also been considered for use in lithium-ion batteries.[32,33] These generally involve displacement reactions of binary metal-containing compounds (eq 1), rather than intercalation, although some materials will undergo intercalation prior to conversion.

$$nLi^+ + ne^- + M^{n+}X_m \leftrightarrow M + nLiX_{m/n}$$

$$(X = O, F, N, S) \tag{1}$$
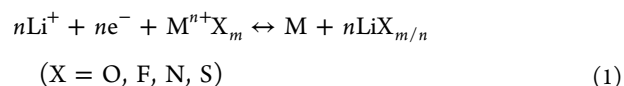
The theoretical gravimetric capacities of these reactions can be enormous (e.g., 571 mAh/g for FeF_2),[34] but the electrodes are plagued by large volume expansion, sluggish kinetics, high Coulombic inefficiencies, and poor round-trip energy efficiencies. Most conversion electrodes are intended for use as anode materials because of the relatively low potentials at which they are redox active. However, several binary metal fluorides are electroactive above 3 V versus Li^+/Li, making them possible candidates for use as positive electrode materials in metallic lithium cells, if solutions can be found for the problems outlined above.

Most other emerging cathode materials are based on variants of NMC, due to their ease of synthesis, and other attractive characteristics.[35] In particular, there is potential for higher practical capacities at accessible voltages than is achievable now (usually about 160 mAh/g when charged to 4.3 V versus Li^+/Li, compared to a theoretical capacity of ∼280 mAh/g). Approaches for improving energy density include charging conventional NMCs to higher voltages, to allow more capacity

to be accessed. This often results in faster capacity fading, and a large body of work is directed toward understanding the high voltage behavior.[36] There is also interest in developing Ni-rich NMCs, in which the Ni content is greater than that of Mn and Co, because of their generally higher practical capacities under normal cycling conditions compared to NMCs in which the Ni content is matched to that of Mn.[37] These materials exhibit high surface reactivity, and a greater tendency for antisite mixing, in which Ni sites occupy Li sites in the van der Waals' gaps, and vice versa, compared to NMCs with lower Ni content. The former results in poorer cycling behavior and potential safety issues (e.g., inferior thermal stability), whereas the latter can lead to diminished rate capability.

A category of materials known variously as LMR-NMCs (lithium and manganese-rich NMCs), OLOs (overlithiated oxides), or "layered−layered" composites has been the focus of intense interest from the battery research community because of the very high capacities that can be obtained upon discharge after activation, often in excess of 250 mAh/g.[38,39] A number of different compositions having more than one Li per formula unit and Mn content larger than that of Ni and Co have been studied. The structures of the LMR-NMCs have been a subject of controversy, with materials described as either solid solutions (i.e., $Li_{1+x}M_{1−x}O_2$, where M stands for Ni, Co, and Mn)[40] or as composites containing Li_2MnO_3, written as $x(Li_2MnO_3)\cdot 1− x(LiMO_2)$.[41−43] A recent careful transmission electron microscopic study of several of the most well-studied materials, however, indicated that commercially available materials are best described as solid solutions.[44] In fact, the structures of these materials are likely determined by the method of preparation and can be sensitive to thermal treatment.

The electrochemical behavior of the LMR-NMCs is significantly different from that of conventional and Ni-rich NMCs in several key aspects. Upon initial charge to potentials above about 4.5 V versus Li^+/Li, a plateau is generally observed in their voltage profiles. Oxygen release accompanies the deintercalation of lithium ions from the structure on this plateau, for a net loss of Li_2O. An alternative explanation, however, holds that some of the oxygen anions are partially oxidized at this stage. At any rate, the process renders the manganese ions, which do not normally participate in redox processes in conventional NMCs, electro-active, leading to the very high discharge capacities that are observed subsequently. Unfortunately, the LMR-NMCs suffer from a number of problems, which make them difficult to employ in most applications. The most significant of these is voltage fading due to structural changes as the material is cycled; in other words, the average voltage upon discharge decreases with cycle number, leading to a loss of energy density. The Department of Energy recently funded a three-year "deep dive" effort, which included synchrotron techniques, aimed at understanding this phenomenon better.[45] To date, however, there is no effective cure for voltage fading that does not compromise the high capacities that made the LMR-NMCs so attractive initially for use as cathode materials.

The observation of oxygen redox activity in the LMR-NMCs and the discussion surrounding its nature has led some researchers to propose the use of electrodes based on the oxygen.[46,47] Several oxides containing second or third row transition metals such as Ru, Sn,[48] Ir,[49] and Nb[50] show evidence of reversible formation of peroxo bonds when charged to high potentials, instead of oxygen gas release. The high initial capacities that some of these materials exhibit make them potentially interesting for many practical applications, although their cycling behavior and safety characteristics still need to be assessed and improved.

2.2. "Beyond Lithium-ion" Batteries

"Beyond Lithium-Ion" batteries include a number of systems of interest due to their potential for lowering cost, increasing energy density, or improving safety, among other benefits.[51−53] They are in varying stages of development, ranging from exploratory to the demonstration phase, and, in many cases, are not based on new chemistries but rather re-evaluations of promising but problematic systems introduced in the past. This is particularly true for secondary battery systems with lithium metal anodes, which tend to form mossy deposits and/or dendrites during cycling. This characteristic has extremely negative implications for safety and cycle life, and has stymied widespread deployment, in spite of over 40 years of mitigating efforts. Still, the possibility of high energy density, based on the large theoretical capacity (3860 mAh/g) and electropositive nature of lithium (−3.04 V vs S.H.E.), provides a compelling rationale for development of these batteries, especially those with lightweight sulfur or air cathodes. In particular, lithium metal anodes could be possibly enabled by solid-state electrolyte separators because of their potential to inhibit the dendritic growth of lithium, although many daunting challenges still exist.[54]

Lithium/sulfur batteries have a high theoretical specific energy of ∼2600 Wh/kg but suffer from short cycle lives due to precipitation of insulating Li_2S and high self-discharge rates due to the shuttling of soluble polysulfide intermediates during operation. While significant progress has been made in their development in recent years, due to improvements in cathode fabrication, the use of additives to suppress shuttling, and special polymeric or ceramic membranes to protect the lithium anode and prevent crossover, they fail to beat modern lithium-ion batteries on several important benchmarks, notably volumetric energy density.[55] In particular, the need to restrict the amount of electrolytic solution in the cell to ensure high energy density leads to shortened cycle life because of the greater tendency for precipitation to occur and the exacerbated effect of electrolyte decomposition.

Likewise, lithium/air systems fall short on several critical performance metrics. Depending on the cell configuration (using aprotic, solid, or alkaline aqueous electrolytes in a hybrid configuration with a protected lithium anode), the reaction product is usually insoluble Li_2O_2 or LiOH, which has limited solubility in water.[56] As is the case with lithium/sulfur batteries, the precipitation of insulating reaction products usually leads to premature polarization before the theoretical capacities are reached (1168 mAh/g for Li_2O_2 or 1119 mAh/g for LiOH). In addition, poor round trip efficiencies, short cycle lives, and side reactions with components in the electrolytic solutions and with H_2O, CO_2, and other contaminants in air, all pose significant challenges for these devices, no matter what the configuration.[57,58] The latter, in particular, has important implications for the design of practical devices, as complex gas-handling systems, which add considerably to the weight and volume, may be required.[59] Still, recent research efforts have shown that some of these problems can be overcome; for example, good cycling to a LiOH product has been achieved using a LiI mediator and small amounts of water in a cell with an organic electrolytic solution.[60] A cell in which a stable LiO_2 product was formed, by utilizing an Ir catalyst and limiting the
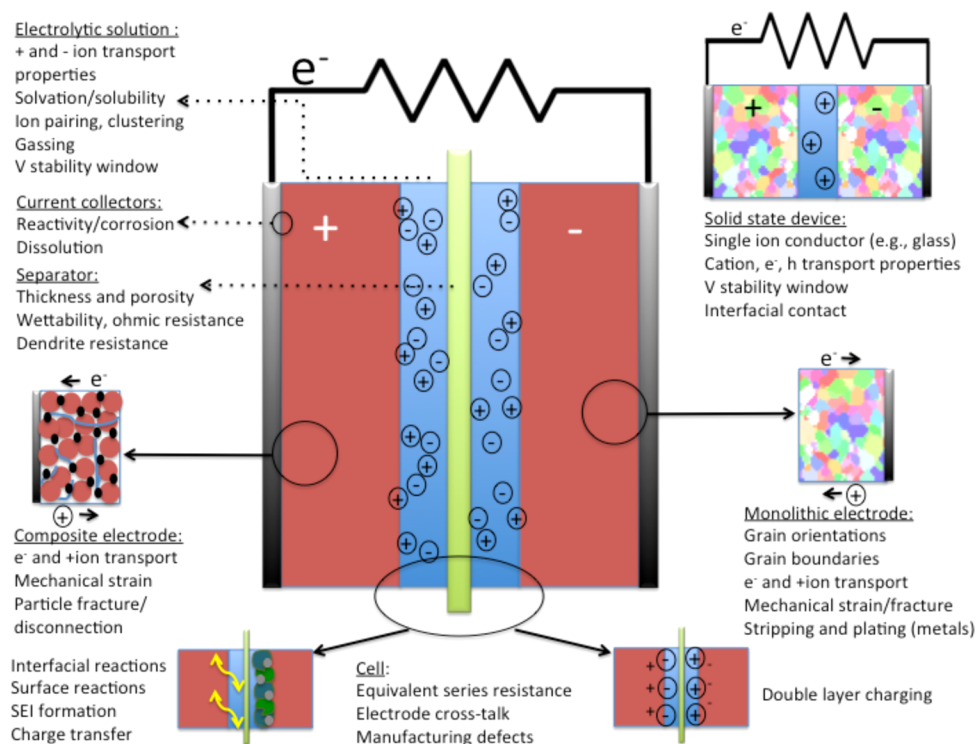
Figure 2. A scheme showing the components of an electrochemical device (solid state device shown in the upper right corner). In spite of the fact that these devices are made up of only a few components, there are myriad complex phenomena over a range of temporal and spatial scales that govern their behavior, many of which are shown here.

time of discharge, showed much lower overpotential upon charge than cells in which Li_2O_2 is the discharge product.[61] Lower overpotentials (better round-trip efficiencies) are also observed for sodium/air batteries, which form stable NaO_2 as a discharge product, rather than a peroxide.[62] This observation has led some researchers to propose sodium/air as an alternative to lithium/air batteries.

In addition to the challenges associated with sulfur or air cathodes, there are still safety and reliability concerns associated with the cycling of lithium metal in these cells. This has prompted renewed interest in solid electrolytes, whether used in a hybrid design as a protective layer for lithium metal combined with an aqueous or organic electrolytic solution on the cathode side or in completely solid-state devices. Thin film solid-state lithium microbatteries utilizing glassy electrolytes[63,64] have long been known to exhibit impressive cycle lives without dendritic growth. They require expensive vacuum deposition techniques to make, however, and the thin formats result in low energy densities, limiting practical applications. The recent discovery of several new high conductivity glasses, glass-ceramic, and crystalline materials such as garnet structures (e.g., $Li_{7-x}La_3Zr_2O_{12}$, LLZO) and $Li_{10}GeP_2S_{12}$ (LGPS)[65,66] have reignited activity in the field, along with the promise of solving the safety and cycling problems of secondary batteries with lithium anodes. To become reality, lower cost processing techniques are needed, as well as careful engineering of solid–solid interfaces to ensure reliable cycling of capacities comparable to those in lithium-ion batteries. Solid polymer electrolytes, which have been studied since the late 1980's, are another solution for ensuring reliable cycling of lithium;[67] these are used in the short term rental cars available in Paris, known as the BlueCar (http://www.pininfarina.com/en/pininfarina_bluecar/?category_nav=sustainable).

Batteries based on other alkali metals or alkaline earths are also under consideration. Concerns over lithium supply security[68] have stimulated research on sodium-ion batteries, which, in principle, operate like the lithium-ion analogs. Research has focused primarily on development of new electrode materials,[69] particularly for anodes, because graphite does not intercalate sodium to any significant degree. The ability to leverage engineering knowledge gained over 25 years of work on lithium ion batteries means that progress has been rapid in this field. For example, Na-ion batteries with energy densities exceeding that of Li-ion batteries containing $LiFePO_4$ have already been demonstrated in a 3 Ah prismatic cell format, with claims of better safety for the sodium-containing cells (http://www.faradion.co.uk/technology/sodium-ion-technology/).

Batteries with Mg anodes are in a much less advanced stage of development. A report of a magnesium battery using a Chevrel phase MoS_8 cathode and a magnesium organohaloaluminate electrolyte[70] demonstrated the feasibility of the system. However, cathodes with higher voltages and/or capacities, such as oxides, are needed to fully realize the high theoretical energy density promised by this system.[71] Better electrolytes that both allow stripping and plating of magnesium and operation of higher voltage cathodes also need to be developed. Recent reports of reversible stripping and plating of calcium[72] in an organic electrolytic solution, and insertion of calcium ions into a Prussian blue host,[73] raise the intriguing possibility of a rechargeable calcium battery, but this is still at the proof-of-principle stage.

Details of the operation of these batteries, whether in advanced states-of-development like Li-ion systems, or nascent, as in some of the Beyond Lithium Ion chemistries described above, are amenable to study using synchrotron techniques.

The ability to study multiple length scales from the macroscopic (e.g., systems level problems such as battery safety) to the microscopic (behavior of electrodes and materials during cycling under a variety of conditions) and below (e.g., electronic structures of materials) at synchrotron facilities provides ample opportunities for understanding the functioning of these devices. Ex situ studies using laboratory X-ray sources and other characterization techniques are important for understanding equilibrium behavior of battery materials, and improved fundamental understanding of battery operation may be obtained from high-energy synchrotron X-ray studies. Particularly for fast charge rates, which are technologically most relevant, in situ properties can significantly change from the equilibrium behavior. Understanding of nonequilibrium pathways are indispensable for achieving better battery operation. Synchrotron sources, due to their high power and flux, are ideally suited for rapid in situ studies. Materials can be studied in the real environment, and structural information can be gained in seconds.[74,75] At this point, it is necessary to define the terms "in situ" and "in operando". In situ means in position, while in operando represents a special case of in situ, where the battery is in operation. In this review, most studies satisfy both in situ and in operando definitions because X-ray characterizations are done during the operation of batteries and the position of batteries are not moved during data acquisition. Therefore, these two terms can be used interchangeably. We would also like to emphasize that in situ provides the benefit of measuring a real-world sample, but in soft X-ray spectroscopy, data from in situ experiments are much more complicated to interpret and the much worse signal-to-noise ratio eliminates many possibilities of detailed quantitative analysis. At this time, unless the intention is specifically to study dynamic processes, ex situ spectroscopic experiments will not be replaced by in situ ones for soft X-rays, and they will remain as the major probe technique for technical reasons. In the next section, we outline the grand challenges associated with the rechargeable batteries described above, and subsequently, we review the applications of synchrotron X-ray analytical techniques in understanding battery chemistries (ex situ, in situ, and in operando) and describe how the obtained knowledge can help better design next-generation rechargeable batteries.

2.3. Grand Challenges in Rechargeable Batteries

The electrochemical cells that make up batteries are, at first glance, simple devices consisting of only a few components. A closer look, however, reveals their complexity (Figure 2). Phenomena pertinent to the functioning of batteries occur over wide spatial and temporal ranges. For example, double-layer charging occurs in milliseconds or less,[76] but degradation contributing to capacity decay may occur quickly or very slowly, on timescales that can span from fractions of seconds to months or even years. These may be chemical reactions that occur on the molecular level at interfaces that may span only a few nanometers across, or they can be in the form of bulk changes over large areas, such as mechanical degradation due to volume changes in electrode active materials undergoing redox reactions. To complicate matters further, electrochemical, mechanical, and chemical processes can be coupled (e.g., particle fracture due to volume changes induced by redox reactions, which exposes fresh reactive surfaces, results in excessive consumption of electrolytic solution to form fresh SEI layers on these surfaces, a well-known problem for silicon anodes for LIBs). These processes are often dependent on state-of-charge and whether the system is at rest (in equilibrium) or operating under dynamic conditions (far from equilibrium) as well as the rate at which the cell is being charged or discharged. In some cases, performance is dependent upon certain physical characteristics of a material, such as particle size. Nanometric materials may exhibit considerably different phase behavior than conventionally sized powders, as well as exacerbated reactivity with electrolytic solutions because of increased surface area, in some cases. These complexities can present considerable challenges to the scientist wishing to understand the behavior of battery materials. Time constraints often require that experiments be carried out ex situ (it is not usually practical to carry out long cycling experiments at a beamline, for example), but then only information about the system in equilibrium is captured. These experiments may be necessary and important as a first step, particularly for new battery systems where little is known, but more sophisticated in situ or in operando experiments are often required to gain a sufficient understanding about systems undergoing dynamic changes. In addition to the aforementioned time constraint issue, cell design may introduce artifacts into the data, and signals from cell hardware can interfere with those arising from the materials of interest, so that these experiments must be designed and interpreted with care.

These complexities often mean that a multimodal approach is needed to fully understand the functioning of a battery material as it is charged, discharged, cycled, aged, or subjected to abuse testing. Depending on the question being asked, a high degree of chemical specificity and sensitivity or temporal and/or spatial resolution may be required. A number of sophisticated synchrotron techniques are now available, which can be combined with advanced microscopy and conventional laboratory physical and electrochemical characterization to form a full picture of the behavior of battery materials of interest. A short discussion of typical problems of interest to battery scientists follows directly, and Table S1 summarizes techniques covered in this article.

As the redox active components in a functioning battery undergo charge and discharge, changes to their bulk crystal and electronic structures occur, which may have profound effects on the functioning of devices. Candidate electrodes may exhibit solid solution behavior and/or one or more reversible or irreversible phase transitions during normal or abusive cycling conditions, such as overcharge or overdischarge, which may be encountered during use in the real world. Capacity loss could occur even in chemically reversible processes if changes in lattice parameters or unit cell volumes are enough to create significant strain or even particle fracture, and may further lead to disconnection in the composite electrodes. Detailed information about structural changes during electrochemical processes not only lend insight into failure modes of devices but also allow a rapid assessment as to the possible utility of new electrode materials, as well as optimal operating conditions such as voltage limits. This is particularly important for Beyond Lithium systems such as Na-ion or Mg and Ca batteries, where the search for new electrode materials is very active and relatively little is known.

Understanding what bulk structural changes occur under a variety of abuse conditions (e.g., at elevated operational temperatures) is also critical for assessing aspects of safety. For example, the temperature at which phase conversions involving loss of oxygen occur in oxide electrodes provides information about thermal stability, which in turn has

implications for the propensity of a device to catch fire or explode. In electrode materials containing more than one electroactive metal, there may be questions as to which one is undergoing changes in redox states at any given point during charge or discharge. This can help narrow options when the potential compositional space is large and complex (such as for oxides containing Li, Ni, Mn, and Co).

Subtle structural features such as cation ordering may affect electrochemical properties but also may be difficult to detect using common laboratory techniques. For example, ordered (space group $P4_332$) and disordered (space group $Fd\bar{3}m$) $LiNi_{0.5}Mn_{1.5}O_4$ spinel samples show different phase behavior during charge, and the former appears to be more kinetically limited than the latter,[77] but it is often difficult to distinguish the two types of polymorphs using laboratory diffractometers. High-resolution X-ray diffraction is often required to discern these subtle structural variations. Orientation effects of grains in polycrystalline thin films of electrode active materials or solid electrolytes affect both total conductivities and rates of ion diffusion profoundly. Micro- or nanoscale structural details are needed to understand these effects.

The interfacial and surface characteristics of components in electrochemical cells are also extremely important in determining cycling behavior. It is not an exaggeration to say that successful functioning of Li-ion batteries depends crucially on the proper formation of the solid electrolyte interface on anode surfaces. Although the phenomenon of lithium intercalation into graphite was known for years before the advent of the modern lithium-ion battery,[78] it was not until researchers discovered the critical role of ethylene carbonate in passivating carbon surfaces that the system could be made reversible and practical devices could be engineered. Inefficiencies in SEI formation associated with large volume changes (such as for silicon electrodes) or under some abuse conditions adversely affect cycle life and, in extreme cases, compromise the safety of devices. Understanding the SEI presents numerous challenges, as it is normally very thin (a few to a few hundred nanometers thick) and its composition and physical characteristics vary with the conditions of the formation cycle, type of anode and system (Na-ion vs Li-ion, for example), the use of additives, temperature, etc.

In addition to the all-important SEI, reaction layers on cathode surfaces are of interest. While rarely completely passivating, these cathode electrolyte interfaces (CEI) can impact the functioning of batteries by, for example, increasing cell impedance. The composition and thickness of the CEI varies with cell cycling conditions including operating temperature and voltage limits used. For example, even at slightly elevated temperatures of about 50 °C, dissolution of transition metals may be exacerbated. Dissolved ions may form complexes with decomposition products of the electrolytic solution and precipitate at cathode surfaces.[79] Alternatively, dissolved ions or complexes may migrate to the anode and disrupt the SEI. The latter process is thought to be a factor in the relatively short cycle life of cells containing manganese oxide spinel cathodes.[80]

The surfaces of active electrode materials themselves may undergo phase reconstruction during cycling or storage under a variety of conditions. These surface layers often have a strong impact on the electrochemistry, particularly if phases are formed through which lithium ions have low mobility. Because these layers are often extremely thin, they are not detectable using techniques that probe bulk structures such as conventional X-ray diffraction. Even sophisticated transmission

electron microscopy (TEM) plus core level spectroscopy techniques such as electron energy loss spectroscopy (EELS) can usually provide detailed information on only a few particles at a time, so that there is always a question of whether the results are anomalous or typical of the sample as a whole. To provide a complete picture, it is necessary to employ techniques that allow probing of a much larger number of particles in addition to the microscopy.

Surface and interfacial properties of solid electrolytes, such as those consisting of ceramic materials, also strongly affect their electrochemical behavior. Ideally, these components are extremely thin (on the order of microns or tens of microns), so that any interfacial or surface reactions (e.g., occurring during processing) resulting in the production of impurity phases bear an outsize influence on their properties and can be extremely difficult to characterize due to the small amounts that are produced. Likewise, the chemistry of grain boundaries in polycrystalline films is similarly difficult to probe but can dominate the electrochemical behavior.

Interfaces and surface regions vary considerably in their structure, complexity, and composition and have a profound impact on electrochemical behavior. They are frequently not homogeneous throughout their thicknesses, so the ability to study buried interfaces is particularly valuable. Their study requires surface-sensitive techniques, preferably those with depth profiling capabilities.

Redox processes involving battery materials can be quite complex, encompassing a variety of behaviors including dissolution/precipitation reactions, one or multiple phase transitions, and/or solid solution reactions. Active materials are often solids, but some dissolve into the electrolytic solutions and some are even gases. In some cases, one or both end-members and/or intermediates have low electronic or ionic conductivity. Cell malfunctioning and premature failure may occur as a result of interrupted electron and ion conducting pathways due to the distribution of these insulating phases. Fundamental information about how these reactions proceed is necessary to optimize cell and electrode design and guarantee robust and safe cycling. For example, in Li/S batteries, polysulfide intermediates formed upon cell discharge dissolve into the electrolytic solution and shuttle between the negative and positive electrodes. Eventually, insulating Li_2S precipitates, preventing further passage of current and causing premature polarization. To prevent or minimize crossover of intermediates, cells have been designed with protective or size-excluding membranes and specialized carbon morphologies in cathodes, which can act as traps for polysulfides. To determine the efficacy of these approaches, specific information about speciation is required, particularly in operating cells with realistic loadings and low amounts of electrolytic solution.

Similarly, Li/O_2 cells may polarize prematurely, well before reactants are completely consumed, because the insoluble Li_2O_2 product is electronically insulating. Once there is enough Li_2O_2 to completely cover the carbon electrode to a critical thickness, the flow of electrons to the active surfaces is inhibited and further reaction cannot occur.[56] Conversion electrodes discharge to form a mixture of metallic nanoparticles and an insulating phase such as Li_2O. Many of these electrodes can be recharged, implying that unbroken electronically conducting pathways are formed, sufficient to support electron transport, but details on this are scarce. Another example involves the $LiFePO_4$ electrode, which undergoes a two-phase charge/discharge process throughout the entire composition range,
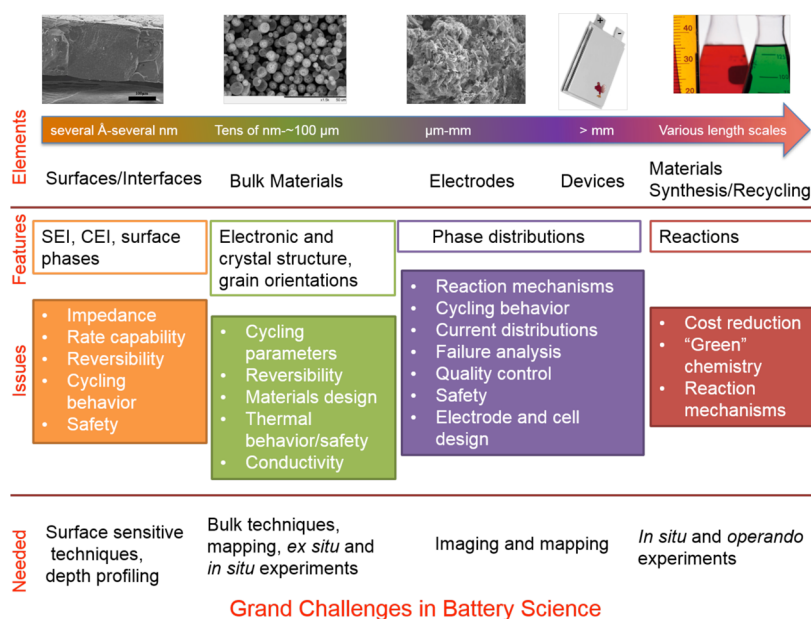
Figure 3. Schematic of grand challenges for rechargeable batteries.

with $FePO_4$ produced as the oxidation product. Both $LiFePO_4$ and $FePO_4$ have low electronic conductivities, and yet electrodes can be cycled successfully, often at very high rates. To explain this, researchers have postulated the existence of solid solutions, Li_xFePO_4 and $Li_{1-x}FePO_4$, close to the end of charge and discharge, which can support transport of ions and electrons. Considerable evidence for the existence of solid solutions, particularly in nanometric olivine $LiFePO_4$, has now been observed to support this theory.[80] Clearly, the distribution of these phases in particles and/or electrodes as a function of state-of-charge is key to understanding how these systems function or how they fail. In addition, information about how phases propagate in composite electrodes may give valuable clues to reaction mechanisms. In all of these cases, methods to map or image phase distributions in particles or in electrodes are extremely useful, and may be especially helpful in optimizing particle morphologies, composite electrode fabrication, and cell design.

Other instances in which imaging and mapping techniques may be of use involve identifying inhomogeneities in cells that have been cycled at high rates or under abuse conditions, have fabrication flaws, or in those that have unusual designs, such as thicker-than-normal electrodes. The latter is particularly important because one straightforward way to increase energy density in batteries may simply be to increase electrode areal capacity. How to do this without compromising power capability or complicating manufacturing is not yet clear, however. The distribution of phases throughout cycled electrodes may give useful information about current distributions in operating cells, important from the standpoints of safety, quality control, and cell design.

Finally, the need for greener, less costly, and less energy-intensive manufacturing and recycling processes is becoming more apparent as lithium-ion batteries increasingly penetrate the vehicular market and are being considered for large-scale energy storage. The ability to monitor the synthesis or recapture of battery materials in real time under realistic conditions would be a real boon for achieving these goals.

Figure 3 summarizes the grand challenges in battery science as outlined in this section. As will be demonstrated in the following sections, a wide variety of synchrotron X-ray techniques are available, which can offer deep insights into these questions. The nearly nondestructive nature of these techniques, as well as options to perform a wide range of experiments in or ex situ or in operando are particular advantages to using these facilities. As time has gone on, these experiments have become increasingly sophisticated, matching the explosive growth in interest in battery science.

3. BRIEF OVERVIEW OF SYNCHROTRON RADIATION

3.1. Generation of X-rays

Synchrotron radiation is based on an important theorem of classical electrodynamics: if a charged particle undergoes a change of direction at a relativistic speed, electromagnetic radiation will be emitted as a narrow cone tangent to the path of the moving particle. In a synchrotron facility, bunches of electrons are filled and accelerated to a final energy of about 1.5−8 GeV, close to the speed of light, and maintain at a fixed energy in the storage ring (by a RF field in a microwave cavity). Electromagnetic radiation is generated when the electron bunches are accelerated (bent) by magnetic fields. In the simplest case, a single dipole (bending) magnet causes the electrons to move along a curved trajectory (according to F = v × B, following the right-hand rule), corresponding to an (centrifugal) acceleration that emits a wide fan of electromagnetic radiation that covers a broad energy range along the moving curve, as schematically shown in Figure 4a. In straight sections, more intensity can be emitted in, and a periodic magnetic structure, the so-called undulator, causes the electrons to move with angular excursions without a net change of direction. For small angular excursions, the emitted radiation can add up coherently, causing constructive (and destructive) interference at particular wavelengths giving rise to harmonics. As indicated in Figure 4b, the energy bandwidth from harmonics is inversely proportional to the number of magnetic groups, N, and the angular spread is further reduced by the inverse square root of N. Modern synchrotron facilities operate
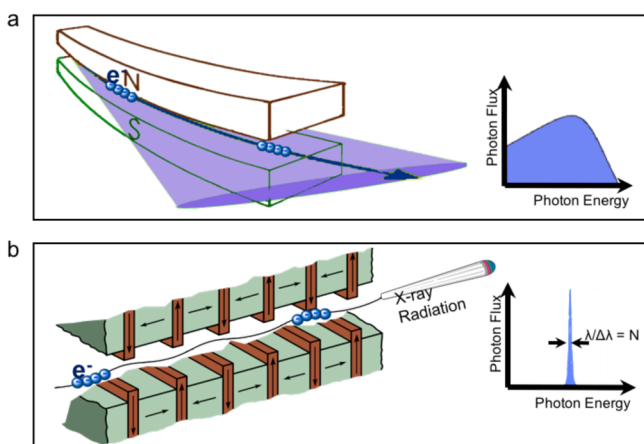
Figure 4. Schematic diagrams of the generation of synchrotron radiation by injecting electron bunches into (a) one group of bending magnets or (b) an undulator with a parodic magnetic structure. (a) The photon spectra on the right show the broad energy distribution of the radiation based on bending magnets, (b) compared with the narrow energy range with a small angular divergence of the beam based on undulator.

with various other kinds of magnetic structures both to maintain the focus of the electron orbits and to obtain X-ray radiation with different properties. A complete discussion of the physics of synchrotron radiation is outside the scope of this review, but interested readers are referred to more detailed reviews and books on synchrotron radiation.[81]

3.2. Differences between Hard and Soft X-rays

Compared with laboratory X-ray sources, one of the advantages of synchrotron radiation is the continuously tunable photon energy across a wide range with pertained high brightness and flux. Figure 5 shows one classification of the different photon energy ranges that can be accessed through synchrotron radiation. The colored bands indicate the narrow range of light that is visible to human eyes. At this time, the whole range of wavelengths has been utilized for studying battery materials through both ex situ and in situ experiments. For example, synchrotron-based infrared (IR) provides superior brightness and spatial resolution for FTIR studies;[82] ultraviolet (UV) and soft X-rays are widely used for chemical analysis at surfaces, and hard X-rays have been broadly employed in the battery field for probing bulk lattice and electronic structures. This review is by no means able to cover the vast field of all the synchrotron techniques, instead focusing specifically on the synchrotron-based X-ray techniques with the highest applicability for understanding and improving battery materials.

The definition of X-ray "hardness" intuitively stems from the fact that the soft and hard X-ray photons penetrate shallow and thick matters, respectively. Soft X-rays have a photon energy range of several tens of electron volts (eVs) to about 2 keV, whereas hard X-rays are classified to start from a few keV to tens of keV. The intermediate energy range that falls in the middle of the soft and hard X-ray ranges (including sulfur K-edge energy), designated "tender" X-rays, has attracted increased attention recently, partly due to the rapidly growing interest in battery materials such as S. The different energies (i.e., wavelengths) of the X-ray photons determine their applicability in probing the real-space ordering in materials through diffraction. Short wavelengths allow bulk lattice structure determination through XRD, while the longer
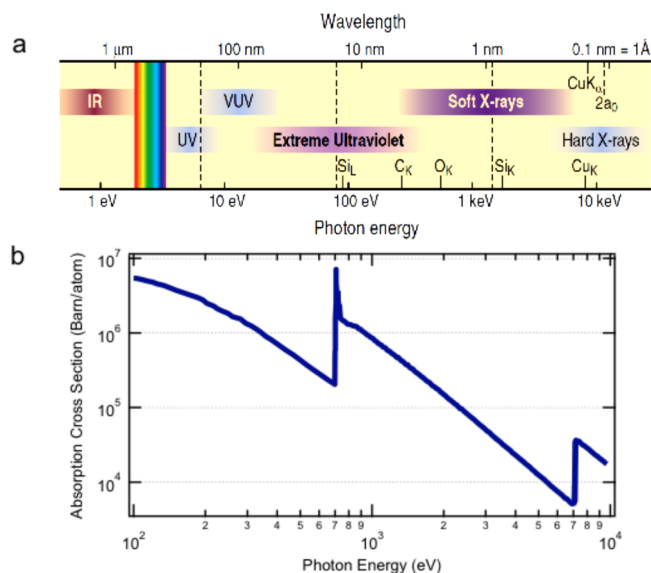
Figure 5. (a) Nominal classification of the different photon energy ranges that are accessible through synchrotron radiation, where the colored bands represent the visible light range. Note that today's synchrotron X-ray experiments sometimes utilize hard X-ray energy beyond the scale shown in (a) and above 10^2 keV. (b) Absorption cross section of iron (Fe) within the full energy range of 100−10000 eV. The photoionization cross section for an iron atom across the soft and hard X-ray regime, showing the Fe core-ionization (edges) in the soft (Fe 2p core ionization, Fe L-edge, about 710 eV) and hard (Fe 1s core ionization, Fe K-edge, about 7100 eV) X-ray region. The figure was used with permission from ref 81. Copyright 2000 Cambridge University Press.

wavelengths of the soft X-rays enable the probes of the long-range order of the electronic structure and overall morphology in the scale from a few nanometers to hundreds of nanometers.[83]

In addition to the differences in the photon energy range, there are several other contrasting properties between the hard and soft X-ray techniques that are relevant to battery material studies. Fundamentally, these differences result from the different scales of the interactions of X-ray photons with matter. The strength of the interaction is described in the terms of the atomic scattering cross section and/or absorption cross section, which defines the energy-dependent effective area of an atom when an X-ray photon strikes it. Figure 5b displays an example of the photoabsorption cross section of an Fe atom within the full energy range of 100−10000 eV. The cross-section values at the soft (about 710 eV) and hard (about 7100 eV) X-ray absorption edges correspond to the excitations of a 2p and 1s core−electron, respectively. As is generally true across the periodic table, the absorption cross section in the soft X-ray range is over two orders of magnitude stronger than that in the range of hard X-rays. These different levels of the interaction strength lead to very different probing depths. For the photon-in-photon-out (PIPO) techniques, the probe depths of soft X-ray techniques vary from about 100 nm to hundreds of nanometers depending on the incident photon energies. However, hard X-ray techniques can easily provide probing depths in the microns and millimeters ranges, which allow for directly studying reactions under a variety of conditions. Benefiting from its deep penetration depth, in situ experiments with hard X-rays have been extensively employed for studying battery materials under operating conditions.
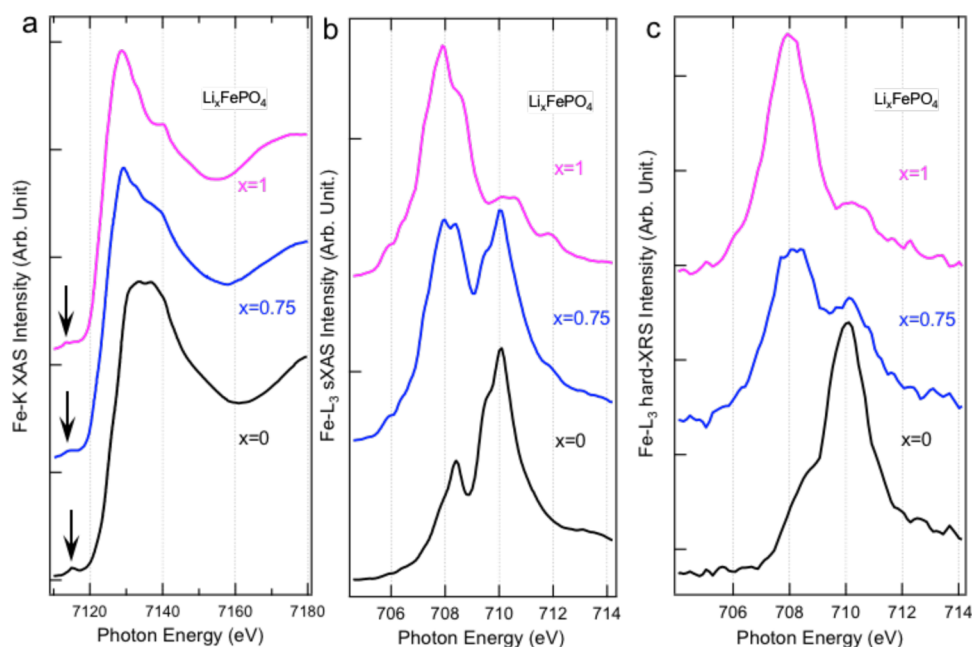
Figure 6. Direct comparison of (a) the hard X-ray Fe−K edge XAS, (b) the soft X-ray Fe-L$_3$ edge soft XAS, and (c) the hard X-ray Raman Scattering of the same batches of Li$_x$FePO$_4$ with lithiation levels of x = 0., 0.75, and 1. The arrows in (a) indicate the 1s-3d quadrupole excitations but without the multiplet effects that often manifest themselves as the sharp features in the L edge spectra. Hard X-ray Raman scattering benefits from its deep probe depth but with relatively low detection efficiency. Data reproduced from ref 84. Copyright 2014 John Wiley and Sons. Data reproduced from ref 85. Copyright 2012 American Chemical Society.

Although modern soft X-ray systems also enable various kinds of in situ experiments in electrochemical devices,[84] the information obtained through hard X-ray and soft X-ray analytical techniques are often complementary and with points of interest at different length scales. Another critical contrast between the hard and soft X-ray PIPO spectroscopy is the very different excitation/decay channels when the X-ray photon energy is absorbed by the electrons. In core-level spectroscopy techniques, if the excited core electrons remain in the material (i.e., not directly onto the detector as a photoelectron), the excitation or transaction probability W is governed by the Fermi Golden Rule: $W_{fi} = (2\pi/\hbar)|<\Phi_f|T|\Phi_i>|^2 \delta(E_f - E_i - \hbar\Omega)$, between the initial state Φ_i and final state Φ_f, with the transition operator T that is regulated by the dipole selection rule of $\Delta l = \pm 1$. Therefore, the K and L edges of X-ray techniques intrinsically correspond to the excitations of the s and p core electrons to the p and d states, respectively. The dipole selection rule defines the orbitals of the final states with high enough count rate to be detected by experiments. This leads to an important difference of the excited states between the soft and hard X-ray core-level excitation processes, in addition to the typical coverage of the low Z (soft X-ray) and high Z (hard X-ray) elements due to the core level binding energies. A typical example is the absorption and emission process of 3d transition metals, where soft X-ray probes the 3d states through 2p to 3d excitations, but hard X-ray probes the 4p states through the 1s to 4p excitations with a weak quadrupole 3d feature at a lower energy. The different excitation processes also determine the very different theoretical approaches in the interpretation of the experimental spectra, and the 3d state features detected through the soft and hard X-ray spectroscopy principally comprises different levels of information on the 3d transition metals. For photon-in-electron-out (PIEO) techniques using electron yield including X-ray photoelectron spectroscopy (XPS) and X-ray absorption spectroscopy

(XAS), the probe depth depends on the electron escape depth at different kinetic energies. The probing depth varies from several Ångströms to several nanometers (in the soft X-ray regime) to 10s of nanometers for harder X-rays.

Figure 6 shows the comparison of the hard X-ray Fe K-edge XAS and the soft X-ray Fe-L$_3$ edge soft XAS of Li$_x$FePO$_4$ with lithiation levels of x = 0, 0.75, and 1. The Fe−K XAS displays the leading edge shift of the main 1s to 4p excitation, with a weak quadrupole 1s to 3d feature at about 7113 eV indicated by the arrows. The Fe-L$_3$ soft XAS displays a complete change of the spectral line shape, which directly corresponds to the reconfiguration of the Fe 3d electron states at different lithiation levels.[85] This increased sensitivity at the L-edge is a combination of the direct dipole transition into the 3d-derived frontier orbitals and the sharper line widths in the soft X-ray regime. This sensitivity often comes at the cost of less flexibility in the sample environment than what is offered at higher energies.

An alternative technique, hard X-ray Raman Scattering (hard XRS) can access soft X-ray edges through inelastic scattering, and when measured within the low-momentum transfer regime (i.e., a small deflection angle), the c transitions provide identical information to soft XAS[86] (dipole) transitions. The hard XRS, although with low statistics and resolution compared with soft XAS, circumvents the issue with the shallow probing depth of low-energy soft X-rays, and uniquely provides a bulk probe of low-energy excitations in the materials of interest.[87] Figure 6c is the hard XRS spectra collected on the same samples used for the soft XAS. Although the resolution and signal-to-noise ratio of hard XRS is relatively low, the contrast of the bulk signal of the Li$_{0.75}$FePO$_4$ with that of the soft XAS result is clearly shown. The hard XRS line shape at the intermediate lithiation level shows a lithiation level that is consistent with the bulk lithiation level of x = 0.75. However, the soft XAS shows a much lower lithiation level (x = 0.48) on the surface, indicating
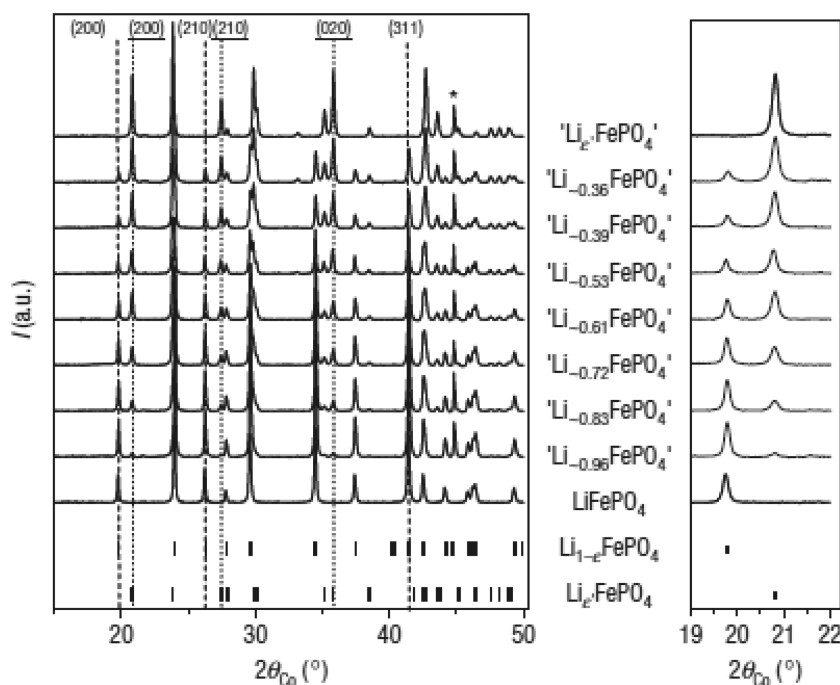
Figure 7. Ex situ XRD patterns of Li_xFePO_4 electrodes collected at various states of charge during the 1st cycle of Li/LiFePO$_4$ cells. Miller indices are given in the *Pnma* space group for selected reflections for the Li-rich phase ($Li_{1-\varepsilon}PO_4$) and for the Li-deficient phase ($Li_\varepsilon FePO_4$). The Miller indices of $Li_\varepsilon FePO_4$ are underlined in the figure. Shown on the right is the magnified view of the (200) diffraction lines. Reprinted with permission from ref 127. Copyright 2008 Macmillan Publishers Ltd.

the surfaces of the particles consist of a lithium poor (oxidized) phase.[84] This observation is in contrast to what was observed in NMC materials using soft XAS, where the surface nickel is less oxidized than in the bulk.[88,89] At this time, the detection efficiency has been greatly improved, which broadens the applications of XRS in energy materials studies.[86] A combination of diverse X-ray techniques is often needed to conduct thorough studies for the structural and electronic properties of the surface, interface, and bulk of a battery component. Many studies of batteries combine several techniques to reveal the chemistry at multiple length scales.[90,91] The combination entails a number of X-ray techniques including diffraction, spectroscopy, and imaging, most of which are covered in this work.

## 4. APPLICATION OF SYNCHROTRON X-RAYS TO RECHARGEABLE BATTERIES

4.1. X-ray Diffraction (XRD)

XRD is widely applied to determine the structural properties of crystalline or partially crystalline battery materials. The obvious advantages of X-rays as compared to other probes are their high penetration power combined with the exceptional sensitivity of Bragg diffraction, allowing the study of structural dynamics. In an XRD experiment, the X-ray beam typically illuminates a large ensemble of particles, which are randomly oriented, but in the illuminated ensemble there will be a number of particles, which satisfy the Bragg condition. XRD data is collected for a range of scattering angles, and analysis allows determination of the crystal structure of the material under study. X-ray powder diffraction can be used to identify the lattice parameters of different phases and the relative contents of the different phases in a mixture. Microstructure information, such as crystal or grain size, strain, and texture, can also be quantitatively determined by analyzing the XRD patterns. The high intensity

of X-ray photon fluxes provided by synchrotron facilities are advantageous for time-resolved studies, but the basic principle of synchrotron-based XRD is the same as conventional XRD using laboratory X-ray sources. In fact, most powder XRD measurements can be performed in the laboratory, even for in situ or in operando experiments, provided that the data collection time is long enough to obtain a satisfactory signal/noise ratio. In practice, the high brilliance, high collimation, and widely tunable energy range of synchrotron facilities confer significant benefits due to the capability of penetrating through cell components and collecting data with high spatial and temporal resolution. Using high-energy synchrotron X-ray beams, even commercial batteries (e.g., coin cells, 18650 cells) can be investigated directly without any modification.[92−95]

In situ or in operando XRD measurements have been widely used to study structural changes of battery materials during electrochemical processes using synchrotron light sources. Almost all lithium ion battery electrode materials, such as insertion type materials (i.e., $LiCoO_2$, $LiMn_2O_4$, $LiFePO_4$, etc.),[96−116] conversion-type materials,[117−119] and alloy materials[120−124] have been studied by ex situ or in situ synchrotron XRD. In the following discussion, we will discuss the application of XRD to LiFePO$_4$ materials, solid-state electrolytes, layered cathode materials, and silver batteries. We will also discuss the pair distribution function (PDF) analysis of scattering data and the comparison between XRD and neutron diffraction.

4.1.1. XRD During Electrochemical Processes: Equilibrium and Non-Equilibrium Phase Transitions. LiFePO$_4$ is a cathode material of great scientific interest and has been used in some commercial batteries.[125] A two-phase reaction mechanism occurs during charge and has been verified by many in situ and ex situ XRD studies.[105,126,127] It is known that both
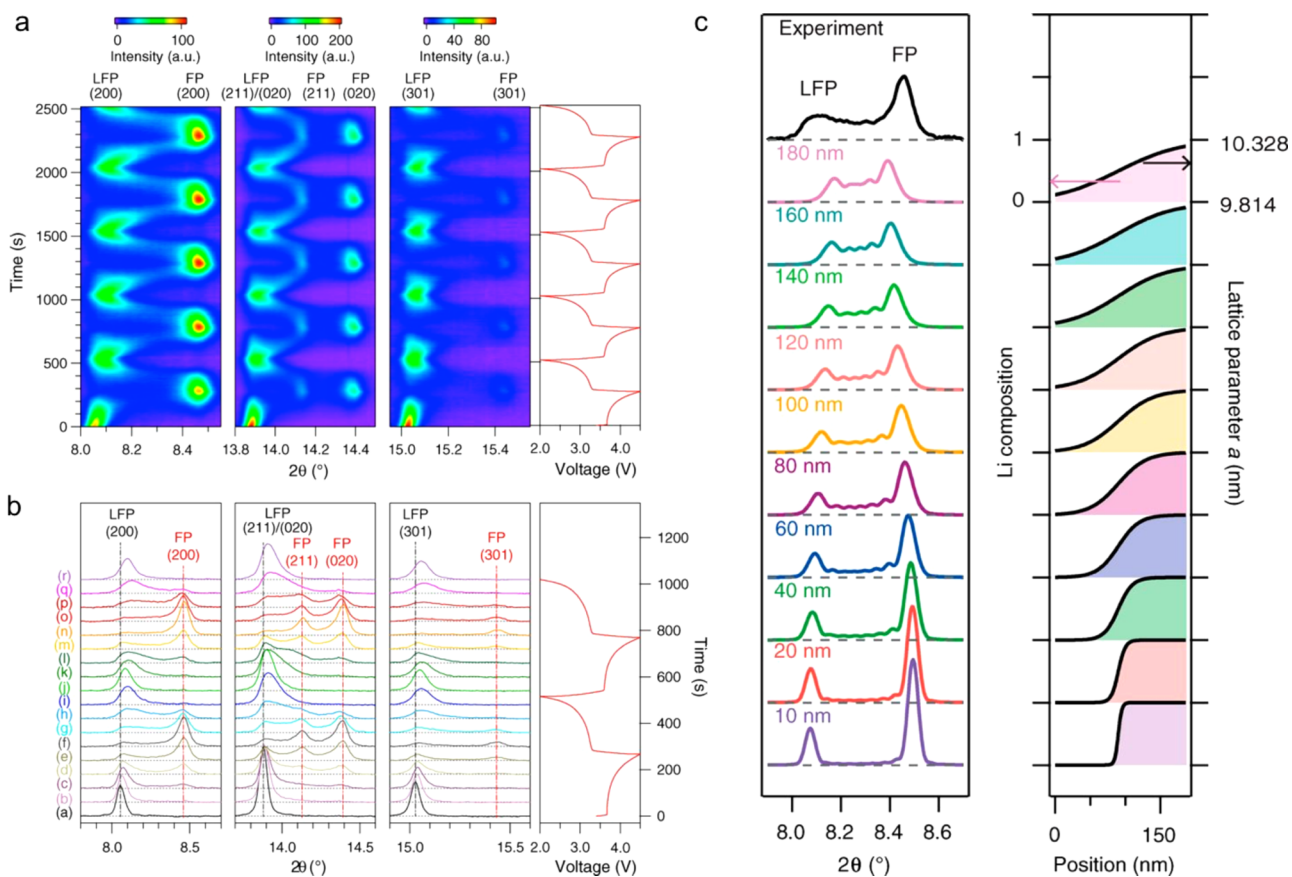
Figure 8. In situ XRD patterns of a Li/LiFePO$_4$ cell at a rate of 10 C. (a) The image plot for (200), (211), (020), and (301) reflections during the first five cycles and (b) selected individual diffraction patterns during the first two cycles are stacked. (c) Simulated reflection profiles with a continuous Li compositional variation in Li$_x$FePO$_4$. Reprinted with permission from ref 113. Copyright 2014 American Association for the Advancement of Science.

LiFePO$_4$ and FePO$_4$ are very poor electronic and ionic conductors. However, LiFePO$_4$ displays good rate capability when the primary particles are nanosized. Many studies have been performed to reveal how the intercalation reaction occurs in LiFePO$_4$ at the microscopic scale. The most widely accepted model, named the "domino-cascade" model, was proposed by Delmas and co-workers.[127] They carefully analyzed the ex situ XRD data collected at different states of charge (SOCs) and found that the coherent domain length of both LiFePO$_4$ and FePO$_4$ did not change significantly during the entire delithiation process (Figure 7). This indicates that the individual particles were either fully delithiated or fully lithiated and none were partially lithiated. They concluded that the lithium intercalation/deintercalation process proceeded through a LiFePO$_4$/FePO$_4$ two-phase reaction at a very high rate. Once the delithiation was initiated in a given LiFePO$_4$ particle, it proceeded very rapidly through the whole particle. Their work stimulated intensive theoretical and experimental work thereafter.[128−130]

However, this work was based on steady-state results (either after relaxation or under quasi-equilibrium conditions with low charge rates). Ab initio calculations predict that delithiation of a single LiFePO$_4$ particle (or lithiation of a single FePO$_4$ particle) may proceed via a nonequilibrium single phase Li$_x$FePO$_4$ (0 < x < 1) with overpotential, bypassing the nucleation and LiFePO$_4$−FePO$_4$ two-phase pathway.[131] The metastable Li$_x$FePO$_4$ phase relaxes to form LiFePO$_4$ and FePO$_4$ once the overpotential is removed. Phase field simulation also

suggests that the phase separation is suppressed through the formation of an intermediate phase under high currents. In order to verify this hypothesis as well as to understand the high rate behavior of LiFePO$_4$, it is important to probe the phase transformation under high rate cycling conditions in real time. In situ synchrotron XRD provides a tool for fast data collection to capture the structural changes of the material under high rate cycling conditions.

Orikasa et al. studied the phase transformation between LiFePO$_4$ and FePO$_4$ during nonequilibrium battery operation using time-resolved in situ synchrotron XRD.[132] A metastable crystal phase with an intermediate composition of Li$_{0.6−0.75}$FePO$_4$ was observed in micron-sized LiFePO$_4$ under high rate conditions (10C). This was the first observation of the metastable phase during electrochemical delithiation of LiFePO$_4$, and it supports the hypothesis of formation of a nonequilibrium solid solution under high rate cycling, rather than the distinct LiFePO$_4$/FePO$_4$ interface seen at low rate cycling. Liu et al. also observed the nonequilibrium solid solution phase (Li$_x$FePO$_4$) in nanosized LiFePO$_4$ (~190 nm) during high rate cycling.[113] They observed that the reflections of the XRD patterns started to broaden asymmetrically toward higher angles, which cannot be explained by size induced peak broadening (Figure 8, nucleation of the new phase). By comparing the experimental results with the simulated XRD, it was revealed that the asymmetric peak broadening was caused by compositional variation of the intermediate Li$_x$FePO$_4$ phase. In addition, the composition of the intermediate phase in
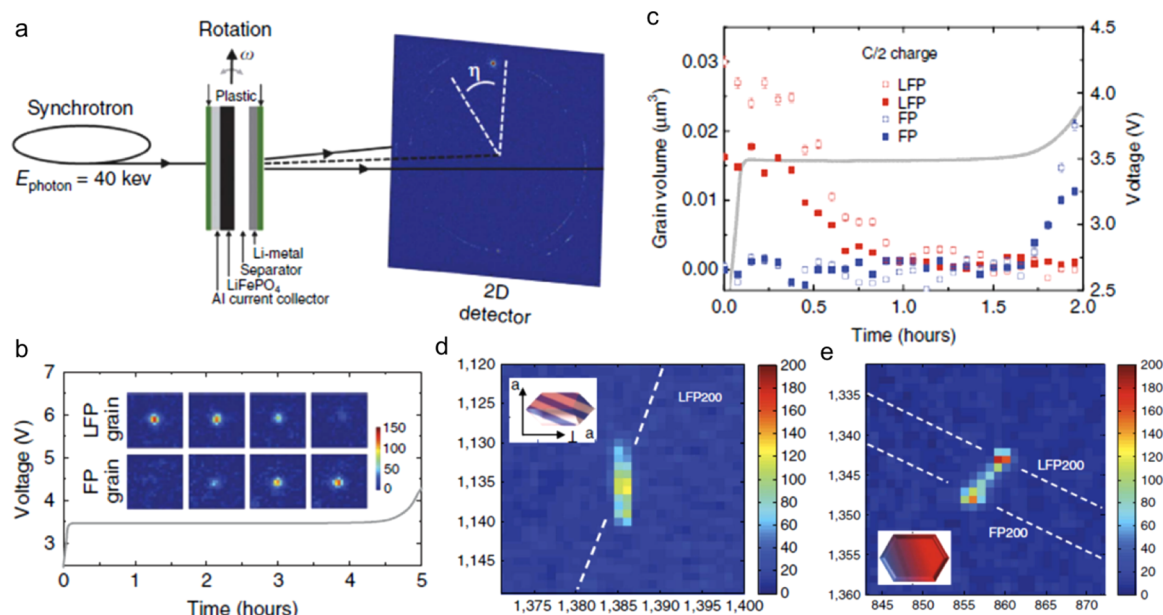
Figure 9. (a) Schematic representation of microbeam X-ray diffraction experimental setup. During the exposure, the sample was continuously rotated around the vertical axis. (b) Charging voltage curve (C/5) including the evolution of a 2D (200) LFP and (200) FP peak showing the progressive FP formation and LFP disappearance. (c) Volume evolution of two LFP and FP domains during C/2 discharge rate estimated from the diffraction spot. (d) Vertical streaks are observed for the LFP (200) reflections, indicating the formation of platelet-shaped domain. (e) (200) Reflection at 2C charging rate showing coexistence of the LFP and FP phases within a single grain. The dashed lines indicate the powder rings for the (200) reflections of the LFP and FP phases, indicated as LFP200 and FP200, respectively. Used with permission from ref 115. Copyright 2015 Nature Publishing Group.

nanosized $LiFePO_4$ was found to span the entire range between $LiFePO_4$ and $FePO_4$ (Li_xFePO_4, $0 < x < 1$), rather than the relatively narrow region ($Li_{0.6-0.75}FePO_4$) observed by Orikasa et al. in microsized $LiFePO_4$. This confirms the hypothesis that phase transitions in $LiFePO_4$ proceed via continuous structural changes (or intermediate phases) at high cycling rates instead of the distinct $LiFePO_4/FePO_4$ phase transition at low rate and helps to explain the good high rate capability of the $LiFePO_4$. These studies also highlight the importance of studying the nonequilibrium phase transition behavior of the battery materials under high rate cycling conditions, which might be quite different than the equilibrium phase transition behavior. Time-resolved in situ synchrotron XRD is a powerful tool for studying fast structural changes with appropriate temporal resolution.

4.1.2. Microbeam XRD and Grazing Incidence XRD.

The advent of highly efficient X-ray focusing optics allied with the high flux and high collimation available at synchrotron sources have made the use of X-ray microprobes routine on many beamlines. In the hard X-ray domain, both Fresnel zone plates and multilayer mirrors in Kirkpatrick-Baez configuration have achieved X-ray spot size below 20 nm.[133,134] Maintaining spot sizes that small could be quite challenging, requiring in addition to state-of-the-art optics, a sophisticated vibration damping system, beam stabilization, and temperature control. That is why, today, most hard X-ray microprobe beamlines provide X-ray beam sizes on the order of 0.2 to 5 μm.[135−139]

Hard X-ray microprobes are ideal for probing crystal structure (X-ray microdiffraction) and chemistry (X-ray microabsorption and microfluorescence spectroscopies). When used in scanning mode (sample is raster scanned under the X-ray microbeam), a hard X-ray microprobe provides spatially resolved maps of the distribution of phases, chemical states, and elements in the sample. X-ray microdiffraction and

microspectroscopic techniques are often used in combination on the same beamline. With its capability of quantitatively probing microstructure (identification of minute particles of crystalline phases, measurement of local crystal orientation, strain and defect density), synchrotron X-ray microdiffraction has been successfully employed for a number of materials science related problems, such as monitoring strain and defect buildups during in situ electromigration experiment on interconnects,[140] measuring residual stress in quartz samples from the San Andreas fault,[141] or monitoring crystal phase distribution in VO_2.[142] With X-ray microdiffraction, sample rotation should in general be avoided as rotation has the effect of modifying the sample probed volume and thus of removing the benefit of spatial resolution provided by a micron or submicron X-ray beam. Sample rotation is also generally not possible for composite materials such as batteries as different components of the sample and ancillary equipment would come into diffraction at different rotation angles. X-ray microdiffraction with a monochromatic beam should therefore be limited to cases when the diffracting materials are polycrystalline with grain size well below the size of the beam such as nanocrystallized samples with a micron size beam. This consists in adopting the powder diffraction approach of microdiffraction when a multitude of grains will statistically be in Bragg conditions to diffract. For samples with grain size on the order or larger than the X-ray beam size, an alternative approach is to use polychromatic (white or pink) radiation, so that Bragg conditions are satisfied simultaneously for multiple wavelengths for each grain. This consists of adopting the Laue diffraction approach of microdiffraction. The first three examples below are of monochromatic X-ray microdiffraction, the last one is of Laue (or polychromatic) X-ray microdiffraction.

The use of synchrotron microdiffraction for battery materials has been so far limited and to date only a handful of studies have taken advantage of it. Robert et al.[143] looked at lithiation into the copper-based oxysulfide $Sr_2MnO_2Cu_{3.5}S_3$. In this work, X-ray microfluorescence imaging was used to map elemental distribution within the electrode at different lithiation stages, in conjunction with X-ray absorption spectroscopy (XAS, discussed later) to probe oxidation state and X-ray microdiffraction, to identify crystalline species at selected locations on the sample. The measurements were performed with a monochromatic X-ray beam spot size of 9 μm by 5 μm. The data show that lithiation occurs in a two-step process. At first, Li ions insert themselves in the vacant sites of the electrode crystalline structure (intercalation). At a later stage, when all vacant sites are occupied, further Li ions are accommodated in the structure by displacing the Cu atoms, as seen by the appearance of the extruded copper reflections in the microdiffraction powder patterns.

A microbeam X-ray diffraction study on the rate-dependent phase transition mechanisms in $LiFePO_4$ particles in lithium ion batteries was reported by Zhang et al. for the first time.[115] For most powder XRD experiments, the X-ray beam probes a large number of particles with random orientations and the intensity of a segment or the whole (hkl) reflection ring collected by the 2D detector is integrated. Therefore, the results are averaged over a large number of particles (i.e., ensemble-averaged), and it is unlikely to distinguish intraparticle or interparticle multiphase reactions. The uniqueness of this work is the capability to study several groups of individual crystal grains with the same orientation by analyzing the individual diffraction spots with same η angles on different (hkl) rings. The η value is related to the orientation of the crystallite, and the shape and size of the spot is related to the shape and dimension of the phase domain being probed. Therefore, if multiphase spots appear at the same η angle, an intraparticle reaction can be assumed. The experiment setup and important results are shown in Figure 9. Because of the microsized X-ray beam (1.7 μm) used, the diffraction rings are broken into individual spots. By rotating the in situ cell to bring more grains into the beam, hundreds of $LiFePO_4$ grains could be monitored with good statistics. The results reveal that the average time of phase transformation time for individual $LiFePO_4$ crystallites is relatively slower than that expected by widely advocated particle-by-particle (mosaic) transformation. The two-phase coexistence within individual particles can be clearly seen in Figure 9b. Additionally, the observation of streak-like diffraction spots during charging in Figure 9 (panels d and e) indicates the platelet-shaped domains of $LiFePO_4$ and $FePO_4$ in individual crystallites. This is thought to be due to the fact that the thin platelet-shaped domains with well-defined interfaces may be responsible for the slow phase transformation observed under low C-rate discharge, due to the pinning of the domain walls by defects. With the increase of the charge C-rate, the thickness of the platelet-shaped domains increases and the sharp interface boundary becomes more diffuse, resulting in fast phase transformation. This work provided a new picture of phase transformations in $LiFePO_4$ as plate-shaped nanodomains ($LiFePO_4$ and $FePO_4$) coexist in individual particles and transform into each other during the charge−discharge process, which is quite different than the widely accepted particle-by-particle transformation mechanism.

Another study by Liu et al. used X-ray microdiffraction to probe the charge distribution in a $LiFePO_4$ containing composite electrode.[144] This was obtained by raster-scanning the sample with a 2 × 5 μm 6.02 keV monochromatic beam, and the measurement was done on the cross section of a battery electrode that had been charged to a 50% overall state of charge. The analysis of the diffraction patterns provided the relative concentration of the $LiFePO_4$ and $FePO_4$ phases, and the SOC information was accessible by calculating the $FePO_4$/$LiFePO_4$ ratio. Results showed an uneven distribution of SOC across the electrode at a high charge rate. The authors compared the SOC distributions for electrodes collected from a prismatic cell and a coin cell. It was observed that in the prismatic cell, the area closest to the current collector tab had the highest SOC, whereas in the coin cell the electrode surface showed higher SOCs. Note that these measurements were done ex situ, so they represent the equilibrium distribution of phases in the electrodes.

Microbeam diffraction has also been applied to study the influence of surface microstructure on the battery performance of a garnet-structured solid electrolyte (Al-substituted $Li_{7−x}Al_xLa_3Zr_2O_{12}$). Garnet structures have a chemical formula of $A_3B_2(XO_4)_3$, where A, B, and X are 8, 6, and 4 oxygen-coordinated cationic sites. Li-stuffed garnets contain more than three lithium ions per formula (e.g., $Li_7La_3Zr_2O_{12}$ (LLZO) and $Li_5La_3Ta_2O_{12}$).[145−147] Weppner and co-workers were the first to explore garnet lithium ionic conductors.[146−149] Cubic LLZO (space group $Ia3d$) has approximately 2 orders of magnitude higher conductivity than the tetragonal variant. This material was first successfully synthesized by Murugan et al. in 2007.[145] Its high ionic conductivity (>$10^{−4}$ S/cm)[145] and apparent stability against reduction by lithium metal, even when in direct contact with molten or evaporated lithium, have subsequently generated a great deal of interest in LLZO and related garnet structures for use in solid state batteries. Dense solid samples of ceramic electrolytes prepared for electrochemical and physical characterization are typically polycrystalline and contain numerous grain boundaries. Both the bulk structure and the grain boundaries determine the electrochemical behavior of polycrystalline ceramic electrolyte conductors.[65] For example, ion transport pathways along low-angle grain boundaries are more efficient than those along high-angle ones. This is because high-angle grain boundaries are usually energetically unstable and can undergo radical structural and compositional deviations, as has been reported in lithium lanthanum titanate (LLTO) and lithium aluminum titanium phosphate LATP, two other important crystalline lithium ion conductors.[150,151] Thus, it is valuable to study how grain boundary orientations affect electrochemical behaviors. Grain orientation and grain boundary misorientation distributions can be studied by synchrotron X-ray Laue microdiffraction, which was done for LLZO solid electrolyte bulk materials.[152] In this technique, X-ray energies between 6 and 22 keV are usually used, which delivers a probing depth close to 15 μm. Using the microbeam diffraction tool, it was found that in both large- and small-grained LLZO solid electrolytes, the distribution of grain orientation and grain boundary misorientations were, in fact, very similar (Figure 10).[153] Thus, the observed enhancement in the electrical properties of the small-grained sample could be attributed to grain boundary densities but not differences in geometries.

Grazing incidence X-ray diffraction (GIXRD) has also been used to characterize thin films of Al-doped LLZO fabricated by pulsed laser deposition.[154] In this technique, the X-ray beam is directed onto a flat sample at a shallow angle. By varying the
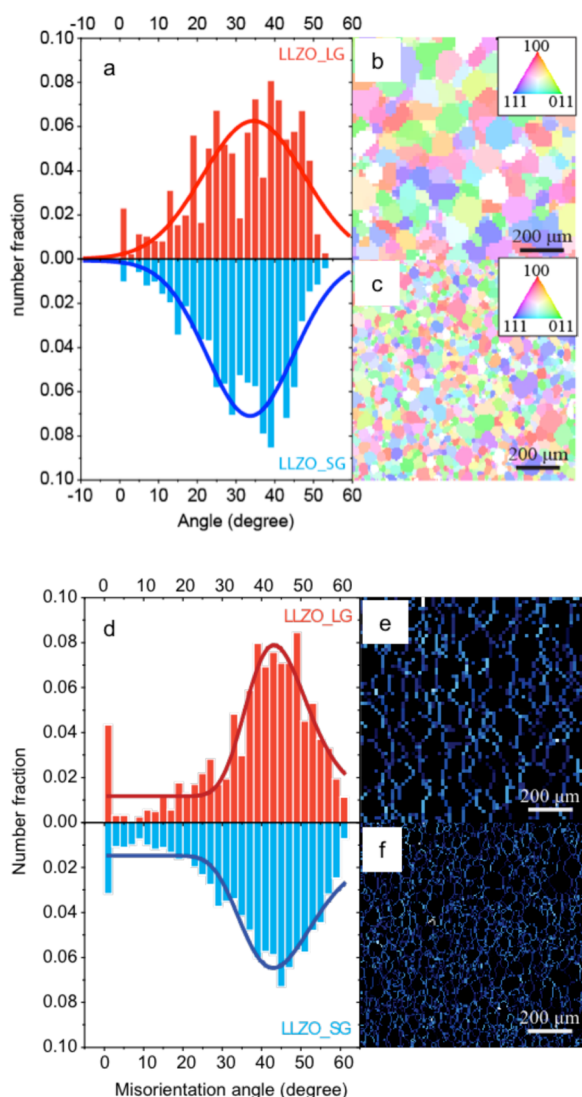
Figure 10. (a) Histograms of angles between grain orientation (100) direction and sample plane normal for a large-grained sample of LLZO (top) and a small-grained sample (bottom). (b and c) Grain orientation mapping of large- and small-grained LLZO, respectively. (d) Histograms of misorientation angles for large-grained LLZO (top) and small-grained LLZO (bottom). (e and f) Misorientation angle mapping of large- and small-grained LLZO, respectively. Reprinted with permission from ref 153. Copyright 2015 American Chemical Society.

incident angle, different probing depths can be accessed. GIXRD is particularly useful for surface characterization and for profiling the structure of thin samples as a function of depth. For this study, films were deposited on substrates heated to various temperatures. The conductivities of these films varied considerably, although all appeared to be amorphous when characterized by laboratory X-ray diffraction techniques. Using GIXRD, it was shown that the topmost surface (<5 nm, probed at 0.25 degrees) of the most conductive film (1.61×10^{-3} mS/cm) actually consisted of a mixture of tetragonal and cubic LLZO, and that less conductive films contained a $La_2Zr_2O_7$ impurity to a depth of about 300 nm (incident angle of 2 degrees).
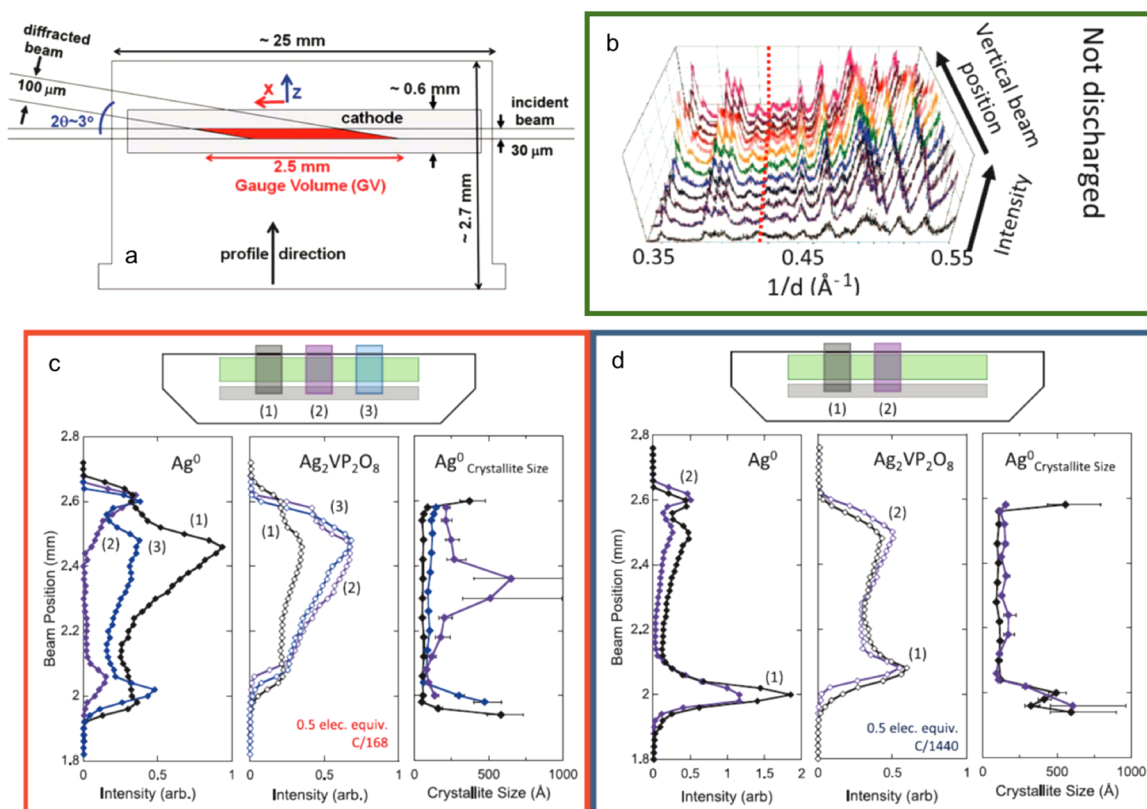
4.1.3. Energy Dispersive X-ray Diffraction. Taking advantage of high intensity X-rays covering a large range of energies from synchrotron X-ray sources, energy dispersive X-

ray diffraction (EDXRD) has been developed and applied recently to battery material studies. In contrast to most other powder XRD techniques, where monochromatic X-ray beams are used and 2θ angles are scanned, EDXRD uses polychromatic X-ray beams (or so-called white beams) and the signal is collected at a fixed angle to satisfy the Bragg conditions using a high-resolution energy dispersive detector. For powder XRD using monochromic beams, the entire signal from every part of the in situ cell is recorded, as long as it is in the optical path of the incident beam. This greatly restricts the geometry, components, and window materials that can be used in the cell design. In contrast, for EDXRD, as shown in the experimental setup (Figure 11), only the diffraction beams from the red "gauge volume" can reach the detector when a 100 μm aperture is used.[155] This provides not only the capability to penetrate real battery cells with thick metal cases but also to probe the electrode materials at different locations in the cell, such as at interfaces or near the current collector. The Bragg condition for EDXRD is shown in eq 2, where E is the X-ray energy in electron volts, d_{hkl} is the spacing associated with a special interatomic plane (hkl), and $b = hc/2$ (h is Planck's constant, and c is the speed of light).

$$E = b/[d_{hkl} \sin \theta] \tag{2}$$

The length of the X-ray beam perpendicular to the incident plane can be restricted to tens of micrometers, providing the capability to profile the phase distribution spatially along this direction. Takeuchi and co-workers conducted the in situ EDXRD experiment on Li batteries using real coin cells without windows.[155−157] Their work revealed the spatial phase distribution of $Ag_2VO_2PO_4$ and the reduction product Ag in $Li/Ag_2VO_2PO_4$ cells as well as their phase evolution during discharge. The reaction front, associated with reduction of the Ag^+ and formation of Ag nanoparticles was visualized and found to progressively move from the electrode/electrolyte interface through the thickness of the electrode. Recently, they reported the rate-dependent spatial phase growth behavior and correlated it with the rate performance of the $Li/Ag_2VP_2O_8$ battery. As shown in Figure 11 (panels c and d), the in situ EDXRD analysis shows that by using lower current densities in the early stage of discharge, it is possible to form a conducting metallic silver matrix that is more evenly distributed, resulting in the opportunity for more complete usage of cathode (higher practical capacity). Liang et al. also used *in situ* EDXRD to monitor the spatial phase distribution in a $LiMn_2O_4$-based 2032 coin cell, which is the first application of in situ EDXRD for studying rechargeable lithium ion batteries.[158] Their data show a moving reaction front within the cell from one electrode to the other during charge−discharge cycling. The region of the electrode close to the lithium side reacted ahead of the region of electrode near the current collector. The inhomogeneous behavior of phase growth took place on a macroscopic level inside the coin cell during the entire discharge process.

Paxton et al. also reported observing inhomogeneous behavior of $LiFePO_4$ cathodes during cycling.[159] They studied the spatial reaction inhomogeneity of an 8 Ah high-capacity $LiFePO_4$ cell using in situ EDXRD and revealed asynchronous discharge behavior and incomplete electrode utilization. They attributed the inhomogeneous behavior to a heterogeneous conductive coating on $LiFePO_4$ particles. These examples show the importance of studying real batteries under operando conditions, since materials at different locations in real batteries

Figure 11. (a) A scheme of the coin cell with the diffraction geometry indicated for energy-dispersive XRD (EDXRD). (b) EDXRD patterns obtained on a fresh Li/Ag$_2$VP$_2$O$_8$ cell. (c) Intensities of Ag and Ag$_2$VP$_2$O$_8$ and crystallite size of Ag as a function of beam position along the z direction. Cathode discharged to 0.5 elec. equiv. at (c) the faster rate (C/168) and (d) the slower rate (C/1440). Three and two x-direction locations were measured, respectively. Reproduced in part with permission from ref 155. Copyright 2013 Royal Society of Chemistry. Reproduced in part with permission from ref 157. Copyright 2015 American Association of the Advancement of Science.

may behave quite differently from the overall electrode, especially in large size cells or during high rate cycling.

Recently, an alternative technique called energy scanning confocal XRD or spectroscopic XRD[160] has been applied to battery materials. As in EDXRD, the sample remains fixed restricting the probed region to a small "gauge volume" as explained above, but in contrast to EDXRD, the energy (wavelength) of the incident radiation is varied rather than the detector angle. To that effect, a small gap monochromator and a set of slits are used to fix the incident beam angle and position onto the sample as the monochromator angle and thus beam energy is scanned. The technique offers better peak resolution than EDXRD but comes at the cost of longer measurement times as the monochromatic beam is used instead of a polychromatic beam as the incident radiation. With this technique, the variations of the lattice parameters of a 150 μm thick LiNi$_{1/3}$Co$_{1/3}$Mn$_{1/3}$O$_2$ sheetlike composite electrode for lithium-ion batteries could be monitored precisely during the discharge reaction and subsequent rest processes with a resolution of 50 μm.[160] These measurements could then be directly linked to the Li$^+$ concentration in the electrode as a function of depths.[161]

Resonant elastic X-ray scattering (REXS) merges the technique of XRD with X-ray absorption spectroscopy (XAS). In this method, the intensity of a Bragg reflection is monitored as the incident X-ray wavelength is varied around an element absorption edge and as the Bragg condition is maintained by tilting the sample, allowing chemical and structural information to be obtained simultaneously. The

technique has, for instance, been used to follow the migration of transition metals from the transition metal layer to the lithium layer in a lithium-rich layered oxide cathode material.[162]

4.1.4. Coordinating Synchrotron XRD with Other Reaction Processes. In addition to the synchrotron in situ XRD studies of electrode materials during electrochemical cycling, studies have been performed using in situ XRD to follow battery materials undergoing chemical reactions. Wang et al. designed an apparatus to perform in situ XRD during chemical delithiation of LiFePO$_4$.[163] The main advantage of the chemical delithiation over the electrochemical delithiation is the high-quality XRD patterns that are free from current collector peaks and can be used for detailed structural analysis. In addition, strategies to overcome the electronic conductivity limitations in electrochemical cells, such as carbon coating cathode particles or adding carbon to composite electrodes, can be eliminated to allow for better understanding of the intrinsic kinetic properties of the active material. In the study mentioned above, the evolution of the phase transition in LiFePO$_4$ upon chemical delithiation was studied and the size-dependent phase transition behavior was also reported.

Several groups have developed in situ XRD techniques to track the structural changes occurring during the synthesis of battery materials.[164] Chen and Bai developed a time-resolved in situ synchrotron XRD method to investigate the phase growth of LiFePO$_4$ during hydrothermal synthesis.[165] Using an in situ reaction vessel for hydrothermal synthesis, the details of the phase growth of LiFePO$_4$ with time at certain temperatures and pressures could be monitored by recording XRD patterns
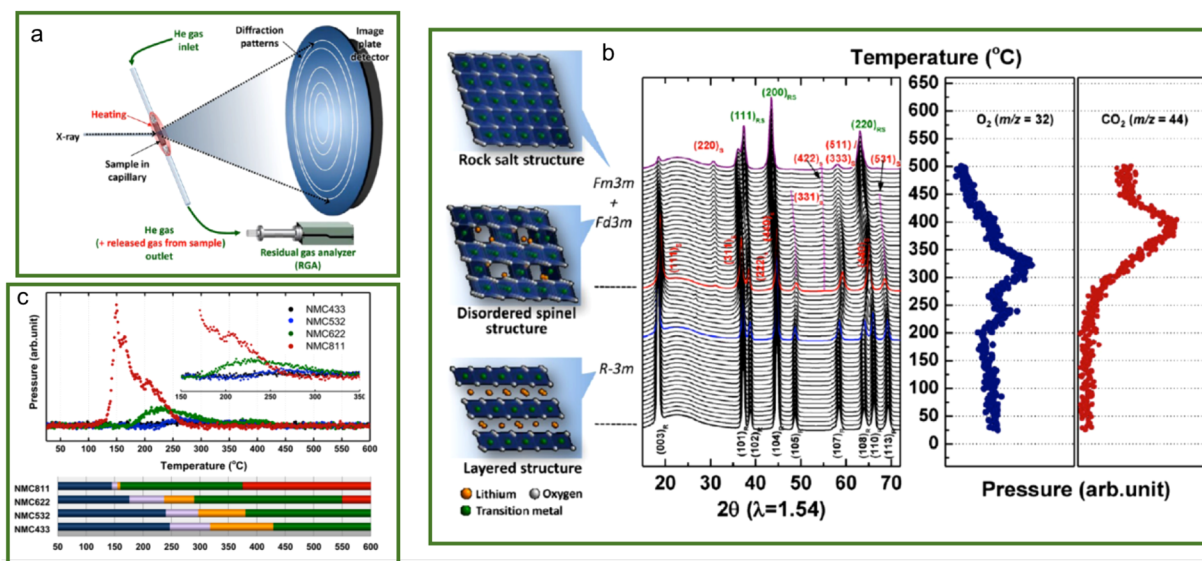
Figure 12. (a) Experimental setup for the combined in situ time-resolved X-ray diffraction (TR-XRD) and mass spectroscopy (MS) experiments. (b) TR-XRD patterns and simultaneously measured mass spectra (MS) for O_2 and CO_2, released from $Li_{0.5}Ni_{0.8}Co_{0.15}Al_{0.05}O_2$ during heating to 500 °C. The left panel shows the models of ideal crystals with rhombohedral, spinel, and rock-salt structures. (c) Mass spectroscopy profiles for the oxygen collected simultaneously during measurement of TR-XRD and the corresponding temperature region of the phase transitions for different NMC samples (i.e., NMC433, NMC532, NMC622, and NMC811). Reprinted with permission from ref 177. Copyright 2014 American Chemical Society. Reprinted with permission from ref 455. Copyright 2013 John Wiley and Sons.

simultaneously. Recently, Bai et al. extended this capability to solvothermal reaction processes.[166] They applied a time-resolved in situ synchrotron XRD technique (TRXRD) to study the reaction mechanisms during the solvothermal synthesis of olivine-structured cathode materials, for example, $LiFePO_4$, $LiMnPO_4$, and $LiFe_{0.4}Mn_{0.6}PO_4$. The evolution of the crystal structure changes of the Fe and/or Mn-containing phases were tracked. These results and the in situ technique are valuable in providing guidance for material design and synthesis.

The potential for thermal instability of electrode materials is one of the most critical factors responsible for thermal runaway and safety-related problems in batteries.[167−179] Investigating the evolution of phase transitions of the electrode materials during heating can provide valuable insight into evaluating the safety characteristics of the materials from a structural point of view. Pioneering work was initiated by a research group at Brookhaven National Laboratory led by McBreen, and the first experiment was carried out by Yoon et al.[167] Since then, the phase transition behaviors during heating of several important cathode materials have been studied by TRXRD, and their effects on the safety characteristics of these electrode materials have been reported. Later on, Nam and co-workers in the same group developed a technique that combined mass spectroscopy (MS) and in situ XRD measurements.[176] It is known that the oxygen release from oxide cathodes is a key factor in accelerating heat generation causing thermal runaway. Therefore, it is important to study the gas release and correlate it with the structural changes during heating. The experimental set up of the in situ XRD-MS experiment and some results are shown in Figure 12. The charged cathode material is placed in a quartz tube connected to the MS. They were able to heat the quartz tube at a controlled ramping rate. An inert atmosphere is applied to the system by purging with helium gas (Figure 12a). During heating, the structural information on charged cathode is probed and recorded using the synchrotron XRD in a time-

resolved fashion, while the outlet gas information is analyzed and recorded by the MS. By applying this technique to $LiNi_{0.8}Co_{0.15}Al_{0.05}O_2$ (NCA), a series of phase transformations from layered to spinel to rock salt during heating was revealed (Figure 12b). The amount of oxygen released owing to the spinel to rock salt phase transition was monitored by MS, which is considerably larger than that for the layered to spinel transition, indicating that spinel to rock-salt transition is more dangerous for thermal runaway. Therefore, suppressing this transition or delaying it to higher temperatures would improve the safety characteristics of cathode materials. This group also investigated $LiNi_xMn_yCo_zO_2$ (NMC) materials.[177,179] The results of this work presented in Figure 12c show that the spinel to rock salt phase transformation and associated oxygen gas release could be postponed to higher temperatures if the Co and Mn contents are increased and Ni content is reduced. This observation is consistent with a study reported by Sun and co-workers that Ni-rich NMCs have inferior thermal stability to those with lower Ni content.[180]

4.1.5. Complementing XRD with Neutron Scattering Techniques. Neutron diffraction based techniques provide useful complementary information to X-ray based synchrotron diffraction techniques. Both XRD and neutron diffraction provide structural information, but neutron diffraction allows better distinction of transition metals and low Z elements such as lithium.[181,182] In addition, neutron diffraction is also much more sensitive to oxygen anions than XRD. Another advantage of neutron scattering is that commercial-sized batteries can be studied in operando.[183−188] However, compared to synchrotron X-ray techniques, neutron scattering requires relatively larger amounts of specimen and longer data collection time. In addition, for Li-containing energy materials, isotopic labeling might have to be considered for maximizing counts for practical experiments. This poses challenges in capturing phase/structure evolution in operando at relatively high rates. Readers are referred to references in this section for more information

about neutron scattering techniques applied to battery materials and batteries.

4.1.6. Pair Distribution Function (PDF) Analysis. Pair distribution function analysis, also known as total scattering analysis,[189] refers to the analysis of both the Bragg peaks and the diffuse scattering components of neutron, X-ray, or electron diffraction data. While it can be used for information obtained from traditional laboratory equipment such as X-ray diffractometers[190] or electron microscopes,[191] the discussion here will focus exclusively on synchrotron X-ray data. Because diffuse scattering is weak and covers large reciprocal space volumes, it can be difficult to separate from background noise and other artifacts.[192] The high brilliance and excellent resolution of synchrotron X-ray sources have obvious advantages, and improvements in detectors and monochromators as well as data collection, reduction, and analysis methods over the past ten or so years have resulted in an acceleration of the use of the PDF technique at synchrotron facilities. Because of the need for a wide range of momentum transfer ($Q > 30$ Å), short wavelength/high-energy X-rays (>45 keV or $\lambda = 0.27$ Å) are required,[193] such as those available at beamline X7A at the National Synchrotron Light Source at Brookhaven National Laboratory, beamline 11-ID-B at the Advanced Photon Source (Argonne National Laboratory), or beamline I15 at the Diamond Light Source in the U.K., to name a few.

The PDF technique can be applied to crystalline materials but is particularly useful for the analysis of materials that lack long-range order, including nanocrystals, glasses, and even gels or liquids.[193] While a detailed explanation of the PDF experiment and data analysis is beyond the scope of this review (interested readers can consult ref 194 for more information), the general procedure to obtain structural information is briefly summarized as follows. An X-ray scattering pattern is first obtained and corrected for anomalous effects (e.g., fluorescence, scattering from the sample holder, air, etc.), and then the data is Fourier transformed to yield the reduced PDF $G(r)$ function (Figure 13).

$G(r)$ is a measure of the probability of finding two atoms in a material separated by the distance r. The peak positions indicate atom pair distances, their integrated intensities are related to the number of atoms at these locations (coordination), peak widths and shapes give information about the probability distributions of the pairs (disorder), and r_{max} indicates particle size or coherence. This is reminiscent of information that can be obtained in EXAFS experiments (see following section), although it is not element-specific (in the case of X-ray PDF) and is carried out to much larger values of r.

The experimental data (insets) in Figure 13 show that the $V_2O_5 \cdot nH_2O$ xerogel has much less long-range order than crystalline V_2O_5. Modeling of the PDF data indicated that the xerogel structure consists of an assembly of stacked bilayers of VO_5 square pyramidal units with considerable turbostratic disorder, in contrast to stacks of corrugated single layers of VO_5, as previously thought.[195]

To understand local environments and short-range ordering in layered $LiNi_{0.5}Mn_{0.5}O_2$ electrode materials, combined neutron and X-ray PDF methods have been used, along with NMR and X-ray and neutron diffraction.[196] These experiments revealed clustering of $LiMn_6$ and $LiMn_5Ni$ units in the transition metal layers in a honeycomb pattern, which could not be easily detected using conventional diffraction experiments.
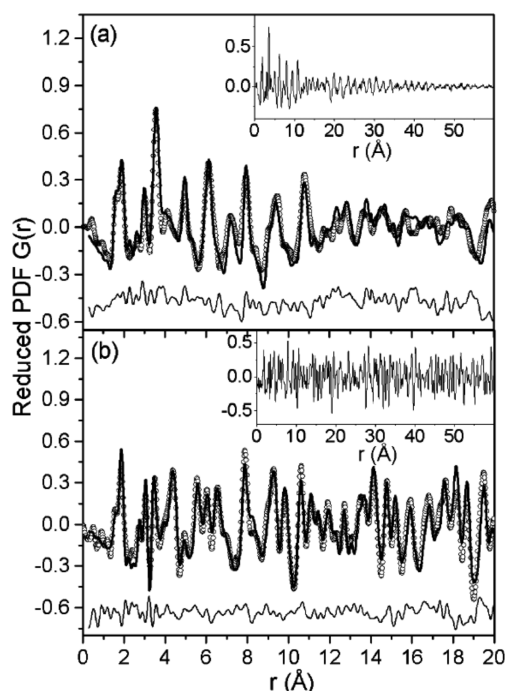
Figure 13. Experimental (dots) and fitted (lines) PDFs for (a) $V_2O_5 \cdot nH_2O$ xerogel and (b) crystalline V_2O_5, with residual differences shown below. The experimental data is shown in an expanded scale in the insets. Reprinted from ref 195. Copyright 2002 American Chemical Society.

Reactions of battery electrode materials that result in the generation of amorphous or nanostructured components are particularly well-suited for PDF analysis. For example, the conversion electrode $RuO_2 \cdot 2H_2O$, which reacts to form Li_2O and metallic Ru in lithium cells, exhibits an anomalously high capacity. Using PDF along with NMR, XRD, and XAS experiments, it was shown that the source of the excess capacity involved the reversible reaction of LiOH with lithium to form Li_2O and LiH in the amorphous solid electrolyte interphase layer.[197] Other conversion electrodes have been studied in operando (e.g., FeOF),[198,199] showing that the material first transforms to metallic Fe via a rock salt intermediate but cycles as a two-phase nanocomposite thereafter.

Lithium intercalation into the layered compound MoS_2 results in the product $LiMoS_2$, which is poorly diffracting. PDF analysis indicates that $LiMoS_2$ is actually nanocrystalline.[200] The best fit to the data suggests that the structure consists of a chain of diamond motifs of bonded Mo atoms.

A recent study of the electrochemical alloying mechanism of tin anodes with sodium, which included in operando PDF, elucidated the structure of several intermediate phases, including an amorphous one with approximate composition $Na_{1.2}Sn$, with chain connectivity.[201] In another study, an intermediate phase with only short-range order, which forms during electrochemical desodiation of olivine $NaFePO_4$, was detected using the PDF method.[202] The appearance of this phase during the redox process is thought to buffer the large volume mismatch of 17% between the $NaFePO_4$ and $FePO_4$ end members in this system by accommodating strain.

One of the most interesting recent uses of PDF has been applied to a series of solutions with common anions and solvent, but with differing cations, including Mg. The use of

principle component analysis allowed dissimilar features (e.g., cation-solvent interactions) to be isolated from those that were common to all of the solutions (anion-solvent interactions).[198] Demonstrating the applicability of the PDF method to solutions should aid in development of new electrolytic solutions, which will be particularly useful for Beyond Lithium Ion systems such as those based on Mg.

4.2. Hard X-ray Absorption Spectroscopy

Synchrotron X-ray absorption spectroscopy (XAS) is a powerful tool for studying the structure of materials and the oxidation state of certain elements in a given material by measuring the X-ray absorption coefficient as a function of X-ray photon energy. When the incident X-ray photon energy scans through the threshold to excite core electrons of the probing element, a sharp increase of absorption can be identified as the absorption edge. XAS can be used to study the local environment and the oxidation state of the probing atom in an elemental selective way. The interested reader is referred to several comprehensive books and review articles on the basic principles of XAS techniques.[203−207] Unlike X-ray diffraction, which is only effective for materials with long-range ordering, the XAS technique can provide useful information such as bond length, coordination numbers, and oxidation states for materials in gas, liquid, or solid states with or without long-range ordering. Researchers have increasingly recognized the complementary nature of the XAS technique to XRD, and it has been widely applied in structural studies for battery materials.[208,209]

A full XAS spectrum can be divided in two parts, the X-ray near edge structure (XANES) which refers to the part of the spectrum in the energy range within ∼30−50 eV near the absorption energy, and extended X-ray absorption fine structure (EXAFS), which refers to the extended part starting at 20−30 eV above the absorption edge. The XANES region contains information in the edge energy position, the shape of the XANES spectrum, and the pre-edge features. The edge energy position, which is normally chosen at the inflection point on the spectrum (the first peak of derivative curve), is used to quantitatively identify the oxidation state of the probed atom using reference compounds with known oxidation states. This is because more X-ray energy is required to eject a core electron from an atom at higher oxidization state with less shielding effect. The shape of the XANES spectrum is sensitive to the local geometric structure around the central absorbing atom. The interaction of the photon absorber with ligand atoms sometimes introduces shoulder features on the edge of the XANES spectrum that reflect the electronic structure of the system. The pre-edge structures are sensitive to the coordination environment of the probed atom. For instance, a pre-edge peak is often seen in the K-edge spectra of 3d transition metals, due to the 1s to 3d transition, which is formally dipole forbidden but quadrupole allowed. It gains intensity from pure electric quadrupole coupling and/or 3d-4p orbital mixing induced by a noncentrosymmetric chemical environment.[210] In general, the peak intensity increases with the geometry in the order of octahedral < square-pyramidal < tetrahedral. Therefore, the pre-edge peaks can be used as a probe for geometry. In addition to the local geometric and electronic structure information obtained from XANES, EXAFS can provide further local structure information around the central atom. The theory of EXAFS has been better developed than that of XANES, and quantitative comparison between theoretical modeling and experiments can be made.[211] Specifically for EXAFS, X-rays of definite energy are absorbed and excite core electrons. The excited electrons are scattered by near neighbor atoms and interfere constructively or destructively. Oscillations above the absorption edge can be used to characterize distances between scattering atoms and absorbing atoms. The EXAFS takes contributions from multiple scattering atoms, multiple scattering, and shifts in phase and inelastic scattering. At the same time, the EXAFS is an average of all the absorbing atoms, which may have different local environments and thermal disorders. Thus, the EXAFS equation physically describing the above can be expressed as

$$\chi(k) = S_0^2 \sum_i N_i \frac{f_i(k)}{kD_i^2} e^{-2k^2\sigma_i^2} e^{-2D_i/\lambda} \sin[2kD_i + \delta_i(k)]$$

(3)

Modeling and fitting of the EXAFS spectrum commonly takes bond length D, coordination number N, mean square relative displacement σ_i^2, and reference energy E_0 as parameters. By curve fitting the experimental EXAFS data using model structures, accurate local environments (i.e., coordination number, interatomic distance, and geometry) around the probed atom can be determined. By properly constraining the initial fitting input, such as coordination number N in phase pure and well-crystallized systems, bond distances can be accurately determined.

XANES measurements are used to determine the valence states of specific elements as a function of state-of-charge to study the charge compensation mechanism as well as the reversibility of redox reactions. EXAFS is the technique of choice for studying the structures of electrode materials with low crystallinity, or even those that are amorphous, either in the as-synthesized state or after prolonged cycling. XAS is an elemental-specific technique allowing for the selection of a specific metal threshold to obtain the local chemical environment surrounding the selected atoms. This is particularly important when dealing with materials containing different elements with similar X-ray scattering cross sections. For these materials, it is difficult to obtain element-dependent structural information by XRD only. However, XAS is able to differentiate them by tuning the X-ray energy to different edge positions corresponding to those elements. In situ XAS may be used to study the structural changes and kinetics of battery materials during cycling. The XAS spectra can be collected during charging and discharging to track the dynamic process of electrochemical reactions, including structural changes surrounding specific element sites and the reaction kinetics (i.e., rate capability associated with different redox centers).

Most XAS experiments performed at synchrotron light sources use transmission or fluorescence detection modes. In transmission mode, the sample is placed between I_0 and I_t detection chambers. The intensity of the incoming and outgoing (i.e., after traveling through the sample) X-ray beam are recorded by I_0 and I_t detectors, respectively. Then the absorption coefficient μ of the material can be determined by the Bouguer−Lambert−Beer law (eq 4):

$$I = I_0 \exp(-\mu x)$$

(4)

In the fluorescence mode, the sample is tilted by ∼45 deg relative to the incident X-ray beam, and the detector is positioned at a right angle to the incident beam to collect the fluorescence X-rays. The choice of preferred detection mode is
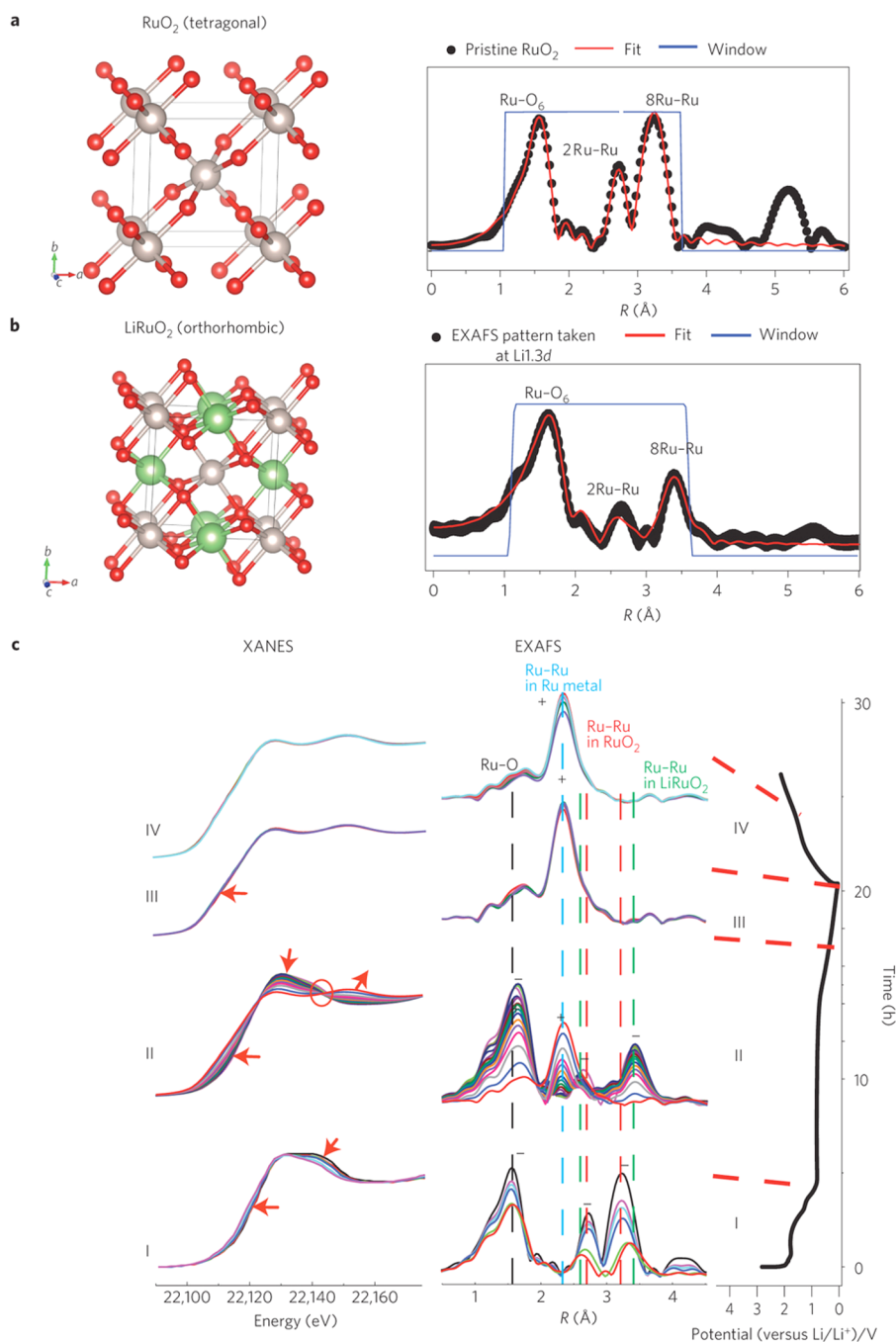
Figure 14. In situ XAS analyses of the RuO₂/Li system reveal the changes in the average oxidation state of ruthenium, phase composition, and bond lengths. (a) The extended EXAFS pattern of pristine RuO_2 and (b) the pattern taken at Li1.3d. (c) The electrochemistry profile of the discharge process/beginning of charge and the corresponding in situ XANES and EXAFS patterns, divided into four stages on discharge (I–III) and on charge (IV). Used with permission from ref 197. Copyright 2013 Nature Publishing Group.

made based on the sample thickness and concentration of the element being probed. In general, if the sample can be made thin enough and the concentration of the excited element is sufficient, the transmission mode is preferred. Otherwise, the fluorescence mode should be used.[212,213]

One of the advantages of using XAS in battery research is the capability to perform in situ or in operando structural studies during charging and discharging. To conduct this type of experiment, specially designed electrochemical cells with windows to pass X-rays are necessary. Because the photon absorption is approximately proportional to Z,[4] window

materials containing only low Z elements are desirable. Beryllium ($Z = 4$) is intuitively the first choice, but it is difficult to handle when assembling an electrochemical cell and becomes very toxic if oxidized. For many experiments, Kapton film and other polymer films are widely used window materials. The sample in the electrochemical half-cell is stacked with current collector, lithium metal foil counter electrode, and separator. The cell is filled with electrolytic solution containing $LiPF_6$ salt and carbonate-based solvents. The X-ray beam should be able to pass through all these cell components and reach the detector with enough photon flux if the transmission
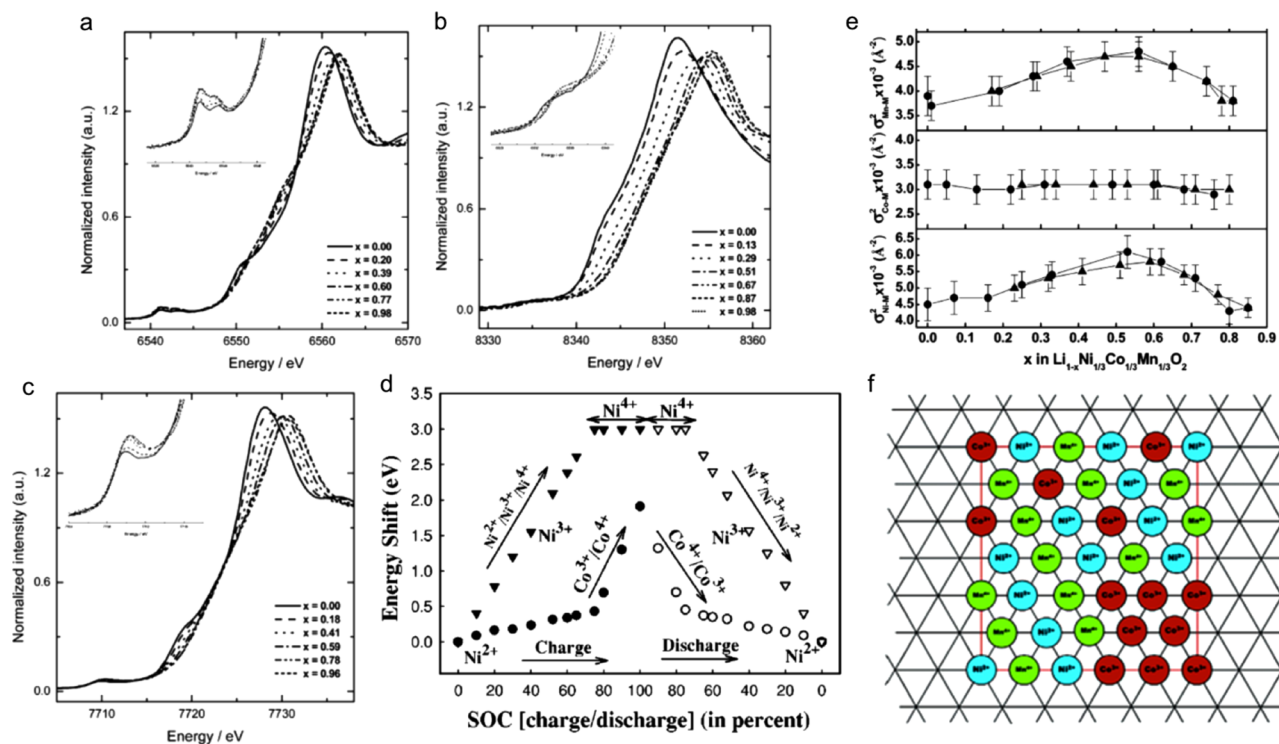
**Figure 15.** Normalized (a) Mn, (b) Ni, and (c) Co K-edge XANES spectra of $Li_{1-x}Co_{1/3}Ni_{1/3}Mn_{1/3}O_2$ electrode during charge. (d) Plot of the white line energy shift vs the state-of-charge (SOC) for Co and Ni K edge; (e) Structural parameter (Debye−Waller) changes simulated at the second shell Mn-M, Co-M, and Ni-M for $Li_{1-x}Co_{1/3}Ni_{1/3}Mn_{1/3}O_2$ at different lithium contents during first charge and discharge cycle. (f) Local phase segregation as suggested from analysis of the Debye−Waller factors, where the cyan, green, and wine dots represent Ni, Mn, and Co. Adapted with permission from ref 217. Copyright 2005 AIP Publishing. Adapted from ref 218. Copyright 2005 American Chemical Society. Adapted with permission from ref 89. Copyright 2005 American Chemical Society.

detection mode is chosen. Readers who are interested in the assembly of in situ battery cells may refer to a recent video article.[95] Using carbon sheet current collectors to replace Cu and Al has been reported in several studies aiming to reduce the absorption and improve the signal-to-noise ratio (S/N) of the spectrum.[214] When probing low-Z elements (i.e., S, P, Si, etc.), only fluorescence detection mode can be used because the organic electrolyte in the electrochemical cell will absorb most of the photons. The first in situ XAS study on batteries was carried out at Brookhaven National Laboratory and was used to probe the nickel oxidation state for nickel metal hydride batteries in a platelike cell.[3] After that, in situ techniques were applied to other rechargeable battery systems. Modified in situ coin and pouch cells[121,215] have been designed and used in XAS studies in order to fit various X-ray beamline setups. Lithium-ion battery materials such as layered transition metal oxides,[89,216−222] spinels,[178,223−225] polyanionic structures,[105,226−229] conversion electrodes,[117,197,230−235] and intercalation anodes[111,236,237] have been studied. Selected examples of these studies are discussed below.

4.2.1. Probing Local Structure. In contrast to insertion electrodes, which reversibly accommodate the insertion and extraction of alkali metal ions with minimal change to the host structures, conversion electrodes undergo dramatic structural and phase changes during electrochemical cycling. Upon reduction, they form composites consisting of metal nanoparticles embedded in a lithium salt (LiF, Li_2O, etc.); sometimes the metal nanoparticles are connected to form metallic networks.[91,238] One puzzling phenomenon is the observation of capacities in excess of the theoretical values

frequently observed in conversion compounds. Hu et al. unraveled the charge storage mechanism in a conversion material RuO_2, using a suite of high-resolution solid-state NMR and synchrotron in situ XAS techniques.[197]

The XANES and EXAFS data obtained on this system can be divided into three components as shown in Figure 14. During stage I (0−1.2 lithium), the lithiation of RuO_2 was accompanied by a shift to lower energy in the XANES spectra, suggesting ruthenium reduction. A reduction of the intensity of the peaks related to the RuO_2 structure was observed in the EXAFS spectra, consistent with a solid solution reaction to form $LiRuO_2$, which is completed near the end of stage I. In stage II, the two-phase conversion reaction (eq 5)

$$LiRuO_2 + 3Li^+ + 3e^- = 2Li_2O + Ru \qquad (5)$$
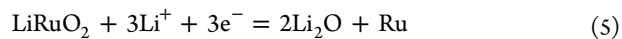
is clearly indicated by the isosbestic point[239,240] in the XANES patterns, where the intensity of the $LiRuO_2$-related peaks decreases and that of Ru metal peaks increases. The EXAFS and XANES results indicate that the conversion reaction is completed at the end of region II as shown in Figure 14, and the lithium storage capacity in region I and II is related to the redox reaction of Ru^{4+}/Ru^0. The capacity observed in region III is not related to either bulk structure changes or redox reaction on Ru centers at all. These results inspired the search of other sources for the extra capacity in stage III. Further NMR experiments reveal that the additional capacity in region III mainly arises from the reversible reaction of LiOH with Li and suggest that reversible SEI formation and Li adsorption on the Ru nanoparticles may only have minor contributions. This study clearly demonstrates the necessity of combining regular
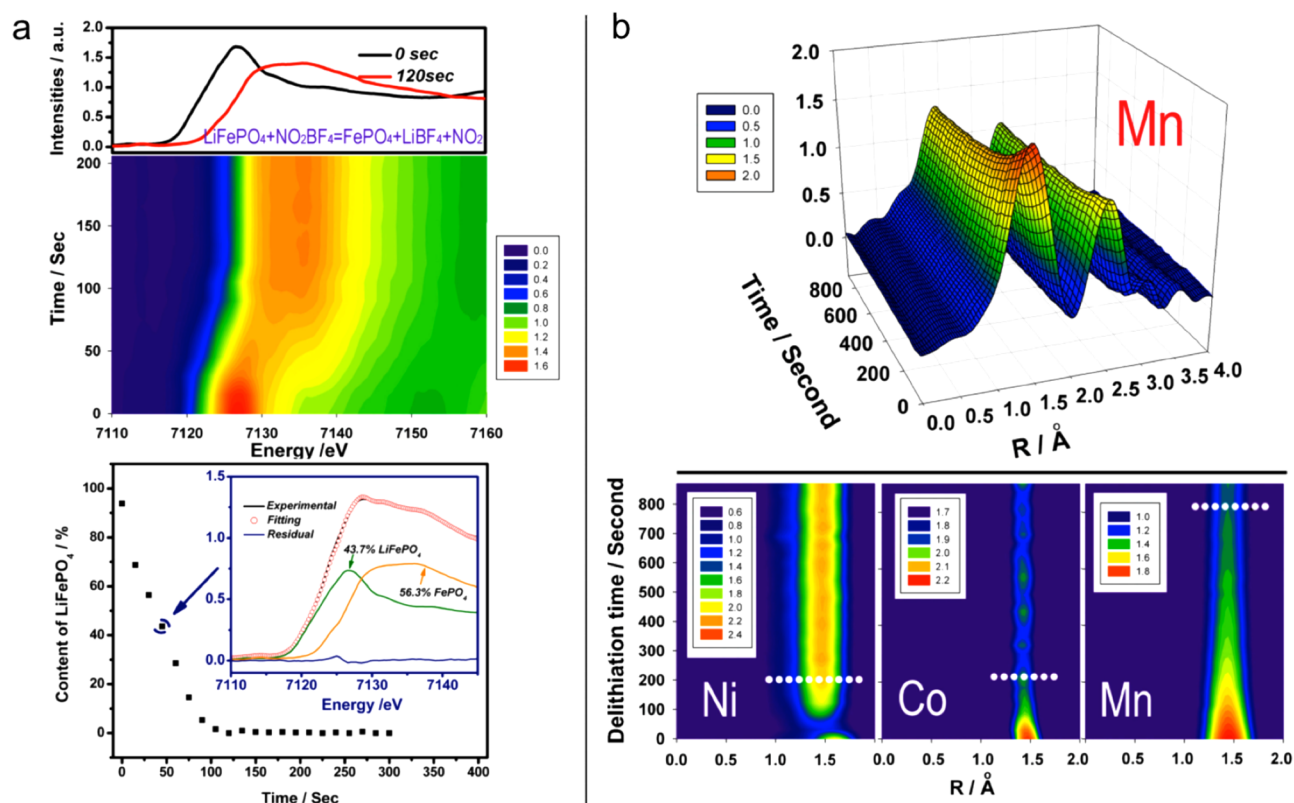
Figure 16. (a) Fe K-edge XANES spectra of pristine and chemically delithiated $LiFePO_4$ after 120 s. The evolution and linear combination fitting of Fe K-edge XANES spectra during in situ chemical delithiation of $LiFePO_4$ are plotted. (b) (top) Magnitude of the Fourier transformed Mn K-edge spectra of $Li_{1.2}Ni_{0.15}Co_{0.1}Mn_{0.55}O_2$ collected during 5 V constant voltage charging. (bottom) Projection view of the corresponding Ni−O, Co−O, and Mn−O peak magnitudes of the Fourier transformed K-edge spectra as functions of charging time. Reproduced with permission from ref 41. Copyright 2014 John Wiley and Sons. Reproduced with permission from ref 229. Copyright 2012 The Royal Society of Chemistry.

analytical techniques with synchrotron techniques to reveal the unknown in battery science.

Another example of the use of EXAFS involves a study of an intercalation electrode. Quantitative analysis of a transition metal oxide cathode material containing Mn and Ni had been successfully conducted, and detailed local structure information was obtained. Yoon et al. carried out a very careful in situ EXAFS study on $LiMn_{0.5}Ni_{0.5}O_2$.[241] Atomic distances with accuracy down to 0.02 Å could be determined by fitting the EXAFS data. Upon electrochemical deintercalation, the Mn−O and Ni−O bond distances were accurately determined and provide supporting evidence of lithium transition metal ion exchange in the layer structure. Their observation also supports that the redox takes place via oxidation of Ni^{2+} to Ni^{3+} and Ni^{3+} to Ni^{4+}.

4.2.2. Monitoring Redox Reactions. A great advantage of XAS is its element selectivity, which allows for studying the chemical environment and oxidation state of an individual element in a material containing multiple elements, to determine which contributes to redox processes at various SOCs. This is particularly important for electrodes containing multiple metals like the technologically important NMCs ($LiNi_xMn_yCo_zO_2$, where $x + y + z = 1$). The redox reaction of each transition metal in $LiNi_{1/3}Co_{1/3}Mn_{1/3}O_2$ was first studied by Deb et al.[242] and later by Yoon et al.[243] (Figure 15). During the deintercalation of Li ion, the Mn XANES spectrum exhibited subtle variations in the shape of the edge because the Mn local environment changed, but there was no rigid shift to higher energy values, showing that Mn remains tetravalent

during charging. In contrast, the entire Ni K-edge XANES spectra shifted to higher energies during charging consistent with increasing nickel oxidation state from Ni^{2+} to Ni^{4+}. The Co K-edge XAS also showed changes in the edge shape during charge, ascribable to changes in bond length and covalency. The theoretical calculations showed that the Co^{3+}/Co^{4+} oxidation can contribute to the capacity, but the redox potential was at 4.8−5.2 V, where the electrolyte decomposition can occur. Yoon et al. and Lin et al. independently conducted soft XAS measurements on NMC materials and revealed that the charge compensation during charging was achieved at the oxygen site in addition to transition metal sites.[88,89] Similar observation was reported by Whittingham and co-workers.[244] These studies highlighted the ability of the XANES measurements to provide a direct link between the redox reaction and the lithium storage capacity recorded on the charge curve.

EXAFS analysis can be used to investigate the local structure around each element in electrode materials. It is difficult to differentiate Ni, Co, and Mn in NMCs by XRD because of their similar X-ray scattering cross sections. XRD analysis could only show that $LiNi_{1/3}Co_{1/3}Mn_{1/3}O_2$ has a similar crystal structure as $LiCoO_2$, but no more information is accessible to differentiate the Ni, Co, and Mn sites. In contrast, EXAFS studies reveal that element-dependent local ordering exists in the transition metal layers of the NMC material. Tsai et al. did quantitative analysis on the EXAFS spectra of Ni, Co, and Mn of a NMC material during charging.[245] They found that the trends of the variations for the bond length and Debye−Waller factor[207,246] (representing the distortion of the local structure) of Mn and Ni are quite
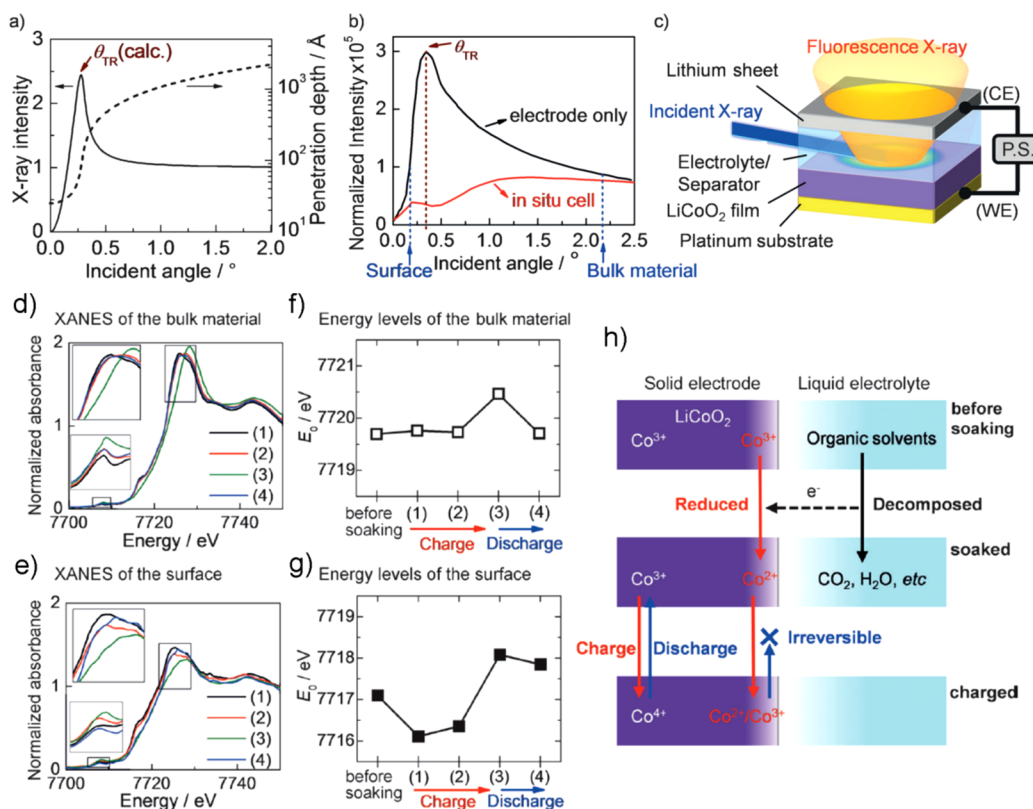
Figure 17. (a) Calculated X-ray intensity and penetration depth of the 7.7 keV incident X-ray to $LiCoO_2$. (b) Incident X-ray angle dependence of the Co fluorescence from $LiCoO_2/Pt$, obtained before electrolyte soaking (black) and after electrolyte soaking (red). (c) The spectro-electrochemical cell used for in situ TRF-XAS measurements. (d–g) Co K-edge XANES spectra of the $LiCoO_2$ film measured at four different points by applying a voltage and measuring the corresponding absorption energy levels of the bulk material (d and f) and the surface (e and g), respectively. (h) The proposed reaction of the initial degradation that occurs at the electrode/electrolyte nanointerface. Reproduced with permission from ref 255. Copyright 2012 John Wiley and Sons.

similar but completely different from those of Co. Therefore, they concluded that short-range ordering between Ni and Mn does exist, as shown in Figure 15, a fact not revealed by XRD analysis.

Another example involves LMR-NMCs, whose structures have been the subject of much controversy. The EXAFS analysis provided interesting clues about the local structure of such materials. These results have confirmed the existence of Li_2MnO_3 domains in some materials, providing some support for the nanocomposite notation.[42,43] However, the nature of LMR-NMCs, whether solid solution or nanocomposite, is likely determined by the method of synthesis, and different analytical techniques tend to come to different conclusions depending on the source of the sample.

4.2.3. Time-Resolved Hard XAS and its Application to Dynamic Studies. The dispersive XAS instrumentation is able to collect one high-quality time-resolved XAS spectrum in a time scale as short as milliseconds, making it possible to probe the dynamic process of a battery under high rate operating conditions.[247] The first application of time-resolved XAS for lithium ion batteries was conducted by Yu et al.[229] This study was performed on a $LiFePO_4$ material during chemical (Figure 16a) and electrochemical delithiation. Phase fractions of $LiFePO_4$ (or $FePO_4$) during charge at various C-rates were estimated. Their results indicated that the average structural changes of $LiFePO_4$ upon lithium extraction proceeds via a $LiFePO_4/FePO_4$ two-phase reaction under both low (1C) and high (30C) charge rates. In addition, the phase fraction of

$FePO_4$ could be accurately determined, and its evolution monitored during charge, providing information on the phase growth dynamics. The kinetics of the $LiFePO_4$ to $FePO_4$ phase transition was analyzed using the Avrami-John-Mehl-Eroofev (AJME) equation.[248] It was concluded that there was one-dimensional growth of $FePO_4$ in $LiFePO_4$, which agrees well with transmission electron microscopy results and theoretical calculations.[249−251] Thereafter, Orikasa and co-workers also performed time-resolved XANES measurements on $LiFePO_4$ and reached similar conclusions about its phase-growth mechanism.[252] At first glance, this seems to contradict the evidence obtained during the in operando XRD experiments described in section 4.1.1, in which solid solution regions were observed during charge/discharge of cells containing $LiFePO_4$. The phase behavior of $LiFePO_4$ is complex and depends on temperature, particle size, and other factors. As of this writing, it is not clear if the different observations seen in the XAS and XRD experiments are due to artifacts such as strain or differences in sample type and conditions.

The time-resolved XAS technique is particularly useful for studying rate capability related structural changes of the electrode materials with multiple redox centers. A good example is the time-resolved XAS studies of the LMR-NMC $Li_{1.2}Ni_{0.15}Co_{0.1}Mn_{0.55}O_2$ ($0.5LiNi_{0.375}Co_{0.25}Mn_{0.375}O_2\cdot0.5Li_2MnO_3$), aimed toward understanding rate-limiting factors.[253] LMR-NMCs often suffer from poor rate capability. Although the poor kinetics of the Li_2MnO_3 nanodomains in lithium-rich layered compounds has been proposed as the

origin of such poor rate capability, experimental evidence has been lacking. The authors of this study applied a constant voltage of 5 V on $Li_{1.2}Ni_{0.15}Co_{0.1}Mn_{0.55}O_2$ cathode to oxidize Ni, Co, and Mn ions simultaneously. At the same time, the time-resolved Ni, Co, and Mn K-edge XAS spectra were collected as functions of time. The comparative Fourier transformed magnitude of the corresponding Ni, Co, Mn K-edge EXAFS spectra shown in Figure 16b demonstrated the different kinetic behaviors of the three metals. The first coordination peak (Ni−O) shows dramatic changes in both position and intensity within the first 100 s, indicating the oxidation of Ni^{2+} to Ni^{3+}, then to Ni^{4+}. The EXAFS features remain unchanged after 160 s, indicating the oxidation of Ni^{2+} to Ni^{4+} was almost completed within the first 3 min. In contrast, for Mn, the first coordination shell peak (Mn−O) intensities shows a continuous decrease all the way to the end of the experiment (900 s), indicating much slower delithiation kinetics around Mn sites, whereas the changes in the Co−O peak ended after 200 s. These results clearly showed that oxidation of Mn is much slower than Ni and Co, providing the first experimental evidence of Li_2MnO_3 nanodomains as the rate-limiting factor in $Li_{1.2}Ni_{0.15}Co_{0.1}Mn_{0.55}O_2$.

4.2.4. Surface Probing Tool: Hard XAS in Reflection Mode.
Although hard XAS is mainly used as a bulk characterization tool, it can also be utilized to probe surfaces of electrode materials. Taking advantage of the nature of highly collimated synchrotron X-ray beams and using glancing incidence geometry, the X-ray penetration can be restricted to several nanometers of the sample to probe the surface of the electrode only.[254] This surface sensitive technique is particularly important for in operando characterization of the electrode surface under battery operating conditions. Most other surface-sensitive characterization tools, such as XPS and soft XAS, require the sample to be placed in a vacuum chamber, making it difficult to perform in situ or in operando measurements. Takamatsu et al. used this technique first, named total-reflection fluorescence XAS (TRF-XAS), to investigate the surface structural evolution of $LiCoO_2$ during charging and discharging.[255]

The electrochemical cell used for the in operando TRF-XAS measurement is shown in Figure 17c. The glancing-angle-dependent fluorescence X-ray intensities collected experimentally and the penetration depth calculated are also shown. When setting the incident angle to 0.2° and 2.2°, the corresponding X-ray penetration depth was estimated to be about 3 nm (surface probing) and 100 nm (bulk probing), respectively. The measurement shows that the $LiCoO_2$ thin film electrode exhibits gradual degradation at the surface upon electrochemical cycling. The Co ions were reduced right after immersion into the organic electrolyte even before current was passed through the cell. A similar observation was also reported by Lin et al. in NMC materials, where Mn and Co were both reduced after exposure to electrolytic solution.[88] Consequently, irreversible changes of electronic structures took place at the surface of electrode materials upon subsequent charging and discharging cycles. This is quite different from the reversible redox reaction occurring in the bulk. Later on, Yamamoto et al. studied the $LiFePO_4$ thin film electrode using the same TRF-XAS technique.[256] They found that the $LiFePO_4$ electrode/electrolyte interface did not exhibit reduction damage as observed in the case with $LiCoO_2$. This work demonstrates the value of TRF-XAS as a powerful tool to probe surface structures of electrodes under in situ/in operando conditions

and to establish the relationship between the stability of the electrode/electrolyte interface and the electrochemical performance.

The application of hard XAS to battery materials is still rapidly developing, and new techniques and results are being reported every day. This review is necessarily incomplete, as it is not possible to cover all of these new developments. The examples given above are chosen to show the great versatility of hard XAS, in particular, the ability to obtain chemical and structural information on materials under practical operating conditions.

4.3. Soft X-ray Spectroscopy

Soft X-ray absorption spectroscopy (soft XAS) through fluorescence yield, soft X-ray emission spectroscopy (soft XES), and resonant inelastic X-ray scattering (RIXS) are collectively referred to as soft X-ray photon-in-photon-out spectroscopies. The combination of soft XAS and XES provides elemental sensitive electronic structure information on both the occupied and unoccupied electron states in the vicinity of the Fermi level.[257] RIXS is capable of detecting various low-energy excitations during the decay of the core hole, as well as providing orbital character of certain electronic states in battery materials among other things.

XAS, XES, and RIXS all involve the excitation of a core-level electron, and the techniques are element-specific. Figure 18
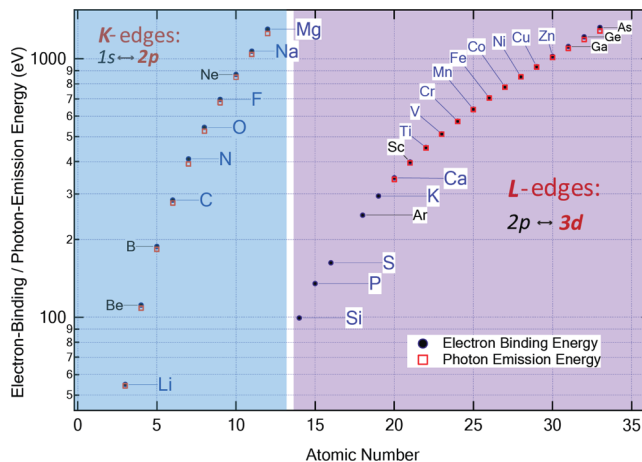
Figure 18. Core-level binding energies and associated X-ray emission energies (primary decay) that are accessible through spectroscopy in the soft X-ray regime (50 eV to 2 keV). Note that this figure focuses on the practical materials for batteries, and the M- and N-edges of the heavy elements are not plotted here. Used with permission from ref 466. Copyright 2016 IOP Publishing Ltd.

displays the electron binding energies and decay-induced emission energies of the orbitals in specific elements that are covered by soft X-ray spectroscopy for battery studies, especially the low-Z element K-edges and the L-edges of 3d TMs. For both low-Z element K edges and TM L-edges, soft X-ray spectroscopy is a direct measurement of the dipole-allowed 2p-3d and 1s-2p transitions, as discussed in section 3. This allows a detailed and high-statistic detection of both the anion-p and TM-3d states involved in the electrochemical operations of battery materials.

Note that modern soft X-ray techniques have been progressing rapidly with many other new and/or enhanced capabilities (e.g., resonant small angle scattering, dichroism, and microscopy etc.), which have been, or potentially could be,
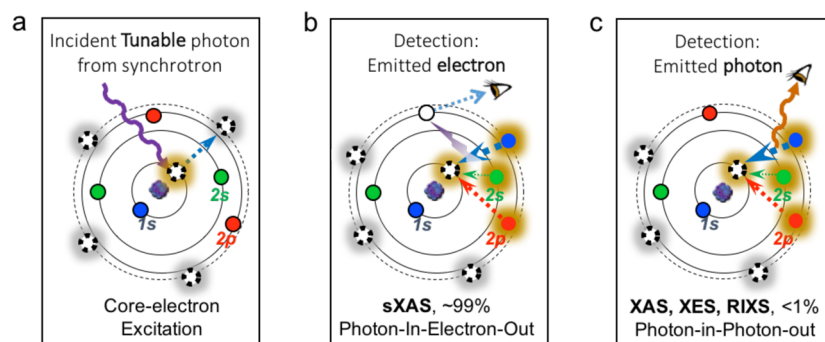
Figure 19. Atomic schemes of the core-level XAS, XES, and RIXS. Contrasting X-ray photoelectron spectroscopy, these techniques require continuously tunable synchrotron photons to excite core electrons to specific unoccupied states. (a) Core–electron excitation, (b) photon-in-electron-out XAS, and (c) photon-in-photon-out XAS, XES, and RIXS. Note that soft XAS is considered surface-sensitive compared to hard XAS. Reprinted with permission from ref 258. Copyright 2013 Elsevier.

capitalized for understanding different aspects of battery materials.

4.3.1. Overview of Soft X-ray XAS, XES, and RIXS.
Figure 19 shows the atomic schemes for the soft XAS, XES, and RIXS techniques.[258] The spectroscopic process starts with the absorption of the continuously tunable synchrotron photons by a core electron that is excited to an unoccupied state (Figure 18a). Soft XAS thus provides the information on the unoccupied electronic structure at the excited states with the existence of core holes. XES generally corresponds to the occupied valence states. RIXS features stem from interband and other low-energy excitations, mixed with the noncoherent XES signals.

The intrinsic absorption coefficient corresponds to the attenuation of incident X-rays; however, the shallow penetration depth of soft X-rays allows the direct measurement of the attenuation to only ultrathin samples. For battery studies, except for scanning transmission X-ray microscopy, the XAS is mostly collected through the intensity of decay products of the core holes. The broadly practiced channels are the decay through the Auger electron yield (AEY), the total electron yield (TEY) (Figure 19b), partial yield of fluorescence photons (PFY), and the total yield of fluorescence photons (TFY) (Figure 19c). The short escaping length of electrons makes the AEY and TEY extremely surface sensitive with probing depth of only a few nanometers. The PFY and TFY mode is relatively bulk sensitive with a probe depth of hundreds of nanometers depending on the photon energy, but compared to hard XAS, the PFY/TFY mode of soft XAS can be considered as more surface sensitive. At this time, almost all soft XAS systems allow simultaneous data collection through both the TEY and TFY channels, which often reveal the contrast between surface and bulk states of battery samples.[259,260] However, caution needs to be taken with any quantitative analysis based on TFY because serious line shape distortions from the self-absorption effect may occur, due to the abrupt change of the penetration depth of the X-rays when the incident photon energy scans through an absorption edge.[261]

It is worthwhile noting that a recently developed soft XAS technique called inverse partial fluorescence yield (IPFY) could potentially solve the technical problem of the self-absorption distortion in fluorescence yield signals. In contrast to TEY and TFY which measure the excited core-hole states by scanning the excitation photon energy through the absorption edge of interest, IPFY is effectively a measure of the X-ray attenuation length, akin to transmission measurement. For studies of battery materials, IPFY provides the opportunity of a quantative analysis of the TM states in the bulk.[262] Typically, IPFY has been collected through commercial silicon drift detectors with energy resolutions of more than 100 eV.[263] This limits the application of IPFY techniques to battery materials with edges close in energy (e.g., Mn and O). Fortunately, recent development of a high-efficiency soft X-ray RIXS spectrometer, such as the modular X-ray spectrometer (MXS),[264] allows IPFY experiments on all edges covered by soft X-rays (Figure 17).[265]

XES is a PIPO technique, involving a core electron excitation, followed by the decay of this excited state by X-ray photon emission (Figure 19c). Contrasting the integrated photon intensity measured by the soft XAS in TFY or PFY modes, XES measures the intensity as a function of energy distribution of the emitted photons through a spectrometer.[266] XES delivers the information about occupied valence electrons that fill the core hole upon the decay process.[257] In this section, we show that XES reveals the key occupied states that are associated with the delithiation process of battery positive electrodes.

The excitations involved in the XES process are from the core electron state to the continuum states well above the XAS threshold. However, if the excitation energy is carefully tuned, so the core electron is resonantly excited to the absorption threshold, the emitted photons will strongly depend on the excitation energy. This resonant process is detected through RIXS. The RIXS probability is determined by the Kramers-Heisenberg Formula, which will not be discussed here; interested readers can refer to many reviews and books on RIXS.[257,267] Improved RIXS (higher resolution) has become an important probing tools for highly correlated physics.[267] Although with its unique capability of probing low energy and interband excitations, as well as its superior sensitivity to specific chemical configurations, the application of RIXS remains limited for studying battery materials at this time. However, recent improvements on RIXS detection efficiency opens up unprecedented windows for employing soft X-ray RIXS to study battery materials.[265]

4.3.2. Electrical Conductivity: Soft XAS of Battery Binders.
The most direct application of soft X-ray spectroscopy is detection of the key electron states that fundamentally determines the physical and chemical properties of battery materials. As elaborated above, soft XAS corresponds to the unoccupied conduction band or lowest unoccupied molecular orbital (LUMO) derived states. Therefore, the low energy leading edge represents the upper edge of the band gap in a
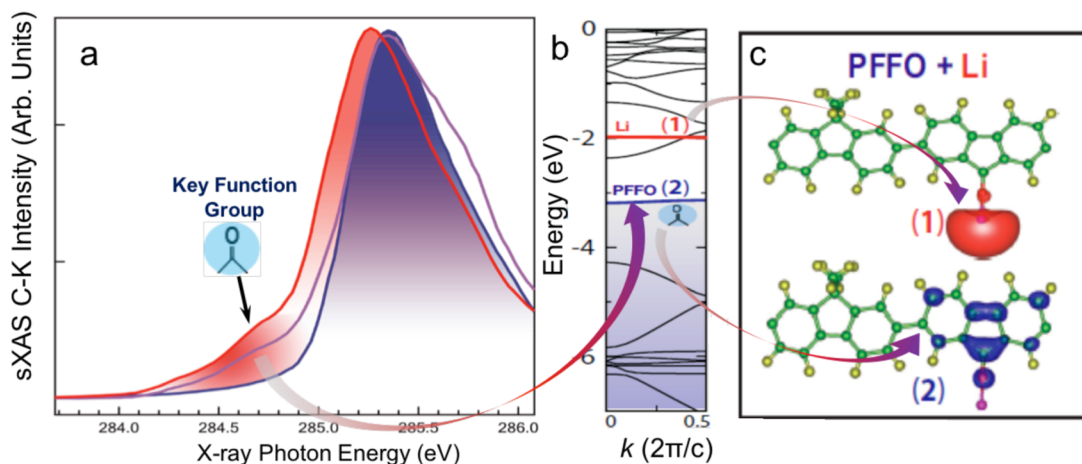
Figure 20. (a) Ex situ C−K XAS spectra of a series of conductive polymers binder materials. Blue, polyfluorene (PF); purple, PF with carbonyl C═O group (PFFO); and red, PF with both carbonyl and methylbenzoic ester groups (PFFOMB). The carbonyl group introduces a low-energy LUMO state at 284.7 eV. (b) The calculated band structure of PFFO. The low-energy electron state is from the carbonyl group and sits below the Li level, leading to electron charge transfer from Li to the polymer backbone, as indicated by the isosurface plots (c). Reprinted with permission from ref 268. Copyright 2011 John Wiley and Sons.
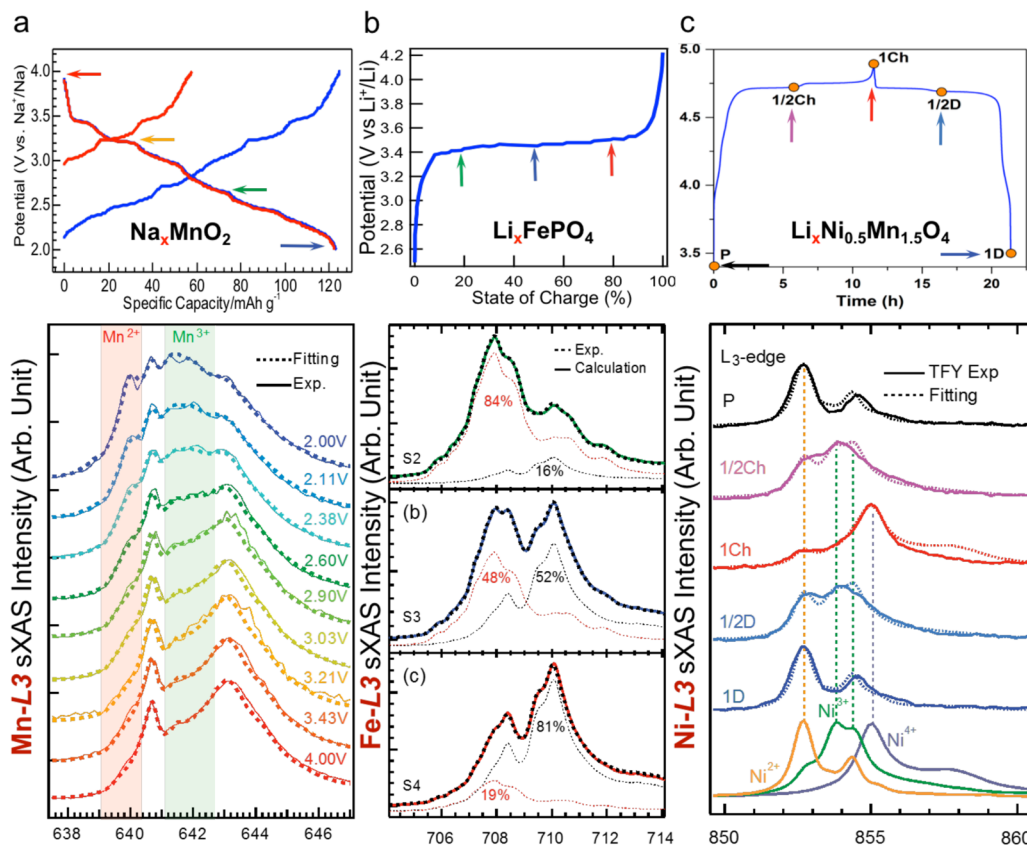
Figure 21. Three examples of the quantitative definition of transition-metal valence distribution through ex situ soft XAS of Mn, Fe, and Ni in the electrodes of Na ion and Li ion batteries. Dotted spectra are simulation results. (a) A quantitative analysis of Mn L-edge soft XAS on a series of $Na_{0.44}MnO_2$ electrode cycled to different electrochemical states; in the charge−discharge cycles, the first cycle and second cycle are shown in red and blue, respectively. (b) A quantitative fitting of the soft XAS data taken on Li_xFePO_4. The two-phase transformation system allows an excellent fitting of the experimental soft XAS by a simple combination of the data obtained from the two end members. Lithiation level could thus be precisely determined. (c) A quantitative fitting of the Ni L-edge soft XAS of $LiNi_{0.5}Mn_{1.5}O_4$ cathodes collected through the TFY channel with more than 100 nm probe depth, based on the calculated Ni^{2+}, Ni^{3+}, and Ni^{4+} TFY spectra at different electrochemical states. Reprinted with permission from ref 276. Copyright 2015 Elsevier. Ltd. Reprinted with permission from ref 284. Copyright 2015 American Chemical Society. Reprinted with permission from ref 466. Copyright 2016 IOP Publishing Ltd.

nonmetallic material, which gives information about electric conductivity. Figure 20 shows the C-K soft XAS collected on a

series of polyfluorene (PF) binders with various functional groups. Binders are an important component in batteries for

maintaining both mechanical and electrical integrity. However, a high volume of conductive additive reduces both the volumetric and gravimetric energy density. Additionally, for high-capacity active materials, electrical disconnection takes place due to the severe volume expansion during electrochemical operation; for example, the silicon anode is known to suffer a volume expansion of almost 4 times during lithiation. An ideal binder system should integrate mechanical stability and electrical conductivity, so both factors can be maintained throughout electrochemical operation.

As shown in Figure 20, soft XAS reveals a LUMO state sitting at a very low energy in samples with carbonyl groups. This carbonyl induced $\pi^*_{C=O}$ transition is even lower in energy compared with that of the typically low-energy $\pi^*_{C=C}$ states. This soft XAS finding also agrees with ab initio density functional theory (DFT) calculations. The calculation further predicts that charge transfer to this low-energy state, which improves the overall electric conductivity, will take place if such materials are used under reducing environment in batteries. Such information provides unambiguous understanding of the improved electric conductivity in the battery binder system. Electrodes made by mixing commercial Si particles with the PFFOMB polymer binder and without any other conductive additives show improved cycling performance compared to those made with conventional formulations.[268] These data advance development of a functioning silicon electrode[269] and provide understanding of the performance variation between different conductive polymer materials.

4.3.3. Quantitative Analysis of Transition Metal Redox.
Soft XAS is a direct probe of the excited TM3d states through the dipole allowed 2p to 3d (L-edge) electron excitations, which fingerprints the formal valence, spin state, and chemical bond configuration.[257,270] There are several unique advantages of studying TM L-edges in battery materials. First, because the TM L-edge spectral line shape is defined largely by the atomic multiplet effects, sharp and well-defined features can be observed in soft XAS results, which provides a unique opportunity for detailed and quantitative analysis. By virtue of the sensitivity to the TM3d states and the sharp features from multiplet effects, TM L-edge soft XAS is arguably the most direct probe of the TM redox in battery electrodes. Second, due to the intrinsically different penetration depths of electrons and phonons, the probe depth of soft XAS in the electron and photon detection modes ranges from several nanometers to about 150 nm and can be tuned. This enables soft XAS to probe the differences between the surface and the bulk in battery materials. Third, with high brilliance third generation synchrotron facilities, it is now possible to utilize TM-L soft XAS as not only a sensitive and quantitative probe of the TM3d states, but also to perform experiments in situ and operando,[271−274] with nanometer scale spatial resolution for imaging charge diffusion in battery materials (although with some caveats).[275]

Figure 21 is a summary of three selected examples of quantitative soft XAS studies of Mn, Fe, and Ni cations in battery cathodes for Na ion and Li ion batteries. For the $Na_{0.44}MnO_2$ electrodes, a quantitative analysis of Mn L-edge soft XAS on a series of $Na_{0.44}MnO_2$ electrodes cycled to different SOCs was performed.[276] The dotted lines are simulated spectra obtained through a straightforward linear combination of three spectra of Mn^{2+}, Mn^{3+}, and Mn^{4+} reference samples.[277,278] The simulation completely reproduces all the high-resolution features in the experimental soft XAS

data, which provides a precise determination of the surface Mn valence distribution at different SOCs.

The analysis showed that, when the electrode was discharged from 4 to 2.6 V and Na ions were inserted, the Mn^{4+} concentration decreased monotonically and the Mn^{3+} concentration rose. $Na_{0.44}MnO_2$ based electrodes have been assumed to undergo only $Mn^{3+/4+}$ redox reactions during cycling under normal conditions.[279,280] However, this quantitative analysis showed that when the cell was further discharged below 2.6 V, the Mn^{2+} concentration increased rapidly. The comparison between soft XAS in TEY mode and hard XRS further proved that Mn^{2+} formation occurs only on the surface.[276] The surface Mn^{2+} is likely to be detrimental to performance because of its solubility in the electrolytic solution but could be suppressed by limiting the discharge cutoff voltage to 2.6 V or higher, which could improve the capacity retention over extended cycles. Indeed by limiting the discharge cutoff to 3 V, negligible capacity loss and surface Mn^{2+} formation was observed after 100 cycles.[276]

Quantitative analysis of the TM redox in battery electrodes is the most straightforward in systems that undergo two-phase transformations with a single redox TM cation, where only two end member phases are involved throughout the electrochemical cycling, as with the $LiFePO_4$ electrode. Figure 21 demonstrates another perfect quantitative fitting of the soft XAS data taken on $LiFePO_4$ electrodes at different states-of-charge. A linear combination of soft XAS spectra of the two end states $LiFePO_4$ and $FePO_4$ can be used for quantitative spectra simulations. The SOC of the intermediate states can be precisely determined.[281]

It is worthwhile noting that the high sensitivity and precise definition of the Fe valence state in $LiFePO_4$ through soft XAS provides a unique opportunity to detect the SOC distribution or the Li-ion diffusion dynamics throughout electrodes. The advantage of soft XAS has been well-utilized in recent in situ microscopic studies of $LiFePO_4$ electrodes (more discussion later).[129,282,283] Additionally, the surface sensitivity of the TEY mode of soft XAS enables position sensitive measurements on the TM redox states on the two different sides of an electrode (i.e., the sides facing the separator and current collector). Although the electrolytic solution typically soaks through the whole electrode, the (10 nm) surface sensitivity of the soft XAS TEY signals allows the detection of the contrast between the electrode particles attached directly to the current collector (after peeling off) and the particles directly contacting the separator, which are wet first during assembly of the cell. Such contrast provides two important pieces of information on the electrode: the charge diffusion and the lateral SOC gradient in electrodes[85] and the effect of electrolytic solution exposure on the surface of the electrode particles.[277]

It is relatively easy for soft XAS to probe the TM states on the surface of a battery electrode, but it is desirable to provide the TM redox contrast between the surface and the bulk of electrode particles. The TFY signal of soft XAS probes to depths of hundreds of nanometers but suffers from self-absorption distortion. There are two ways to conquer this technical problem. One is to utilize the IPFY (described above) that is a bulk probe without self-absorption distortions,[262,263] another is through theoretical calculations that takes the distortion into account. Because the multiplet effect in the TM L-edge leads to distinct features in the soft XAS spectra,[257,270] it is possible to achieve a quantitative analysis of the TM redox with the aid of multiplet calculations. Figure 21 shows the
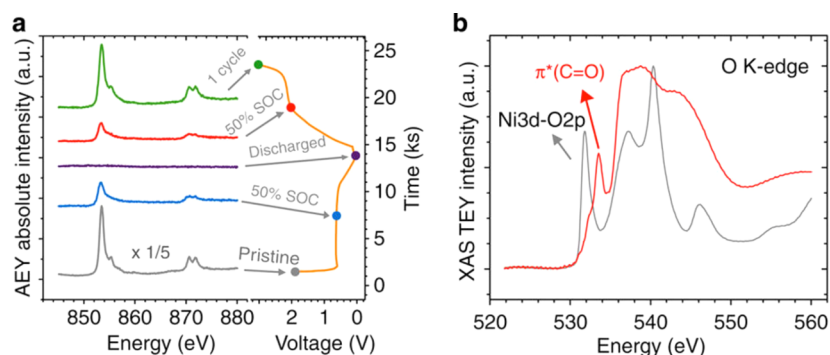
Figure 22. (a) Ex situ soft XAS of NiO based composite electrodes at different SOCs, where the XAS measurement was done using the AEY mode, and the voltage profile is provided in parallel to indicate the SOCs and (b) soft XAS O K-edge spectra for electrodes in the pristine state (gray) and in the 50% SOC (red). Reprinted with permission from ref 91. Copyright 2014 Nature Publishing Group.
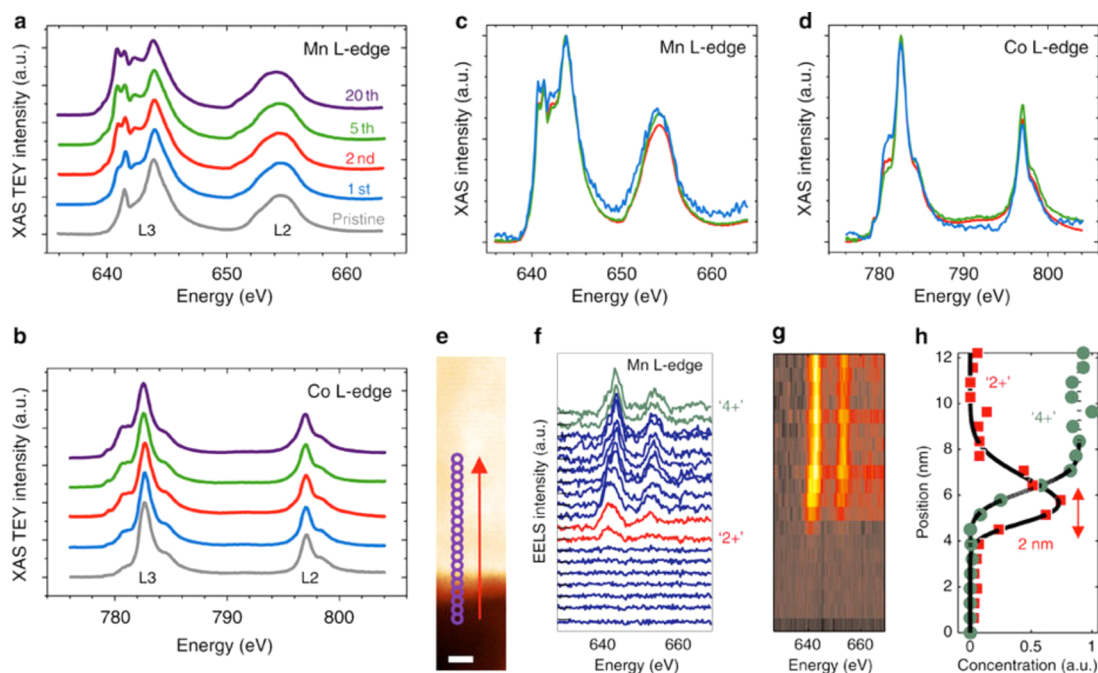
Figure 23. (a) Ex situ XAS of Mn L-edge spectra and (b) Co L-edge XAS spectra after different cycles at 2.0−4.7 V vs Li$^+$/Li in organic electrolyte; the same color scheme applies to (a) and (b). (c) Mn L-edge spectra and (d) Co L-edge spectra after two charge−discharge cycles in the AEY (blue), TEY (red), and FY (green) detection modes. EELS line scan profile for an NMC particle along the <001> direction after five cycles: (e) STEM image shows the EELS scanning path, (f) Mn L-edge EELS spectra along the scanning path, where the red and green spectra represent Mn^{2+} and Mn^{4+} spectra, respectively. (g) 2D EELS map and (h) concentration profiles for Mn^{2+} and Mn^{4+}. The scale bar in (e) is 2 nm. Reprinted with permission from ref 90. Copyright 2014 Nature Publishing Group.

comparison of the calculated Ni^{2+}, Ni^{3+}, and Ni^{4+} TFY spectra with the soft XAS data collected in TFY mode of a LiNi$_{0.5}$Mn$_{1.5}$O$_4$ cathode material.[284] The Ni-L edge soft XAS collected on a series of Li$_x$Ni$_{0.5}$Mn$_{1.5}$O$_4$ electrodes at different SOCs could be perfectly fitted again with the calculated spectra of Ni^{2+}, Ni^{3+}, and Ni^{4+} in an octahedral crystal field.[284] In contrast to the LiFePO$_4$ cathode in which the soft XAS TEY spectra of intermediate states could be well-reproduced by linear combination of two end member spectra, the Ni-L edge absorption spectra of Li$_x$Ni$_{0.5}$Mn$_{1.5}$O$_4$ electrodes have distinctive features at different photon energies from the two end states at 50% state of charge. Therefore, the intermediate states of Li$_x$Ni$_{0.5}$Mn$_{1.5}$O$_4$ cannot be reproduced by mixing the features of Ni^{2+} and Ni^{4+}, which implies the appearance of a stable intermediate Ni^{3+} valence state in the half-charged state. The theoretical multiplet calculation was based on the single impurity, and the Anderson model proves that the distinctive

features arise from the Ni^{3+} state. Such a quantitative analysis via the combination of experimental soft XAS spectra and theoretical calculated spectra provides the evidence of a single electron transfer mechanism and sequential redox reactions of Ni^{2+}/Ni^{3+} and Ni^{3+}/Ni^{4+}.

Therefore, the sensitivity of the soft XAS to the TM 3d states enables various approaches for quantitatively determining the TM redox in a battery electrode. This analysis can be performed with both surface and bulk sensitivity, under ex situ and in situ conditions and for different types of phase transformations. The details revealed through such soft XAS studies clarify the TM redox processes as a function of the positioning and the electrochemical potential of a battery electrode.

4.3.4. Soft XAS to Probe Surface Chemistry. Because of its unique capabilities of surface probing and depth profiling, soft XAS has been widely applied to investigate surfaces of
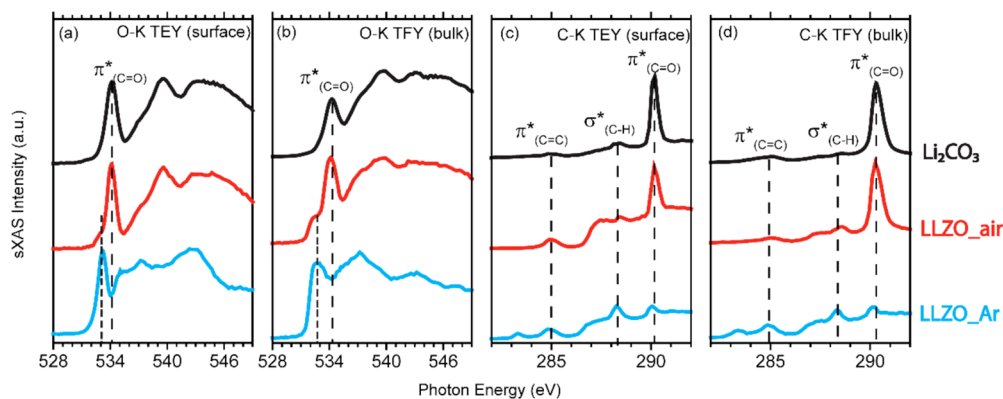
Figure 24. O *K*-edge ex situ soft XAS spectra of LLZO_Ar (cyan), LLZO_air (red), and Li$_2$CO$_3$ (black) in (a) TEY mode and (b) FY mode; C *K*-edge soft XAS spectra of LLZO_Ar (cyan), LLZO_air (red), and Li$_2$CO$_3$ (black) in (c) TEY mode and (d) FY mode. Reproduced with permission from ref 287. Copyright 2014 PCCP Owner Societies.

anodes, cathodes, and solid electrolyte materials. The soft XAS measurement, particularly when it is performed using electron yield modes (e.g., AEY, TEY), can be used to monitor the growth and decomposition of electrode−electrolyte interphases, for example, the solid-electrolyte interphase (SEI) between the anode and the organic liquid electrolyte. Some of our coauthors have studied the changes of the SEI layer on an electrode containing a conversion material (i.e., NiO).[91] Due to the small mean free path of Auger electrons in the SEI layer, the absolute intensity of Ni *L*-edge soft XAS/AEY is sensitive to the thickness of SEI, and exponentially decays as a function of the thickness. The intensity decreased as the electrode was discharged and increased as the electrode was charged, indicating the growth and decomposition of the SEI layer, respectively (Figure 22a). The subsequent soft XAS/TEY O *K*-edge study showed that the oxygen local environment changed from NiO (Ni3d-O2p hybridization) to carbonate-dominated species (Figure 22b). A STEM-EELS (scanning transmission electron microscopy-electron energy loss spectroscopy) study (Li *K*-edge, C *K*-edge, and O *K*-edge) on the same set of electrodes confirmed the presence of Li$_2$CO$_3$ in the SEI layer.[91]

NMC materials undergo surface reconstruction to form a rocksalt phase under a variety of conditions. It is particularly severe when they are cycled to high voltages, and increased cell impedance and poorer rate capability is observed as a consequence of this as well as CEI formation (the product of electrolyte decomposition, see more in Figure 30 and the associated discussion). Lin et al. performed soft XAS measurements on composite electrodes containing NMC442 materials after electrochemical cycling under a variety of conditions.[88,90] In particular, the authors focused on the changes of oxidation states of Mn and Co at the electrode surfaces. Measured by soft XAS in the TEY mode, Mn and Co ions were both gradually reduced as the cycle number increased, as evidenced by the intensified shoulders at the lower energy of L3 edges (Figure 23, panels a and b). The direct comparison between the spectra collected using AEY, TEY, and FY showed that the reduction of Mn and Co were more severe at the surface (Figure 23, panels c and d). STEM-EELS can probe electronic structure of these transition metals at a much smaller length scale and provide complementary information to the ensemble-averaged soft XAS. Figure 23 (panels e and f) clearly substantiated that the reduction occurred at the surface, with a thickness of the order of several nanometers. This was one of the first studies to combine core-

level spectroscopic analytical tools at the identical energy edge but complementary length scales (STEM-EELS and soft XAS) and directly illustrated the origin(s) of the challenges when cycling NMC materials to elevated voltages. Soft XAS has also been used to monitor the impact of synthesis conditions on the electrochemical performance.[285,286] Xu et al. discussed the importance of excess lithium precursor in the synthesis of LiNiO$_2$, they determined, from the soft XAS study, that a higher amount of excess lithium (∼10%) helped inhibit the formation of NiO on the surface and yielded a product with the best practical discharge capacity and rate performance.[286]

Soft XAS was also employed to estimate the thickness of the Li$_2$CO$_3$ layer formed on air-exposed LLZO using the same samples studied by XPS described in section 4.4.2. Cheng et al. designed an experiment where LLZO pellets were exposed to different ambient conditions (e.g., air exposure vs Ar exposure).[287] The O K-edge soft XAS is sensitive to the local chemical environment and can be used to monitor the buildup of Li$_2$CO$_3$, in particular when it is combined with C K-edge soft XAS. As shown in Figure 24 (panels a and b), the pure Li$_2$CO$_3$ spectrum (top) exhibited a peak at 534.1 eV, originating from the electron transition from the O 1s to π^* (C=O) orbital, similar to that in Figure 22b. However, the LLZO sample that was exposed to Ar only showed a lower absorption peak at 533.0 eV, related to the lattice oxygen in LLZO, and no Li$_2$CO$_3$ signal was detected. The TEY of LLZO_air (middle) is similar to that of the pure Li$_2$CO$_3$ reference. In other words, Li$_2$CO$_3$ was detected on the LLZO_air pellets but was not on LLZO_Ar. When the probing depth increased to ∼100 nm using the FY mode, LLZO_air and the LLZO_Ar samples both showed LLZO peaks at 533.0 eV. An additional O K-edge peak at 534.1 eV was detected for the former because of the Li$_2$CO$_3$ on the pellet surface (Figure 24b, middle and bottom). In addition, the C K-edge soft XAS spectra (Figure 24, panels c and d) on the same samples provide supporting evidence for the assignment of Li$_2$CO$_3$ on the air-exposed sample (i.e., LLZO_Ar). The appearance of a minor peak at 533.0 eV in the TEY spectrum of LLZO_air implies that the Li$_2$CO$_3$ thickness is near or slightly lower than the detection depth of the TEY mode (∼10 nm). The study not only confirmed the XPS finding in section 4.4.2 but also semiquantitatively estimated the thickness of surface Li$_2$CO$_3$ layer to be close to or slightly lower than the 10 nm detection depth of the TEY mode. This study confirmed the findings of the XPS experiment, which estimated a lower limit of ∼3 nm for this layer.
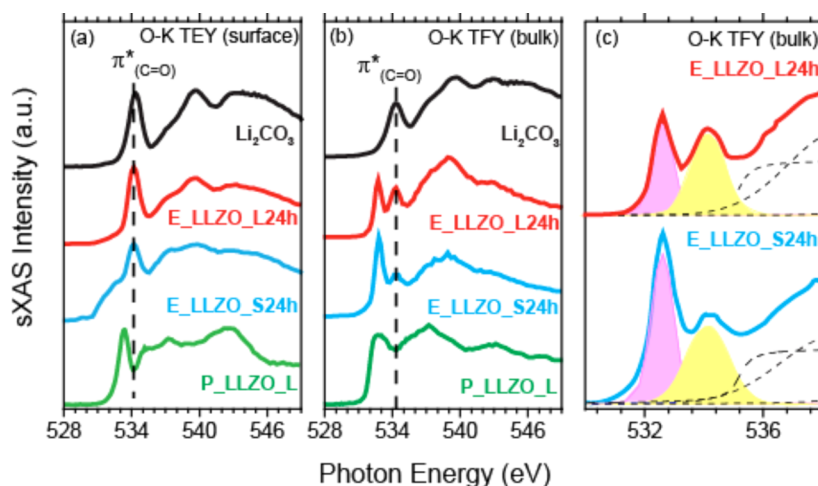
Figure 25. (a) O K-edge ex situ soft XAS spectra for pristine large-grained LLZO (green), small-grained LLZO exposed to air for 24 h (cyan), large-grained LLZO exposed to air for 24 h (red), and Li_2CO_3 (black) in the TEY mode. (b) O K-edge soft XAS spectra for pristine LLZO (green), small-grained LLZO exposed to air for 24 h (cyan), large-grained LLZO exposed to air for 24 h (red), and Li_2CO_3 in the FY mode. (c) The deconvolution of the O K-edge pre-edge peak to separate the contributions from oxygen of Li_2CO_3 (yellow) and oxygen of LLZO (purple). Reprinted from ref 288. Copyright 2015 American Chemical Society.
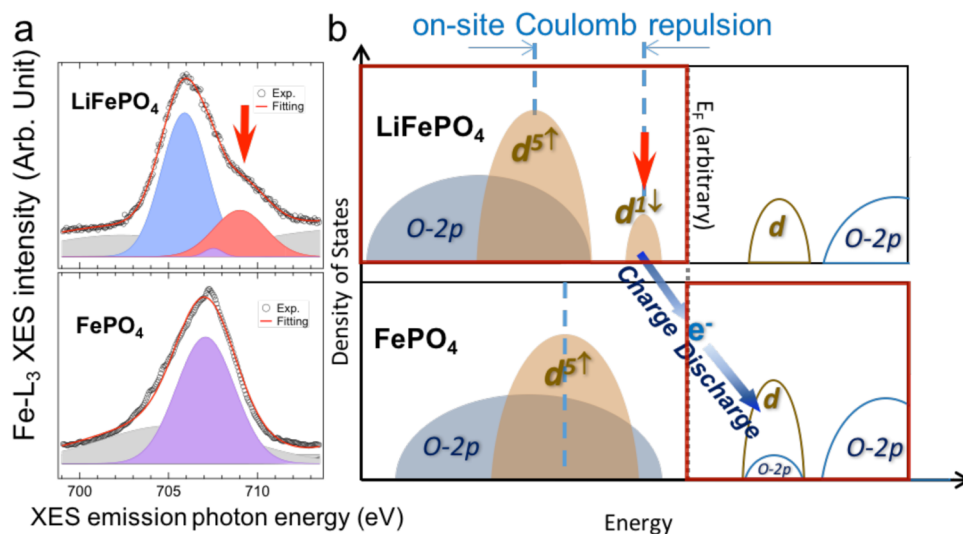
Figure 26. (a) The ex situ Fe L_3-edge XES results collected on $LiFePO_4$ and $FePO_4$. For the lithiated state in $LiFePO_4$, an occupied minority-spin Fe3d state is separated from the majority-spin state and sits at high energy close to the Fermi level (red arrow). (b) Schematic of the occupied and unoccupied electron states that correspond to the main characterization of the states involved in a battery charge and discharge process, respectively. These states could be experimentally determined through soft X-ray XES and soft XAS. Reproduced with permission from ref 296. Copyright 2015 PCCP Owner Societies.

Cheng et al. also studied the air stability of Al-substituted LLZO solid electrolytes made from different processing routes[288] that resulted in two distinct microstructures. The first one consisted of grains about 10−20 μm across (LLZO_S) at the surface of the pellet, and the second sample had much larger grains of about 150−200 μm across (LLZO_L). As shown in Figure 25, after being exposed to air for 24 h, both samples developed a layer of Li_2CO_3 at the surface, but the thickness of the Li_2CO_3 layer differed markedly for the two types of samples. By evaluating the garnet versus carbonate peak ratio in the O K-edge TFY soft XAS spectra, it was determined that much less Li_2CO_3 formed on the small-grained sample than on the large-grained sample. Synchrotron XPS analysis of the pristine samples revealed that the top surfaces of the small-grained LLZO samples contained less lithium and more aluminum than the large-grained samples. The processing

conditions used to make the large-grained sample caused some aluminum to segregate into the lower-lying grain boundaries, enriching the grains with lithium. The high lithium content of the grains made the large-grained LLZO sample more sensitive to air.

4.3.5. Valence Electron Configuration: Anionic Redox and XES. As a typical "electronic" device, a lithium-ion battery operates with evolving electronic states in its active components, including the electrodes and the interfaces. The potentials and kinetics of the electronic states determine the transport of the charge carriers (i.e., Li ions and electrons). The configurations of the electronic states regulate the chemical reactivity at the surface and interfaces and determine the chemical reactions at the electrode−electrolyte interfaces. These crucial chemical processes can occur via direct redox reactions within the electrodes or electrolyte and indirect

interfacial catalytic reactions. Two critical electron state configurations are thus relevant to a battery performance.[260] One is the surface electron state that determines or affects the surface activity of an active material when contacting the electrolyte;[259] the other is the relative configuration of the TM-3d and anion p states in the bulk electrodes. The invention of the first generation of lithium-ion battery cathodes, $LiCoO_2$, by Goodenough's group was inspired by the concept of "redox pinning" in transition metal oxides, which is related to the relative positioning of the TM and anion states on a common energy scale. This fundamental concept determines the safety and voltage limits of a battery electrode.[289,290] Interestingly, the discussions resemble those formulated by the Zaanen-Sawatzky-Allen (ZSA) diagram,[291] which can be experimentally verified by a combination of soft XAS and XES.[292,293]

Clarification of the electron state configurations has recently become more critical with the new realization that anionic redox can occur for some types of battery cathode materials.[46] This concept is fundamentally based on some specific electron state configurations that stem from either the oxygen dimer[294] or a lithium excess environment.[295] Sitting at the center of all these discussions is the configuration of the occupied electron states of the TM and O, which can be systematically studied through soft X-ray XES.[292,293]

Figure 26 presents the Fe L_3-edge XES results collected on $LiFePO_4$ and $FePO_4$.[296] For the Fe^{2+} states in $LiFePO_4$, the Fe L-edge XES displays an occupied Fe3d state that sites at higher energy compared with other 3d states (red arrow). Theoretical analysis shows that the Coulomb interactions of Fe3d electrons lead to such reshuffling of the states with opposite spins. During the delithiation of $LiFePO_4$, only these high-energy Fe3d electrons are removed because they are relatively close to the Fermi level. In the other hand, the O K-edge soft XAS and hard X-ray Raman spectroscopy (XRS) show that the unoccupied Fe-3d states also sit close to the Fermi level (not shown) for the delithiated state of $FePO_4$.[296] Therefore, for both the charge and discharge process, the charge transfer takes place only on the Fe3d states. This finding naturally explains the stability of oxygen in $LiFePO_4$ based electrodes during electrochemical operations, thus providing a fundamental mechanism to understand the better safety of $LiFePO_4$ electrodes compared to other types of electrode materials.

In physics, the design and operation of Li-insertion cathodes are fundamentally defined by the electron states in the vicinity of the Fermi level of the electrode material. Because the soft XAS and XES results correspond to the unoccupied and occupied states, respectively, they become the tools-of-choice to detect the critical electron states associated with the discharge and charge process.[296] As a matter of fact, the fundamental electron state configuration has been one of the key factors triggering the developments of the $LiFePO_4$ and $LiCoO_2$ materials for batteries.[297] Because most battery cathode materials are 3d TM compounds, soft XAS, XES and RIXS are potentially able to provide clarification of the TM and anionic redox and lead to guidelines for optimizing TM-based battery electrodes, particularly as interest grows in the possibility of utilizing anionic redox for next-generation materials.

4.3.6. Soft X-ray In Situ and Operando Techniques.
Soft X-ray techniques have been extensively employed to study the properties and processes under ultrahigh vacuum (UHV) conditions. The intrinsic small penetration depth of soft X-ray photons, with probe depths of several nanometers and hundreds of nanometers, is both advantageous and disadvanta-

geous. On one hand, soft X-ray is a powerful technique for understanding the surface chemistry of electrodes and solid electrolytes; an example already covered here is that of the SEI on anode surfaces.[298] On the other hand, the limited penetration depth of soft X-rays leads to serious limitations for its employment in practical applications, especially at the gas−solid and liquid−solid interfaces under ambient pressure. Fortunately, the combination of synchrotron radiation with high brightness and modern soft X-ray experimental systems have led to tremendous progress in integrating practical sample environments for soft X-ray spectroscopic experiments. Nevertheless, it is important to note the necessity of combined in situ and ex situ experimental methods. The in situ and operando soft X-ray experiments involve complicated instrumentation systems and often have low signal-to-noise level and mixed signals with artificial effects, making it difficult for in-depth and/or precise analysis. The decades of work from ex situ studies still serves as the foundation of soft X-ray sciences, and they will continue to be an indispensable part of soft X-ray spectroscopy. In the meantime, the past decade has witnessed rapid progress on designing different in situ/operando cells for use with soft X-ray spectroscopy.[299−306] Various in situ/operando soft X-ray techniques have been rapidly developed and optimized, including those with operando electrochemical cycling.[304−306] At this time, almost all the aforementioned soft X-ray PIPO techniques can be performed under in situ or operando conditions.[84]

There are various ways to achieve measuring soft X-ray signals of samples under electrochemical operation. First, a solid-state battery system could be easily incorporated into a modern soft X-ray experimental system with some straightforward in-vacuum electric connections.[283] Second, the detection instrumentation could be designed for working under real world conditions, typically through differential pumping (e.g., for ambient pressure XPS). Third, a very thin soft X-ray window about a hundred nanometers thick could be used to isolate the sample environment from the UHV chamber. Demonstrations of membrane windows have been reported for operando soft X-ray PIPO spectroscopy of both static and flow through liquid and gas,[305,306] as well as battery cells.[304]

4.4. X-ray Photoelectron Spectroscopy (XPS)

X-ray photoelectron spectroscopy is a ubiquitous tool in surface analysis, which has seen a tremendous growth over the past 30 years into one of the primary techniques for chemical analysis. Core-level photoemission has the ability to provide atomic fractions of the elemental composition down to 0.1% sensitivity, and as shown already in the seminal work of Siegbahn et al.,[307] through the screening and/or charge transfer between the core-excited atom and its environment, superb sensitivity to the chemical state of the atom. Traditionally, XPS has been performed in lab-based setups, where a fixed photon source (typically Mg or Al $K\alpha$ X-rays at 1253.6 and 1486.6 eV, respectively) of about 1 eV resolution is used in conjunction with a hemispherical or cylindrical electron analyzer. With a fixed energy, the kinetic energy of the outgoing electron varies from a few hundred eV up to and above 1000 eV, which results in an inelastic mean free path (IMFP) from 1 nm up to about a few nm, making the technique very surface sensitive.

Synchrotron radiation has played an important role in the applicability of XPS to interfacial studies of materials, through the improved photon flux and energy resolution allowing for routine high-resolution XPS, the enabled small spot focus from
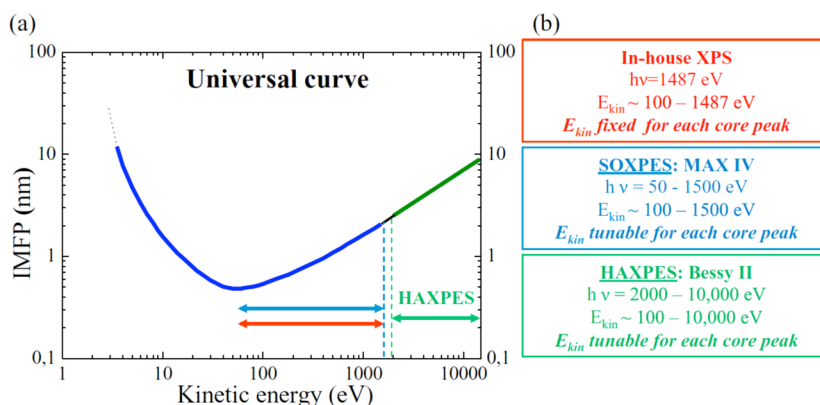
Figure 27. (a) Universal curve for the inelastic mean free path (IMFP) versus the kinetic energy of the photoelectrons. (b) Illustration of the energy range (*hν* and Ek) reached by using monochromatic (Al Kα X-ray) or synchrotron (soft X-ray and hard X-ray) sources. For a particular beamline, constraints in the monochromator configuration control the accessible energy range. Grazing incidence grating monochromators are equipped on soft X-ray beamlines to reach 1−2 keV with high efficiencies, whereas for X-ray energies higher than 2000 eV crystal monochromators are needed. Reproduced with permission from ref 308. Copyright 2016 Electrochemical Society.

high brilliance insertion devices, and the ability to change the photon energy which strongly affects cross section and probing depths through the varying outgoing electron kinetic energies. The variability in cross section and probing depth enabled by synchrotron radiation has increased the utility of XPS for battery materials and rendered the technique complementary to XAS, since they both can access the chemical state of the elements in the surface and near-surface region, respectively. XPS does not display the same sensitivity as XAS and typically cannot resolve symmetry, spin-state, and local distortions for the same valence. However, the reduced complexity is often preferred when the main components of each element (e.g., metallic vs oxide or single-bonded vs double-bonded) is sought, or when a full account of the elemental composition is required from the surface region. Moreover, in XAS, when the energy region does not offer a direct transition from the core hole of an element into the frontier orbitals of the material, the better choice might be to extract chemical information from a sharp core-level peak arising from that same element via XPS (which can be at any binding energy below the excitation energy). XPS also remains the most widely applied and classical tool for extracting information about elemental composition and chemical states described in the scientific literature, which makes the observations easier to analyze, and, when disseminated, more widely accepted by a large audience. In the following, we address soft/tender X-ray photoelectron spectroscopy and hard X-ray photoelectron spectroscopy separately, with the primary distinction being the degree of surface sensitivity. Overall, XPS is generally considered as a surface sensitive technique compared to hard XAS, where X-rays can penetrate deep through the probed materials. Also, caution needs to be taken when comparing the XPS elemental quantification with the global composition of the probed materials.

4.4.1. Hard X-ray Photoelectron Spectroscopy. Hard X-ray photoelectron spectroscopy (abbreviated HAXPES, HXPS, or HX-PES) generally refers to synchrotron XPS experiments in the energy range between 2000 and 15000 eV, in contrast to soft XPS (SXPS) where the energy range is much lower[308] (see Figure 27). The ability to tune the kinetic energy ranges of the analyzed photoelectrons allows for variable depth analysis,[309] as with SXPS, but to a different extent. The higher energy range of HXPS means that depths up to several tens of

nanometers (i.e., into the bulk of the sample) can be probed in a nondestructive manner, about an order of magnitude greater than what is accessible by SXPS.[310,311] Although HXPS was first demonstrated in 1974,[312] its application to battery science is much more recent, occurring primarily after development of advanced beamlines at synchrotron facilities such as BESSY 2 in Germany and SPring-8 in Japan in the mid-2000's.[313]

One of the earliest HXPS studies involved an investigation of NCA electrodes removed from cells cycled at different temperatures.[314] Increased amounts of carbonate species, degradation products of the electrolyte, and a Li-deficient cubic phase on NCA electrode surfaces were correlated with the power fade exhibited at elevated temperatures. HXPS was also used to identify and quantify the thickness of reaction layers on LiCoO$_2$ electrodes stored in electrolytic solutions at room temperature and 60 °C.[315] Thin film electrodes deposited on nickel substrates were used as model systems to determine component thicknesses and compared to results with composite electrodes. Thicknesses of about 30−40 nm for LiF, CH$_3$OCO$_2$Li, and Li$_2$CO$_3$ were estimated on composite LiCoO$_2$ electrodes stored at 60 °C.

A later study of NCA electrodes taken from cells cycled more than 1000 times at room temperature also showed evidence of surface degradation.[316] A comparison of the Ni 2p$_{3/2}$ core level spectra of the NCA electrodes before and after cycling was consistent with generation of an inert NiO phase at the surface (probing depth of the experiment was about 10 nm). The ability to probe into the bulk of the electrode allows information about transition metal oxidation states as a function of SOC or cycling history to be obtained without interference from reaction layers or any coatings that are present (i.e., "buried interfaces" can be studied). For example, evidence for the participation of both Ni and Ti ions during cycling of a Ni$_{0.5}$TiOPO$_4$ conversion electrode was observed in Ni 2p$_{3/2}$ and Ti 2p core level spectra, in addition to formation of an SEI layer in the C 1s spectra.[317] Likewise, differences in Mn oxidation states could be observed in epitaxial thin films of LiNi$_{0.5}$Mn$_{1.5}$O$_4$ with and without Li$_3$PO$_4$ coatings 1−4 nm thick.[318] Depth profiling of thin film LiNi$_{0.5}$Mn$_{1.5}$O$_4$ electrodes coated with Li$_4$Ti$_5$O$_{12}$ carried out by a stepwise increase in photon energy[319] revealed intermixing of Mn and Ni ions with Ti in the Li$_4$Ti$_5$O$_{12}$ layer, as well as a surface layer approximately 3 nm thick consisting of organic polymers and

metal fluorides and fluorophosphates. Depths probed ranged from 6 to 20 nm, based on eq 6, where d_p is the probing depth, $\lambda(\text{K.E.})$ is the IMFP of the photoelectrons in the substrate, and θ is the electron takeoff angle (TOA), which was fixed for this particular study.

$$d_p = 3\lambda(\text{K.E.})\sin\theta \tag{6}$$

Changing the TOA also allows the probing depth to be varied, as was done in a recent study of an Al_2O_3-coated $Li_{1.2}Ni_{0.18}Co_{0.03}Mn_{0.58}O_2$ (LMR-NMC) electrode.[320] The HXPS data revealed that a $LiM_{1-x}Al_xO_2$ interlayer formed as a consequence of the coating procedure (Figure 28). SEI layer
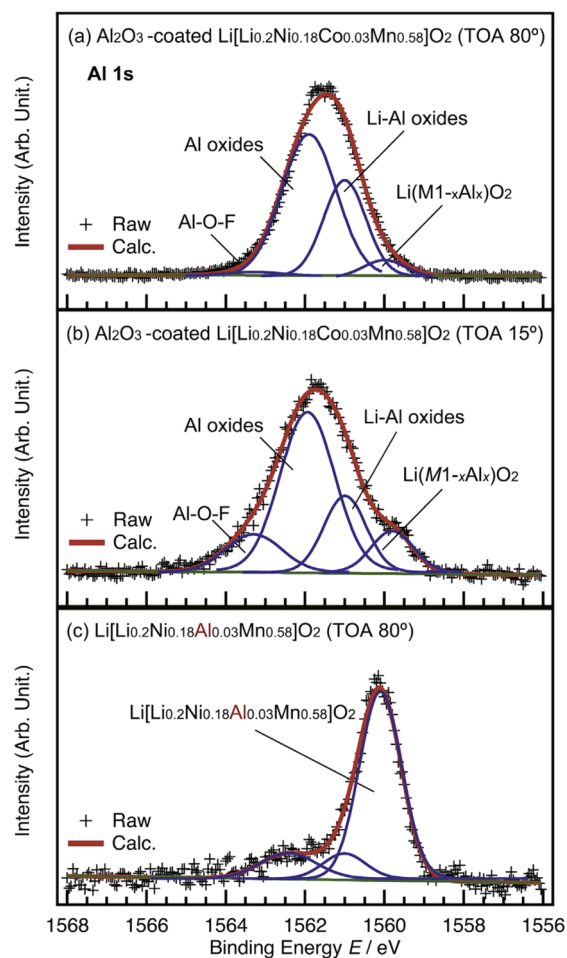
Figure 28. Al 1s HXPS spectra of uncoated and alumina-coated LMR-NMC samples obtained at takeoff angles of (a) 80° (coated), (b) 15° (coated), and (c) 80° (uncoated). The red and blue lines represent fitted curves and their components, respectively. Reprinted with permission from ref 320. Copyright 2016 Elsevier Ltd.

formation on graphite anodes has also been studied as a function of SOC,[321] temperature, aging,[322] and/or the presence or absence of additives in the electrolytic solutions.[323,324] These studies reveal a complex and dynamic process, with both the nature of the components and the thicknesses of the SEI layers changing depending on cell history and additive used, in contrast to reaction layers on a positive $LiFePO_4$ electrode, which appear to be thinner and less variable.[325] In the study referenced in ref 325, HXPS was combined with SXPS, allowing tuning of probing depths over a range of 2−50 nm to be carried out. Figure 29 shows the PES spectra obtained on a lithiated

graphite anode from this work and clearly illustrates the complex nature of the SEI. There was a gradient distribution of chemical environments for all the probed elements as a function of depth from 2 nm on the surface to 45 nm in the subsurface.

Buried interfaces on hard carbon electrodes have been studied with HXPS, allowing elucidation of the mechanism of lithium insertion into the carbon below the SEI layer.[326] C 1s and Li 1s spectra were obtained on hard carbon electrodes at different states-of-charge in conjunction with conventional XPS data, which allowed components of the SEI to be identified. The deeper penetration depths allowed contributions from the SEI layer to be deconvoluted from those of the carbon electrode itself.

The effects of additives on SEI formation on Si[327,328] and Sn[329] anodes have also been examined and compared to processes on graphite electrodes. Ref 330 describes SEI formation from electrolytic solutions containing a promising new salt, lithium 4,5-dicyano-2-(trifluoromethyl)imidazolide (LiTDI), on Si electrodes. While LiTDI partially decomposes upon cycling, unwanted side reactions involving Si do not appear to occur because HF, a common decomposition product of $LiPF_6$, does not form from LiTDI. The SEI layer appears to be thicker than those formed on Si or graphite electrodes from $LiPF_6$-containing carbonate solutions but contains similar reaction products such as organic compounds formed from carbonate decomposition and LiF.

The relative newness of the HXPS technique, and the fact that it is available at only a few synchrotron facilities in the world mean that few Beyond Lithium Ion systems have been investigated. It has, however, recently been applied to the study of the sodium-ion battery cathode material, P2−$Na_xCo_{2/3}Mn_{2/9}Ni_{1/9}O_2$.[331] Transition metal oxidation states as a function of SOC were determined from analysis of Co 2p, Mn 3s, and Ni 2p core-level spectra and revealed that all metals were electrochemically active, although at different stages in the cycling. The evolution of the reaction layer on the surfaces of the electrode was also followed. Both NaF and Na_2CO_3 were present on the pristine electrode prior to electrolyte exposure, where the former stemmed from binder decomposition and the latter originated from synthesis. During charging, these species gradually disappeared, possibly due to dissolution into the electrolytic solution, but then reprecipitated onto the electrode surface upon discharging. Voltage-dependent phosphate and fluorophosphate decomposition products of the $NaPF_6$ salt were also observed during cycling.

4.4.2. Soft and Tender X-ray Photoelectron Spectroscopy. The soft X-ray region provides high-resolution and high cross section for most elements of interest to the battery materials scientists. In particular, both the 2p and 3s/3p edges are available from the 3d transition metals. The light elements that form the surface reaction layer are also accessible. By tuning the excitation energy from above 1000 eV down to a few hundred eV or below, the surface sensitivity can be varied from a few nanometers to below a nanometer. This sensitivity has recently been used extensively to study ex situ the surface composition and chemical state of the reaction layer during its formation. Due to the electrolyte oxidation when cycling to high potentials, the chemical environment at the surface of cathode materials can be extremely complicated. A recent study of this subject was conducted by Lin et al. using soft XPS for Ti-containing $LiNi_{0.4}Mn_{0.4}Co_{0.2}O_2$.[88] Three incident photon energies (1150, 650, and 280 eV) were used to probe the near
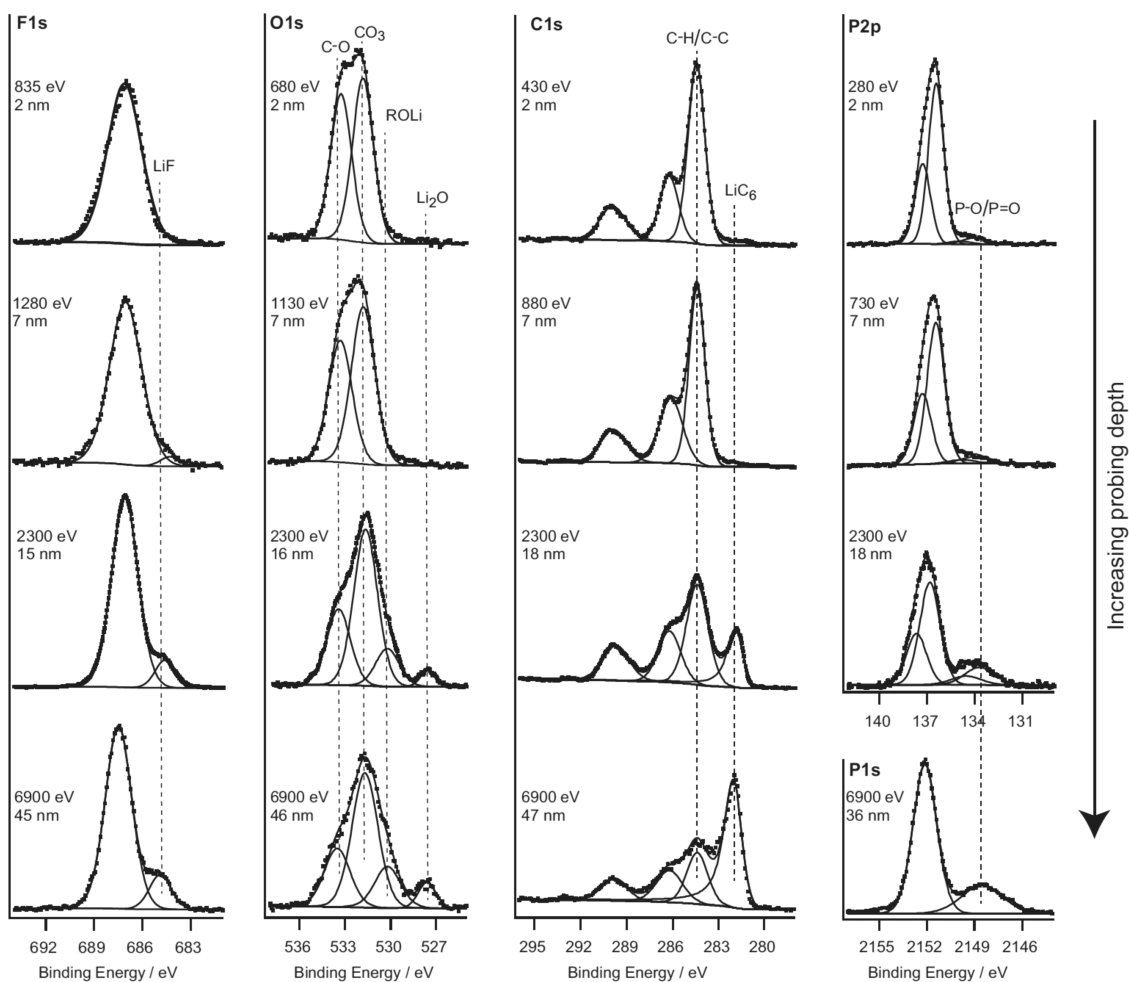
Figure 29. Lithiated graphite anode PES spectra. The lines in the figure mark observed depth gradients. Each spectrum was normalized by the area of the respective elemental signal. Reprinted with permission from ref 325. Copyright 2013 Elsevier Ltd.
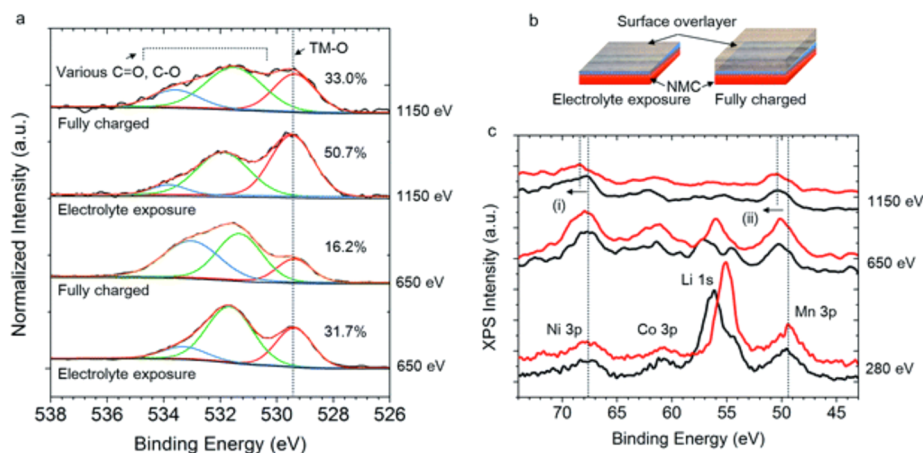
Figure 30. XPS spectra for Ti-containing $LiNi_{0.4}Mn_{0.4}Co_{0.2}O_2$ electrodes after electrolyte exposure and in the charged state using different incident X-rays. (a) O 1s XPS spectra using incident photon energies of 650 and 1150 eV, where the O 1s associated with Ni, Mn and Co locates at the lower binding energy and that associated with C=O and C−O locates at the higher binding energy. (b) Schematic representation of surface phenomenon in the electrodes, where the surface is covered by the organic overlayer. The thickness of this overlayer increases when the electrode is charged. (c) TM3p and Li 1s XPS spectra using incident photon energies of 280, 650, and 1150 eV, where the black and red curves represent the electrodes after electrolyte exposure and in the charged state, respectively. Reproduced with permission from ref 88. Copyright The Royal Society of Chemistry.

surface chemical environment. According to the universal mean-free path equation reported by Seah,[332] these photon energies probe 1.36, 0.83, and 0.43 nm into the surface, respectively, for Li 1s and TM3p XPS in $LiNi_{1−x−y}Mn_xCo_yO_2$

materials. Figure 30 shows the XPS O 1s, TM3p, and Li 1s spectra after the electrode exposed to electrolyte and in the charged state (4.7 V vs Li^+/Li). The intensity of O 1s associated with the NMC material changes as a function of the thickness
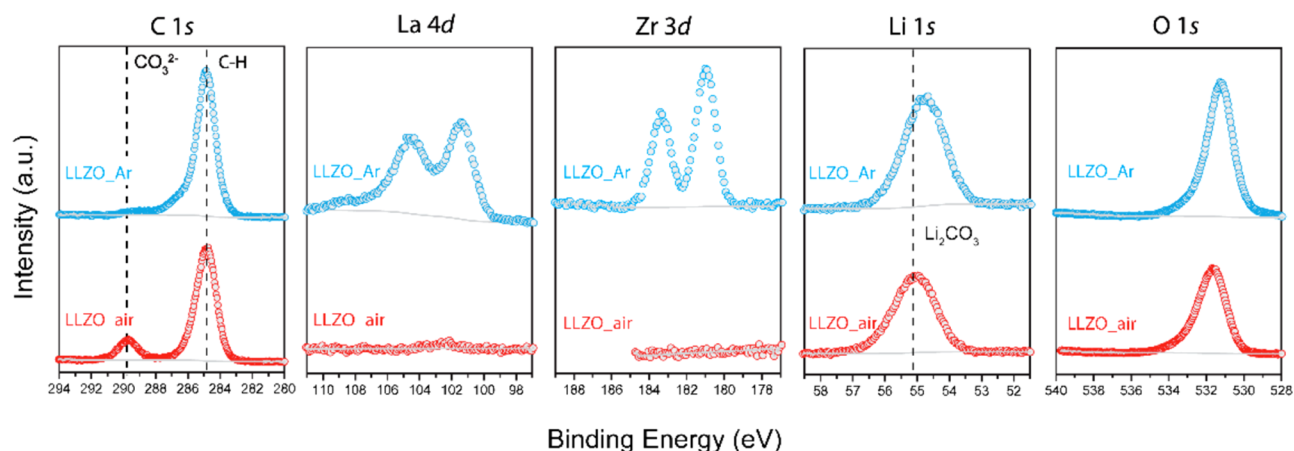
Figure 31. XPS spectra of C 1s, La 4d, Zr 3d, Li 1s, and O 1s collected from LLZO samples exposed to air (red) and protected in Ar (cyan). The incident photon energy was 640 eV. Reproduced with permission from ref 287. Copyright 2014 PCCP Owner Societies.

of the surface organic overlayer. Figure 30a shows that its intensity increases as the probing depth increases (compare O 1s spectra of 650 and 1150 eV incident X-rays). In addition, due to the electrolyte decomposition during the charging process, the surface reaction layer in the charged sample is thicker than that formed from simple exposure to the electrolyte, as schematically shown in Figure 30b. The most striking change in the lower binding energy region is the decreased intensity of the L 1s signal as the probing depth increases (Figure 30c), which strongly suggests that the surface reaction layer is rich in lithium whereas the portion underneath is poor in lithium. This is consistent with coulometry. In the charged sample (red plots in Figure 30c), a gradual increase of Ni 3p and Mn 3p binding energies was observed as the incident photon energy increases, indicating that the surface of the cathode particles is less oxidized than that in the bulk. The sample exposed to electrolyte shows a similar Mn oxidation state gradient. These XPS observations are consistent with an earlier soft XAS and STEM-EELS study that the TMs at the surfaces of $LiNi_{1-x-y}Mn_xCo_yO_2$ materials are less oxidized compared to those in the bulk.[90]

Li-containing compounds such as Li_2O_2 and Li_2CO_3 are frequently found on the surfaces of inorganic oxide materials that contain lithium and may affect the electrochemistry.[333] The presence of such Li-rich layers would decrease the XPS signals of inorganic oxide materials underneath the layers.[333] Recent studies have shown that even very thin layers of Li_2CO_3 on the surface of solid-state electrolytes are responsible for high interfacial impedances observed in Li/LLZO/Li cells (LLZO = $Li_7La_3Zr_2O_{12}$).[287] Cheng et al. used synchrotron XPS to investigate the surface chemistry of Al-substituted LLZO exposed for several days to ambient atmosphere and compared them to samples protected under Ar.[287] They found that air exposure resulted in a surface carbonate layer on the LLZO-air, which was thick enough to block the photoelectron signals of La and Zr. On the basis of the physics of this and other synchrotron experiments, the thickness was determined to be at least 2 nm thick. This analysis was further supported by both the Li 1s and O 1s spectra, which showed signals belonging to Li_2CO_3 (Figure 31).

The ability to use tender and high photon energy excitation has enabled near-ambient sample environments and a new suite of in situ studies of solid/gas and liquid/gas interfaces. Several important studies using tender XPS were initiated at the

Advanced Light Source at Lawrence Berkeley National Laboratory. In particular, the team recently reported the direct probing of solid−liquid interfaces using tender X-ray ambient pressure XPS,[334−337] using a custom spectrometer with differential pumping and specially developed entrance apertures for the electrons. This allowed XPS data to be collected from a sample environment of nearly 100 Torr, which enabled probing of the interface between an aqueous solution and the electrode material under background pressure of the liquid−gas equilibrium. The experimental design was called "dip & pull", where a stable nanometers-thick aqueous electrolyte was created on the working electrode and electrochemically connected to the bulk solution in the beaker (schematically shown in Figure 32).[338] Due to the relative deeper probing
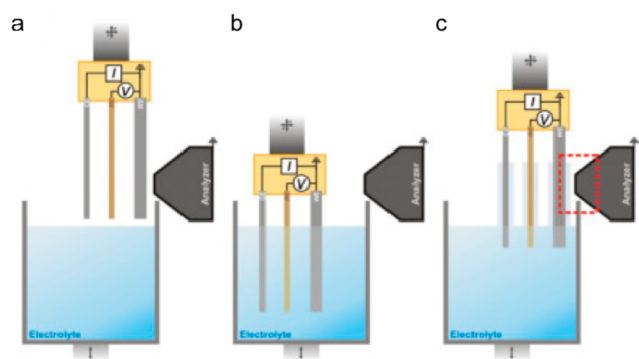
Figure 32. Scheme for the "dip & pull" procedure, where (a) XPS spectra can be collected before the working electrode is submerged in the electrolytic solution, (b) electrochemistry can be performed by submerging the electrode in electrolytic solution, and (c) XPS spectra can be collected while partially pulling it out and maintaining a thin layer (nanoscale) of electrolytic solution on the electrode. Reprinted with permission from ref 338. Copyright 2015 Elsevier B.V.

depth of tender X-rays compared to soft X-rays, the electrons have enough kinetic energy to escape from the interface between the working electrode and the aqueous electrolyte through the nanometer thick liquid layer. Most recently, the team applied a similar experimental setup to probe the potential distribution in the electrochemical double layer at a solid/liquid interface under electrochemical conditions. Apart from a few exceptions,[334−337] this technique has not yet been widely used in the study of rechargeable batteries but has obvious relevance.
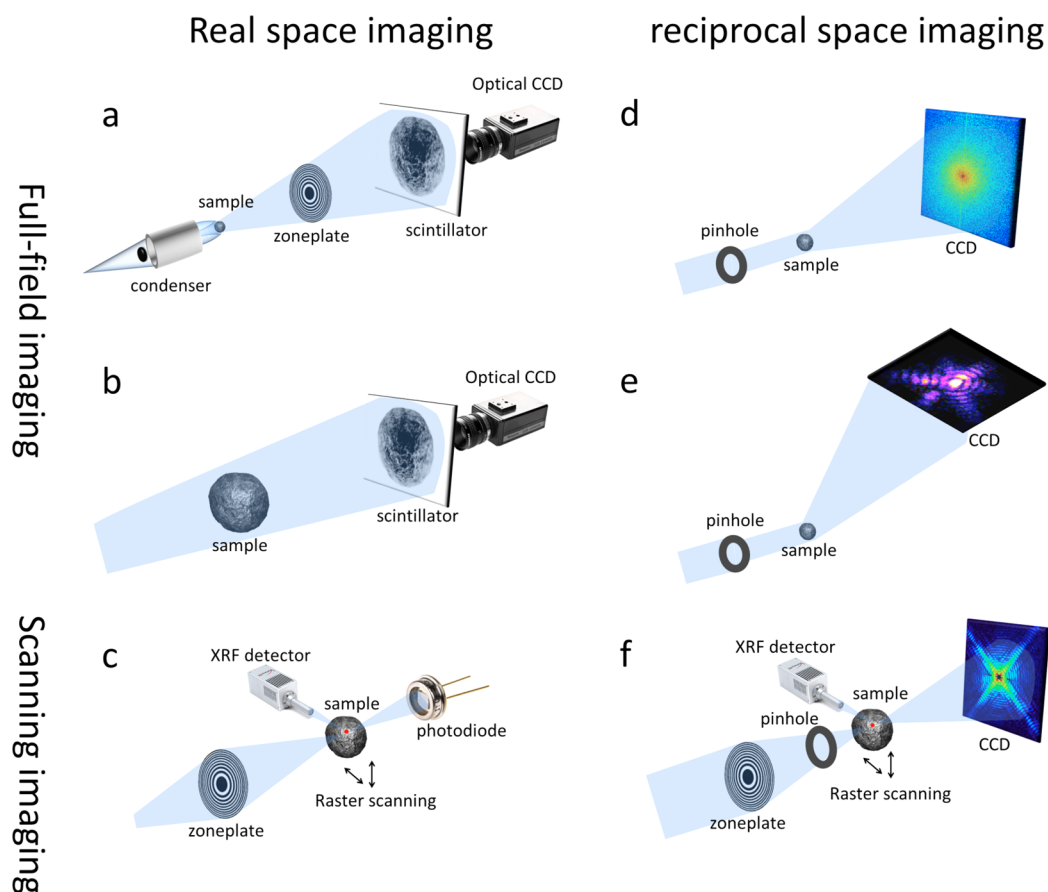
Figure 33. Schematic drawings of different X-ray imaging methods. (a and b) are the nanoscale and microscale full-field transmission X-ray microscopy, respectively; (c) is the scanning micro/nano probe, in which the size of the focal spot determines the resolving power; (d) is the plane wave coherent diffraction imaging; (e) is the Bragg coherent diffraction imaging, in which the diffraction pattern surrounding a Bragg peak is recorded; and (f) is scanning coherent diffraction imaging method also known as Ptychography.

Further improvement of the technique should allow for probing nonaqueous systems with good spectral resolution and signal-to-noise ratio in a more routine approach. This will enable a new set of studies, such as the reported in situ probing of the reaction layer on the $Li_xV_2O_5$ surface during cycling,[339] indicating that in situ probing of the formation mechanism of solid electrolyte interphases in batteries are possible.

4.5. Synchrotron X-ray Imaging

X-rays have been used for imaging since late 19th century when they were first discovered.[340] Owing to the exceptional penetration capability of X-rays, X-ray microscopy offers the possibility for the direct visualization of battery materials in a noninvasive manner and, possibly, under operando conditions.[341] This capability offers a "seeing is believing" way of studying and understanding the structure and function characteristics of battery materials. The implementation of X-ray micro/nano imaging using synchrotron X-ray sources has been a game changer thanks to the excellent quality of the synchrotron generated X-rays including high brightness, wide energy bandwidth, and adequate coherence.

Depending on the setup of the imaging systems and the corresponding principles of the information extraction, the synchrotron X-ray imaging techniques can be grouped into two categories: real space imaging methods and reciprocal space imaging methods (Figure 33). In real space imaging methods, the directly acquired raw data are the real space images, which are straightforward to visualize. However, the ultimate spatial resolution of real space imaging methods is limited by the quality of the optics used in the system, which can be on the order of 10 nm for soft X-rays and slightly worse for hard X-rays (see ref 342 for reviews). On the other hand, reciprocal space imaging makes use of the coherence property of the incoming X-ray beam to encode the sample's structural information in the diffraction pattern (see Figures 33, panels d–f, as well as ref 343 for a review). Without any optics placed between the sample and the detector, the restriction on the quality of optics is dropped and the resolution is, in principle, limited by the wavelength, which can be as low as 0.1 nm for hard X-rays. However, a more severe limitation on the resolution is the amount of scattered radiation,[344,345] which is inevitably dependent on the radiation dose on the sample. Typically, this resolution is on the order of 5–10 nm dependent on the sample, in some special cases a sub-5 nm resolution has been achieved with hard X-ray radiation (comprehensive reviews of the technique can be found in refs 346 and 347). In reciprocal space imaging, a 2D detector, such as a charge coupled device (CCD) or a photon counting detector, records coherent diffraction patterns requiring sophisticated phase retrieval algorithms[348] for reconstruction of the real space images. This requirement is the major obstacle for the non-CDI (coherent diffraction imaging) expert conducting scientific research using this method.

Another way of categorizing the X-ray imaging methods is by the data acquisition strategy. When a full image can be recorded

without mechanical movements of the sample, we refer to these methods as full-field imaging methods. On the other hand, when the images are built up point-by-point through a mechanical raster scan of the sample, these methods are referred to as scanning imaging methods. We show in Figure 33 the schematics of several major X-ray imaging configurations that have been applied to battery studies. More details about these imaging methods will be discussed along with scientific case studies in the sections below.

4.5.1. Real-Space Full-Field Imaging Methods. In real-space full-field imaging methods an area detector, typically a charge-coupled device (CCD) coupled with a scintillator screen, is used to record the X-rays transmitted through the sample in near field (Figure 33, panels a and b). The scintillator crystal converts the incoming X-rays into visible photons, allowing the optical lenses to be utilized for improving the spatial resolution to (sub-) micron level (Figure 33b),[349] which is limited by the wavelength of the crystal-emitted visible photons at a few hundreds of nanometers.[350] Additional magnification can be achieved by inserting a Fresnel zoneplate between the sample and the scintillator screen (Figure 33a), resulting in spatial resolution close to a few tens of nanometers for hard X-rays[351] and sub-15 nm for soft X-rays.[352] The real-space full-field imaging methods are usually superior in terms of data acquisition speed, especially when coupled with a synchrotron light source. The typical exposure time of a single micrograph can be as short as a few tens of milliseconds.[353] While the image contrast caused by the difference in the X-ray attenuation is the most commonly used contrast mechanism for full-field imaging methods and can be quantified by applying white field background correction using the Beer−Lambert law, the phase contrast[354] and the dark-field contrast[355−357] can also be achieved through some modifications of the imaging system, for instance, by adding additional analyzer optics[358−360] or by moving the detector further downstream of the sample.[361]

As discussed, the ability to visualize the battery electrode in real-time operation using real-space full-field imaging methods is important and can lead to interesting findings that are otherwise hard to discover. One example is the in operando investigation of lithium/sulfur batteries by Nelson et al. (Figure 34).[362] It is believed that the structural and morphological change of the active material in the electrode during electrochemical cycling plays an important role in affecting the overall behavior of this type of battery. While transmission/scanning electron microscopy and atomic force microscopy have been successfully applied in the study of sulfur electrodes to visualize the morphologies at different states-of-charge,[363,364] the limitations in the penetration capability in the above-mentioned probes has restricted these studies to ex situ work on sulfur electrodes. Often times, cycled cells are disassembled, and the electrolyte is washed away by solvents before characterization.

With the use of transmission X-ray microscopy that provides spatial resolution down to tens of nanometers scale, Nelson et al. monitored active sulfur particles in a pouch cell as it underwent electrochemical cycling.[362] Direct observation of the TXM micrographs (shown in Figure 34) suggested that only a small amount of the sulfur in the sulfur/super P composite particles was dissolved during the first discharging plateau. The efficient crystallization of sulfur at the end of the charge cycle was promoted by this trapping of the polysulfides. Nevertheless, the cycle lives of these batteries were impacted by the minor amount of polysulfides lost to the electrolyte.
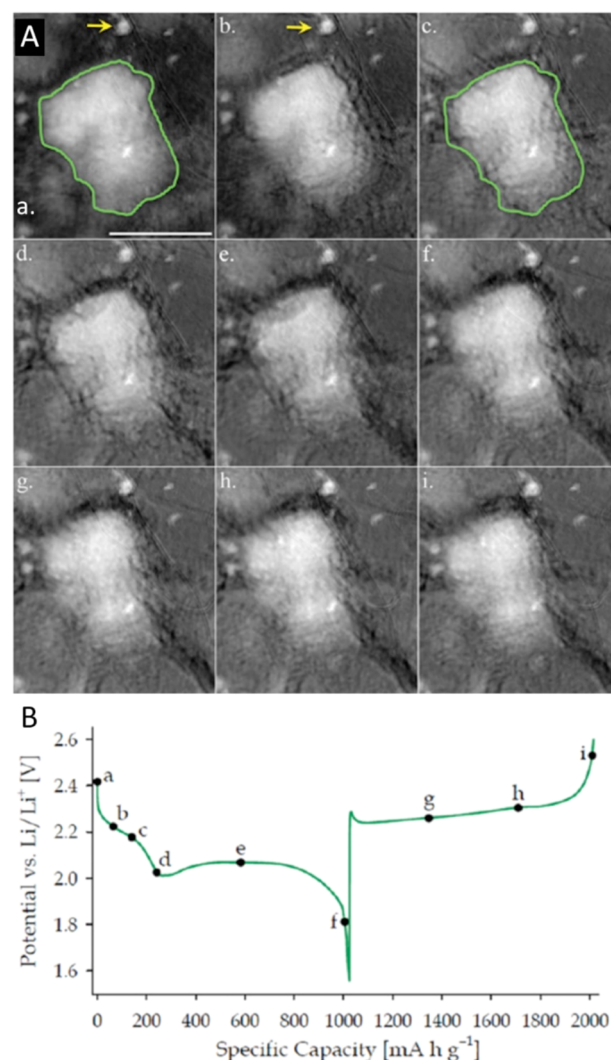
Figure 34. (A) In operando full-field TXM images of a sulfur/super P composite particle undergoing electrochemical cycling, where the letters represent points along the charging−discharging curve labeled a−i in (B). The majority of morphological changes occur between images a and c, corresponding to the first plateau of the discharge. The green outline around the particle in (a) is replicated in (c) to show the shrinkage of the particle and increased porosity. The yellow arrows show a small particle that expands between (a) and (b). The scale bar is 10 μm. Reprinted with permission from ref 362. Copyright 2012 American Chemical Society.

There is a possibility that X-ray induced radiation damage could also cause changes in the sulfur particle's morphology.[365] As a result, it is critical to evaluate the maximum tolerable dose prior to performing the in situ imaging of the sulfur electrode particle (and all battery electrodes in general) and to manage the dose properly to ensure that the observed localized morphological change is electrochemical reaction related.

4.5.2. Scanning Imaging Methods. Another type of X-ray imaging is the scanning imaging methods, in which X-rays are focused to a small spot (typically at the micron level or tens of nanometers level depending on the focusing optics used) and the sample is raster scanned in the focal plane (Figure 33c).[366−369] Multiple detectors can be integrated to simultaneously record different signals (such as transmission,[370] fluorescence,[215,371] and diffraction[372]) as a function of the sample position. Two-dimensional images are, therefore, built
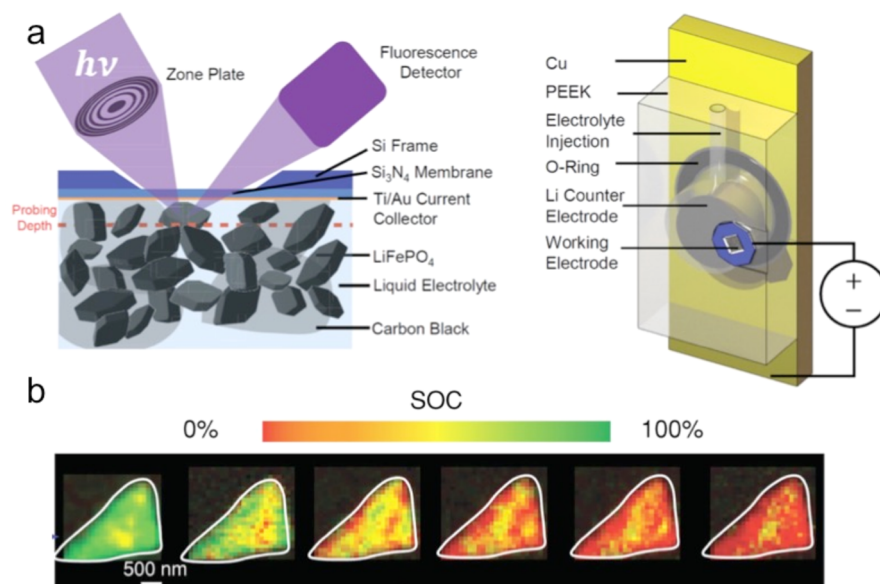
Figure 35. (a) Schematic of the operando fluorescence-yield X-ray microscopy (FY-XRM) to track the dynamics of the Fe valence distribution in LiFePO$_4$ nanoparticles during electrochemical cycling. (b) The Fe^{3+}(green) and Fe^{2+} (red) in a single LiFePO$_4$ particle during the electrochemical cycling. A strong particle shape and cycling rate dependence has been observed. Reprinted with permission from ref 271. Copyright 2015 John Wiley and Sons.

up through the raster mapping. While multiple maps of different signals can be recorded concurrently, the mechanical scanning of the sample becomes the major limitation of speed of data acquisition. With the development of next generation synchrotron light sources (i.e., the diffraction limited storage ring)[20] and advanced X-ray focusing optics,[373−375] it is anticipated that significantly more photons can be focused into a smaller focal spot. This could greatly reduce the required dwell time at each sample position and, subsequently, improve the data acquisition speed.

One of the most recent developments in the scanning imaging methods is known as ptychography (Figure 33f).[376,377] By making use of the coherence property of the incoming X-rays, ptychography resolves the sample features that are smaller than the illuminating spot size. Both amplitude maps and phase maps can be recovered through a sophisticated phase retrieval algorithm,[376−378] while the fluorescence signal can still be acquired simultaneously although at a coarser spatial resolution.[379] Another recent noticeable development is small angle scattering tomography, which provides a survey of macroscopic (mm scale) sample's nanoscale structural information on samples[380,381] and is believed to be very useful for linking material's macro properties to the structure of its micro/nano building blocks.

A few good examples of scanning imaging studies for batteries include Li et al. using STXM (scanning transmission X-ray microscopy) to map out the state of charge within LiFePO$_4$ particles,[271,275,382] Ohmer et al. using STXM to investigate the phase evolution in a micro battery configuration,[383] and Yu et al. studying the particle size dependency of the nanoscale chemical phase distribution.[384] Figure 35 depicts an operando fluorescence-yield X-ray microscopy (FY-XRM) experiment to track the dynamics of the Fe valence distribution in LiFePO$_4$ nanoparticles during electrochemical cycling.[271] Soft X-ray TM-L edge spectra are sensitive to the 3d TM valences,[85,260,276−278] as well as their spin states that are relevant to the electrochemical profile.[385,386] Therefore, an in situ soft X-ray mapping of the TM valence directly corresponds to the state-of-charge distribution in the electrode particles. Here, Li et al. assembled a LiFePO$_4$ working electrode of about 10 μm thickness into a soft X-ray operando cell by using a Si$_3$N$_4$ membrane. The focused soft X-ray penetrated through the membrane and probed the individual particles during the electrochemical operation with a spatial resolution of about 25 nm.[271] Figure 35 shows the distribution of the Fe^{3+} (green) and Fe^{2+} (red) in a single LiFePO$_4$ particle as it changed during the electrochemical cycling. A strong particle shape and cycling rate dependence has been observed through such operando experiments, demonstrating their importance for detecting the dynamics in battery electrodes. More recently, with a more sophisticated flow liquid cell design, the same group presented a more detailed investigation of the dynamic behavior of LiFePO$_4$ at the subparticle level.[387] Nanodomains with different ion insertion kinetics were identified at the subparticle level through the quantification of the local current density based on the imaging data. This study suggested that the nanoscale spatial variations in rate and in composition control the lithiation pathway at the subparticle length scale.

It worth emphasizing that the strength of synchrotron-based X-ray imaging methods (in both the full-field imaging methods and the scanning imaging methods) goes beyond taking well-resolved 2D micrographs. The X-ray tomography technique, which noninvasively probes the samples' internal structure, combined with X-ray spectroscopic imaging methods, which adds chemical information to the morphology, makes the synchrotron-based imaging methods even more powerful for battery research. Some discussion of these two types of imaging methods can be found in the next two sections.

4.5.3. X-ray Tomography. In the 1970s, a new era with the groundbreaking computed tomography (CT) technique was established by Allan M. Cormack and Godfrey Newbold Hounsfield.[388] In X-ray tomography, a number of images are acquired in different viewing angles as the sample is rotated along an axis that is perpendicular to the incoming X-rays. The
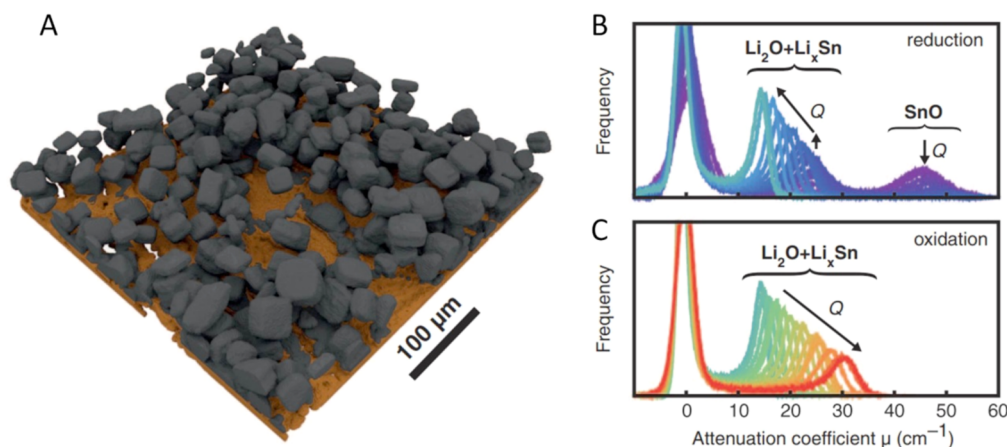
Figure 36. (a) 3D Visualization of X-ray tomograms recorded during battery operation. X-ray attenuation coefficient histograms during electrochemical (b) reduction and (c) oxidation. Reprinted with permission from ref 401. Copyright 2013 AAAS.

real space 3D structure of the sample can then be numerically reconstructed, which allows for visualization and quantification of the 3D morphology nearly nondestructively.[389] A number of different algorithms have been developed for tomographic reconstruction,[390−395] many of which are designed to handle incomplete data sets with nonoptimal data quality. X-ray tomography has made tremendous contribution to a number of research fields and clinical applications. Especially when implemented with synchrotron light sources, it becomes capable of studying the dynamic of 3D morphological changes[396] and opens vast opportunities in energy science including battery research. For example, Villevieille et al. combined in operando XRD with operando synchrotron microtomography to investigate the influence of particle morphology on the core−shell phase transformation process of an Sb/TiSb$_2$ alloy electrode as it was lithiated.[397] Wang et al. studied three-dimensional structural/chemical evolution of tin electrodes for sodium-ion batteries with in situ synchrotron hard X-ray nanotomography.[398] Zielke et al. performed carbon binder modeling with the input from synchrotron-based microtomography data to understand how the morphology of the carbon binder domain affects the performance of cells containing LiCoO$_2$.[399] Eastwood et al. employed a synchrotron-based X-ray phase contrast tomography technique to study the microstructures of the electrodeposited lithium, critical to the understanding of dendrite formation, the main cause of failure in batteries with lithium anodes.[400]

One case study that utilized the synchrotron-based microtomography technique to study the dynamic change of the battery electrode in real-time is discussed in more detail here (Figure 36). In this work by Ebner et al.,[401] tin(II) oxide (SnO) was studied as a model material that undergoes a conversion reaction and subsequent alloying with lithium. Tomograms were recorded every 15 min during galvanostatic reduction (lithiation) at 110 mA hour g^{-1} over a period of 12 h and during oxidation (delithiation) at 167 mA hour g^{-1} over 5 h. In addition to the 3D visualization of the electrode (a typical rendering at a certain time frame is shown in Figure 36a), the chemical reaction can be tracked by studying the attenuation coefficient of the electrode. Detailed investigation of this four-dimensional data (the three spatial dimensions and time) suggests that the irreversible distortion of the electrode occurs in the investigated system; the crack initiates and grows along pre-existing defects. This study highlights the synchrotron-

based tomography's capability of investigating the dynamic changes that take place in the real battery ensemble.

Phase contrast can also be achieved in the X-ray full-field imaging setups through some modifications of the optical system.[354] This imaging modality is very attractive when it is desirable to visualize low Z materials directly. While we rely on the use of hard X-rays to penetrate through a real-life battery configuration, the material's low absorption contrast when interacting with the hard X-ray leads to difficulties in visualization of lithium. For example, it is a research focus for the battery community to study lithium metal because of its importance as an anode material, but it is practically a phase object, meaning almost zero absorption when working with hard X-rays. The hard X-ray phase contrast imaging becomes the go-to technique in this scenario.

For high elastic modulus solid electrolyte materials, it has been postulated that lithium dendrite growth is prevented due to the high mechanical strength of the material. However, dendritic features have been observed in garnet electrolytes.[153,402,357] The fundamental mechanism was not clearly understood in Li ion conductors, although there are some previous studies of sodium dendrite/filament formation in beta alumina suggesting that there are multiple failure modes, with the fracture toughness and surface quality of the interface being critical factors.[403] Harry et al. used full-field hard X-ray phase contrast tomography to study the formation of lithium dendrites in a polymer electrolyte battery configuration.[404] Dendritic features were clearly observed and attributed to the root cause of failure. Through direct visualization of the dendrite forming in the operating battery system, this study suggested that the subsurface structure forming in the lithium electrode plays a critical role in affecting the dendrite growth in the polymer electrolytes. As discussed above, the tomography data provides a large amount of the structural and chemical information on the specimens studied. Many numerical methods have been developed to extract scientifically relevant information from the 3D imaging data. We refer to a recent review by Liu et al. for detailed discussions of tomographic data analysis.[389]

4.5.4. X-ray Spectroscopic Imaging. Another big advantage offered by the synchrotron is the energy tunability, which adds chemical/elemental sensitivity to the imaging data. As discussed in the previous sections, synchrotrons generate photons with wide bandwidths, covering ultraviolet light to γ
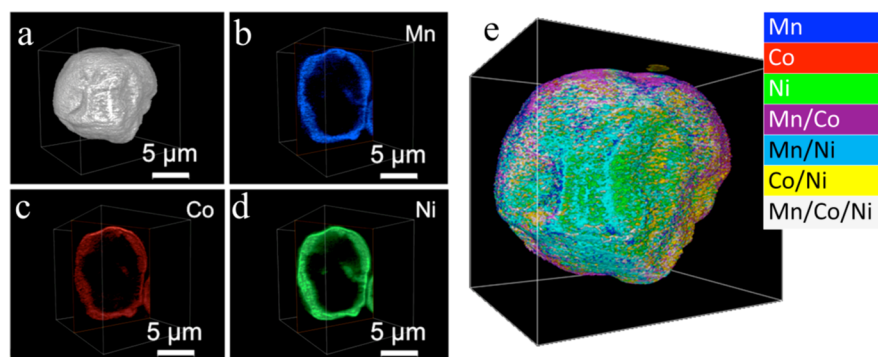
Figure 37. 3D Elemental sensitivity nanotomography reveals the transition metal segregation within a secondary particle. (a) shows the tomography result at a single X-ray energy, which shows the 3D morphology of this particle. (b−d) present the elemental distributions of Mn, Co, and Ni over single voxel thick slices through the center of the particle. (e) shows the 3D distributions of the elemental associations. The 3D rendering is color-coded to the labels shown in the inset. Used with permission from ref 410. Copyright 2016 Nature Publishing Group.

rays. In a typical synchrotron beamline, the photons with desired wavelength are selected by X-ray optics resulting in (quasi-) monochromatic illumination of the sample. By studying the sample's response to the X-rays of different wavelength through tuning the monochromator, different elemental/chemical species can be identified. When such spectroscopic analysis is coupled with the imaging methods in either the full-field imaging mode[405] or the scanning imaging mode,[406] the distribution of different elemental/chemical species can be resolved. It is worth emphasizing that the spectroscopic imaging method is also compatible with the tomography technique[405−407] for resolving the elemental/chemical distribution in 3D.

X-ray spectroscopic imaging has demonstrated its strength in the field of battery research, especially, when it is of interest to visualize the morphological and chemical changes of the electrode materials in detail. There are a large number of case studies that utilize the synchrotron-based spectroscopic imaging. Some recent examples include the in operando tracking of the phase transformation evolution in LiFePO$_4$ by Wang et al.,[408] the systematic investigations of electrochemical reaction induced morphological and chemical changes in Li-rich Li$_2$Ru$_{0.5}$Mn$_{0.5}$O$_3$ cathode particles at the meso to nano scale by Xu et al.,[409] the 3D nanoscale mapping of transition metals segregation in hierarchically structured cathode materials LiNi$_{0.4}$Mn$_{0.4}$Co$_{0.2}$O$_2$ by Lin et al.,[410] and the 3D oxidation state mapping of halfway discharged NiO particles by Meirer et al.[405]

Here we discuss the study of transition metal segregation in LiNi$_{0.4}$Mn$_{0.4}$Co$_{0.2}$O$_2$ electrodes by Lin et al.[410] As shown in Figure 37, the elemental sensitivity provided by the energy-resolved full-field hard X-ray transmission nanotomography allowed the researchers to resolve the distribution of all the transition metals within the secondary particles, which are ∼10 μm in diameter. The quantitative measurement of the elemental distribution at this scale can then be converted into the 3D maps of elemental associations, which is shown in Figure 37e. A more detailed investigation of the depth profile of all the transition metals (Mn, Co, and Ni) within the secondary particles suggested that the metal segregation in the secondary particles synthesized by spray pyrolysis resulted in a Mn-rich surface, which, in turn, made it more robust against surface reconstruction to a rocksalt structure[90] and, subsequently, led to the improved cycling performance.

As shown in Figure 38, in the study by Meirer et al. on a NiO conversion electrode, different chemical species, which are
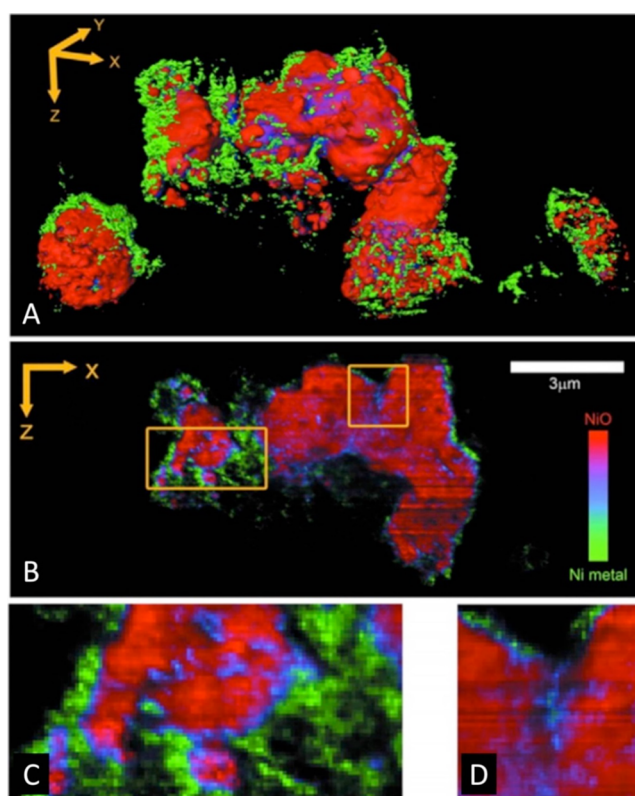
Figure 38. Three-dimensional visualization of partially reduced NiO battery electrode particles. (A) is the perspective rendering of three-dimensional data set of the electrode particle. (B) is a single-voxel-thick slice cutting through the center of the 3D matrix with magnified views of the highlighted regions shown in (C) and (D). The scale bar in panel b is 3 μm. Reproduced with permission from ref 405. Copyright 2011 International Union of Crystallography.

identified by their spectroscopic signature, heterogeneously coexist at the subparticle length scale in a partially discharged material. A 2D slice (Figure 38b) cutting the center of the particle also shows the complex reaction front with mixed valence states. This behavior was likely a result of subpixel heterogeneity. This study highlights the strength of synchrotron-based full-field spectroscopic imaging methods by spatially
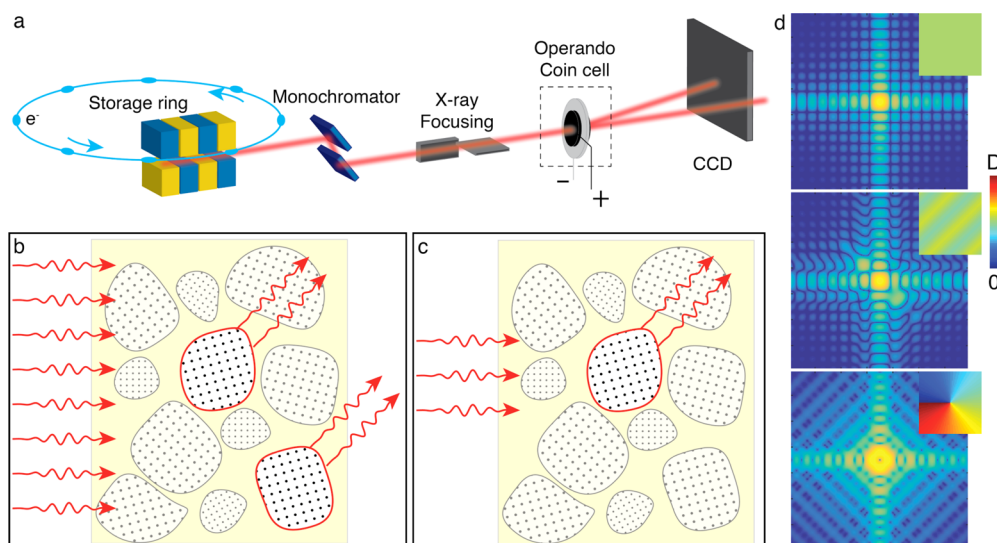
Figure 39. (a) Typical in situ X-ray diffraction experiment at a synchrotron source. The wavelength is selected by a monochromator, and the beam is focused. The X-ray diffraction signal from an in situ battery is recorded by a 2D detector, such as CCD. (b) A schematic representation of coherent X-ray Bragg scattering inside a battery cell. High-power X-ray radiation is incident on an in situ cell, and many particles are illuminated. The dots represent the crystal lattice. In this case, only two particles satisfy the Bragg condition. (c) Schematic of operando Bragg coherent diffractive imaging (BCDI), only one particle satisfies the Bragg condition and the sample is rocked to collect a 3D representation of the scattered intensity around the Bragg peak, which is inverted using phase retrieval technique. (d) 2D slices through 3D BCDI diffraction maps (logarithmic scale) simulated with identical particle shape (cube) but different displacement fields inside the nanoparticle (shown in the insets). No displacement (top), stripe domains (middle), and a screw dislocation (bottom) are shown (D in the color bar is the lattice parameter).

and chemically resolving the features of interest within the NiO electrode particle.

In a more recent study, Wang et al. studied LiFePO$_4$ electrodes using this type of measurement in operando.[411] XANES tomography was performed on a selected LiFePO$_4$ particle as it is cycled, leading to a five dimensional data set (the three spatial dimensions, X-ray energy, and time) that reveals that the propagation of the reaction front changes from anisotropic to isotropic manner within this particle as it is charged. This study highlights the strength of the full-field hard X-ray spectro-microscopic technique through the complexity of the multidimensional data. It is expected that the developments in the scientific big data mining methods,[172,412−414] for example, PCA (principal component analysis), ICA (independent component analysis), and DBSCAN (density-based spatial clustering of applications with noise), can further enhance the strength of this technique and allow more efficient discovery of unexpected local minority phases (if any) that are functionally important.

4.5.5. Hard X-ray Diffraction for Coherent Imaging. Coherence is another key property of the synchrotron X-ray source. Generally, synchrotron generated X-rays are partially coherent. With the use of small pinholes and slits, one can improve the spatial coherence of the beam at the sample location. The coherent property of the X-ray source allows the sample's structural information to be encoded in its diffraction pattern, which can be reconstructed into real space images through sophisticated phase retrieval algorithms.[348] A particularly powerful imaging technique that can be applied to image nanocrystals is a combination of Bragg diffraction and CDI[415−417] (coherent diffractive imaging see Figure 33e). By measuring the interference patterns around the Bragg peak while rocking the nanocrystal by a small angle (typically 0.1−1 degree around the Bragg angle) a three-dimensional (3D) data set can be recorded. By using phase retrieval, this data set can

be converted to a 3D electron density map of the nanocrystal, as well as the 3D displacement field along the scattering vector. Although the spatial resolution achieved is limited to 10 nm,[418] the exceptional sensitivity of the Bragg diffraction to atomic positions allows the study of strain fields that correspond to displacement of atomic positions as small as 0.05% per unit cell.[419−421]

The sketch of a typical in situ diffraction experiment for coherent imaging at a synchrotron source is depicted in Figure 39a. The X-ray beam generated by circulating electrons is monochromatized, focused, and incident on a battery cell. A small portion of the cell casing is replaced by an X-ray transparent material, made, for example, from Kapton. While conventional X-ray diffraction measurements provide essential information on the crystal structure of large ensembles of battery particles, the information on single particles is lost due to the massive averaging. The X-ray flux at synchrotron sources is orders of magnitude higher as compared with X-ray tubes, which not only can be used to reduce the measurement time significantly and study fast charge rates (as demonstrated in ref 74, see Figure 8), but also is sufficient to record X-ray diffraction from single nanoparticles and gain unique insights into structural dynamics of single constituents of a battery.[74] In the article by Singer et al.,[422] the authors have conducted powder diffraction on an ensemble of ∼20 particles, while maintaining single particle sensitivity (see Figure 39, panels b and c).

The main concept of the experiment is schematically depicted in Figure 39 (panels a and b). X-rays are incident on the in situ cell and a 2D detector collects Bragg diffraction at a specified angle. While a large number of particles are illuminated, due to their random orientation, only a small portion of these particles will satisfy the Bragg condition. The high angular sensitivity of Bragg diffraction guarantees that amorphous material (for instance liquid electrolyte, or the
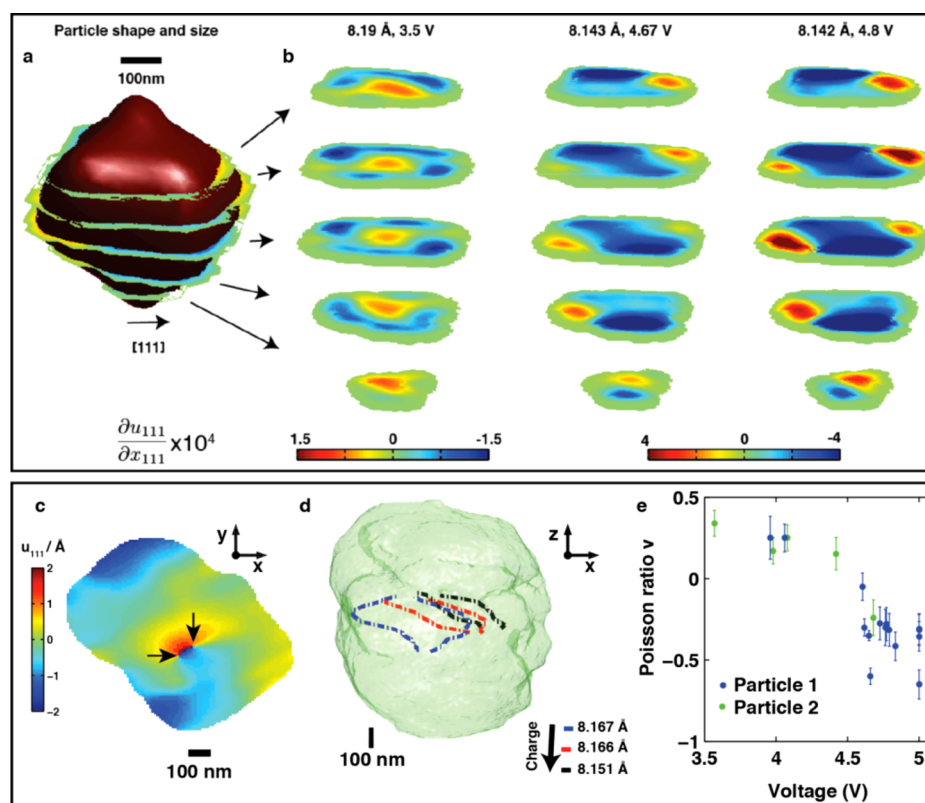
Figure 40. (a and b) The cross sections of interior strain distribution on a selected particle at different locations. (c) A cross section of the dislocation field in an in situ battery nanoparticle, two edge dislocations are indicated by arrows. (d) The particle shape is represented by a green isosurface, and the evolution of the dislocation line at three different charge states is shown. (e) shows Poisson's ratio values measured as a function of voltage for two different particles. Reprinted with permission from ref 75. Copyright 2015 AAAS. Reprinted with permission from ref 419. Copyright 2014 American Chemical Society.

binder matrix, yellow in Figure 39b or even crystalline material with a different lattice constant (smaller particles in Figure 39b) do not scatter in the direction of the detector and are not observed in the experiment. The position of the detector selects the crystal lattice studied and the size of the beam defines the number of particles observed on the detector.

This technique was particularly useful in studying non-equilibrium structural evolution in a $LiNi_{1/2}Mn_{3/2}O_4$ spinel material upon fast cycling.[422] The measurement elucidated the interplay between distinct transformation mechanisms at the single nanoparticle level, namely solid solution and two-phase reactions. In addition, the authors observed a hysteretic behavior of the structure during electrochemical cycling. At high lithium concentrations, solid solutions dominated upon both charge and discharge. At low lithium concentrations, concurrent solid solution and two-phase reactions occurred, while a pure two-phase reaction was observed upon discharge. The unique particle sensitivity also was used to study particle kinetics, which in this example did not show a significant mobility during cell operation. The comparison of the electrochemical data with the structural data demonstrated how the chemistry affects the structural dynamics of battery nanoparticles.

The Bragg coherent diffractive imaging (BCDI) allows one to go one step further and to look inside a single nanoparticle buried in an in situ battery by focusing the X-ray beam (see Figure 39c). The information on the particle shape and even more importantly on the strain distribution yields unique insights on the nanomechanics, chemistry, and elastic properties on the nanoscale (see Figure 39d).

In a recent example,[419] the strain dynamics of a spinel material was studied using BCDI (see Figure 40, panels a and b). The nanoscale stripe morphologies and coherency strain were directly observed, and a critical size for stripe formation in this material was found at 50 nm. The elastic energy landscape of single nanoparticle mapped with femtojoule precision was determined for various lithium concentrations during charge and discharge. The observation indicated hysteresis at the single particle level. The strain evolution in the solid solution regime combined with Vegard's law was used to reveal the lithiation pathways during battery operation.

In another example, the role of topological defects on battery operation was studied[75] (Figure 40, panels c-e). Not only was a single edge dislocation observed and tracked in a single nanoparticle in situ, the displacement field due to the dislocation served as a local nanoprobe for elastic properties as a function of the material chemistry or charge state. The Poisson ratio, which describes the relative expansion of the material in the direction transverse to compression, was found to be negative at a high voltage. The negative Poisson ratio was interpreted in terms of the enhanced Mn−O bonds upon Mn oxidation, which explains why this material is resistant to oxygen loss and structural collapse. It was also found that the dislocations were stable at room temperature but immediately became mobile during charge or discharge.

Bragg CDI in battery materials is a relatively recent development but nevertheless has been proven to be a

promising technique to shed light on chemical processes in nanocrystals. For instance, during the onset of the structural phase transformation, the lithium-rich phase nucleated near the dislocation and spread inhomogeneously throughout the spinel material.[75] Further studies will ultimately be able to track the nucleation and propagation of multiple phases during a phase transformation. A combination of the CDI technique with spectroscopy seems within reach and would, if successful, yield 3D information on electron density, strain, atomic distribution, and oxidation state in single nanoparticles under operando conditions.

4.6. High Energy Electrons as Broad Band Light Sources for Imaging in Batteries

The heterogeneities of battery electrodes, particularly those that developed after extensive cycling demand multiscale studies that cover a wide range of length scales. In this respect, transmission electron microscopy complements X-ray microscopy when nanometric and atomic-scale structural and chemical information is needed.[88,90,91,410,423] In recent years, there has been increasing interest in combining the capabilities of synchrotron X-rays and electron microscopy for studying battery chemistries at complementary length scales, from atomic scale to macroscale. Some of these studies revealed chemical and structural information that would not be possible without such a combination. Furthermore, the fundamental principles of electron spectroscopy [such as energy dispersive X-ray spectroscopy (EDS) or electron energy loss spectroscopy (EELS)] are fairly close to that of X-ray spectroscopy. For this reason, we discuss the power of transmission electron microscopy and spectroscopy in this section, to complement our discussion of X-ray techniques in the review. With the development of aberration correctors and brighter electron sources in the past decade, (scanning) transmission electron microscopy (S/TEM) has improved extensively in terms of both resolution and spectroscopic capabilities.[424] Now, using aberration-corrected instruments, sub-angstrom resolution imaging and atomic-resolution spectroscopic mapping can be routinely achieved.[425] Under optimal conditions, structural determination with few-picometer precision[426] and single-atom spectroscopy[427,428] are accessible.

The working principle of a transmission electron microscope is relatively simple. In the conventional TEM (CTEM) imaging mode, a relatively collimated wide-field electron beam illuminates the sample and the transmitted electron wave that encodes the structural information on the sample is subsequently imaged and magnified by an objective lens and a series of intermediate and projector lenses. The acquired image under optimal conditions reflects the projected atomic potential, which, however, in practice is always sensitive to the diffracting condition of the samples. Therefore, even though the CTEM imaging mode is widely used for structural characterization of electrode materials, a single image is not sufficient to provide direct interpretable information about atomic column positions unless special treatment is applied.

In contrast, a scanning transmission electron microscope (STEM) can easily provide directly interpretable images. In the STEM imaging mode, the electron beam is converged and focused down to a very small spot and rastered on the sample. An image can be built up by recording the transmitted electrons with an annular dark-field detector (ADF). The detector collects high-angle Rutherford scattered electrons and avoids the collection of any strongly diffracted beams, and, therefore,

the resulting image can closely reproduce the projected atomic-mass contrast. Owing to the excellent sensitivity to the atomic-mass contrast (Z-contrast), ADF-STEM imaging mode has been offering tremendous help to the local structural analysis of a series of intercalation electrode materials that have lithium channels, for example stoichiometric layered NMC materials[90,410] and Li and Mn rich materials.[429−431] With the integration of ensemble-averaged efficient soft X-ray absorption spectroscopy and spatially resolved electron spectroscopy and microscopy, Lin et al. report structural reconstruction and chemical evolution at the surface of Ti-containing Li-Ni$_{0.4}$Mn$_{0.4}$Co$_{0.2}$O$_2$ particles (discussed in section 4.3.4). It provides a direct visualization of the layer to spinel and to rocksalt reconstruction process that occur on the surfaces of the layered cathode materials as the cells are cycled. Similar information regarding the surface degradation can be indirectly deduced from the XAS studies, however with a complete loss of the information regarding the microscopic degree of freedoms in the samples, such as any facet-dependent degradation pathways. Using atomic-resolution ADF-STEM imaging, it has been found that in layered NMC materials, the layer-to-rocksalt transition is much faster on the surfaces that exposed lithium channels than the channel-projected (001) surfaces.[90]

Apart from collecting the high-angle scattered electrons, electrons that scattered at low-angles can also be used to produce useful contrast. For example, low-angle ADF-STEM (LAADF-STEM) imaging used in conjunction with high-angle ADF-STEM is useful in revealing any strain fields in the samples.[432] By optimizing the collection angles of the bright-field detector in STEM (BF-STEM), the imaging of oxygen octahedral tilts can be optimized for perovskite-based lithium-ion conductors.[433] More recently, annular bright-field STEM (ABF-STEM) imaging was developed for the imaging of light elements such as hydrogen,[434] lithium,[435] and oxygen.[436]

In a (scanning) transmission electron microscope, spectroscopic signals are primarily produced by the inelastic scattering of the incident electrons with the core-binding and valence electrons. In the classical electrodynamics picture, the binding electrons in the sample would experience a sudden pulse of Coulombic repulsion exerted by the fast traveling incident electron. The time width of the pulse is related to how close the incident electron can travel to the binding electron. The shortest distance between the pair of electrons is called the impact parameter. The pulse width is proportional to the impact parameter by the relationship $\Delta t = \frac{b}{\gamma v}$, where b is the impact parameter, γ is the Lorentz factor, and v is the speed of the incident electron. A simple inversion of the characteristic pulse width gives the frequency cut off of the time varying field (i.e., $f_{cutoff} \sim \frac{1}{\Delta t} = \frac{\gamma v}{b}$) and hence the energy cutoff is $hf_{cutoff} \sim \frac{h\gamma v}{b}$, where h is Planck's constant. For a 200 keV incident electron, for example, with an impact parameter of $b = 1$ Å, the energy cut off is 11.9 keV. It is easy to see that a high-energy electron can be equivalently viewed as broadband light/X-ray source through the time-varying Coulombic interaction, given that it can get sufficiently close to or directly impinge on the sample. In other words, the incident electron beam essentially exchanges energy with the binding electrons through the emittance and absorption of virtual photons.

Through the absorption of the virtual photon, the binding electrons in the sample can be excited into an unfilled bound state or ejected from the bonding environment to form a
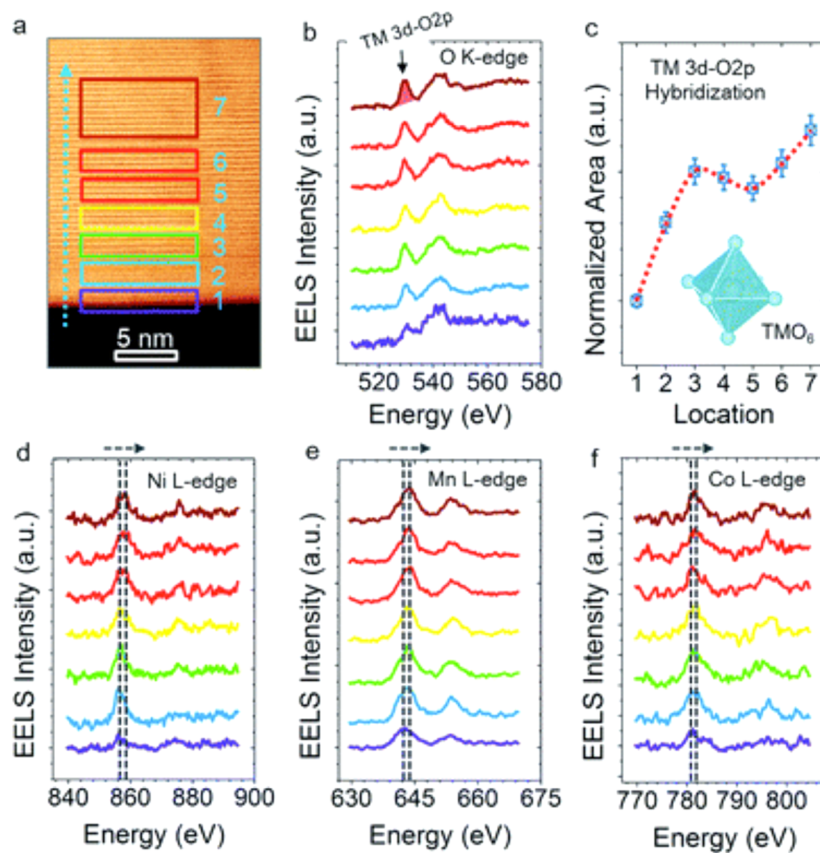
Figure 41. Depth profiling of electronic structure for a charged NMC particle shown in (a), (b) EELS O K-edge, (c) integrated O K-edge pre-edge intensity, (d) Ni L-edge, (e) Mn L-edge, and (f) Co L-edge. Reproduced with permission from ref 88. Copyright 2014 The Royal Society of Chemistry.

secondary electron. Once excited, it leaves an unfilled state that can be filled by other outer shell binding electrons. Through this filling process, X-rays are generated. The emitted X-rays can be collected and analyzed by an energy-dispersive X-ray spectrometer (EDS) to produce an X-ray emission spectrum. This signal is the counterpart of the fluorescence signal in X-ray experiments. Due to the fundamental Poisson limit of silicon drift detectors used in EDS, the energy resolution is not yet enough to resolve the fine structure in the X-ray emission spectrum to deduce the bonding and valence states of the elements in the sample. However, the characteristic X-ray emission lines are useful in analyzing elemental compositions. Therefore, EDS is widely used in the characterization of battery materials particularly as a way to monitor the composition. Coupled with scanning transmission electron microscopy, EDS mapping with 1 nm spatial resolution has become a routine analysis in field-emission instruments. However, atomic-resolution EDS mapping has only been realized in the past few years benefiting from the development of aberration-correctors, brighter electron sources, and the development of detectors with large collection angles and improved geometries. Recently, Wang and his co-workers successfully applied atomic-resolution STEM-EDS to the study of the interlayer mixing in NMC materials and found that Ni exhibits a higher degree of cation intermixing with Li than Mn and Co do. Furthermore, the fraction of Ni ions residing in the Li layer was with a near linear relationship with the total Ni concentration.[437]

The incident electrons that have lost one or multiple virtual photon energies can be analyzed by an electron energy loss spectrometer after they pass through the sample. The spectrometer disperses the electrons using a magnetic prism and records the dispersed pattern by a pixelated detector. An electron energy loss spectrum (EELS) can be formed by integrating the signals along the nondispersing direction of the detector. An EELS spectrum documents the probability that an incident electron loses a certain energy. A full EELS spectrum is composed of three features. The first feature is the sharp peak that sits at zero-energy loss, which are the electrons that did not inelastically scatter in the sample or those that lost very little energy. The feature is most often referred to as the zero-loss peak. The shape and the width of the zero-loss peak encode the information regarding how electrons are extracted from the emitter/filament and the instrumental broadening. Its full width at half-maximum characterizes the energy resolution of the system for electron energy loss spectroscopy. A 0.8−1 eV energy resolution is routinely achievable in most Schottky field emission instruments. The energy resolution of cold field emission instrument is typical around 0.35 to 0.45 eV, depending on the extracting conditions. With a Wien-filter-type of monochromator, 0.1 eV energy resolution can be achieved. In a recent development, the energy resolution has been pushed down to 10 meV for probing Raman and IR activated vibrational modes in materials.[438]

The second component of the EELS spectrum is the valence loss or low-loss signal, which is typically between a few eV to 50 eV. The signals in this range can give information about dielectric responses and in optimal conditions, the band gap of the materials. The spectral feature in this region is generally

very broad and does not necessarily track the chemistry of the sample. However, there are exceptions. For example, electrochromic materials would have relatively sharp changes in the imaginary part of the dielectric function in the visible spectrum, and hence, it would be reflected as spectral feature changes in the low-loss EELS. It has been demonstrated by Holtz et al. using EELS that $LiFePO_4$ is an electrochromic material, albeit in the UV range.[439] A sharp feature would appear at 5 eV as Fe is oxidized from 2+ to 3+. The spectral feature developed at 5 eV can be used to map the valence distribution of Fe in $LiFePO_4$.

The third component of the EELS spectrum is the core-loss edges that sit on a power-law background. The core-loss edges probe the unfilled local density of states. They are first partitioned by elements, because their onset energies are associated with the characteristic binding energies of the core electrons that are being excited. Therefore, core-loss edges can be used to quantify the elemental information on the sample similar to EDS. Apart from giving elemental and compositional information, the fine structures in the first 35 eV of the core-loss edges encode information regarding the bonding environment. The interpretation of these fine structures is identical to that of the X-ray absorption near edge structures (XANES) with the except that the nondipole transitions are not exactly forbidden. However, in the near edge region, the nondipole component is an ignorable perturbation except for the special case of angular-resolved EELS. The other caveat of EELS is that the spectral shape is dependent on the sample thickness because the probing electrons would undergo multiple low-loss plasmon scattering in a finite thick sample. With careful treatments, such as the use of thin samples and deconvolution, this problem can be mediated. Among applications of EELS to lithium-ion batteries, Li K-edge, TM $L_{2,3}$-edges and the O K-edge are the most frequently used edges for probing the chemistry of the electrode materials. Li K-edges have an edge onset of 55 eV. The near edge fine structures have rich fingerprints relating to bonding environment. For example, it is reasonable to identify the presence of LiF, Li_2CO_3, Li_2O, or Li_2O_2 by simply reading the Li K-edge. However, the application of Li K-edge to cathode materials has been very problematic due to the overlap of the Li K edge with the 3d TM $M_{2,3}$-edges and the direct correlation of the lithium content with the 3d TM valence. Therefore, there is no simple way to extract the pure Li spectrum when 3d TMs are present in the system. In this case, a direct tracking of the 3d TMs $L_{2,3}$-edges can be used instead. (Details about the TM $L_{2,3}$-edges can be found in the XAS section in this review.) In addition to the TM $L_{2,3}$-edges, the O K-edge contains sensitive information regarding both its first nearest and second nearest neighbors. In particular, the prepeak of the O K-edge is sensitive to the valence of the nearest-neighboring TMs due to TM3d-O2p hybridization. Because the O K-edge is lower-lying than most 3d TM $L_{2,3}$-edges, its cross section is much larger and thus it is a widely used tool to monitor the 3d TM bonding environment when the higher edges are not available. The gradient distribution of transition metal oxidation states is a prevailing phenomenon in oxide cathode materials. Lin et al. performed EELS experiments on a charged NMC particle using EELS O K-edge and TM L-edge (Figure 41). They observed that transition metals were less oxidized at the surface compared to those in the bulk. The TM3d-O2p hybridization state is responsible for the pre-edge peak in the O K-edge EELS spectra, and its intensity gradually increased moving into the bulk due to the decreased occupancy of O2p orbitals that are hybridized with TM3d orbitals. The authors compared the STEM-EELS data with soft XAS results and concluded that this gradient distribution of oxidation states originated primarily from the surface reconstruction (population of low-valence TMs and rocksalt structure), although the likelihood of radial distribution of lithium ions could not be completely ruled out.

The real power of transmission electron microscopy is its spatial resolution. EELS can be coupled with both CTEM and STEM to form spectroscopic images. In the TEM condition, the spectrometer is operated in an energy-filtered mode to form images of inelastically scattered electrons within a selected energy window. The energy-filtered TEM (EF-TEM) images are useful in mapping elemental distributions at the nanoscale. Muller and his co-workers have advanced this technique and used EF-TEM to track in real time the nanoscale lithiated/delithiated patches during charging and discharging $LiFePO_4$ particles in 0.5 M Li_2SO_4 aqueous electrolytes. Because inelastic scattering is a relatively small angle scattering compared to elastic scattering, the diffraction contrast in the elastic channel is always preserved in the inelastic channel. Therefore, special caution needs to be taken when interpreting EF-TEM images. Particularly, with the development of chromatic aberration correctors, atomic resolution EF-TEM maps can be achieved in state-of-the-art instruments. However, any atomic-scale information acquired in the EF-TEM mode is not directly interpretable and has the same artifacts as CTEM images.

STEM-EELS, in contrast to EF-TEM, can give directly interpretable spectroscopic images if operated under the correct conditions. The coherent diffraction contrast can be removed from the spectroscopic signals by collecting all the strongly diffracted beams. This means that more compression to the diffraction pattern needs to be performed or the entrance aperture of the spectrometer needs to be widened. This can be easily achieved in most instruments manufactured in the past decade, however with a loss of energy resolution if the older generations of spectrometers are used. The spatial resolution of STEM-EELS is determined by both the size of the focused beam and the delocalization of the inelastic scattering process. In an aberration corrected STEM, the electron probe can be routinely made sub-one angstrom in size. Therefore, the spatial resolution of STEM-EELS is frequently limited by delocalization. Delocalization of EELS signal is significant in the low-loss regime. In this energy regime, dipole allowed transitions would not render a spatial resolution better than 1 nm. Atomic-resolution EELS mapping is typically achievable with edges that have an energy loss larger than 200 eV. STEM-EELS has been extensively applied to the spectroscopic mapping of active electrode materials. In the study of the capacity fading of NMC and Li Mn-rich materials, the STEM-EELS mapping of Mn $L_{2,3}$-edges provides spatially resolved spectroscopic evidence that can correlated with the atomic-scale imaging of the surface reconstruction.[90,429,430,440] In conversion electrodes, the phase segregation of the 3d TM can be tracked readily with the mapping of the TM $L_2,3$-edges.[91,441]

S/TEM is well poised for the study of battery electrode materials while they undergo physical/chemical transformations at the primary-particle length scales and below. These in situ battery experiments in the TEM can be classified into three categories: (1) temperature-varying (heating) experiments, (2) biasing/dry-cell experiments, and (3) electrochemical liquid-cell experiments.

In situ heating experiments have been applied to monitoring the thermal stability of the cathode materials. The change of local compositional and bonding environment, morphology, and atomic structures of the primary particles can be probed by EELS and S/TEM imaging simultaneously during the heating of the experiment. Heating in TEM was traditionally achieved through integrating a miniaturized Joule-heating furnace into the TEM holder. Since 2008, however, heating in TEM has been transformed by a local heating technology. Local heating is enabled by fabricating MEMS devices with heating elements that are only tens of microns in size. This design allows high temperature ramp rate with low thermal drift. Owing to this technological improvement, the layered to spinel to rocksalt degradation process of delithiated NCA cathode materials has been captured live using high-resolution TEM.[442] It is worth noting that even though the electrode material degradation that happens during a heating experiment is not exactly the same as that happening during charging/discharging, they do share at least one common root cause: oxygen loss.[443]

The most prominent imaging technique development for lithium-ion batteries in the field of in situ TEM is the biasing/dry-cell experiment. Prior to the development of liquid-cell holders for TEM, it had been difficult to perform in operando lithium-ion battery experiments in the TEM due to the involvement of liquid electrolytes that are not compatible with the vacuum environment in the TEM. The team of Li, Wang, Huang, and their colleagues found a shortcut that can bypass the problem.[444] Instead of using volatile organic electrolytes, they identified an ionic liquid that has extremely low vapor pressure and does not evaporate in the TEM. They scraped lithium metal on an ultrashape indenter, an etched tungsten tip, and dipped it into the ionic liquid. A cathode/electrolyte/lithium interface can be formed in the TEM by using a piezo-driven indentation holder. Using this approach, lithiation processes of SnO_2, silicon, etc. have been studied with high spatial resolution and high analytical sensitivity. Other incremental variations of this approach exist, but they all adopted this lithium-coated indenter approach. Lately, it has been more common to replace the ionic liquid with a thin layer of lithium oxide by exposing the scraped lithium to air for a short period of time.[445,446] It is worth noting that this approach is beneficial to TEM imaging and spectroscopy due to the removal of the ionic liquid that coats the surface of electrode materials; however, in most cases the reaction is not electrochemically driven, a shortage frequently occurs and lithium directly reacts with the electrode materials. It is acceptable to use this approach to study conversion reactions; however, it is not sensible to use this approach for intercalation materials where the control of the reaction voltage is critical.

In parallel to the dry cell experiments, in operando TEM experiments for solid-state batteries (SSB) have also been developed using similar approaches.[447] The challenge for this type of experiment is two-fold. (1) A cross-sectional sample of the SSB needs to be prepared by the focused ion beam lift-out technique. For batteries that contain polymer electrolyte, which are prone to ion and electron beam damage, special care needs to be taken to lower the dose for both sample preparation and imaging. (2) Due to the limited area of the electrode interface in the cross-sectional sample, the small battery needs to be charged in the pico-amp regime. To achieve sensible charge/discharge profile, it requires low-background Ohmic contacts, which are difficult to achieve with a regular indentation holder. Despite the fact that the experimental setup for solid-state

batteries is straightforward, due to the aforementioned challenge, limited success has been achieved in this area.

To perform electrochemical liquid-cell experiments, one needs to create a miniaturized device that can fit the size of an EM holder and can store/flow liquids. Zheng and her colleagues pioneered the reservoir approach; they make a reservoir cell by gluing two silicon chips together with a prescribed gap in between. The surface of the silicon chip is patterned with electrodes for two/three electrode electrochemical experiments.[448,449] Muller, Wang, and Unocic have pioneered the flow cell approach. In situ cycling of $LiFePO_4$ and silicon nanowires have been observed in the flow cell setup.[439,450]

The S/TEM characterization of lithium ion battery materials is in many ways similar to the characterization of many complex oxide materials.[451] However, due to the use of lithium in these electrode materials, they are much more prone to electron beam radiation damage. Characterization of these materials in some cases is limited by the dose sensitivity because electron beams can very quickly induce redox of the materials similar to what happens in electrochemical cells. For example, in NMC materials, lithium and oxygen can be knocked out of the materials if the dose rate is higher than a given threshold. This would induce the layered to spinel to rock-salt reconstruction that also occurs during the electrochemical cycling.[440] Therefore, to eliminate these artifacts, special attention must be paid to the calibration of the critical dose and critical dose-rate for damage-free imaging of these materials.

It is extremely important to emphasize that special caution needs to be taken when analyzing TEM results. Under normal conditions of data collection, where most of the reported studies were performed, only a limited number of particles were studied. The structural and electronic observations by TEM can sometimes be biased. Synchrotron X-ray techniques can probe an enormous number of battery particles and are ensemble-averaged. Therefore, the combination of synchrotron X-ray and TEM techniques allows for studying battery materials with complementary length sensitivities.

4.7. Experimental Design and Beam Effects

As ex situ experiments remain important in many X-ray techniques (in particular soft X-rays, discussed in section 4.3.6), in situ and operando experiments have received increasing attention due to their advantages. First of all, it circumvents the considerable efforts needed to prepare multiple ex situ samples to cover the electrochemical cycling process being studied, as well as providing increased reliability and precision in the ensuing analysis by continuously monitoring the electrochemical process occurring in a single sample. Second, it allows the investigation of time-dependent processes and thus is able to reveal short-lived or nonequilibrium intermediate states, which may not be detected with ex situ characterization.[74,452] Last but not least, it avoids the potential for contamination or relaxation of highly reactive products during ex situ sample preparation and handling (e.g., reaction with solvent solution during sample washing),[453] and the reaction products can be more reliably identified. However, it is sometimes not easy to conduct in situ and operando experiments, as the electrochemical cells must be fully operational under the circumstances imposed by the diagnostic tools, and many of the requirements for acquisition of high quality X-ray data and reliable electrochemical cycling performances are incompatible. Specially designed electrochemical cells

(e.g., geometry and cell components) and measurement setups are often demanded in light of the requirements by different synchrotron techniques. Coin cells, pouch cells, coffee bag cells, Swagelok type cells (e.g., Argonne's multipurpose in situ X-ray AMPIX electrochemical cell),[454] and capillary type cells have been reported, all of which show unique advantages for specific types of in situ and operando experiments.[74,452,455,215,283,398,454,456−458]

Several issues are worth noting for designing electrochemical in situ and operando cells with proper electrochemical functionality. (1) An X-ray transparent window often needs to be incorporated into the in situ or operando cell in order to allow X-rays to reach the investigated sample region. An ideal window material should be able to prevent the permeation of oxygen and moisture, as well as apply uniform pressure to enable a uniform electrochemical reaction. In general, it is easier to conduct in situ and operando experiments with hard X-rays due to their deeper penetration depths compared to soft X-rays, and there are more options for the selection of window materials, such as glassy carbon and beryllium. Kapton film is another type of window material for in situ and operando cells, which has been successfully used in many hard X-ray in situ and operando experiments. However, thin Kapton films are not able to maintain constant pressure, causing the sample underneath the window region to fail to react uniformly. It is even more challenging to perform in situ and operando experiments when decreasing the energy of the X-rays. In the tender X-ray region, very thin window materials, such as Mylar or polyethylene film, have to be used.[215] The short penetration depth of soft X-rays requires ultrahigh vacuum or high vacuum environments for the experiments, and the in situ and operando cell has to be specially designed (e.g., a solid battery with no window material or cell with ultrathin silicon nitride window, etc.).[283] We have discussed the soft X-ray in situ and operando approaches in section 4.3.6. (2) Cell components or materials along the X-ray beam path need to be carefully selected to avoid the interference of the X-ray signal from the detected samples. For example, glassy fiber separators rather than more commonly used thin Celgard separators are often used for in situ and operando experiments, in order to ensure enough liquid electrolyte within the in situ and operando cell. However, the thicker separator with more liquid electrolyte will excessively absorb X-ray photons, resulting in poorer signal-to-noise ratio (S/N) of the detected X-ray signal. This will sometimes cause trouble in obtaining high quality EXAFS data when performing in situ and operando hard XAS measurements. Another example is for PDF measurements, where the acquisition of high quality PDF data requires accurate measurement of the Bragg and diffuse scattering (total scattering) signal from the sample. The diffuse scattering signal (namely background) from cell components (window materials, separator, electrolyte, etc.) will also be included in the outgoing X-ray signal and needs to be precisely measured and excluded for the quantitative data analysis afterward. Therefore, the in situ and operando cell setups need to be highly reproducible for obtaining background signal data. The efforts from scientists at Argonne National Laboratory highlight the importance of cell design for in situ and operando PDF experiments, and their AMPIX electrochemical cell is able to accurately measure the background signal for in situ and operando PDF measurements while providing reliable electrochemical performance.[454] (3) In situ and operando cells must be able to be incorporated into the beamline setup and also be compatible with the X-ray detection mode. For example, for the in situ and operando X-ray tomography measurements, the cell needs to rotate through 180° to obtain a series of 2D images for the reconstruction of the 3D image, and thus an in situ or operando cell with a cylindrical shape made from a highly X-ray transparent material is preferred.[398] On the other hand, synchrotron X-ray measurements can be performed on materials synthesized with special geometries, for example, single crystals and films.[459−463] Although these model materials are unlikely to be used in practical cell applications, they offer excellent convenience to study the fundamental questions in batteries. For example, using a thin film model electrode, one can study the surface phenomena in the bulk material using hard XAS.

Although in situ and operando measurements show unique capabilities for directly monitoring the electrochemical processes occurring in a battery, ex situ measurements are still useful as they often provide high quality data for quantitative analysis. Since synchrotron radiation resources are precious, it is also not always necessary to perform in situ and operando measurements unless tracking dynamic processes is of real importance. Additionally, ex situ measurements can provide guidance if performed prior to the in situ and operando measurements, as they may provide critical information to confirm whether the in situ and operando cell functions properly.

Although X-ray radiation is weakly interacting with matter, X-rays can induce changes in the material under study. X-ray radiation-induced effects depend on the particular energy storage material, environment (electrolyte, binder, etc.) and on the details of the experimental setup (photon energy, beam size, and total deposited dose). During in situ and operando experiments, one can monitor effects of radiation globally through the electrochemical performance of the cell and locally at the single particle level through X-ray imaging. If beam damage is present, it can be mitigated by adapting the sample environment or changing the experimental conditions, for example, using higher X-ray energy,[464] modifying the cell setup,[454] or adjusting the size of the beam.[75,421,422] In many studies, radiation damage has been found to be negligible especially at low state of charge (e.g., low degree of delithiation of cathodes); for example, single particle imaging experiments showed no damage for exposure durations of several days.[75,421,422]

5. CONCLUSION AND PERSPECTIVES

The past 25 years has been a time of rapid development not only in battery science but also in the synchrotron techniques used to study phenomena ex situ, in situ, and operando relevant to the functioning of devices. Experiments can now be designed that probe interfacial regions less than a nanometer thick or subtle structural changes in one or just a few particles undergoing redox reactions as they happen. Increasingly sophisticated methods have been developed allowing direct observation of short-lived intermediates in electrodes as they charge and discharge in operando, under a variety of conditions. Tomographic techniques allow imaging of particles or even entire battery components in three dimensions. Such complex techniques do not come without their perils. The possibility of beam damage during S/TEM experiments is covered above, but this is also an issue for synchrotron work, especially for soft X-ray experiments,[464] where X-rays are concentrated into a very thin surface region. Poor design of in situ cells may also result

in anomalous behavior, particularly when systems are far from equilibrium (e.g., high charge or discharge rates).

The increasing ability to study liquids or solutions in beamlines is also one of the most exciting developments in synchrotron science and is in an active state of development. Electrolytic solutions lie at the very heart of many rechargeable battery systems in that they often dictate performance characteristics such as rate capability and predicate design choices such as electrode thicknesses. Identification of suitable electrolytes for several "Beyond Lithium Ion" systems such as Mg batteries is absolutely critical to their development.

It has become increasingly obvious that multimodal approaches on multiple length scales are needed to fully understand most battery systems. An example covered above is the study of surface reconstruction in NMC cathode materials by soft XAS and STEM/EELS. The soft XAS experiment probed a large ensemble of NMC particles in charged and cycled electrodes, revealing that the metals on the surfaces were reduced in comparison to those in the bulk, on average, but giving little information as to the exact nature of the transformation. STEM/EELS showed that the reduction was associated with surface reconstruction to a rocksalt structure, but it was possible to image only a relatively few particles. The samples were considerably heterogeneous, with particles (and even different facets on the same particle) showing differing degrees of reconstruction. There is always a question of whether a few particles imaged by microscopy are typical of a sample, but the XAS results lent additional credence to the interpretation of surface structural rearrangement in this case.

We emphasize here that it is still challenging to characterize matter away from equilibrium. However, the knowledge of the battery material's dynamic behaviors, such as the formation of metastable intermediate phases and the propagation of the reaction front that governs the phase transformation pathway, is very desirable because it offers critical insights into the device's degradation and failure mechanisms. Depending on the specific types of the experiments, the temporal resolution of general synchrotron based measurements can be very different and range from milliseconds to hours. For example, the hard X-ray powder diffraction patterns can be recorded using 2D area detectors with exposure time at millisecond level. On the other hand, nanoscale 3D XANES mapping[405] usually takes a few hours. Consequently, different strategies have been developed for different techniques to probe the material at a state that is away from equilibrium. For experimental techniques that are relatively fast, the measurements are simply repeated multiple times to record the change of the signal over time. For those techniques that require long data acquisition time, samples could be handled in a way so that the "fossil" evidence of the dynamic phase transition[465] are preserved in order to facilitate the study.

Although synchrotrons are generally used as CW (continuous wave) light sources, we would point out that synchrotron generated X-rays are not. The samples at a synchrotron beamline are actually exposed to short pulses of X-rays ($\sim 10^{-10}$ seconds) at very high repetition rate. Time-resolved synchrotron experiments can reach down to nanosecond to picosecond regimes, which is on the order of ion hopping in fast ion conductors. The X-ray free electron lasers can further push the temporal resolution to the femtosecond level. There are very exciting scientific opportunities at these ultrafast time scales. However, the relevance of the ultrafast time scales to battery sciences, which are ultimately diffusion-limited processes, remains unclear at present.

The need for multimodal studies on a variety of length and time scales is inspiring the next generation of synchrotron facilities, such as ALS-U at Lawrence Berkeley National Laboratory (https://als.lbl.gov/als-u/overview/). This planned upgrade, which includes provisions for the production of soft X-ray beams up to 1000 times brighter than currently available, is designed to improve resolution and sensitivity to the nanometer scale and on time scales down to nanoseconds. While still a number of years from realization, one goal is to allow several types of experiments to be carried out on the same sample sequentially, without the need for manual exchange. Instead, modules containing the sample of interest could be moved in and out of beamlines as needed, periodically, while they undergo testing under conditions of interest, such as long-term cycling. During down times, other types of experiments such as microscopy could be performed, ideally without the need to transfer samples, which risks exposure to atmosphere. This setup offers the maximum flexibility for the study of battery materials, and could provide valuable life-cycle information, critical for demanding applications such as electric vehicles.

The huge amount of raw data that is generated can be difficult to store, process, and handle. For that matter, it is likely to miss important details about how (for example) structural changes occur during in situ experiments because of the difficulties involved in handling so much information. Scientific big data mining is one of the next frontiers in cutting edge energy science at large scale X-ray facilities, requiring input not only from battery researchers and synchrotron scientists but also computer scientists and applied mathematicians. The novel developments in both the synchrotron facilities and the associated state-of-the-art experimental capabilities have made it possible to acquire huge volumes of experimental data within a short amount of time, which will be further amplified, dramatically, by the projected improvements in the next generation X-ray facilities including the APS-U, ALS-U, and LCLS-II. Such development brings vast opportunities in battery science, for example, the studies of battery systems' fast dynamic behavior and their hierarchically structured morphology and chemical complexity. These exciting research opportunities are unavoidably accompanied by the challenges in handling and mining of scientific big data. This is because the scientifically important portion of the experimental data is often small in quantity and weak in signal. Efficiently identifying, extracting, and studying the scientifically important subset of the big data requires more advanced data clustering and mining algorithms, which is an essential component of our future research effort in batteries, and energy science in general. As exciting as the past 20 years at the intersection of synchrotron and battery science have been, the increased power and brightness of new synchrotron facilities such as these are sure to result in even greater knowledge and productivity.

ASSOCIATED CONTENT

ⓢ Supporting Information

The Supporting Information is available free of charge on the ACS Publications website at DOI: 10.1021/acs.chemrev.7b00007.

Comparison of all analytical techniques (PDF)

AUTHOR INFORMATION

Corresponding Authors

*E-mail: fenglin@vt.edu.
*E-mail: mmdoeff@lbl.gov.

ORCID

Feng Lin: 0000-0002-3729-3148
Yijin Liu: 0000-0002-8417-2488
Ying Shirley Meng: 0000-0001-8936-8845

Present Address

△Department of Materials Science and Engineering, Cornell University, Ithaca, NY 14853.

Author Contributions

F.L. led the project. All coauthors participated in the planning, discussion, and writing of the review.

Notes

The authors declare no competing financial interest.

Biographies

Dr. Feng Lin is currently an Assistant Professor of Chemistry, with a courtesy appointment in the Department of Materials Science and Engineering at Virginia Tech. He holds Bachelor's degree in Materials Science and Engineering (2009) from Tianjin University, and MSc degree (2011) and Ph.D. degree (2012) in Materials Science from Colorado School of Mines. Prior to Virginia Tech, Feng worked at QuantumScape Corporation as a Senior Member of the Technical Staff, Lawrence Berkeley National Lab as a Postdoctoral Fellow, and National Renewable Energy Lab as a Graduate Research Assistant. Feng is fascinated by energy sciences, materials electrochemistry, and synchrotron X-rays.

Dr. Yijin Liu received his B.S. and Ph.D. in Optics from the University of Science and Technology of China in 2004 and 2009, respectively. He was a postdoctoral scholar at the Stanford Synchrotron Radiation Lightsource before he became an associate staff scientist in 2012 and, later, a staff scientist in 2015 at the SLAC National Accelerator Laboratory. His research interest is in the X-ray based multilength-scale spectroscopic imaging techniques with scientific focus on the energy material study and the related scientific big data mining.

Dr. Xiqian Yu is currently an Associate Professor at the Institute of Physics, Chinese Academy of Sciences (IOP, CAS). He received his Bachelor's degree in applied physics (2005) from Wuhan University and Ph.D. degree in condensed matter physics (2010) from IOP, CAS. Prior to IOP, he worked at Brookhaven National Laboratory as a postdoctoral fellow (2010−2013) and Physics Associate (2013−2016). His research interest is in the field of electrochemical energy storage with the main focus on the characterization of the electrode materials for rechargeable batteries.

Dr. Lei Cheng received his Ph.D. in Material Sciences and Engineering, under the supervision of Prof. Lutgard De Jonghe and Dr. Marca Doeff, in 2015 from University of California, Berkeley, where he worked on the development of garnet-type solid state ionic conductors, with a focus on the understanding of the interfaces using both synchrotron spectroscopy and electrochemical techniques. His research interests include solid electrolyte processing and integration, and advanced diagnostics of electrochemical devices.

Dr. Andrej Singer is an Assistant Professor in the Department of Materials Science and Engineering at Cornell University. He received his Ph.D. in Physics from the University of Hamburg in Germany and worked as a postdoctoral scholar at the University of California San Diego. His research focuses on the understanding of the nanoscale structure and its dynamics in complex materials by using novel x-ray characterization techniques.

Dr. Oleg G. Shpyrko is currently a Professor of Physics at the University of California San Diego. He holds a Ph.D. Degree in Physics from Harvard University (2004) and has served as Distinguished Postdoctoral Fellow at the Center for Nanoscale Materials at the Argonne National Lab (2005−2007) before joining UC San Diego in 2007. Shpyrko's group is focused on development and application of advanced X-ray synchrotron-based characterization probes of a wide range of nanoscale phenomena, including energy-storage materials.

Dr. Huolin Xin is currently an Associate Scientist at Brookhaven National Laboratory. He holds a Bachelor's degree in Physics (2005) from Peking University and a Ph.D. degree (2011) in Physics from Cornell University. Prior to Brookhaven Lab, Xin worked at Lawrence Berkeley National Lab as a Postdoctoral Fellow. Xin is an electron microscopist and spectroscopist.

Dr. Nobumichi Tamura is a staff scientist at the Advanced Light Source of the Lawrence Berkeley National Laboratory. He received his Ph.D. degree in Materials Science at the Laboratoire de Thermodynamique et de Physicochimie des Materiaux, Institut National Polytechnique, Grenoble, France, in 1993. He has been working in the field of advanced x-ray diffraction techniques including synchrotron microdiffraction for more than 15 years and has published over 300 papers, including book chapters during his scientific career. His current interests include the development of synchrotron x-ray microdiffraction technique and their applications to Materials, Environmental, and Geosciences, and the study of materials reliability and mechanical properties by x-ray diffraction techniques.

Dr. Chixia Tian is currently a Research Scientist at Virginia Tech. Prior to this position, she was a Chemist Postdoctoral Fellow at Lawrence Berkeley National Laboratory (2015−2017). She holds a Bachelor's degree in Polymer Science and Technology (2009) from Beijing University of Chemical Technology and a Ph.D. degree in Chemistry (2015) from Colorado School of Mines. Her research focuses on developing cathode materials for lithium ion batteries and novel polymeric materials for energy applications.

Dr. Tsu-Chien Weng is a staff scientist at the Center for High Pressure Science & Technology Advanced Research (HPSTAR). He received his BSc and MSc degrees in Chemistry from National Taiwan University and his Ph.D. degree in Chemistry from the University of Michigan. He worked as a staff scientist at the European Synchrotron Radiation Facility from 2006 to 2010 and Stanford Synchrotron Radiation Lightsource from 2010 to 2015 before joining HPSTAR in 2015. Weng's research interests include the electronic structure characterization in bio/chemical catalysis and the in situ study of energy materials using XAS, XES, and related techniques, as well as x-ray instrumentation R&D for synchrotrons and XFELs for studying ultrafast processes.

Dr. Xiao-Qing Yang is currently the group leader of the electrochemical energy storage group in the Chemistry Division of Brookhaven National Laboratory (BNL). He is the Principal Investigator (PI) for several Battery Material Research (BMR) programs including the Battery 500 consortium at BNL funded by the Office of Vehicle Technologies, EE&RE, U.S. Department of Energy (USDOE). He received his B.S. in Material Science from Shannxi Mechanic Engineering Institute in Xi'an, China, in 1976 and Ph.D. in Physics, from University of Florida, Gainesville, Florida, in 1986.

Dr. Y. Shirley Meng received her Ph.D. in Advanced Materials for Micro & Nano Systems from the Singapore-MIT Alliance in 2005, after which she worked as a postdoc research fellow and became a research scientist at MIT. Shirley is currently the Professor of NanoEngineering and Materials Science at University of California San Diego (UCSD). She is the founding Director of Sustainable Power and Energy Center at UCSD.

Dr. Dennis Nordlund obtained his Ph.D. (in 2004) in Chemical Physics. Following a 2-year Wenner-Gren Fellowship (2005−2006) he joined Stanford Synchrotron Radiation Lightsource in 2007, where he currently holds a Staff Scientist position. He is an expert in electronic structure and chemical bonding characterization using photon science techniques, employing X-ray spectroscopy to disentangle outstanding questions in the basic energy sciences, broadly, using state-of-the-art techniques at ring-based third generation and linac-based fourth generation light-sources, primarily at SSRL and LCLS. He has published more than 200 peer-reviewed articles that have received over 10000 citations.

Dr. Wanli Yang is a physicist staff scientist at the Advanced Light Source division of Lawrence Berkeley National Laboratory. He received his bachelor's degree in Physics (1995) from Shandong University and Ph.D. degree in condensed matter physics (2000) from Institute of Physics, CAS. Yang was a postdoctoral associate at Stanford University and a staff scientist at GLAM of Stanford before he came to work at Berkeley Lab. Yang's research interest is soft X-ray spectroscopy of energy materials.

Dr. Marca M. Doeff is a staff scientist at Lawrence Berkeley National Laboratory (LBNL) and a principle investigator in battery programs funded by the U.S. Department of Energy. Her research focuses on materials for Li-ion, Na-ion, and solid-state batteries, and she has published over 200 papers, abstracts, and book chapters on these topics. She is currently vice-chair of the Battery division of the Electrochemical Society and is a Fellow of the Electrochemical Society and of the Royal Society of Chemistry.

GLOSSARY

AEY	auger electron yield
ADF	annular dark field
BCDI	Bragg coherent diffractive imaging
CEI	cathode electrolyte interphase
CCD	charge-coupled device
CT	computed tomography
CDI	coherent diffractive imaging
CTEM	conventional transmission electron microscopy
DFT	density functional theory
DBSCAN	density-based spatial clustering of applications with noise
EDXRD	energy-dispersive X-ray diffraction
EDS	energy dispersive X-ray spectroscopy
EELS	electron energy loss spectroscopy
EF-TEM	energy filtered-transmission electron microscopy
EV	electric vehicle
EXAFS	extended X-ray absorption fine structure
FTIR	Fourier transform infrared spectroscopy
FY-XRM	fluorescence-yield X-ray microscopy
GIXRD	grazing incidence X-ray diffraction
HOMO	highest occupied molecular orbital
Hard XRS	hard X-ray Raman scattering
HXPS	hard X-ray photoelectron spectroscopy
IR	infrared
IMFP	inelastic mean free path
IPFY	inverse partial fluorescence yield
ICA	independent component analysis
LUMO	lowest unoccupied molecular orbital
LAADF-STEM	low-angle annular dark field-scanning transmission electron microscopy
NCA	$LiNi_{0.8}Co_{0.15}Al_{0.05}O_2$
NMC	$LiNi_xMn_yCo_zO_2$; $x + y + z = 1$
NMR	nuclear magnetic resonance spectroscopy
PIEO	photon-in-electron-out
PIPO	photon-in-photon-out
PDF	pair distribution function
RIXS	resonant inelastic X-ray scattering
SEI	solid electrolyte interphase
SHE	standard hydrogen electrode
Soft XAS	soft X-ray absorption spectroscopy
SOC	state of charge

SXPS	soft X-ray photoelectron spectroscopy
STXM	scanning transmission X-ray microscopy
STEM	scanning transmission electron microscopy
TEM	transmission electron microscopy
TRF-XAS	total-reflection fluorescence X-ray absorption spectroscopy
TEY	total electron yield
TFY	total fluorescence yield
TXM	transmission X-ray microscopy
UV	ultraviolet
UHV	ultra-high vacuum
XRD	X-ray diffraction
XANES	X-ray absorption near edge structure
XPS	X-ray photoelectron spectroscopy
XAS	X-ray absorption spectroscopy
XES	X-ray emission spectroscopy

REFERENCES

(1) Naguara, T.; Tozawa, K. Lithium Ion Rechargeable Battery. *Progress in Batteries and Solar Cells*; JEC Press Inc., 1990; Vol. *9*, pp 209−219.

(2) Nykvist, B.; Nilsson, M. Rapidly Falling Costs of Battery Packs for Electric vehicles. *Nat. Clim. Change* **2015**, *5*, 329−332.

(3) McBreen, J.; O'Grady, W. E.; Pandya, K. I. Exafs: A New Tool for the Study of Battery and Fuel Cell Materials. *J. Power Sources* **1988**, *22*, 323−340.

(4) Skotheim, T. A.; Yang, X. Q.; Xue, K. H.; Lee, H. S.; Mcbreen, J.; Lu, F. X-Ray Absorption Studies on Organo-Disulfide Redox Cathodes. *Electrochim. Acta* **1992**, *37*, 1635−1637.

(5) Yang, X. Q.; Xue, K. H.; Lee, H. S.; Mcbreen, J.; Skotheim, T. A.; Lu, F. X-Ray-Absorption Studies of Organodisulfide Redox Polymeric Electrodes. *Phys. Rev. B: Condens. Matter Mater. Phys.* **1992**, *45*, 5733−5736.

(6) Mcbreen, J.; Yang, X. Q.; Lee, H. S.; Okamoto, Y. Xas Studies of Peo Based Polymer Electrolytes. *Mater. Res. Soc. Symp. Proc.* **1994**, *369*, 559−564.

(7) Thurston, T. R.; Jisrawi, N. M.; Mukerjee, S.; Yang, X. Q.; McBreen, J.; Daroux, M. L.; Xing, X. K. Synchrotron X-Ray Diffraction Studies of the Structural Properties of Electrode Materials in Operating Battery Cells. *Appl. Phys. Lett.* **1996**, *69*, 194−196.

(8) McBreen, J.; Mukerjee, S.; Yang, X. Q. In Situ Synchrotron X-ray Studies of Battery and Fuel Cell Materials. *Synchrotron Radiation News* **1998**, *11*, 18−22.

(9) Mukerjee, S.; Thurston, T. R.; Jisrawi, N. M.; Yang, X. Q.; McBreen, J.; Daroux, M. L.; Xing, X. K. Structural Evolution of $Li_xMn_2O_4$ in Lithium-Ion Battery Cells Measured in Situ Using Synchrotron X-Ray Diffraction Techniques. *J. Electrochem. Soc.* **1998**, *145*, 466−472.

(10) Yang, X. Q.; Sun, X.; McBreen, J. New Findings on the Phase Transitions in Li1-Xnio2: In Situ Synchrotron X-Ray Diffraction Studies. *Electrochem. Commun.* **1999**, *1*, 227−232.

(11) Kam, K. C.; Doeff, M. M. Electrode Materials for Lithium Ion Batteries. *Mater. Matters* **2012**, *7*, 56−58.

(12) Zhang, S. S. A Review on the Separators of Liquid Electrolyte Li-Ion Batteries. *J. Power Sources* **2007**, *164*, 351−364.

(13) Xu, K. Nonaqueous Liquid Electrolytes for Lithium-Based Rechargeable Batteries. *Chem. Rev.* **2004**, *104*, 4303−4417.

(14) Zhang, S. S. A Review on Electrolyte Additives for Lithium-Ion Batteries. *J. Power Sources* **2006**, *162*, 1379−1394.

(15) Doughty, D.; Roth, E. P. A General Discussion of Li Ion Battery Safety. *Electrochem. Soc. Interface* **2012**, *21*, 37−44.

(16) Hochgatterer, N. S.; Schweiger, M. R.; Koller, S.; Raimann, P. R.; Wohrle, T.; Wurm, C.; Winter, M. Silicon/Graphite Composite Electrodes for High-Capacity Anodes: Influence of Binder Chemistry on Cycling Stability. *Electrochem. Solid-State Lett.* **2008**, *11*, A76−A80.

(17) Pietsch, P.; Westhoff, D.; Feinauer, J.; Eller, J.; Marone, F.; Stampanoni, M.; Schmidt, V.; Wood, V. Quantifying Microstructural

Dynamics and Electrochemical Activity of Graphite and Silicon-Graphite Lithium Ion Battery Anodes. *Nat. Commun.* **2016**, *7*, 12909.

(18) Mizushima, K.; Jones, P. C.; Wiseman, P. J.; Goodenough, J. B. Li_xCoO_2 (0 < x < 1): A New Cathode Material for Batteries of High Energy Density. *Mater. Res. Bull.* **1980**, *15*, 783−789.

(19) Andre, D.; Kim, S. J.; Lamp, P.; Lux, S. F.; Maglia, F.; Paschos, O.; Stiaszny, B. Future Generations of Cathode Materials: An Automotive Industry Perspective. *J. Mater. Chem. A* **2015**, *3*, 6709−6732.

(20) Eriksson, M.; van der Veen, J. F.; Quitmann, C. Diffraction-Limited Storage Rings-A Window to the Science of Tomorrow. *J. Synchrotron Radiat.* **2014**, *21*, 837−842.

(21) Obrovac, M. N.; Christensen, L.; Le, D. B.; Dahn, J. R. Alloy Design for Lithium-Ion Battery Anodes. *J. Electrochem. Soc.* **2007**, *154*, A849.

(22) Park, C. M.; Kim, J. H.; Kim, H.; Sohn, H. J. Li-Alloy Based Anode Materials for Li Secondary Batteries. *Chem. Soc. Rev.* **2010**, *39*, 3115−3141.

(23) Obrovac, M. N.; Chevrier, V. L. Alloy Negative Electrodes for Li-Ion Batteries. *Chem. Rev.* **2014**, *114*, 11444−11502.

(24) Beattie, S. D.; Larcher, D.; Morcette, M.; Simon, B.; Tarascon, J. M. Si Electrodes for Li-Ion Batteries-A New Way to Look at an Old Problem. *J. Electrochem. Soc.* **2008**, *155*, A158.

(25) Szczech, J. R.; Jin, S. Nanostructured Silicon for High Capacity Lithium Battery Anodes. *Energy Environ. Sci.* **2011**, *4*, 56−72.

(26) Su, X.; Wu, Q.; Li, J.; Xiao, X.; Lott, A.; Lu, W.; Sheldon, B. W.; Wu, J. Silicon-Based Nanomaterials for Lithium-Ion Batteries: A Review. *Adv. Energy Mater.* **2014**, *4*, 1−23.

(27) Luo, F.; Liu, B.; Zheng, J.; Chu, G.; Zhong, K.; Li, H.; Huang, X.; Chen, L. Review-Nano-Silicon/Carbon Composite Anode Materials Towards Practical Application for Next Generation Li-Ion Batteries. *J. Electrochem. Soc.* **2015**, *162*, A2509−A2528.

(28) Mazouzi, D.; Karkar, Z.; Reale Hernandez, C.; Jimenez Manero, P.; Guyomard, D.; Roué, L.; Lestriez, B. Critical Roles of Binders and Formulation at Multiscales of Silicon-Based Composite Electrodes. *J. Power Sources* **2015**, *280*, 533−549.

(29) Wolfenstine, J.; Allen, J. L.; Read, J.; Foster, D. *Chemistry and Structure of Sony's Nexelion Li-Ion Electrode Materials*; Technical Report for Army Research Laboratory ARL-TN-0257; 2006.

(30) Ferguson, P. P.; Martine, M. L.; George, A. E.; Dahn, J. R. Studies of Tin−Transition Metal−Carbon and Tin−Cobalt−Transition Metal−Carbon Negative Electrode Materials Prepared by Mechanical Attrition. *J. Power Sources* **2009**, *194*, 794−800.

(31) Whittingham, M. S. Materials Challenges Facing Electrical Energy Storage. *MRS Bull.* **2008**, *33*, 411−419.

(32) Cabana, J.; Monconduit, L.; Larcher, D.; Palacin, M. R. Beyond Intercalation-Based Li-Ion Batteries: The State of the Art and Challenges of Electrode Materials Reacting through Conversion Reactions. *Adv. Mater.* **2010**, *22*, E170−192.

(33) Hassoun, J.; Scrosati, B. Review—Advances in Anode and Electrolyte Materials for the Progress of Lithium-Ion and Beyond Lithium-Ion Batteries. *J. Electrochem. Soc.* **2015**, *162*, A2582−A2588.

(34) Li, H.; Balaya, P.; Maier, J. Li-Storage Via Heterogeneous Reaction in Selected Binary Metal Fluorides and Oxides. *J. Electrochem. Soc.* **2004**, *151*, A1878−A1885.

(35) Xu, J.; Lin, F.; Doeff, M. M.; Tong, W. A Review of Ni-Based Layered Oxides for Rechargeable Li-Ion Batteries. *J. Mater. Chem. A* **2017**, *5*, 874.

(36) Lin, F.; Markus, I. M.; Nordlund, D.; Weng, T. C.; Asta, M. D.; Xin, H. L.; Doeff, M. M. Surface Reconstruction and Chemical Evolution of Stoichiometric Layered Cathode Materials for Lithium-Ion Batteries. *Nat. Commun.* **2014**, *5*, 3529.

(37) Liu, W.; Oh, P.; Liu, X.; Lee, M. J.; Cho, W.; Chae, S.; Kim, Y.; Cho, J. Nickel-Rich Layered Lithium Transitional-Metal Oxide for High-Energy Lithium-Ion Batteries. *Angew. Chem., Int. Ed.* **2015**, *54*, 4440−4457.

(38) Lu, Z.; MacNeil, D. D.; Dahn, J. R. Layered Cathode Materials $Li[Ni_xLi_{(1/3−2x/3)}Mn_{(2/3−x/3)}]O_2$ for Lithium-Ion Batteries. *Electrochem. Solid-State Lett.* **2001**, *4*, A191.

(39) Thackeray, M. M.; Kang, S.-H.; Johnson, C. S.; Vaughey, J. T.; Benedek, R.; Hackney, S. A. Li_2MnO_3-Stabilized $LiMO_2$ (M = Mn, Ni, Co) Electrodes for Lithium-Ion Batteries. *J. Mater. Chem.* **2007**, *17*, 3112.

(40) Ohzuku, T.; Nagayama, M.; Tsuji, K.; Ariyoshi, K. High-Capacity Lithium Insertion Materials of Lithium Nickel Manganese Oxides for Advanced Lithium-Ion Batteries: Toward Rechargeable Capacity More Than 300 Ma H G−1. *J. Mater. Chem.* **2011**, *21*, 10179.

(41) Yu, X.; Lyu, Y.; Gu, L.; Wu, H.; Bak, S.-M.; Zhou, Y.; Amine, K.; Ehrlich, S. N.; Li, H.; Nam, K.-W.; et al. Understanding the Rate Capability of High-Energy-Density Li-Rich Layered $Li_{1.2}Ni_{0.15}Co_{0.1}Mn_{0.55}O_2$ cathode Materials. *Adv. Energy Mater.* **2014**, *4*, 1300950.

(42) Yoon, W.-S.; Kim, N.; Yang, X.-Q.; McBreen, J.; Grey, C. P. 6Li MAS NMR and in Situ X-Ray Studies of Lithium Nickel Manganese Oxides. *J. Power Sources* **2003**, *119−121*, 649−653.

(43) Bareño, J.; Balasubramanian, M.; Kang, S. H.; Wen, J. G.; Lei, C. H.; Pol, S. V.; Petrov, I.; Abraham, D. P. Long-Range and Local Structure in the Layered Oxide $Li_{1.2}Co_{0.4}Mn_{0.4}O_2$. *Chem. Mater.* **2011**, *23*, 2039−2050.

(44) Shukla, A. K.; Ramasse, Q. M.; Ophus, C.; Duncan, H.; Hage, F.; Chen, G. Unravelling Structural Ambiguities in Lithium- and Manganese-Rich Transition Metal Oxides. *Nat. Commun.* **2015**, *6*, 8711.

(45) Croy, J. R.; Balasubramanian, M.; Gallagher, K. G.; Burrell, A. K. Review of the U.S. Department of Energy's "Deep Dive" Effort to Understand Voltage Fade in Li- and Mn-Rich Cathodes. *Acc. Chem. Res.* **2015**, *48*, 2813−2821.

(46) Grimaud, A.; Hong, W. T.; Shao-Horn, Y.; Tarascon, J. M. Anionic Redox Processes for Electrochemical Devices. *Nat. Mater.* **2016**, *15*, 121−126.

(47) Seo, D.-H.; Urban, A.; Ceder, G. Calibrating Transition-Metal Energy Levels and Oxygen Bands in First-Principles Calculations: Accurate Prediction of Redox Potentials and Charge Transfer in Lithium Transition-Metal Oxides. *Phys. Rev. B: Condens. Matter Mater. Phys.* **2015**, *92*, 115−118.

(48) Sathiya, M.; Rousse, G.; Ramesha, K.; Laisa, C. P.; Vezin, H.; Sougrati, M. T.; Doublet, M. L.; Foix, D.; Gonbeau, D.; Walker, W.; et al. Reversible Anionic Redox Chemistry in High-Capacity Layered-Oxide Electrodes. *Nat. Mater.* **2013**, *12*, 827−835.

(49) McCalla, E.; Abakumov, A. M.; Saubanere, M.; Foix, D.; Berg, E. J.; Rousse, G.; Doublet, M.-L.; Gonbeau, D.; Novak, P.; Tendeloo, G. V. Visualization of O-O Peroxo-Like Dimers in High-Capacity Layered Oxides for Li-Ion Batteries. *Science* **2015**, *350*, 1516−1521.

(50) Yabuuchi, N.; Takeuchi, M.; Nakayama, M.; Shiiba, H.; Ogawa, M.; Nakayama, K.; Ohta, T.; Endo, D.; Ozaki, T.; Inamasu, T.; et al. High-Capacity Electrode Materials for Rechargeable Lithium Batteries: Li_3NbO_4-Based System with Cation-Disordered Rocksalt Structure. *Proc. Natl. Acad. Sci. U. S. A.* **2015**, *112*, 7650−7655.

(51) van Noorden, R. A Better Battery. *Nature* **2014**, *507*, 26−28.

(52) Crabtree, G.; Kócs, E.; Trahey, L. The Energy-Storage Frontier: Lithium-Ion Batteries and Beyond. *MRS Bull.* **2015**, *40*, 1067−1078.

(53) Sapunkov, O.; Pande, V.; Khetan, A.; Choomwattana, C.; Viswanathan, V. Quantifying the Promise of 'Beyond' Li−Ion Batteries. *Transl. Mater. Res.* **2015**, *2*, 045002.

(54) Kerman, K.; Luntz, A.; Viswanathan, V.; Chiang, Y.-M.; Chen, Z. Review—Practical Challenges Hindering the Development of Solid State Li Ion Batteries. *J. Electrochem. Soc.* **2017**, *164*, A1731−A1744.

(55) Hagen, M.; Hanselmann, D.; Ahlbrecht, K.; Maça, R.; Gerber, D.; Tübke, J. Lithium-Sulfur Cells: The Gap between the State-of-the-Art and the Requirements for High Energy Battery Cells. *Adv. Energy Mater.* **2015**, *5*, 1401986.

(56) Girishkumar, G.; McCloskey, B.; Luntz, A. C.; Swanson, S.; Wilcke, W. Lithium−Air Battery: Promise and Challenges. *J. Phys. Chem. Lett.* **2010**, *1*, 2193−2203.

(57) Christensen, J.; Albertus, P.; Sanchez-Carrera, R. S.; Lohmann, T.; Kozinsky, B.; Liedtke, R.; Ahmed, J.; Kojic, A. A Critical Review of Li/Air Batteries. *J. Electrochem. Soc.* **2012**, *159*, R1.

(58) Kraytsberg, A.; Ein-Eli, Y. Review on Li−Air Batteries—Opportunities, Limitations and Perspective. *J. Power Sources* **2011**, *196*, 886−893.

(59) Gallagher, K. G.; Goebel, S.; Greszler, T.; Mathias, M.; Oelerich, W.; Eroglu, D.; Srinivasan, V. Quantifying the Promise of Lithium−Air Batteries for Electric Vehicles. *Energy Environ. Sci.* **2014**, *7*, 1555.

(60) Liu, T.; Leskes, M.; Yu, W.; Moore, A. J.; Zhou, L.; Bayley, P. M.; Kim, G.; Grey, C. P. Cycling $Li-O_2$ Batteries Via Lioh Formation and Decomposition. *Science* **2015**, *350*, 530−533.

(61) Lu, J.; Lee, Y. J.; Luo, X.; Lau, K. C.; Asadi, M.; Wang, H. H.; Brombosz, S.; Wen, J.; Zhai, D.; Chen, Z.; et al. A Lithium-Oxygen Battery Based on Lithium Superoxide. *Nature* **2016**, *529*, 377−382.

(62) Hartmann, P.; Bender, C. L.; Vracar, M.; Durr, A. K.; Garsuch, A.; Janek, J.; Adelhelm, P. A Rechargeable Room-Temperature Sodium Superoxide (Nao2) Battery. *Nat. Mater.* **2013**, *12*, 228−232.

(63) Jones, S. D.; Akridge, J. R. A Thin Film Solid-State Microbattery. *J. Power Sources* **1993**, *44*, 505−513.

(64) Bates, J. B.; Dudney, N. J.; Neudecker, B.; Ueda, A.; Evans, C. D. Thin-Film Lithium and Lithium-Ion Batteries. *Solid State Ionics* **2000**, *135*, 33−45.

(65) Knauth, P. Inorganic Solid Li Ion Conductors: An Overview. *Solid State Ionics* **2009**, *180*, 911−916.

(66) Cao, C.; Li, Z.-B.; Wang, X.-L.; Zhao, X.-B.; Han, W.-Q. Recent Advances in Inorganic Solid Electrolytes for Lithium Batteries. *Front. Energy Res.* **2014**, *2*, 25.

(67) Wang, Y.; Chen, Y.; Gao, J. W.; Yoon, H. G.; Jin, L. Y.; Forsyth, M.; Dingemans, T. J.; Madsen, L. A. Highly Conductive and Thermally Stable Ion Gels with Tunable Anisotropy and Modulus. *Adv. Mater.* **2016**, *28*, 2571−2578.

(68) Slater, M. D.; Kim, D.; Lee, E.; Doeff, M.; Johnson, C. S. Sodium-Ion Batteries. *Adv. Funct. Mater.* **2013**, *23*, 947−958.

(69) Palomares, V.; Casas-Cabanas, M.; Castillo-Martínez, E.; Han, M. H.; Rojo, T. Update on Na-Based Battery Materials. A Growing Research Path. *Energy Environ. Sci.* **2013**, *6*, 2312.

(70) Aurbach, D.; Lu, Z.; Schechter, A.; Gofer, Y.; Gizbar, H.; Turgeman, R.; Cohen, Y.; Moshkovich, M.; Levi, E. Prototype Systems for Rechargeable Magnesium Batteries. *Nature* **2000**, *407*, 724−727.

(71) Muldoon, J.; Bucur, C. B.; Gregory, T. Quest for Nonaqueous Multivalent Secondary Batteries: Magnesium and Beyond. *Chem. Rev.* **2014**, *114*, 11683−11720.

(72) Ponrouch, A.; Frontera, C.; Bardé, F.; Palacin, M. R. Towards a Calcium-Based Rechargeable Battery. *Nat. Mater.* **2016**, *15*, 169−172.

(73) Lipson, A. L.; Pan, B.; Lapidus, S. H.; Liao, C.; Vaughey, J. T.; Ingram, B. J. Rechargeable Ca-Ion Batteries: A New Energy Storage System. *Chem. Mater.* **2015**, *27*, 8442−8447.

(74) Liu, H.; Strobridge, F. C.; Borkiewicz, O. J.; Wiaderek, K. M.; Chapman, K. W.; Chupas, P. J.; Grey, C. P. Batteries. Capturing Metastable Structures During High-Rate Cycling of $LiFePO_4$ Nanoparticle Electrodes. *Science* **2014**, *344*, 1252817.

(75) Ulvestad, A.; Singer, A.; Clark, J. N.; Cho, H. M.; Kim, J. W.; Harder, R.; Maser, J.; Meng, Y. S.; Shpyrko, O. G. Topological Defect Dynamics in Operando Battery Nanoparticles. *Science* **2015**, *348*, 1344−1347.

(76) Nakamura, M.; Kaminaga, H.; Endo, O.; Tajiri, H.; Sakata, O.; Hoshi, N. Structural Dynamics of the Electrical Double Layer During Capacitive Charging/Discharging Processes. *J. Phys. Chem. C* **2014**, *118*, 22136−22140.

(77) Hai, B.; Shukla, A. K.; Duncan, H.; Chen, G. Y. The Effect of Particle Surface Facets on the Kinetic Properties of $LiMn_{1.5}Ni_{0.5}O_4$ Cathode Materials. *J. Mater. Chem. A* **2013**, *1*, 759−769.

(78) Dresselhaus, M. S.; Dresselhaus, G. Intercalation Compounds of Graphite. *Adv. Phys.* **2002**, *51*, 1−186.

(79) Jarry, A.; Gottis, S.; Yu, Y. S.; Roque-Rosell, J.; Kim, C.; Cabana, J.; Kerr, J.; Kostecki, R. The Formation Mechanism of Fluorescent Metal Complexes at the $Li_xNi_{0.5}Mn_{1.5}O_4$-Delta/Carbonate Ester Electrolyte Interface. *J. Am. Chem. Soc.* **2015**, *137*, 3533−3539.

(80) Doeff, M. M. *Batteries: Overview of Battery Cathodes*; Springer Science+Business Media, LLC, 2012.

(81) Attwood, D. *Soft X-Rays and Extreme Ultraviolet Radiation*; Cambridge University Press: Cambridge UK, 2000.

(82) Muller, E. A.; Pollard, B.; Raschke, M. B. Infrared Chemical Nano-Imaging: Accessing Structure, Coupling, and Dynamics on Molecular Length Scales. *J. Phys. Chem. Lett.* **2015**, 6, 1275−1284.

(83) Park, S. J.; Zhao, H.; Ai, G.; Wang, C.; Song, X.; Yuca, N.; Battaglia, V. S.; Yang, W.; Liu, G. Side-Chain Conducting and Phase-Separated Polymeric Binders for High-Performance Silicon Anodes in Lithium-Ion Batteries. *J. Am. Chem. Soc.* **2015**, 137, 2565−2571.

(84) Liu, X.; Yang, W.; Liu, Z. Recent Progress on Synchrotron-Based in-Situ Soft X-Ray Spectroscopy for Energy Materials. *Adv. Mater.* **2014**, 26, 7710−7729.

(85) Liu, X.; Liu, J.; Qiao, R.; Yu, Y.; Li, H.; Suo, L.; Hu, Y.-S.; Chuang, Y.-D.; Shu, G.; Chou, F.; et al. Phase Transformation and Lithiation Effect on Electronic Structure of Li_xFePO_4: An in-Depth Study by Soft X-Ray and Simulations. *J. Am. Chem. Soc.* **2012**, 134, 13708−13715.

(86) Sokaras, D.; Nordlund, D.; Weng, T.-C.; Alonso Mori, R.; Velikov, P.; Wenger, D.; Garachtchenko, A.; George, M.; Borzenets, V.; Johnson, B.; Qian, Q.; Rabedeau, T.; Bergmann, U. A High Resolution and Large Solid Angle X-Ray Raman Spectroscopy End-Station at the Stanford Synchrotron Radiation Lightsource. *Rev. Sci. Instrum.* **2012**, 83, 043112.

(87) Braun, A.; Nordlund, D.; Song, S.-W.; Huang, T.-W.; Sokaras, D.; Liu, X.; Yang, W.; Weng, T.-C.; Liu, Z. Hard X-Rays in−Soft X-Rays Out: An Operando Piggyback View Deep into a Charging Lithium Ion Battery with X-Ray Raman Spectroscopy. *J. Electron Spectrosc. Relat. Phenom.* **2015**, 200, 257−263.

(88) Lin, F.; Nordlund, D.; Markus, I. M.; Weng, T.-C.; Xin, H. L.; Doeff, M. M. Profiling the Nanoscale Gradient in Stoichiometric Layered Cathode Particles for Lithium-Ion Batteries. *Energy Environ. Sci.* **2014**, 7, 3077−3085.

(89) Yoon, W.-S.; Balasubramanian, M.; Chung, K. Y.; Yang, X.-Q.; McBreen, J.; Grey, C. P.; Fischer, D. A. Investigation of the Charge Compensation Mechanism on the Electrochemically Li-Ion Deintercalated $Li_{1-x}Co_{1/3}Ni_{1/3}Mn_{1/3}O_2$ Electrode System by Combination of Soft and Hard X-Ray Absorption Spectroscopy. *J. Am. Chem. Soc.* **2005**, 127, 17479−17487.

(90) Lin, F.; Markus, I. M.; Nordlund, D.; Weng, T.-C.; Asta, M. D.; Xin, H. L.; Doeff, M. M. Surface Reconstruction and Chemical Evolution of Stoichiometric Layered Cathode Materials for Lithium-Ion Batteries. *Nat. Commun.* **2014**, 5, 3529.

(91) Lin, F.; Nordlund, D.; Weng, T.-C.; Zhu, Y.; Ban, C.; Richards, R. M.; Xin, H. L. Phase Evolution for Conversion Reaction Electrodes in Lithium-Ion Batteries. *Nat. Commun.* **2014**, 5, 3358.

(92) Liu, Q.; He, H.; Li, Z. F.; Liu, Y.; Ren, Y.; Lu, W.; Lu, J.; Stach, E. A.; Xie, J. Rate-Dependent, Li-Ion Insertion/Deinsertion Behavior of $LiFePO_4$ Cathodes in Commercial 18650 $LiFePO_4$ Cells. *ACS Appl. Mater. Interfaces* **2014**, 6, 3282−3289.

(93) Moriya, M.; Miyahara, M.; Hokazono, M.; Sasaki, H.; Nemoto, A.; Katayama, S.; Akimoto, Y.; Hirano, S.-i.; Ren, Y. High-Energy X-Ray Powder Diffraction and Atomic-Pair Distribution-Function Studies of Charged/Discharged Structures in Carbon-Hybridized Li_2MnSiO_4 Nanoparticles as a Cathode Material for Lithium-Ion Batteries. *J. Power Sources* **2014**, 263, 7−12.

(94) Lin, C.-K.; Ren, Y.; Amine, K.; Qin, Y.; Chen, Z. In Situ High-Energy X-Ray Diffraction to Study Overcharge Abuse of 18650-Size Lithium-Ion Battery. *J. Power Sources* **2013**, 230, 32−37.

(95) Doeff, M. M.; Chen, G.; Cabana, J.; Richardson, T. J.; Mehta, A.; Shirpour, M.; Duncan, H.; Kim, C.; Kam, K. C.; Conry, T. Characterization of Electrode Materials for Lithium Ion and Sodium Ion Batteries Using Synchrotron Radiation Techniques. *J. Visualized Exp.* **2013**, e50594.

(96) Thurston, T. R.; Jisrawi, N. M.; Mukerjee, S.; Yang, X. Q.; McBreen, J.; Daroux, M. L.; Xing, X. K. Synchrotron X-Ray Diffraction Studies of the Structural Properties of Electrode Materials in Operating Battery Cells. *Appl. Phys. Lett.* **1996**, 69, 194.

(97) Mukerjee, S.; Thurston, T. R.; Jisrawi, N. M.; Yang, X. Q.; McBreen, J.; Daroux, M. L.; XIng, X. K. Structural Evolution of $Li_xMn_2O_4$ in Lithium-Ion Battery Cells Measured in Situ Using Synchrotron X-Ray Diffraction Techniques. *J. Electrochem. Soc.* **1998**, 145, 466−472.

(98) Yang, X. Q.; Sun, X.; McBreen, J. New Phases and Phase Transitions Observed in $Li_{1-x}CoO_2$ During Charge: In Situ Synchrotron X-Ray Diffraction Studies. *Electrochem. Commun.* **2000**, 2, 100−103.

(99) Sun, X.; Yang, X. Q.; Balasubramanian, M.; McBreen, J.; Xia, Y.; Sakai, T. In Situ Investigation of Phase Transitions of $Li_{1+y}Mn_2O_4$ Spinel During Li-Ion Extraction and Insertion. *J. Electrochem. Soc.* **2002**, 149, A842.

(100) Nikolowski, K.; Baehtz, C.; Bramnik, N. N.; Ehrenberg, H. A Swagelok-Typein Situcell for Battery Investigations Using Synchrotron Radiation. *J. Appl. Crystallogr.* **2005**, 38, 851−853.

(101) Baehtz, C.; Buhrmester, T.; Bramnik, N. N.; Nikolowski, K.; Ehrenberg, H. Design and Performance of an Electrochemical in-Situ Cell for High Resolution Full-Pattern X-Ray Powder Diffraction. *Solid State Ionics* **2005**, 176, 1647−1652.

(102) Chang, H.-H.; Chang, C.-C.; Wu, H.-C.; Yang, M.-H.; Sheu, H.-S.; Wu, N.-L. Study on Dynamics of Structural Transformation During Charge/Discharge of $LiFePO_4$ Cathode. *Electrochem. Commun.* **2008**, 10, 335−339.

(103) Kao, Y.-H.; Tang, M.; Meethong, N.; Bai, J.; Carter, W. C.; Chiang, Y.-M. Overpotential-Dependent Phase Transformation Pathways in Lithium Iron Phosphate Battery Electrodes. *Chem. Mater.* **2010**, 22, 5845−5855.

(104) Hirayama, M.; Ido, H.; Kim, K. S.; Cho, W.; Tamura, K.; Mizuki, J.; Kanno, R. Dynamic Structural Changes at $LiMn_2O_4/$ Electrolyte Interface During Lithium Battery Reaction. *J. Am. Chem. Soc.* **2010**, 132, 15268−15276.

(105) Leriche, J. B.; Hamelet, S.; Shu, J.; Morcrette, M.; Masquelier, C.; Ouvrard, G.; Zerrouki, M.; Soudan, P.; Belin, S.; Elkaïm, E.; et al. An Electrochemical Cell for Operando Study of Lithium Batteries Using Synchrotron Radiation. *J. Electrochem. Soc.* **2010**, 157, A606.

(106) Wang, X.-J.; Jaye, C.; Nam, K.-W.; Zhang, B.; Chen, H.-Y.; Bai, J.; Li, H.; Huang, X.; Fischer, D. A.; Yang, X.-Q. Investigation of the Structural Changes in $Li_{1-x}FePO_4$ Upon Charging by Synchrotron Radiation Techniques. *J. Mater. Chem.* **2011**, 21, 11406.

(107) Xu, B.; Fell, C. R.; Chi, M.; Meng, Y. S. Identifying Surface Structural Changes in Layered Li-Excess Nickel Manganese Oxides in High Voltage Lithium Ion Batteries: A Joint Experimental and Theoretical Study. *Energy Environ. Sci.* **2011**, 4, 2223.

(108) Omenya, F.; Chernova, N. A.; Zhang, R.; Fang, J.; Huang, Y.; Cohen, D.; Dobrzynski, N.; Senanayake, S.; Xu, W.; Whittingham, M. S. Why Substitution Enhances the Reactivity of $LiFePO_4$. *Chem. Mater.* **2013**, 25, 85−89.

(109) Xiao, J.; Yu, X.; Zheng, J.; Zhou, Y.; Gao, F.; Chen, X.; Bai, J.; Yang, X.-Q.; Zhang, J.-G. Interplay between Two-Phase and Solid Solution Reactions in High Voltage Spinel Cathode Material for Lithium Ion Batteries. *J. Power Sources* **2013**, 242, 736−741.

(110) Wen, B.; Chernova, N. A.; Zhang, R.; Wang, Q.; Omenya, F.; Fang, J.; Whittingham, M. S. Layered Molybdenum (Oxy) Pyrophosphate as Cathode for Lithium-Ion Batteries. *Chem. Mater.* **2013**, 25, 3513−3521.

(111) Guo, B.; Yu, X.; Sun, X.-G.; Chi, M.; Qiao, Z.-A.; Liu, J.; Hu, Y.-S.; Yang, X.-Q.; Goodenough, J. B.; Dai, S. A Long-Life Lithium-Ion Battery with a Highly Porous Tinb2o7 Anode for Large-Scale Electrical Energy Storage. *Energy Environ. Sci.* **2014**, 7, 2220.

(112) Roberts, M. R.; Madsen, A.; Nicklin, C.; Rawle, J.; Palmer, M. G.; Owen, J. R.; Hector, A. L. Direct Observation of Active Material Concentration Gradients and Crystallinity Breakdown in $LiFePO_4$ Electrodes During Charge/Discharge Cycling of Lithium Batteries. *J. Phys. Chem. C* **2014**, 118, 6548−6557.

(113) Liu, H.; Strobridge, F. C.; Borkiewicz, O. J.; Wiaderek, K. M.; Chapman, K. W.; Chupas, P. J.; Grey, C. P. Batteries. Capturing Metastable Structures During High-Rate Cycling of $LiFePO_4$ Nanoparticle Electrodes. *Science* **2014**, 344, 1252817.

(114) Sasaki, T.; Villevieille, C.; Takeuchi, Y.; Novák, P. Understanding Inhomogeneous Reactions in Li-Ion Batteries: Operando

Synchrotron X-Ray Diffraction on Two-Layer Electrodes. *Adv. Sci.* **2015**, *2*, 1500083.

(115) Zhang, X.; van Hulzen, M.; Singh, D. P.; Brownrigg, A.; Wright, J. P.; van Dijk, N. H.; Wagemaker, M. Direct View on the Phase Evolution in Individual LiFePO4 Nanoparticles During Li-Ion Battery Cycling. *Nat. Commun.* **2015**, *6*, 8333.

(116) Conry, T. E.; Mehta, A.; Cabana, J.; Doeff, M. M. Structural Underpinnings of the Enhanced Cycling Stability Upon Al-Substitution in $LiNi_{0.45}Mn_{0.45}Co_{0.1-y}Al_yO_2$ positive Electrode Materials for Li-Ion Batteries. *Chem. Mater.* **2012**, *24*, 3307−3317.

(117) Lowe, M. A.; Gao, J.; Abruña, H. D. In Operando X-Ray Studies of the Conversion Reaction in Mn3o4 lithium Battery Anodes. *J. Mater. Chem. A* **2013**, *1*, 2094−2103.

(118) Hua, X.; Robert, R.; Du, L.-S.; Wiaderek, K. M.; Leskes, M.; Chapman, K. W.; Chupas, P. J.; Grey, C. P. Comprehensive Study of the CuF_2 conversion Reaction Mechanism in a Lithium Ion Battery. *J. Phys. Chem. C* **2014**, *118*, 15169−15184.

(119) Parzych, G.; Mikhailova, D.; Oswald, S.; Eckert, J. R.; Ehrenberg, H. Study of the Conversion Reaction Mechanism for Copper Borate as Electrode Material in Lithium-Ion Batteries. *J. Electrochem. Soc.* **2011**, *158*, A898.

(120) Wang, X. L.; Chen, H.; Bai, J.; Han, W. Q. Cosn5 Phase: Crystal Structure Resolving and Stable High Capacity as Anodes for Li Ion Batteries. *J. Phys. Chem. Lett.* **2012**, *3*, 1488−1492.

(121) Misra, S.; Liu, N.; Nelson, J.; Hong, S. S.; Cui, Y.; Toney, M. F. In Situ X-Ray Diffraction Studies of (De)Lithiation Mechanism in Silicon Nanowire Anodes. *ACS Nano* **2012**, *6*, 5465−5473.

(122) Wang, F.; Wu, L.; Key, B.; Yang, X.-Q.; Grey, C. P.; Zhu, Y.; Graetz, J. Electrochemical Reaction of Lithium with Nanostructured Silicon Anodes: A Study by in-Situ Synchrotron X-Ray Diffraction and Electron Energy-Loss Spectroscopy. *Adv. Energy Mater.* **2013**, *3*, 1324−1331.

(123) Darwiche, A.; Marino, C.; Sougrati, M. T.; Fraisse, B.; Stievano, L.; Monconduit, L. Better Cycling Performances of Bulk Sb in Na-Ion Batteries Compared to Li-Ion Systems: An Unexpected Electrochemical Mechanism. *J. Am. Chem. Soc.* **2012**, *134*, 20805−20811.

(124) Cui, Y.; Abouimrane, A.; Lu, J.; Bolin, T.; Ren, Y.; Weng, W.; Sun, C.; Maroni, V. A.; Heald, S. M.; Amine, K. (De)Lithiation Mechanism of Li/SeS_x (x = 0−7) Batteries Determined by in Situ Synchrotron X-Ray Diffraction and X-Ray Absorption Spectroscopy. *J. Am. Chem. Soc.* **2013**, *135*, 8047−8056.

(125) Padhi, A. K.; Nanjundaswamy, K. S.; Goodenough, J. B. Phospho-Olivines as Positive-Electrode Materials for Rechargeable Lithium Batteries. *J. Electrochem. Soc.* **1997**, *144*, 1188−1194.

(126) Andersson, A. S.; Kalska, B.; Haggstrom, L.; Thomas, J. O. Lithium Extraction/Insertion in LiFePO4: An X-Ray Diffraction and Mossbauer Spectroscopy Study. *Solid State Ionics* **2000**, *130*, 41−52.

(127) Delmas, C.; Maccario, M.; Croguennec, L.; Le Cras, F.; Weill, F. Lithium Deintercalation in $LiFePO_4$ Nanoparticles Via a Domino-Cascade Model. *Nat. Mater.* **2008**, *7*, 665−671.

(128) Dreyer, W.; Jamnik, J.; Guhlke, C.; Huth, R.; Moskon, J.; Gaberscek, M. The Thermodynamic Origin of Hysteresis in Insertion Batteries. *Nat. Mater.* **2010**, *9*, 448−453.

(129) Li, Y.; El Gabaly, F.; Ferguson, T. R.; Smith, R. B.; Bartelt, N. C.; Sugar, J. D.; Fenton, K. R.; Cogswell, D. A.; Kilcoyne, A. L.; Tyliszczak, T.; et al. Current-Induced Transition from Particle-by-Particle to Concurrent Intercalation in Phase-Separating Battery Electrodes. *Nat. Mater.* **2014**, *13*, 1149−1156.

(130) Brunetti, G.; Robert, D.; Bayle-Guillemaud, P.; Rouvière, J. L.; Rauch, E. F.; Martin, J. F.; Colin, J. F.; Bertin, F.; Cayron, C. Confirmation of the Domino-Cascade Model by LiFePO4/FePO4 precession Electron Diffraction. *Chem. Mater.* **2011**, *23*, 4515−4524.

(131) Malik, R.; Zhou, F.; Ceder, G. Kinetics of Non-Equilibrium Lithium Incorporation in LiFePO4. *Nat. Mater.* **2011**, *10*, 587−590.

(132) Orikasa, Y.; Maeda, T.; Koyama, Y.; Murayama, H.; Fukuda, K.; Tanida, H.; Arai, H.; Matsubara, E.; Uchimoto, Y.; Ogumi, Z. Direct Observation of a Metastable Crystal Phase of Li_xFePO_4 under Electrochemical Phase Transition. *J. Am. Chem. Soc.* **2013**, *135*, 5497−5500.

(133) Kang, H. C.; Yan, H. F.; Winarski, R. P.; Holt, M. V.; Maser, J.; Liu, C. A.; Conley, R.; Vogt, S.; Macrander, A. T.; Stephenson, G. B. Focusing of Hard X-Rays to 16 Nanometers with a Multilayer Laue Lens. *Appl. Phys. Lett.* **2008**, *92*, 221114.

(134) Yamauchi, K.; Mimura, H.; Kimura, T.; Yumoto, H.; Handa, S.; Matsuyama, S.; Arima, K.; Sano, Y.; Yamamura, K.; Inagaki, K.; et al. Single-Nanometer Focusing of Hard X-Rays by Kirkpatrick-Baez Mirrors. *J. Phys.: Condens. Matter* **2011**, *23*, 394206.

(135) Riekel, C. New Avenues in X-Ray Microbeam Experiments. *Rep. Prog. Phys.* **2000**, *63*, 233−262.

(136) Cai, Z.; Lai, B.; Yun, W.; Ilinski, P.; Legnini, D.; Maser, J.; Rodrigues, W. A Hard X-Ray Scanning Microprobe for Fluorescence Imaging and Microdiffraction at the Advanced Photon Source. *X-Ray Microscopy: Proceedings of the VI International Conference. AIP Conference Proceedings* **2000**, *507*, 472−477.

(137) Ice, G. E.; Larson, B. C.; Yang, W.; Budai, J. D.; Tischler, J. Z.; Pang, J. W. L.; Barabash, R. I.; Liu, W. Polychromatic X-Ray Microdiffraction Studies of Mesoscale Structure and Dynamics. *J. Synchrotron Radiat.* **2005**, *12*, 155−162.

(138) Ulrich, O.; Biquard, X.; Bleuet, P.; Geaymond, O.; Gergaud, P.; Micha, J. S.; Robach, O.; Rieutord, F. A New White Beam X-Ray Microdiffraction Setup on the Bm32 Beamline at the European Synchrotron Radiation Facility. *Rev. Sci. Instrum.* **2011**, *82*, 033908.

(139) Tamura, N.; Kunz, M.; Chen, K.; Celestre, R. S.; MacDowell, A. A.; Warwick, T. A Superbend X-Ray Microdiffraction Beamline at the Advanced Light Source. *Mater. Sci. Eng., A* **2009**, *524*, 28−32.

(140) Chen, K.; Tamura, N.; Valek, B. C.; Tu, K. N. Plastic Deformation in Al (Cu) Interconnects Stressed by Electromigration and Studied by Synchrotron Polychromatic X-Ray Microdiffraction. *J. Appl. Phys.* **2008**, *104*, 013503.

(141) Chen, K.; Kunz, M.; Tamura, N.; Wenk, H. R. Residual Stress Preserved in Quartz from the San Andreas Fault Observatory at Depth. *Geology* **2015**, *43*, 219−222.

(142) Mun, B. S.; Yoon, J.; Mo, S. K.; Chen, K.; Tamura, N.; Dejoie, C.; Kunz, M.; Liu, Z.; Park, C.; Moon, K.; et al. Role of Joule Heating Effect and Bulk-Surface Phases in Voltage-Driven Metal-Insulator Transition in VO_2 Crystal. *Appl. Phys. Lett.* **2013**, *103*, 061902.

(143) Robert, R.; Zeng, D. L.; Lanzirotti, A.; Adamson, P.; Clarke, S. J.; Grey, C. P. Scanning X-Ray Fluorescence Imaging Study of Lithium Insertion into Copper Based Oxysulfides for Li-Ion Batteries. *Chem. Mater.* **2012**, *24*, 2684−2691.

(144) Liu, J.; Kunz, M.; Chen, K.; Tamura, N.; Richardson, T. J. Visualization of Charge Distribution in a Lithium Battery Electrode. *J. Phys. Chem. Lett.* **2010**, *1*, 2120−2123.

(145) Murugan, R.; Thangadurai, V.; Weppner, W. Fast Lithium Ion Conduction in Garnet-Type $Li_7La_3Zr_2O_{12}$. *Angew. Chem., Int. Ed.* **2007**, *46*, 7778−7781.

(146) Thangadurai, V.; Kaack, H.; Weppner, W. J. F. Novel Fast Lithium Ion Conduction in Garnet-Type $Li_5La_3M_2O_{12}$ (M = Nb, Ta). *J. Am. Ceram. Soc.* **2003**, *86*, 437−440.

(147) Thangadurai, V.; Weppner, W. $Li_6AlA_2Ta_2O_{12}$ (A = Sr, Ba): Novel Garnet-Like Oxides for Fast Lithium Ion Conduction. *Adv. Funct. Mater.* **2005**, *15*, 107−112.

(148) Thangadurai, V.; Weppner, W. $Li_6AlA_2Ta_2O_{12}$ (a = Ca, Sr, Ba): A New Class of Fast Lithium Ion Conductors with Garnet-Like Structure. *J. Am. Ceram. Soc.* **2005**, *88*, 411−418.

(149) Thangadurai, V.; Adams, S.; Weppner, W. Crystal Structure Revision and Identification of Li^+-Ion Migration Pathways in the Garnet-Like $Li_5La_3M_2O_{12}$ (M = Nb, Ta) Oxides. *Chem. Mater.* **2004**, *16*, 2998−3006.

(150) Gellert, M.; Gries, K. I.; Yada, C.; Rosciano, F.; Volz, K.; Roling, B. Grain Boundaries in a Lithium Aluminum Titanium Phosphate-Type Fast Lithium Ion Conducting Glass Ceramic: Microstructure and Nonlinear Ion Transport Properties. *J. Phys. Chem. C* **2012**, *116*, 22675−22678.

(151) Ma, C.; Chen, K.; Liang, C. D.; Nan, C. W.; Ishikawa, R.; More, K.; Chi, M. F. Atomic-Scale Origin of the Large Grain-Boundary Resistance in Perovskite Li-Ion-Conducting Solid Electrolytes. *Energy Environ. Sci.* **2014**, *7*, 1638−1642.

(152) Kunz, M.; Tamura, N.; Chen, K.; MacDowell, A. A.; Celestre, R. S.; Church, M. M.; Fakra, S.; Domning, E. E.; Glossinger, J. M.; Kirschman, J. L.; et al. A Dedicated Superbend X-Ray Microdiffraction Beamline for Materials, Geo-, and Environmental Sciences at the Advanced Light Source. *Rev. Sci. Instrum.* 2009, 80, 035108.

(153) Cheng, L.; Chen, W.; Kunz, M.; Persson, K.; Tamura, N.; Chen, G. Y.; Doeff, M. Effect of Surface Microstructure on Electrochemical Performance of Garnet Solid Electrolytes. *ACS Appl. Mater. Interfaces* 2015, 7, 2073−2081.

(154) Park, J. S.; Cheng, L.; Zorba, V.; Mehta, A.; Cabana, J.; Chen, G.; Doeff, M. M.; Richardson, T. J.; Park, J. H.; Son, J.-W.; et al. Effects of Crystallinity and Impurities on the Electrical Conductivity of Li-La-Zr-O Thin Films. *Thin Solid Films* 2015, 576, 55−60.

(155) Takeuchi, E. S.; Marschilok, A. C.; Takeuchi, K. J.; Ignatov, A.; Zhong, Z.; Croft, M. Energy Dispersive X-Ray Diffraction of Lithium−Silver Vanadium Phosphorous Oxide Cells: In Situ Cathode Depth Profiling of an Electrochemical Reduction−Displacement Reaction. *Energy Environ. Sci.* 2013, 6, 1465−1470.

(156) Kirshenbaum, K. C.; Bock, D. C.; Zhong, Z.; Marschilok, A. C.; Takeuchi, K. J.; Takeuchi, E. S. Electrochemical Reduction of Ag$_2$VP$_2$O$_8$ Composite Electrodes Visualized Via in Situ Energy Dispersive X-Ray Diffraction (Edxrd): Unexpected Conductive Additive Effects. *J. Mater. Chem. A* 2015, 3, 18027−18035.

(157) Kirshenbaum, K.; Bock, D. C.; Lee, C.-Y.; Zhong, Z.; Takeuchi, K. J.; Marschilok, A. C.; Takeuchi, E. S. In Situ Visualization of Li/Ag$_2$VP$_2$O$_8$ Batteries Revealing Rate-Dependent Discharge Mechanism. *Science* 2015, 347, 149−154.

(158) Liang, G.; Croft, M. C.; Zhong, Z. Energy Dispersive X-Ray Diffraction Profiling of Prototype Limn2o4-Based Coin Cells. *J. Electrochem. Soc.* 2013, 160, A1299−A1303.

(159) Paxton, W. A.; Zhong, Z.; Tsakalakos, T. Tracking Inhomogeneity in High-Capacity Lithium Iron Phosphate Batteries. *J. Power Sources* 2015, 275, 429−434.

(160) Murayama, H.; Kitada, K.; Fukuda, K.; Mitsui, A.; Ohara, K.; Arai, H.; Uchimoto, Y.; Ogumi, Z.; Matsubara, E. Spectroscopic X-Ray Diffraction for Microfocus Inspection of Li-Ion Batteries. *J. Phys. Chem. C* 2014, 118, 20750−20755.

(161) Kitada, K.; Murayama, H.; Fukuda, K.; Arai, H.; Uchimoto, Y.; Ogumi, Z.; Matsubara, E. Factors Determining the Packing-Limitation of Active Materials in the Composite Electrode of Lithium-Ion Batteries. *J. Power Sources* 2016, 301, 11−17.

(162) Takahashi, I.; Fukuda, K.; Kawaguchi, T.; Komatsu, H.; Oishi, M.; Murayama, H.; Hatano, M.; Terai, T.; Arai, H.; Uchimoto, Y.; et al. Quantitative Analysis of Transition-Metal Migration Induced Electrochemically in Lithium-Rich Layered Oxide Cathode and Its Contribution to Properties at High and Low Temperatures. *J. Phys. Chem. C* 2016, 120, 27109−27116.

(163) Wang, X.-J.; Chen, H.-Y.; Yu, X.; Wu, L.; Nam, K.-W.; Bai, J.; Li, H.; Huang, X.; Yang, X.-Q. A New in Situ Synchrotron X-Ray Diffraction Technique to Study the Chemical Delithiation of LiFePO$_4$. *Chem. Commun.* 2011, 47, 7170−7172.

(164) Jensen, K. M.; Tyrsted, C.; Bremholm, M.; Iversen, B. B. In Situ Studies of Solvothermal Synthesis of Energy Materials. *ChemSusChem* 2014, 7, 1594−1611.

(165) Chen, J.; Bai, J.; Chen, H.; Graetz, J. In Situ Hydrothermal Synthesis of LiFePO4 Studied by Synchrotron X-Ray Diffraction. *J. Phys. Chem. Lett.* 2011, 2, 1874−1878.

(166) Bai, J.; Hong, J.; Chen, H.; Graetz, J.; Wang, F. Solvothermal Synthesis of LiMn$_{1−x}$Fe$_x$PO$_4$ Cathode Materials: A Study of Reaction Mechanisms by Time-Resolved in Situ Synchrotron X-Ray Diffraction. *J. Phys. Chem. C* 2015, 119, 2266−2276.

(167) Yoon, W.-S.; Balasubramanian, M.; Yang, X.-Q.; McBreen, J.; Hanson, J. Time-Resolved Xrd Study on the Thermal Decomposition of Li$_{1−x}$Ni$_{0.8}$Co$_{0.15}$Al$_{0.05}$O$_2$ Cathode Materials for Li-Ion Batteries. *Electrochem. Solid-State Lett.* 2005, 8, A83−A86.

(168) Guilmard, M.; Croguennec, L.; Denux, D.; Delmas, C. Thermal Stability of Lithium Nickel Oxide Derivatives. Part I: Li$_x$Ni$_{1.02}$O$_2$ and Li$_x$Ni$_{0.89}$Al$_{0.16}$O$_2$ (x = 0.50 and 0.30). *Chem. Mater.* 2003, 15, 4476−4483.

(169) Guilmard, M.; Croguennec, L.; Delmas, C. Thermal Stability of Lithium Nickel Oxide Derivatives. Part Ii: Li$_x$Ni$_{0.70}$Co$_{0.15}$Al$_{0.15}$O$_2$ and Li$_x$Ni$_{0.90}$Mn$_{0.10}$O$_2$ (x = 0.50 and 0.30). Comparison with Li$_x$Ni$_{1.02}$O$_2$ and Li$_x$Ni$_{0.89}$Al$_{0.16}$O$_2$. *Chem. Mater.* 2003, 15, 4484−4493.

(170) Yabuuchi, N.; Kim, Y.-T.; Li, H. H.; Shao-Horn, Y. Thermal Instability of Cycled Li$_x$Ni$_{0.5}$Mn$_{0.5}$O$_2$ Electrodes: An in Situ Synchrotron X-Ray Powder Diffraction Study. *Chem. Mater.* 2008, 20, 4936−4951.

(171) Chen, Z.; Qin, Y.; Ren, Y.; Lu, W.; Orendorff, C.; Roth, E. P.; Amine, K. Multi-Scale Study of Thermal Stability of Lithiated Graphite. *Energy Environ. Sci.* 2011, 4, 4023−4030.

(172) Boesenberg, U.; Meirer, F.; Liu, Y. J.; Shukla, A. K.; Dell'Anna, R.; Tyliszczak, T.; Chen, G. Y.; Andrews, J. C.; Richardson, T. J.; Kostecki, R.; et al. Mesoscale Phase Distribution in Single Particles of LiFePO$_4$ Following Lithium Deintercalation. *Chem. Mater.* 2013, 25, 1664−1672.

(173) Lin, C.-k.; Piao, Y.; Kan, Y.; Bareño, J.; Bloom, I.; Ren, Y.; Amine, K.; Chen, Z. Probing Thermally Induced Decomposition of Delithiated Li$_{1.2−x}$Ni$_{0.15}$Mn$_{0.55}$Co$_{0.1}$O$_2$ by in Situ High-Energy X-Ray Diffraction. *ACS Appl. Mater. Interfaces* 2014, 6, 12692−12697.

(174) Piao, Y.; Lin, C.-k.; Qin, Y.; Zhou, D.; Ren, Y.; Bloom, I.; Wei, Y.; Chen, G.; Chen, Z. An in-Situ, High-Energy X-Ray Diffraction Study of the Thermal Stability of Delithiated LiVPO$_4$F. *J. Power Sources* 2015, 273, 1250−1255.

(175) Yu, D. Y. W.; Yanagida, K.; Nakamura, H. Surface Modification of Li-Excess Mn-Based Cathode Materials. *J. Electrochem. Soc.* 2010, 157, A1177.

(176) Nam, K. W.; Bak, S. M.; Hu, E.; Yu, X.; Zhou, Y.; Wang, X.; Wu, L.; Zhu, Y.; Chung, K. Y.; Yang, X. Q. Combining in Situ Synchrotron X-Ray Diffraction and Absorption Techniques with Transmission Electron Microscopy to Study the Origin of Thermal Instability in Overcharged Cathode Materials for Lithium-Ion Batteries. *Adv. Funct. Mater.* 2013, 23, 1047−1063.

(177) Bak, S.-M.; Hu, E.; Zhou, Y.; Yu, X.; Senanayake, S. D.; Cho, S.-J.; Kim, K.-B.; Chung, K. Y.; Yang, X.-Q.; Nam, K.-W. Structural Changes and Thermal Stability of Charged LiNi$_x$Mn$_y$Co$_z$O$_2$ Cathode Materials Studied by Combined in Situ Time-Resolved Xrd and Mass Spectroscopy. *ACS Appl. Mater. Interfaces* 2014, 6, 22594−22601.

(178) Hu, E.; Bak, S.-M.; Liu, J.; Yu, X.; Zhou, Y.; Ehrlich, S. N.; Yang, X.-Q.; Nam, K.-W. Oxygen-Release-Related Thermal Stability and Decomposition Pathways of Li$_x$Ni$_{0.5}$Mn$_{1.5}$O$_4$ Cathode Materials. *Chem. Mater.* 2014, 26, 1108−1118.

(179) Bak, S.-M.; Nam, K.-W.; Chang, W.; Yu, X.; Hu, E.; Hwang, S.; Stach, E. A.; Kim, K.-B.; Chung, K. Y.; Yang, X.-Q. Correlating Structural Changes and Gas Evolution During the Thermal Decomposition of Charged Li$_x$Ni$_{0.8}$Co$_{0.15}$Al$_{0.05}$O$_2$ Cathode Materials. *Chem. Mater.* 2013, 25, 337−351.

(180) Noh, H.-Y.; Youn, S.; Yoon, C. S.; Sun, Y.-K. Comparison of the Structural and Electrochemical Properties of Layered Li-[Ni$_x$Co$_y$Mn$_z$]O$_2$ (X = 1/3, 0.5, 0.6, 0.7, 0.8 and 0.85) Cathode Material for Lithium-Ion Batteries. *J. Power Sources* 2013, 233, 121−130.

(181) Han, J. T.; Zhu, J. L.; Li, Y. T.; Yu, X. H.; Wang, S. M.; Wu, G.; Xie, H.; Vogel, S. C.; Izumi, F.; Momma, K.; et al. Experimental Visualization of Lithium Conduction Pathways in Garnet-Type Li$_7$La$_3$Zr$_2$O$_{12}$. *Chem. Commun.* 2012, 48, 9840−9842.

(182) Rettenwander, D.; Redhammer, G.; Preishuber-Pflugl, F.; Cheng, L.; Miara, L.; Wagner, R.; Welzl, A.; Suard, E.; Doeff, M. M.; Wilkening, M.; et al. Structural and Electrochemical Consequences of Al and Ga Cosubstitution in Li$_7$La$_3$Zr$_2$O$_{12}$ Solid Electrolytes. *Chem. Mater.* 2016, 28, 2384−2392.

(183) Liu, H. D.; Fell, C. R.; An, K.; Cai, L.; Meng, Y. S. In-Situ Neutron Diffraction Study of the xLi$_2$MnO$_3$•(1-x)LiMO$_2$ (X = 0, 0.5; M = Ni, Mn, Co) Layered Oxide Compounds During Electrochemical Cycling. *J. Power Sources* 2013, 240, 772−778.

(184) Taminato, S.; Yonemura, M.; Shiotani, S.; Kamiyama, T.; Torii, S.; Nagao, M.; Ishikawa, Y.; Mori, K.; Fukunaga, T.; Onodera, Y.; et al. Real-Time Observations of Lithium Battery Reactions-Operando

Neutron Diffraction Analysis During Practical Operation. *Sci. Rep.* **2016**, *6*, 28843.

(185) Biendicho, J. J.; Roberts, M.; Offer, C.; Noreus, D.; Widenkvist, E.; Smith, R. I.; Svensson, G.; Edstrom, K.; Norberg, S. T.; Eriksson, S. G.; et al. New in-Situ Neutron Diffraction Cell for Electrode Materials. *J. Power Sources* **2014**, *248*, 900−904.

(186) Senyshyn, A.; Muhlbauer, M. J.; Nikolowski, K.; Pirling, T.; Ehrenberg, H. "In-Operando" Neutron Scattering Studies on Li-Ion Batteries. *J. Power Sources* **2012**, *203*, 126−129.

(187) Sharma, N.; Peterson, V. K.; Elcombe, M. M.; Avdeev, M.; Studer, A. J.; Blagojevic, N.; Yusoff, R.; Kamarulzaman, N. Structural Changes in a Commercial Lithium-Ion Battery During Electrochemical Cycling: An in Situ Neutron Diffraction Study. *J. Power Sources* **2010**, *195*, 8258−8266.

(188) Rao, R. P.; Gu, W. Y.; Sharma, N.; Peterson, V. K.; Avdeev, M.; Adams, S. In Situ Neutron Diffraction Monitoring of $Li_7La_3Zr_2O_{12}$ Formation: Toward a Rational Synthesis of Garnet Solid Electrolytes. *Chem. Mater.* **2015**, *27*, 2903−2910.

(189) Ingham, B. X-Ray Scattering Characterisation of Nanoparticles. *Crystallogr. Rev.* **2015**, *21*, 229−303.

(190) Talaie, E.; Bonnick, P.; Sun, X.; Pang, Q.; Liang, X.; Nazar, L. F. Methods and Protocols for Electrochemical Energy Storage Materials Research. *Chem. Mater.* **2017**, *29*, 90−105.

(191) Abeykoon, M.; Malliakas, C. D.; Juhas, P.; Bozin, E. S.; Kanatzidis, M. G.; Billinge, S. J. L. Quantitative Nanostructure Characterization Using Atomic Pair Distribution Functions Obtained from Laboratory Electron Microscopes. *Z. Kristallogr.* **2012**, *227*, 248−256.

(192) Welberry, T. R.; Weber, T. One Hundred Years of Diffuse Scattering. *Crystallogr. Rev.* **2016**, *22*, 2−78.

(193) Billinge, S. J.; Kanatzidis, M. G. Beyond Crystallography: The Study of Disorder, Nanocrystallinity and Crystallographically Challenged Materials with Pair Distribution Functions. *Chem. Commun.* **2004**, *0*, 749−760.

(194) Egami, T.; Billinge, S. *Underneath the Bragg Peaks*, 2nd ed.; Pergamon, 2012; Vol. *16*.

(195) Petkov, V.; Trikalitis, P. N.; Bozin, E. S.; Billinge, S. J. L.; Vogt, T.; Kanatzidis, M. G. Structure of $V_2O_5.Nh_2O$ Xerogel Solved by the Atomic Pair Distribution Function Technique. *J. Am. Chem. Soc.* **2002**, *124*, 10157−10162.

(196) Breger, J.; Dupre, N.; Chupas, P. J.; Lee, P. L.; Proffen, T.; Parise, J. B.; Grey, C. P. Short- and Long-Range Order in the Positive Electrode Material, $Li(Ni,Mn)_{0.5}O_2$: A Joint X-Ray and Neutron Diffraction, Pair Distribution Function Analysis and Nmr Study. *J. Am. Chem. Soc.* **2005**, *127*, 7529−7537.

(197) Hu, Y. Y.; Liu, Z.; Nam, K. W.; Borkiewicz, O. J.; Cheng, J.; Hua, X.; Dunstan, M. T.; Yu, X.; Wiaderek, K. M.; Du, L. S.; et al. Origin of Additional Capacities in Metal Oxide Lithium-Ion Battery Electrodes. *Nat. Mater.* **2013**, *12*, 1130−1136.

(198) Chapman, K. W. Emerging Operando and X-Ray Pair Distribution Function Methods for Energy Materials Development. *MRS Bull.* **2016**, *41*, 231−240.

(199) Wiaderek, K. M.; Borkiewicz, O. J.; Castillo-Martinez, E.; Robert, R.; Pereira, N.; Amatucci, G. G.; Grey, C. P.; Chupas, P. J.; Chapman, K. W. Comprehensive Insights into the Structural and Chemical Changes in Mixed-Anion Feof Electrodes by Using Operando Pdf and Nmr Spectroscopy. *J. Am. Chem. Soc.* **2013**, *135*, 4070−4078.

(200) Petkov, V.; Billinge, S. J. L.; Larson, P.; Mahanti, S. D.; Vogt, T.; Rangan, K. K.; Kanatzidis, M. G. Structure of Nanocrystalline Materials Using Atomic Pair Distribution Function Analysis: Study of $LiMoS_2$. *Phys. Rev. B: Condens. Matter Mater. Phys.* **2002**, *65*, 092105.

(201) Stratford, J. M.; Mayo, M.; Allan, P. K.; Pecher, O.; Borkiewicz, O. J.; Wiaderek, K. M.; Chapman, K. W.; Pickard, C. J.; Morris, A. J.; Grey, C. P. Investigating Sodium Storage Mechanisms in Tin Anodes: A Combined Pair Distribution Function Analysis, Density Functional Theory and Solid-State Nmr Approach. *J. Am. Chem. Soc.* **2017**, *139*, 7273−7286.

(202) Xiang, K.; Xing, W.; Ravnsbaek, D. B.; Hong, L.; Tang, M.; Li, Z.; Wiaderek, K. M.; Borkiewicz, O. J.; Chapman, K. W.; Chupas, P. J.; et al. Accommodating High Transformation Strains in Battery Electrodes Via the Formation of Nanoscale Intermediate Phases: Operando Investigation of Olivine $NaFePO_4$. *Nano Lett.* **2017**, *17*, 1696−1702.

(203) Bunker, G. *Introduction to XAFS: A Practical Guide to X-Ray Absorption Fine Structure Spectroscopy*; Cambridge University Press: Cambridge, United Kingdom, 2010.

(204) Koningsberger, D. C.; Prins, R. *X-Ray Absorption: Principles, Applications, Techniques of EXAFS, SEXAFS, and XANES*; John Wiley & Sons: New York, NY, 1988.

(205) Lee, P. A.; Citrin, P. H.; Eisenberger, P.; Kincaid, B. M. Extended X-Ray Absorption Fine Structure—Its Strengths and Limitations as a Structural Tool. *Rev. Mod. Phys.* **1981**, *53*, 769−806.

(206) Stern, E.; Heald, S. *Handbook on Synchrotron Radiation*; North Holland Publishing Company, 1983.

(207) Rehr, J. J.; Albers, R. C. Theoretical Approaches to X-Ray Absorption Fine Structure. *Rev. Mod. Phys.* **2000**, *72*, 621−654.

(208) Giorgetti, M. A Review on the Structural Studies of Batteries and Host Materials by X-Ray Absorption Spectroscopy. *ISRN Materials Science* **2013**, *2013*, 1−22.

(209) Harks, P. P. R. M. L.; Mulder, F. M.; Notten, P. H. L. In Situ Methods for Li-Ion Battery Research: A Review of Recent Developments. *J. Power Sources* **2015**, *288*, 92−105.

(210) de Groot, F.; Glatzel, P. The 1s X-Ray Absorption Pre-Edge Structures in Transition Metal Oxides. *J. Phys.: Condens. Matter* **2009**, *21*, 104207.

(211) Rehr, J. J.; Albers, R. Theoretical Approaches to X-Ray Absorption Fine Structure. *Rev. Mod. Phys.* **2000**, *72*, 621.

(212) Sharpe, L. R.; Heineman, W. R.; Elder, R. Exafs Spectroelectrochemistry. *Chem. Rev.* **1990**, *90*, 705−722.

(213) Lee, P.; Citrin, P.; Eisenberger, P. t.; Kincaid, B. Extended X-Ray Absorption Fine Structure—Its Strengths and Limitations as a Structural Tool. *Rev. Mod. Phys.* **1981**, *53*, 769.

(214) Wang, J.; Chen-Wiegart, Y.-C. K.; Wang, J. In Situ Chemical Mapping of a Lithium-Ion Battery Using Full-Field Hard X-Ray Spectroscopic Imaging. *Chem. Commun.* **2013**, *49*, 6480−6482.

(215) Yu, X.; Pan, H.; Zhou, Y.; Northrup, P.; Xiao, J.; Bak, S.; Liu, M.; Nam, K.-W.; Qu, D.; Liu, J.; et al. Direct Observation of the Redistribution of Sulfur and Polysufides in Li-S Batteries During the First Cycle by in Situ X-Ray Fluorescence Microscopy. *Adv. Energy Mater.* **2015**, *5*, 1500072.

(216) Lyu, Y.; Zhao, N.; Hu, E.; Xiao, R.; Yu, X.; Gu, L.; Yang, X.-Q.; Li, H. Probing Reversible Multielectron Transfer and Structure Evolution of $Li_{1.2}Cr_{0.4}Mn_{0.4}O_2$ Cathode Material for Li-Ion Batteries in a Voltage Range of 1.0−4.8 V. *Chem. Mater.* **2015**, *27*, 5238−5252.

(217) Deb, A.; Bergmann, U.; Cramer, S. P.; Cairns, E. J. In Situ X-Ray Absorption Spectroscopic Study of the $Li[Ni_{1/3}Co_{1/3}Mn_{1/3}]O_2$ Cathode Material. *J. Appl. Phys.* **2005**, *97*, 113523.

(218) Tsai, Y.; Hwang, B.; Ceder, G.; Sheu, H.; Liu, D.; Lee, J. In-Situ X-Ray Absorption Spectroscopic Study on Variation of Electronic Transitions and Local Structure of $LiNi_{1/3}Co_{1/3}Mn_{1/3}O_2$ Cathode Material During Electrochemical Cycling. *Chem. Mater.* **2005**, *17*, 3191−3199.

(219) Yu, X.; Lyu, Y.; Gu, L.; Wu, H.; Bak, S. M.; Zhou, Y.; Amine, K.; Ehrlich, S. N.; Li, H.; Nam, K. W.; et al. Understanding the Rate Capability of High-Energy-Density Li Rich Layered $Li_{1.2}Ni_{0.15}Co_{0.1}Mn_{0.55}O_2$ Cathode Materials. *Adv. Energy Mater.* **2014**, *4*, 1300950.

(220) Ito, A.; Sato, Y.; Sanada, T.; Hatano, M.; Horie, H.; Ohsawa, Y. In Situ X-Ray Absorption Spectroscopic Study of Li-Rich Layered Cathode Material $Li[Ni_{0.17}Li_{0.2}Co_{0.07}Mn_{0.56}]O_2$. *J. Power Sources* **2011**, *196*, 6828−6834.

(221) Taminato, S.; Hirayama, M.; Suzuki, K.; Kim, K.; Zheng, Y.; Tamura, K.; Mizuki, J. i.; Kanno, R. Mechanistic Studies on Lithium Intercalation in a Lithium-Rich Layered Material Using Li_2RuO_3 Epitaxial Film Electrodes and in Situ Surface X-Ray Analysis. *J. Mater. Chem. A* **2014**, *2*, 17875−17882.

(222) Rumble, C.; Conry, T. E.; Doeff, M.; Cairns, E. J.; Penner-Hahn, J. E.; Deb, A. Structural and Electrochemical Investigation of Li(Ni$_{0.4}$Co$_{0.15}$Al$_{0.05}$Mn$_{0.4}$)O$_2$ Cathode Material. *J. Electrochem. Soc.* **2010**, *157*, A1317.

(223) Chan, H.-W.; Duh, J.-G.; Lee, J.-F. Valence Change by in Situ Xas in Surface Modified LiMn$_2$O$_4$ for Li-Ion Battery. *Electrochem. Commun.* **2006**, *8*, 1731−1736.

(224) Arai, H.; Sato, K.; Orikasa, Y.; Murayama, H.; Takahashi, I.; Koyama, Y.; Uchimoto, Y.; Ogumi, Z. Phase Transition Kinetics of LiNi$_{0.5}$Mn$_{1.5}$O$_4$ Electrodes Studied by in Situ X-Ray Absorption near-Edge Structure and X-Ray Diffraction Analysis. *J. Mater. Chem. A* **2013**, *1*, 10442−10449.

(225) Hu, E.; Bak, S. M.; Liu, Y.; Liu, J.; Yu, X.; Zhou, Y. N.; Zhou, J.; Khalifah, P.; Ariyoshi, K.; Nam, K. W.; et al. Utilizing Environmental Friendly Iron as a Substitution Element in Spinel Structured Cathode Materials for Safer High Energy Lithium-Ion Batteries. *Adv. Energy Mater.* **2016**, *6*, 1501662.

(226) Haas, O.; Deb, A.; Cairns, E. J.; Wokaun, A. Synchrotron X-Ray Absorption Study of LiFePO$_4$ Electrodes. *J. Electrochem. Soc.* **2005**, *152*, A191.

(227) Giorgetti, M.; Berrettoni, M.; Scaccia, S.; Passerini, S. Characterization of Sol-Gel-Synthesized LiFePO$_4$ by Multiple Scattering Xafs. *Inorg. Chem.* **2006**, *45*, 2750−2757.

(228) Lv, D.; Bai, J.; Zhang, P.; Wu, S.; Li, Y.; Wen, W.; Jiang, Z.; Mi, J.; Zhu, Z.; Yang, Y. Understanding the High Capacity of Li$_2$FeSiO$_4$: In Situ Xrd/Xanes Study Combined with First-Principles Calculations. *Chem. Mater.* **2013**, *25*, 2014−2020.

(229) Yu, X.; Wang, Q.; Zhou, Y.; Li, H.; Yang, X. Q.; Nam, K. W.; Ehrlich, S. N.; Khalid, S.; Meng, Y. S. High Rate Delithiation Behaviour of LiFePO$_4$ Studied by Quick X-Ray Absorption Spectroscopy. *Chem. Commun.* **2012**, *48*, 11537−11539.

(230) Zhong, K.; Zhang, B.; Luo, S.; Wen, W.; Li, H.; Huang, X.; Chen, L. Investigation on Porous Mno Microsphere Anode for Lithium Ion Batteries. *J. Power Sources* **2011**, *196*, 6802−6808.

(231) Kim, Y.-U.; Lee, C. K.; Sohn, H.-J.; Kang, T. Reaction Mechanism of Tin Phosphide Anode by Mechanochemical Method for Lithium Secondary Batteries. *J. Electrochem. Soc.* **2004**, *151*, A933.

(232) Chen, C. H.; Hwang, B. J.; Do, J. S.; Weng, J. H.; Venkateswarlu, M.; Cheng, M. Y.; Santhanam, R.; Ragavendran, K.; Lee, J. F.; Chen, J. M.; et al. An Understanding of Anomalous Capacity of Nano-Sized Coo Anode Materials for Advanced Li-Ion Battery. *Electrochem. Commun.* **2010**, *12*, 496−498.

(233) Zhao, L.; Yu, X.; Yu, J.; Zhou, Y.; Ehrlich, S. N.; Hu, Y.-S.; Su, D.; Li, H.; Yang, X.-Q.; Chen, L. Remarkably Improved Electrode Performance of Bulk MnS by Forming a Solid Solution with Fes-Understanding the Li Storage Mechanism. *Adv. Funct. Mater.* **2014**, *24*, 5557−5566.

(234) Permien, S.; Indris, S.; Schürmann, U.; Kienle, L.; Zander, S.; Doyle, S.; Bensch, W. What Happens Structurally and Electronically During the Li Conversion Reaction of CoFe$_2$O$_4$ nanoparticles: An Operando XAS and XRD Investigation. *Chem. Mater.* **2016**, *28*, 434−444.

(235) Marino, C.; Fraisse, B.; Womes, M.; Villevieille, C.; Monconduit, L.; Stievano, L. At the Heart of a Conversion Reaction: An Operando X-Ray Absorption Spectroscopy Investigation of NiSb$_2$, a Negative Electrode Material for Li-Ion Batteries. *J. Phys. Chem. C* **2014**, *118*, 27772−27780.

(236) Venkateswarlu, M.; Chen, C. H.; Do, J. S.; Lin, C. W.; Chou, T. C.; Hwang, B. J. Electrochemical Properties of Nano-Sized Li$_4$Ti$_5$O$_{12}$ Powders Synthesized by a Sol−Gel Process and Characterized by X-Ray Absorption Spectroscopy. *J. Power Sources* **2005**, *146*, 204−208.

(237) Fehse, M.; Ben Yahia, M.; Monconduit, L.; Lemoigno, F.; Doublet, M.-L.; Fischer, F.; Tessier, C.; Stievano, L. New Insights on the Reversible Lithiation Mechanism of TiO$_2$(B) by Operando X-Ray Absorption Spectroscopy and X-Ray Diffraction Assisted by First-Principles Calculations. *J. Phys. Chem. C* **2014**, *118*, 27210−27218.

(238) Wang, F.; Robert, R.; Chernova, N. A.; Pereira, N.; Omenya, F.; Badway, F.; Hua, X.; Ruotolo, M.; Zhang, R. G.; Wu, L. J.; et al. Conversion Reaction Mechanisms in Lithium Ion Batteries: Study of the Binary Metal Fluoride Electrodes. *J. Am. Chem. Soc.* **2011**, *133*, 18828−18836.

(239) Moore, J. W.; Pearson, R. G. *Kinetics and Mechanism*; John Wiley & Sons: New York, 1961.

(240) Yoon, W.-S.; Chung, K. Y.; McBreen, J.; Zaghib, K.; Yang, X.-Q. Electronic Structure of the Electrochemically Delithiated Li$_{1−x}$FePO$_4$ Electrodes Investigated by P K-Edge X-Ray Absorption Spectroscopy. *Electrochem. Solid-State Lett.* **2006**, *9*, A415.

(241) Yoon, W. S.; Grey, C. P.; Balasubramanian, M.; Yang, X. Q.; McBreen, J. In Situ X-Ray Absorption Spectroscopic Study on LiNi$_{0.5}$Mn$_{0.5}$O$_2$ Cathode Material During Electrochemical Cycling. *Chem. Mater.* **2003**, *15*, 3161−3169.

(242) Deb, A.; Bergmann, U.; Cramer, S. P.; Cairns, E. J. In Situ X-Ray Absorption Spectroscopic Study of the Li[Ni$_{1/3}$Co$_{1/3}$Mn$_{1/3}$]O$_2$ Cathode Material. *J. Appl. Phys.* **2005**, *97*, 113523.

(243) Yoon, W.-S.; Balasubramanian, M.; Chung, K. Y.; Yang, X.-Q.; McBreen, J.; Grey, C. P.; Fischer, D. A. Investigation of the Charge Compensation Mechanism on the Electrochemically Li-Ion Deintercalated Li$_{1−x}$Co$_{1/3}$Ni$_{1/3}$Mn$_{1/3}$O$_2$ Electrode System by Combination of Soft and Hard X-Ray Absorption Spectroscopy. *J. Am. Chem. Soc.* **2005**, *127*, 17479−17487.

(244) Petersburg, C. F.; Li, Z.; Chernova, N. A.; Whittingham, M. S.; Alamgir, F. M. Oxygen and Transition Metal Involvement in the Charge Compensation Mechanism of LiNi$_{1/3}$Mn$_{1/3}$Co$_{1/3}$O$_2$ Cathodes. *J. Mater. Chem.* **2012**, *22*, 19993−20000.

(245) Tsai, Y. W.; Hwang, B. J.; Ceder, G.; Sheu, H. S.; Liu, D. G.; Lee, J. F. In-Situ X-Ray Absorption Spectroscopic Study on Variation of Electronic Transitions and Local Structure of LiNi$_{1/3}$Co$_{1/3}$Mn$_{1/3}$O$_2$ Cathode Material During Electrochemical Cycling. *Chem. Mater.* **2005**, *17*, 3191−3199.

(246) Sayers, D. E.; Stern, E. A.; Lytle, F. W. New Technique for Investigating Noncrystalline Structures: Fourier Analysis of the Extended X-Ray Absorption Fine Structure. *Phys. Rev. Lett.* **1971**, *27*, 1204−1207.

(247) Munshi, M. Z. A. *Handbook of Solid State Batteries & Capacitors*; World Scientific: Singapore, 1995.

(248) Avrami, M. Kinetics of Phase Change. I General Theory. *J. Chem. Phys.* **1939**, *7*, 1103.

(249) Morgan, D.; Van der Ven, A.; Ceder, G. Li Conductivity in Li$_x$MPO$_4$ (M= Mn, Fe, Co, Ni) Olivine Materials. *Electrochem. Solid-State Lett.* **2004**, *7*, A30.

(250) Islam, M. S.; Driscoll, D. J.; Fisher, C. A. J.; Slater, P. R. Atomic-Scale Investigation of Defects, Dopants, and Lithium Transport in the LiFePO$_4$ Olivine-Type Battery Material. *Chem. Mater.* **2005**, *17*, 5085−5092.

(251) Chen, G.; Song, X.; Richardson, T. J. Electron Microscopy Study of the LiFePO$_4$ to FePO$_4$ Phase Transition. *Electrochem. Solid-State Lett.* **2006**, *9*, A295.

(252) Orikasa, Y.; Maeda, T.; Koyama, Y.; Minato, T.; Murayama, H.; Fukuda, K.; Tanida, H.; Arai, H.; Matsubara, E.; Uchimoto, Y.; et al. Phase Transition Analysis between LiFePO$_4$ and FePO$_4$ by in-Situ Time-Resolved X-Ray Absorption and X-Ray Diffraction. *J. Electrochem. Soc.* **2013**, *160*, A3061−A3065.

(253) Ito, A.; Sato, Y.; Sanada, T.; Hatano, M.; Horie, H.; Ohsawa, Y. In Situ X-Ray Absorption Spectroscopic Study of Li-Rich Layered Cathode Material Li[Ni$_{0.17}$Li$_{0.2}$Co$_{0.07}$Mn$_{0.56}$]O$_2$. *J. Power Sources* **2011**, *196*, 6828−6834.

(254) Saisho, H.; Gohsi, Y. *Applications of Synchrotron Radiation to Materials Analysis*; Elsevier: Amsterdam, 1996.

(255) Takamatsu, D.; Koyama, Y.; Orikasa, Y.; Mori, S.; Nakatsutsumi, T.; Hirano, T.; Tanida, H.; Arai, H.; Uchimoto, Y.; Ogumi, Z. First in Situ Observation of the Licoo2 Electrode/Electrolyte Interface by Total-Reflection X-Ray Absorption Spectroscopy. *Angew. Chem., Int. Ed.* **2012**, *51*, 11597−11601.

(256) Yamamoto, K.; Minato, T.; Mori, S.; Takamatsu, D.; Orikasa, Y.; Tanida, H.; Nakanishi, K.; Murayama, H.; Masese, T.; Mori, T.; et al. Improved Cyclic Performance of Lithium-Ion Batteries: An Investigation of Cathode/Electrolyte Interface Via in Situ Total-

Reflection Fluorescence X-Ray Absorption Spectroscopy. *J. Phys. Chem. C* **2014**, *118*, 9538–9543.

(257) de Groot, F.; Kotani, A. *Core Level Spectroscopy of Solids*; CRC Press Taylor & Francis Group: Boca Raton, 2008.

(258) Yang, W.; Liu, X.; Qiao, R.; Olalde-Velasco, P.; Spear, J. D.; Roseguo, L.; Pepper, J. X.; Chuang, Y.-d.; Denlinger, J. D.; Hussain, Z. Key Electronic States in Lithium Battery Materials Probed by Soft X-Ray Spectroscopy. *J. Electron Spectrosc. Relat. Phenom.* **2013**, *190*, 64–74.

(259) Qiao, R.; Lucas, I. T.; Karim, A.; Syzdek, J.; Liu, X.; Chen, W.; Persson, K.; Kostecki, R.; Yang, W. Distinct Solid-Electrolyte-Interphases on Sn (100) and (001) Electrodes Studied by Soft X-Ray Spectroscopy. *Adv. Mater. Interfaces* **2014**, *1*, 1300115.

(260) Yang, W.; Qiao, R. Soft X-Ray Spectroscopy for Probing Electronic and Chemical States of Battery Materials. *Chin. Phys. B* **2016**, *25*, 17104.

(261) Eisebitt, S.; Boske, T.; Rubensson, J.; Eberhardt, W. Determination of Absorption Coefficients for Concentrated Samples by Fluorescence Detection. *Phys. Rev. B: Condens. Matter Mater. Phys.* **1993**, *47*, 14103–14109.

(262) Achkar, A. J.; Regier, T. Z.; Monkman, E. J.; Shen, K. M.; Hawthorn, D. G. Determination of Total X-Ray Absorption Coefficient Using Non-Resonant X-Ray Emission. *Sci. Rep.* **2011**, *1*, 182.

(263) Achkar, A. J.; Regier, T. Z.; Wadati, H.; Kim, Y. J.; Zhang, H.; Hawthorn, D. G. Bulk Sensitive X-Ray Absorption Spectroscopy Free of Self-Absorption Effects. *Phys. Rev. B: Condens. Matter Mater. Phys.* **2011**, *83*, 081106.

(264) Chuang, Y. D.; Shao, Y. C.; Cruz, A.; Hanzel, K.; Brown, A.; Frano, A.; Qiao, R. M.; Smith, B.; Domning, E.; Huang, S. W.; et al. Modular Soft X-Ray Spectrometer for Applications in Energy Sciences and Quantum Materials. *Rev. Sci. Instrum.* **2017**, *88*, 013110.

(265) Qiao, R. M.; Li, Q. H.; Zhuo, Z. Q.; Sallis, S. W.; Fuchs, O.; Blum, M.; Weinhardt, L.; Heske, C.; Pepper, J.; Jones, M.; et al. High-Efficiency in Situ Resonant Inelastic X-Ray Scattering (Irixs) Endstation at the Advanced Light Source. *Rev. Sci. Instrum.* **2017**, *88*, 033106.

(266) Nordgren, J.; Guo, J. H. Instrumentation for Soft X-Ray Emission Spectroscopy. *J. Electron Spectrosc. Relat. Phenom.* **2000**, *110–111*, 1–13.

(267) Ament, L. J. P.; van Veenendaal, M.; Devereaux, T. P.; Hill, J. P.; van den Brink, J. Resonant Inelastic X-Ray Scattering Studies of Elementary Excitations. *Rev. Mod. Phys.* **2011**, *83*, 705–767.

(268) Liu, G.; Xun, S.; Vukmirovic, N.; Song, X.; Olalde-Velasco, P.; Zheng, H.; Battaglia, V. S.; Wang, L.; Yang, W. Polymers with Tailored Electronic Structure for High Capacity Lithium Battery Electrodes. *Adv. Mater.* **2011**, *23*, 4679.

(269) Wu, M.; Xiao, X.; Vukmirovic, N.; Xun, S.; Das, P. K.; Song, X.; Olalde-Velasco, P.; Wang, D.; Weber, A. Z.; Wang, L.-W.; et al. Toward an Ideal Polymer Binder Design for High-Capacity Battery Anodes. *J. Am. Chem. Soc.* **2013**, *135*, 12048–12056.

(270) de Groot, F. Multiplet Effects in X-Ray Spectroscopy. *Coord. Chem. Rev.* **2005**, *249*, 31–63.

(271) Li, Y.; Weker, J. N.; Gent, W. E.; Mueller, D. N.; Lim, J.; Cogswell, D. A.; Tyliszczak, T.; Chueh, W. C. Dichotomy in the Lithiation Pathway of Ellipsoidal and Platelet $LiFePO_4$ particles Revealed through Nanoscale Operando State-of-Charge Imaging. *Adv. Funct. Mater.* **2015**, *25*, 3677–3687.

(272) Arthur, T. S.; Glans, P.-A.; Matsui, M.; Zhang, R.; Ma, B.; Guo, J. Mg Deposition Observed by in Situ Electrochemical Mg K-Edge X-Ray Absorption Spectroscopy. *Electrochem. Commun.* **2012**, *24*, 43–46.

(273) Liu, X.; Yang, W.; Liu, Z. Recent Progress on Synchrotron-Based in-Situ Soft X-Ray Spectroscopy for Energy Materials. *Adv. Mater.* **2014**, *26*, 7710–7729.

(274) Yang, W.; Guo, J.; Crumlin, E.; Prendergast, D.; Hussain, Z. Experiments and Theory of in Situ and Operando Soft X-Ray Spectroscopy for Energy Storage. *Synchrotron Radiation News* **2014**, *27*, 4–13.

(275) Li, Y.; El Gabaly, F.; Ferguson, T. R.; Smith, R. B.; Bartelt, N. C.; Sugar, J. D.; Fenton, K. R.; Cogswell, D. A.; Kilcoyne, A. L. D.; Tyliszczak, T.; et al. Current-Induced Transition from Particle-by-Particle to Concurrent Intercalation in Phase-Separating Battery Electrodes. *Nat. Mater.* **2014**, *13*, 1149–1156.

(276) Qiao, R.; Dai, K.; Mao, J.; Weng, T.-C.; Sokaras, D.; Nordlund, D.; Song, X.; Battaglia, V. S.; Hussain, Z.; Liu, G.; et al. Revealing and Suppressing Surface Mn(II) Formation of $Na_{0.44}MnO_2$ Electrodes for Na-Ion Batteries. *Nano Energy* **2015**, *16*, 186–195.

(277) Qiao, R.; Wang, Y.; Olalde-Velasco, P.; Li, H.; Hu, Y.-S.; Yang, W. Direct Evidence of Gradient Mn(II) Evolution at Charged States in $LiNi_{0.5}Mn_{1.5}O_4$ Electrodes with Capacity Fading. *J. Power Sources* **2015**, *273*, 1120–1126.

(278) Qiao, R.; Chin, T.; Harris, S. J.; Yan, S.; Yang, W. Spectroscopic Fingerprints of Valence and Spin States in Manganese Oxides and Fluorides. *Curr. Appl. Phys.* **2013**, *13*, 544–548.

(279) Kim, H.; Kim, D. J.; Seo, D.-H.; Yeom, M. S.; Kang, K.; Kim, D. K.; Jung, Y. Ab Initio Study of the Sodium Intercalation and Intermediate Phases in $Na_{0.44}MnO_2$ for Sodium-Ion Battery. *Chem. Mater.* **2012**, *24*, 1205–1211.

(280) Kruk, I.; Zajdel, P.; van Beek, W.; Bakaimi, I.; Lappas, A.; Stock, C.; Green, M. A. Coupled Commensurate Cation and Charge Modulation in the Tunneled Structure, $Na_{0.40(2)}MnO_2$. *J. Am. Chem. Soc.* **2011**, *133*, 13950–13956.

(281) Liu, X.; Liu, J.; Qiao, R.; Yu, Y.; Li, H.; Suo, L.; Hu, Y. S.; Chuang, Y. D.; Shu, G.; Chou, F.; et al. Phase Transformation and Lithiation Effect on Electronic Structure of Li_xFePO_4: An in-Depth Study by Soft X-Ray and Simulations. *J. Am. Chem. Soc.* **2012**, *134*, 13708–13715.

(282) Li, Y.; Weker, J. N.; Gent, W. E.; Mueller, D. N.; Lim, J.; Cogswell, D. A.; Tyliszczak, T.; Chueh, W. C. Dichotomy in the Lithiation Pathway of Ellipsoidal and Platelet $LiFePO_4$ Particles Revealed through Nanoscale Operando State-of-Charge Imaging. *Adv. Funct. Mater.* **2015**, *25*, 3677–3687.

(283) Liu, X.; Wang, D.; Liu, G.; Srinivasan, V.; Liu, Z.; Hussain, Z.; Yang, W. Distinct Charge Dynamics in Battery Electrodes Revealed by in Situ and Operando Soft X-Ray Spectroscopy. *Nat. Commun.* **2013**, *4*, 2568.

(284) Qiao, R.; Wray, L. A.; Kim, J.-H.; Pieczonka, N. P. W.; Harris, S. J.; Yang, W. Direct Experimental Probe of the Ni(II)/Ni(II)/Ni(IV) Redox Evolution in $LiNi_{0.5}Mn_{1.5}O_4$ Electrodes. *J. Phys. Chem. C* **2015**, *119*, 27228–27233.

(285) Lin, F.; Nordlund, D.; Pan, T. J.; Markus, I. M.; Weng, T. C.; Xin, H. L. L.; Doeff, M. M. Influence of Synthesis Conditions on the Surface Passivation and Electrochemical Behavior of Layered Cathode Materials. *J. Mater. Chem. A* **2014**, *2*, 19833–19840.

(286) Xu, J.; Lin, F.; Nordlund, D.; Crumlin, E. J.; Wang, F.; Bai, J. M.; Doeff, M. M.; Tong, W. Elucidation of the Surface Characteristics and Electrochemistry of High-Performance $LiNiO_2$. *Chem. Commun.* **2016**, *52*, 4239–4242.

(287) Cheng, L.; Crumlin, E. J.; Chen, W.; Qiao, R. M.; Hou, H. M.; Lux, S. F.; Zorba, V.; Russo, R.; Kostecki, R.; Liu, Z.; et al. The Origin of High Electrolyte-Electrode Interfacial Resistances in Lithium Cells Containing Garnet Type Solid Electrolytes. *Phys. Chem. Chem. Phys.* **2014**, *16*, 18294–18300.

(288) Cheng, L.; Wu, C. H.; Jarry, A.; Chen, W.; Ye, Y.; Zhu, J.; Kostecki, R.; Persson, K.; Guo, J.; Salmeron, M.; et al. Interrelationships among Grain Size, Surface Composition, Air Stability, and Interfacial Resistance of Al-Substituted $Li_7La_3Zr_2O_{12}$ Solid Electrolytes. *ACS Appl. Mater. Interfaces* **2015**, *7*, 17649–17655.

(289) Goodenough, J. B. *Advances in Lithium Batteries P.135*; Kluwer Academic/Plenum Publishers: New York, 2002.

(290) Goodenough, J. B.; Kim, Y. Locating Redox Couples in the Layered Sulfides with Application to $CuCr_2S_4$. *J. Solid State Chem.* **2009**, *182*, 2904–2911.

(291) Zaanen, J.; Sawatzky, G. A.; Allen, J. W. Band Gaps and Electronic Structure of Transition-Metal Compounds. *Phys. Rev. Lett.* **1985**, *55*, 418.

(292) Hong, W. T.; Stoerzinger, K. A.; Moritz, B.; Devereaux, T. P.; Yang, W.; Shao-Horn, Y. Probing $LaMo_3$ Metal and Oxygen Partial Density of States Using X-Ray Emission, Absorption, and Photoelectron Spectroscopy. *J. Phys. Chem. C* **2015**, *119*, 2063–2072.

(293) Olalde-Velasco, P.; Jimenez-Mier, J.; Denlinger, J. D.; Hussain, Z.; Yang, W. L. Direct Probe of Mott-Hubbard to Charge-Transfer Insulator Transition and Electronic Structure Evolution in Transition-Metal Systems. *Phys. Rev. B: Condens. Matter Mater. Phys.* **2011**, *83*, 241102.

(294) McCalla, E.; Abakumov, A. M.; Saubanere, M.; Foix, D.; Berg, E. J.; Rousse, G.; Doublet, M. L.; Gonbeau, D.; Novak, P.; Van Tendeloo, G.; et al. Visualization of O-O Peroxo-Like Dimers in High-Capacity Layered Oxides for Li-Ion Batteries. *Science* **2015**, *350*, 1516–1521.

(295) Seo, D.-H.; Lee, J.; Urban, A.; Malik, R.; Kang, S.; Ceder, G. The Structural and Chemical Origin of the Oxygen Redox Activity in Layered and Cation-Disordered Li-Excess Cathode Materials. *Nat. Chem.* **2016**, *8*, 692–697.

(296) Liu, X.; Wang, Y. J.; Barbiellini, B.; Hafiz, H.; Basak, S.; Liu, J.; Richardson, T.; Shu, G.; Chou, F.; Weng, T. C.; et al. Why $LiFePO_4$ Is a Safe Battery Electrode: Coulomb Repulsion Induced Electron-State Reshuffling Upon Lithiation. *Phys. Chem. Chem. Phys.* **2015**, *17*, 26369–26377.

(297) Goodenough, J. B. *Chapter 4 Advances in Lithium Ion Batteries*; Springer, 2002.

(298) Xu, K. Nonaqueous Liquid Electrolytes for Lithium-Based Rechargeable Batteries. *Chem. Rev.* **2004**, *104*, 4303–4418.

(299) Weinhardt, L.; Blum, M.; Fuchs, O.; Benkert, A.; Meyer, F.; Bär, M.; Denlinger, J. D.; Yang, W.; Reinert, F.; Heske, C. Rixs Investigations of Liquids, Solutions, and Liquid/Solid Interfaces. *J. Electron Spectrosc. Relat. Phenom.* **2013**, *188*, 111–120.

(300) Rubensson, J.-E.; Hennies, F.; Pietzsch, A. High-Resolution Resonant Inelastic Soft X-Ray Scattering Applied to Liquids. *J. Electron Spectrosc. Relat. Phenom.* **2013**, *188*, 79–83.

(301) Lange, K. M.; Aziz, E. F. Electronic Structure of Ions and Molecules in Solution: A View from Modern Soft X-Ray Spectroscopies. *Chem. Soc. Rev.* **2013**, *42*, 6840–6859.

(302) Weinhardt, L.; Benkert, A.; Meyer, F.; Blum, M.; Wilks, R. G.; Yang, W.; Bar, M.; Reinert, F.; Heske, C. Nuclear Dynamics and Spectator Effects in Resonant Inelastic Soft X-Ray Scattering of Gas-Phase Water Molecules. *J. Chem. Phys.* **2012**, *136*, 144311–144316.

(303) Weinhardt, L.; Weigand, M.; Fuchs, O.; Bär, M.; Blum, M.; Denlinger, J. D.; Yang, W.; Umbach, E.; Heske, C. Nuclear Dynamics in the Core-Excited State of Aqueous Ammonia Probed by Resonant Inelastic Soft X-Ray Scattering. *Phys. Rev. B: Condens. Matter Mater. Phys.* **2011**, *84*, 104202.

(304) Arthur, T. S.; Glans, P.-A.; Matsui, M.; Zhang, R.; Ma, B.; Guo, J. Mg Deposition Observed by in Situ Electrochemical Mg K-Edge X-Ray Absorption Spectroscopy. *Electrochem. Commun.* **2012**, *24*, 43–46.

(305) Guo, J. The Development of in Situ Photon-in/Photon-out Soft X-Ray Spectroscopy on Beamline 7.0.1 at the Als. *J. Electron Spectrosc. Relat. Phenom.* **2013**, *188*, 71–78.

(306) Blum, M.; Weinhardt, L.; Fuchs, O.; Bar, M.; Zhang, Y.; Weigand, M.; Krause, S.; Pookpanratana, S.; Hofmann, T.; Yang, W.; et al. Solid and Liquid Spectroscopic Analysis (SALSA)–A Soft X-Ray Spectroscopy Endstation with a Novel Flow-through Liquid Cell. *Rev. Sci. Instrum.* **2009**, *80*, 123102–123106.

(307) Nordling, C.; Sokolowski, E.; Siegbahn, K. Precision Method for Obtaining Absolute Values of Atomic Binding Energies. *Phys. Rev.* **1957**, *105*, 1676.

(308) Philippe, B.; Hahlin, M.; Edstro m, K.; Gustafsson, T.; Siegbahn, H.; Rensmo, H. Photoelectron Spectroscopy for Lithium Battery Interface Studies. *J. Electrochem. Soc.* **2016**, *163*, A178–A191.

(309) Panaccione, G.; Kobayashi, K. Hard X-Ray Photoemission Spectroscopy: Variable Depth Analysis of Bulk, Surface and Interface Electronic Properties. *Surf. Sci.* **2012**, *606*, 125–129.

(310) Drube, W. Preface. *J. Electron Spectrosc. Relat. Phenom.* **2013**, *190*, 125–126.

(311) Kövér, L. X-Ray Photoelectron Spectroscopy Using Hard X-Rays. *J. Electron Spectrosc. Relat. Phenom.* **2010**, *178−179*, 241–257.

(312) Lindau, I.; Pianetta, P.; Doniach, S.; Spicer, W. E. X-Ray Photoemission Spectroscopy. *Nature* **1974**, *250*, 214–215.

(313) Gorgoi, M.; Mårtensson, N.; Svensson, S. Haxpes Studies of Solid Materials for Applications in Energy and Information Technology Using the Hike Facility at Hzb-Bessy Ii. *J. Electron Spectrosc. Relat. Phenom.* **2015**, *200*, 40–48.

(314) Shikano, M.; Kobayashi, H.; Koike, S.; Sakaebe, H.; Ikenaga, E.; Kobayashi, K.; Tatsumi, K. Investigation of Positive Electrodes after Cycle Testing of High-Power Li-Ion Battery Cells II. *J. Power Sources* **2007**, *174*, 795–799.

(315) Takanashi, Y.; Orikasa, Y.; Mogi, M.; Oishi, M.; Murayama, H.; Sato, K.; Yamashige, H.; Takamatsu, D.; Fujimoto, T.; Tanida, H.; et al. Thickness Estimation of Interface Films Formed on $Li_{1-x}CoO_2$ Electrodes by Hard X-Ray Photoelectron Spectroscopy. *J. Power Sources* **2011**, *196*, 10679–10685.

(316) Hayashi, T.; Okada, J.; Toda, E.; Kuzuo, R.; Oshimura, N.; Kuwata, N.; Kawamura, J. Degradation Mechanism of Li-$Ni_{0.82}Co_{0.15}Al_{0.03}O_2$ Positive Electrodes of a Lithium-Ion Battery by a Long-Term Cycling Test. *J. Electrochem. Soc.* **2014**, *161*, A1007–A1011.

(317) Eriksson, R.; Lasri, K.; Gorgoi, M.; Gustafsson, T.; Edström, K.; Brandell, D.; Saadoune, I.; Hahlin, M. Electronic and Structural Changes in $Ni_{0.5}TiOPO_4$ Li-Ion Battery Cells Upon First Lithiation and Delithiation, Studied by High-Energy X-Ray Spectroscopies. *J. Phys. Chem. C* **2015**, *119*, 9692–9704.

(318) Konishi, H.; Suzuki, K.; Taminato, S.; Kim, K.; Zheng, Y.; Kim, S.; Lim, J.; Hirayama, M.; Son, J.-Y.; Cui, Y.; et al. Effect of Surface Li_3PO_4 Coating on $LiNi_{0.5}Mn_{1.5}O_4$ Epitaxial Thin Film Electrodes Synthesized by Pulsed Laser Deposition. *J. Power Sources* **2014**, *269*, 293–298.

(319) Sachs, M.; Gellert, M.; Chen, M.; Drescher, H. J.; Kachel, S. R.; Zhou, H.; Zugermeier, M.; Gorgoi, M.; Roling, B.; Gottfried, J. M. Lini0.5mn1.5o4 High-Voltage Cathode Coated with $Li_4Ti_5O_{12}$: A Hard X-Ray Photoelectron Spectroscopy (Haxpes) Study. *Phys. Chem. Chem. Phys.* **2015**, *17*, 31790–31800.

(320) Kobayashi, G.; Irii, Y.; Matsumoto, F.; Ito, A.; Ohsawa, Y.; Yamamoto, S.; Cui, Y.; Son, J.-Y.; Sato, Y. Improving Cycling Performance of Li-Rich Layered Cathode Materials through Combination of Al_2O_3-Based Surface Modification and Stepwise Precycling. *J. Power Sources* **2016**, *303*, 250–256.

(321) Ciosek Högström, K.; Malmgren, S.; Hahlin, M.; Gorgoi, M.; Nyholm, L.; Rensmo, H.; Edström, K. The Buried Carbon/Solid Electrolyte Interphase in Li-Ion Batteries Studied by Hard X-Ray Photoelectron Spectroscopy. *Electrochim. Acta* **2014**, *138*, 430–436.

(322) Klett, M.; Eriksson, R.; Groot, J.; Svens, P.; Ciosek Högström, K.; Lindström, R. W.; Berg, H.; Gustafson, T.; Lindbergh, G.; Edström, K. Non-Uniform Aging of Cycled Commercial $LiFePO_4$//Graphite Cylindrical Cells Revealed by Post-Mortem Analysis. *J. Power Sources* **2014**, *257*, 126–137.

(323) Nie, M.; Demeaux, J.; Young, B. T.; Heskett, D. R.; Chen, Y.; Bose, A.; Woicik, J. C.; Lucht, B. L. Effect of Vinylene Carbonate and Fluoroethylene Carbonate on Sei Formation on Graphitic Anodes in Li-Ion Batteries. *J. Electrochem. Soc.* **2015**, *162*, A7008–A7014.

(324) Ciosek Högström, K.; Hahlin, M.; Malmgren, S.; Gorgoi, M.; Rensmo, H.; Edström, K. Aging of Electrode/Electrolyte Interfaces in $LiFePO_4$/Graphite Cells Cycled with and without Pms Additive. *J. Phys. Chem. C* **2014**, *118*, 12649–12660.

(325) Malmgren, S.; Ciosek, K.; Hahlin, M.; Gustafsson, T.; Gorgoi, M.; Rensmo, H.; Edström, K. Comparing Anode and Cathode Electrode/Electrolyte Interface Composition and Morphology Using Soft and Hard X-Ray Photoelectron Spectroscopy. *Electrochim. Acta* **2013**, *97*, 23–32.

(326) Hori, H.; Shikano, M.; Kobayashi, H.; Koike, S.; Sakaebe, H.; Saito, Y.; Tatsumi, K.; Yoshikawa, H.; Ikenaga, E. Analysis of Hard Carbon for Lithium-Ion Batteries by Hard X-Ray Photoelectron Spectroscopy. *J. Power Sources* **2013**, *242*, 844–847.

(327) Xu, C.; Lindgren, F.; Philippe, B.; Gorgoi, M.; Björefors, F.; Edström, K.; Gustafsson, T. Improved Performance of the Silicon Anode for Li-Ion Batteries: Understanding the Surface Modification Mechanism of Fluoroethylene Carbonate as an Effective Electrolyte Additive. *Chem. Mater.* **2015**, *27*, 2591–2599.

(328) Young, B. T.; Heskett, D. R.; Nguyen, C. C.; Nie, M.; Woicik, J. C.; Lucht, B. L. Hard X-Ray Photoelectron Spectroscopy (Haxpes) Investigation of the Silicon Solid Electrolyte Interphase (SEI) in Lithium-Ion Batteries. *ACS Appl. Mater. Interfaces* **2015**, *7*, 20004–20011.

(329) Seo, D. M.; Nguyen, C. C.; Young, B. T.; Heskett, D. R.; Woicik, J. C.; Lucht, B. L. Characterizing Solid Electrolyte Interphase on Sn Anode in Lithium Ion Battery. *J. Electrochem. Soc.* **2015**, *162*, A7091–A7095.

(330) Lindgren, F.; Xu, C.; Maibach, J.; Andersson, A. M.; Marcinek, M.; Niedzicki, L.; Gustafsson, T.; Björefors, F.; Edström, K. A Hard X-Ray Photoelectron Spectroscopy Study on the Solid Electrolyte Interphase of a Lithium 4,5-Dicyano-2-(Trifluoromethyl)Imidazolide Based Electrolyte for Si-Electrodes. *J. Power Sources* **2016**, *301*, 105–112.

(331) Doubaji, S.; Philippe, B.; Saadoune, I.; Gorgoi, M.; Gustafsson, T.; Solhy, A.; Valvo, M.; Rensmo, H.; Edstrom, K. Passivation Layer and Cathodic Redox Reactions in Sodium-Ion Batteries Probed by Haxpes. *ChemSusChem* **2016**, *9*, 97–108.

(332) Seah, M. P. Simple Universal Curve for the Energy-Dependent Electron Attenuation Length for All Materials. *Surf. Interface Anal.* **2012**, *44*, 1353–1359.

(333) Lin, F.; Nordlund, D.; Weng, T. C.; Sokaras, D.; Jones, K. M.; Reed, R. B.; Gillaspie, D. T.; Weir, D. G. J.; Moore, R. G.; Dillon, A. C.; et al. Origin of Electrochromism in High-Performing Nanocomposite Nickel Oxide. *ACS Appl. Mater. Interfaces* **2013**, *5*, 3643–3649.

(334) Axnanda, S.; Crumlin, E. J.; Mao, B. H.; Rani, S.; Chang, R.; Karlsson, P. G.; Edwards, M. O. M.; Lundqvist, M.; Moberg, R.; Ross, P.; et al. Using "Tender" X-Ray Ambient Pressure X-Ray Photoelectron Spectroscopy as a Direct Probe of Solid-Liquid Interface. *Sci. Rep.* **2015**, *5*, 9788.

(335) Karslioglu, O.; Nemsak, S.; Zegkinoglou, I.; Shavorskiy, A.; Hartl, M.; Salmassi, F.; Gullikson, E. M.; Ng, M. L.; Rameshan, C.; Rude, B.; et al. Aqueous Solution/Metal Interfaces Investigated in Operando by Photoelectron Spectroscopy. *Faraday Discuss.* **2015**, *180*, 35–53.

(336) Lichterman, M. F.; Hu, S.; Richter, M. H.; Crumlin, E. J.; Axnanda, S.; Favaro, M.; Drisdell, W.; Hussain, Z.; Mayer, T.; Brunschwig, B. S.; et al. Direct Observation of the Energetics at a Semiconductor/Liquid Junction by Operando X-Ray Photoelectron Spectroscopy. *Energy Environ. Sci.* **2015**, *8*, 2409–2416.

(337) Lichterman, M. F.; Richter, M. H.; Hu, S.; Crumlin, E. J.; Axnanda, S.; Favaro, M.; Drisdell, W.; Hussain, Z.; Brunschwig, B. S.; Lewis, N. S.; et al. An Electrochemical, Microtopographical and Ambient Pressure X-Ray Photoelectron Spectroscopic Investigation of Si/TiO$_2$/Ni/Electrolyte Interfaces. *J. Electrochem. Soc.* **2016**, *163*, H139–H146.

(338) Crumlin, E. J.; Liu, Z.; Bluhm, H.; Yang, W. L.; Guo, J. H.; Hussain, Z. X-Ray Spectroscopy of Energy Materials under in Situ/Operando Conditions. *J. Electron Spectrosc. Relat. Phenom.* **2015**, *200*, 264–273.

(339) Lu, Y. C.; Crumlin, E. J.; Veith, G. M.; Harding, J. R.; Mutoro, E.; Baggetto, L.; Dudney, N. J.; Liu, Z.; Shao-Horn, Y. In Situ Ambient Pressure X-Ray Photoelectron Spectroscopy Studies of Lithium-Oxygen Redox Reactions. *Sci. Rep.* **2012**, *2*, 715.

(340) Frankel, R. I. Centennial of Rontgen's Discovery of X-Rays. *West J. Med.* **1996**, *164*, 497–501.

(341) Weker, J. N.; Toney, M. F. Emerging in Situ and Operando Nanoscale X-Ray Imaging Techniques for Energy Storage Materials. *Adv. Funct. Mater.* **2015**, *25*, 1622–1637.

(342) Sakdinawat, A.; Attwood, D. Nanoscale X-Ray Imaging. *Nat. Photonics* **2010**, *4*, 840–848.

(343) Miao, J. W.; Ishikawa, T.; Robinson, I. K.; Murnane, M. M. Beyond Crystallography: Diffractive Imaging Using Coherent X-Ray Light Sources. *Science* **2015**, *348*, 530–535.

(344) Mancuso, A. P.; Yefanov, O. M.; Vartanyants, I. A. Coherent Diffractive Imaging of Biological Samples at Synchrotron and Free Electron Laser Facilities. *J. Biotechnol.* **2010**, *149*, 229–237.

(345) Mancuso, A. P.; Gorniak, T.; Staier, F.; Yefanov, O. M.; Barth, R.; Christophis, C.; Reime, B.; Gulden, J.; Singer, A.; Pettit, M. E.; et al. Coherent Imaging of Biological Samples with Femtosecond Pulses at the Free-Electron Laser Flash. *New J. Phys.* **2010**, *12*, 035003.

(346) Chapman, H. N.; Nugent, K. A. Coherent Lensless X-Ray Imaging. *Nat. Photonics* **2010**, *4*, 833–839.

(347) Nugent, K. A. Coherent Methods in the X-Ray Sciences. *Adv. Phys.* **2010**, *59*, 1–99.

(348) Fienup, J. R. Phase Retrieval Algorithms - a Comparison. *Appl. Opt.* **1982**, *21*, 2758–2769.

(349) Heethoff, M.; Helfen, L.; Cloetens, P. Non-Invasive 3D-Visualization with Sub-Micron Resolution Using Synchrotron-X-Ray-Tomography. *J. Visualized Exp.* **2008**, *15*, 737.

(350) Martin, T.; Douissard, P. A.; Couchaud, M.; Cecilia, A.; Baumbach, T.; Dupre, K.; Rack, A. Lso-Based Single Crystal Film Scintillator for Synchrotron-Based Hard X-Ray Micro-Imaging. *IEEE Trans. Nucl. Sci.* **2009**, *56*, 1412–1418.

(351) Liu, Y.; Andrews, J. C.; Meirer, F.; Mehta, A.; Gil, S. C.; Sciau, P.; Mester, Z.; Pianetta, P. Applications of Hard X-Ray Full-Field Transmission X-Ray Microscopy at Ssrl. *AIP Conf. Proc.* **2011**, *1365*, 357–360.

(352) Chao, W. L.; Harteneck, B. D.; Liddle, J. A.; Anderson, E. H.; Attwood, D. T. Soft X-Ray Microscopy at a Spatial Resolution Better Than 15nm. *Nature* **2005**, *435*, 1210–1213.

(353) Park, S. J.; Weon, B. M.; Lee, J. S.; Lee, J.; Kim, J.; Je, J. H. Visualization of Asymmetric Wetting Ridges on Soft Solids with X-Ray Microscopy. *Nat. Commun.* **2014**, *5*, 4369.

(354) Liu, Y.; Nelson, J.; Holzner, C.; Andrews, J. C.; Pianetta, P. Recent Advances in Synchrotron-Based Hard X-Ray Phase Contrast Imaging. *J. Phys. D: Appl. Phys.* **2013**, *46*, 494001.

(355) Pfeiffer, F.; Bech, M.; Bunk, O.; Kraft, P.; Eikenberry, E. F.; Bronnimann, C.; Grunzweig, C.; David, C. Hard-X-Ray Dark-Field Imaging Using a Grating Interferometer. *Nat. Mater.* **2008**, *7*, 134–137.

(356) Simons, H.; King, A.; Ludwig, W.; Detlefs, C.; Pantleon, W.; Schmidt, S.; Stohr, F.; Snigireva, I.; Snigirev, A.; Poulsen, H. F. Dark-Field X-Ray Microscopy for Multiscale Structural Characterization. *Nat. Commun.* **2015**, *6*, 6098.

(357) Vogt, S.; Chapman, H. N.; Jacobsen, C.; Medenwaldt, R. Dark Field X-Ray Microscopy: The Effects of Condenser/Detector Aperture. *Ultramicroscopy* **2001**, *87*, 25–44.

(358) Wang, H. C.; Kashyap, Y.; Sawhney, K. From Synchrotron Radiation to Lab Source: Advanced Speckle-Based X-Ray Imaging Using Abrasive Paper. *Sci. Rep.* **2016**, *6*, 20476.

(359) Zhu, P. P.; Zhang, K.; Wang, Z. L.; Liu, Y. J.; Liu, X. S.; Wu, Z. Y.; McDonald, S. A.; Marone, F.; Stampanoni, M. Low-Dose, Simple, and Fast Grating-Based X-Ray Phase-Contrast Imaging. *Proc. Natl. Acad. Sci. U. S. A.* **2010**, *107*, 13576–13581.

(360) Andrews, J. C.; Brennan, S.; Liu, Y.; Pianetta, P.; Almeida, E. A. C.; van der Meulen, M. C. H.; Wu, Z.; Mester, Z.; Ouerdane, L.; Gelb, J.; et al. Full-Field Transmission X-Ray Microscopy for Bio-Imaging. *J. Phys.: Conf. Ser.* **2009**, *186*, 012081.

(361) Mayo, S. C.; Miller, P. R.; Wilkins, S. W.; Davis, T. J.; Gao, D.; Gureyev, T. E.; Paganin, D.; Parry, D. J.; Pogany, A.; Stevenson, A. W. Quantitative X-Ray Projection Microscopy: Phase-Contrast and Multi-Spectral Imaging. *J. Microsc.* **2002**, *207*, 79–96.

(362) Nelson, J.; Misra, S.; Yang, Y.; Jackson, A.; Liu, Y. J.; Wang, H. L.; Dai, H. J.; Andrews, J. C.; Cui, Y.; Toney, M. F. In Operando X-Ray Diffraction and Transmission X-Ray Microscopy of Lithium Sulfur Batteries. *J. Am. Chem. Soc.* **2012**, *134*, 6337–6343.

(363) Elazari, R.; Salitra, G.; Talyosef, Y.; Grinblat, J.; Scordilis-Kelley, C.; Xiao, A.; Affinito, J.; Aurbach, D. Morphological and Structural Studies of Composite Sulfur Electrodes Upon Cycling by

Hrtem, Afm and Raman Spectroscopy. *J. Electrochem. Soc.* **2010**, *157*, A1131−A1138.

(364) Wang, Y.; Huang, Y. Q.; Wang, W. K.; Huang, C. J.; Yu, Z. B.; Zhang, H.; Sun, J.; Wang, A. B.; Yuan, K. G. Structural Change of the Porous Sulfur Cathode Using Gelatin as a Binder During Discharge and Charge. *Electrochim. Acta* **2009**, *54*, 4062−4066.

(365) Nelson, J.; Yang, Y.; Misra, S.; Andrews, J. C.; Cui, Y.; Toney, M. F. Identifying and Managing Radiation Damage During in Situ Transmission X-Ray Microscopy of Li-Ion Batteries. *Proc. SPIE* **2013**, *8851*, 88510B.

(366) Nazaretski, E.; Lauer, K.; Yan, H.; Bouet, N.; Zhou, J.; Conley, R.; Huang, X.; Xu, W.; Lu, M.; Gofron, K.; et al. Pushing the Limits: An Instrument for Hard X-Ray Imaging Below 20 nm. *J. Synchrotron Radiat.* **2015**, *22*, 336−341.

(367) Chen, S.; Deng, J.; Yuan, Y.; Flachenecker, C.; Mak, R.; Hornberger, B.; Jin, Q.; Shu, D.; Lai, B.; Maser, J.; et al. The Bionanoprobe: Hard X-Ray Fluorescence Nanoprobe with Cryogenic Capabilities. *J. Synchrotron Radiat.* **2014**, *21*, 66−75.

(368) Winarski, R. P.; Holt, M. V.; Rose, V.; Fuesz, P.; Carbaugh, D.; Benson, C.; Shu, D. M.; Kline, D.; Stephenson, G. B.; McNulty, I.; et al. A Hard X-Ray Nanoprobe Beamline for Nanoscale Microscopy. *J. Synchrotron Radiat.* **2012**, *19*, 1056−1060.

(369) Korbas, M.; Blechinger, S. R.; Krone, P. H.; Pickering, I. J.; George, G. N. Localizing Organomercury Uptake and Accumulation in Zebrafish Larvae at the Tissue and Cellular Level. *Proc. Natl. Acad. Sci. U. S. A.* **2008**, *105*, 12108−12112.

(370) Chueh, W. C.; El Gabaly, F.; Sugar, J. D.; Bartelt, N. C.; McDaniel, A. H.; Fenton, K. R.; Zavadil, K. R.; Tyliszczak, T.; Lai, W.; McCarty, K. F. Intercalation Pathway in Many-Particle LiFePO$_4$ Electrode Revealed by Nanoscale State-of-Charge Mapping. *Nano Lett.* **2013**, *13*, 866−872.

(371) Boesenberg, U.; Falk, M.; Ryan, C. G.; Kirkham, R.; Menzel, M.; Janek, J.; Froba, M.; Falkenberg, G.; Fittschen, U. E. A. Correlation between Chemical and Morphological Heterogeneities in Li-Ni$_{0.5}$Mn$_{1.5}$O$_4$ Spinel Composite Electrodes for Lithium-Ion Batteries Determined by Micro-X-Ray Fluorescence Analysis. *Chem. Mater.* **2015**, *27*, 2525−2531.

(372) Mocuta, C.; Stangl, J.; Mundboth, K.; Metzger, T. H.; Bauer, G.; Vartanyants, I. A.; Schmidbauer, M.; Boeck, T. Beyond the Ensemble Average: X-Ray Microdiffraction Analysis of Single Sige Islands. *Phys. Rev. B: Condens. Matter Mater. Phys.* **2008**, *77*, 245425.

(373) Huang, X.; Yan, H.; Nazaretski, E.; Conley, R.; Bouet, N.; Zhou, J.; Lauer, K.; Li, L.; Eom, D.; Legnini, D.; et al. 11 nm Hard X-Ray Focus from a Large-Aperture Multilayer Laue Lens. *Sci. Rep.* **2013**, *3*, 3562.

(374) Yan, H. F.; Conley, R.; Bouet, N.; Chu, Y. S. Hard X-Ray Nanofocusing by Multilayer Laue Lenses. *J. Phys. D: Appl. Phys.* **2014**, *47*, 263001.

(375) Chang, C.; Sakdinawat, A. Ultra-High Aspect Ratio High-Resolution Nanofabrication for Hard X-Ray Diffractive Optics. *Nat. Commun.* **2014**, *5*, 4243.

(376) Rodenburg, J. M.; Hurst, A. C.; Cullis, A. G.; Dobson, B. R.; Pfeiffer, F.; Bunk, O.; David, C.; Jefimovs, K.; Johnson, I. Hard-X-Ray Lensless Imaging of Extended Objects. *Phys. Rev. Lett.* **2007**, *98*, 034801.

(377) Thibault, P.; Dierolf, M.; Menzel, A.; Bunk, O.; David, C.; Pfeiffer, F. High-Resolution Scanning X-Ray Diffraction Microscopy. *Science* **2008**, *321*, 379−382.

(378) Zhang, F. C.; Peterson, I.; Vila-Comamala, J.; Berenguer, A. D. F.; Bean, R.; Chen, B.; Menzel, A.; Robinson, I. K.; Rodenburg, J. M.; Diaz, A. Translation Position Determination in Ptychographic Coherent Diffraction Imaging. *Opt. Express* **2013**, *21*, 13592−13606.

(379) Deng, J. J.; Vine, D. J.; Chen, S.; Nashed, Y. S. G.; Jin, Q. L.; Phillips, N. W.; Peterka, T.; Ross, R.; Vogt, S.; Jacobsen, C. J. Simultaneous Cryo X-Ray Ptychographic and Fluorescence Microscopy of Green Algae. *Proc. Natl. Acad. Sci. U. S. A.* **2015**, *112*, 2314−2319.

(380) Schaff, F.; Bech, M.; Zaslansky, P.; Jud, C.; Liebi, M.; Guizar-Sicairos, M.; Pfeiffer, F. Six-Dimensional Real and Reciprocal Space Small-Angle X-Ray Scattering Tomography. *Nature* **2015**, *527*, 353−356.

(381) Liebi, M.; Georgiadis, M.; Menzel, A.; Schneider, P.; Kohlbrecher, J.; Bunk, O.; Guizar-Sicairos, M. Nanostructure Surveys of Macroscopic Specimens by Small-Angle Scattering Tensor Tomography. *Nature* **2015**, *527*, 349−352.

(382) Li, Y. Y.; Meyer, S.; Lim, J.; Lee, S. C.; Gent, W. E.; Marchesini, S.; Krishnan, H.; Tyliszczak, T.; Shapiro, D.; Kilcoyne, A. L. D.; et al. Effects of Particle Size, Electronic Connectivity, and Incoherent Nanoscale Domains on the Sequence of Lithiation in LiFePO$_4$ Porous Electrodes. *Adv. Mater.* **2015**, *27*, 6591−6597.

(383) Ohmer, N.; Fenk, B.; Samuelis, D.; Chen, C. C.; Maier, J.; Weigand, M.; Goering, E.; Schutz, G. Phase Evolution in Single-Crystalline LiFePO$_4$ Followed by in Situ Scanning X-Ray Microscopy of a Micrometre-Sized Battery. *Nat. Commun.* **2015**, *6*, 6045.

(384) Yu, Y. S.; Kim, C.; Shapiro, D. A.; Farmand, M.; Qian, D.; Tyliszczak, T.; Kilcoyne, A. L. D.; Celestre, R.; Marchesini, S.; Joseph, J.; et al. Dependence on Crystal Size of the Nanoscale Chemical Phase Distribution and Fracture in Li$_x$FePO$_4$. *Nano Lett.* **2015**, *15*, 4282−4288.

(385) Pasta, M.; Wang, R. Y.; Ruffo, R.; Qiao, R.; Lee, H.-W.; Shyam, B.; Guo, M.; Wang, Y.; Wray, L. A.; Yang, W.; et al. Manganese−Cobalt Hexacyanoferrate Cathodes for Sodium-Ion Batteries. *J. Mater. Chem. A* **2016**, *4*, 4211−4223.

(386) Wang, L.; Song, J.; Qiao, R.; Wray, L. A.; Hossain, M. A.; Chuang, Y. D.; Yang, W.; Lu, Y.; Evans, D.; Lee, J. J.; et al. Rhombohedral Prussian White as Cathode for Rechargeable Sodium-Ion Batteries. *J. Am. Chem. Soc.* **2015**, *137*, 2548−2554.

(387) Lim, J.; Li, Y. Y.; Alsem, D. H.; So, H.; Lee, S. C.; Bai, P.; Cogswell, D. A.; Liu, X. Z.; Jin, N.; Yu, Y. S.; et al. Origin and Hysteresis of Lithium Compositional Spatiodynamics within Battery Primary Particles. *Science* **2016**, *353*, 566−571.

(388) Bautz, W.; Kalender, W.; Godfrey, N. Hounsfield and His Influence on Radiology. *Radiologe* **2005**, *45*, 350−355.

(389) Liu, Y. J.; Kiss, A. M.; Larsson, D. H.; Yang, F. F.; Pianetta, P. To Get the Most out of High Resolution X-Ray Tomography: A Review of the Post-Reconstruction Analysis. *Spectrochim. Acta, Part B* **2016**, *117*, 29−41.

(390) Gordon, R.; Bender, R.; Herman, G. T. Algebraic Reconstruction Techniques (Art) for Three-Dimensional Electron Microscopy and X-Ray Photography. *J. Theor. Biol.* **1970**, *29*, 471−481.

(391) Choi, K.; Wang, J.; Zhu, L.; Suh, T. S.; Boyd, S.; Xing, L. Compressed Sensing Based Cone-Beam Computed Tomography Reconstruction with a First-Order Method. *Med. Phys.* **2010**, *37*, 5113−5125.

(392) Shepp, L. A.; Vardi, Y. Maximum Likelihood Reconstruction for Emission Tomography. *IEEE Trans. Med. Imag.* **1982**, *1*, 113−122.

(393) Erdogan, H.; Fessler, J. A. Ordered Subsets Algorithms for Transmission Tomography. *Phys. Med. Biol.* **1999**, *44*, 2835−2851.

(394) Chen, G. H.; Tang, J.; Leng, S. Prior Image Constrained Compressed Sensing (Piccs): A Method to Accurately Reconstruct Dynamic Ct Images from Highly Undersampled Projection Data Sets. *Med. Phys.* **2008**, *35*, 660−663.

(395) Liu, Y. J.; Zhu, P. P.; Chen, B.; Wang, J. Y.; Yuan, Q. X.; Huang, W. X.; Shu, H.; Li, E. R.; Liu, X. S.; Zhang, K.; et al. A New Iterative Algorithm to Reconstruct the Refractive Index. *Phys. Med. Biol.* **2007**, *52*, L5−13.

(396) Jung, J. W.; Lee, J. S.; Kwon, N.; Park, S. J.; Chang, S.; Kim, J.; Pyo, J.; Kohmura, Y.; Nishino, Y.; Yamamoto, M.; et al. Fast Microtomography Using Bright Monochromatic X-Rays. *Rev. Sci. Instrum.* **2012**, *83*, 093704.

(397) Villevieille, C.; Ebner, M.; Gomez-Camer, J. L.; Marone, F.; Novak, P.; Wood, V. Influence of Conversion Material Morphology on Electrochemistry Studied with Operando X-Ray Tomography and Diffraction. *Adv. Mater.* **2015**, *27*, 1676−1681.

(398) Wang, J. J.; Eng, C.; Chen-Wiegart, Y. C. K.; Wang, J. Probing Three-Dimensional Sodiation-Desodiation Equilibrium in Sodium-Ion

Batteries by in Situ Hard X-Ray Nanotomography. *Nat. Commun.* **2015**, *6*, 7496.

(399) Zielke, L.; Hutzenlaub, T.; Wheeler, D. R.; Manke, I.; Arlt, T.; Paust, N.; Zengerle, R.; Thiele, S. A Combination of X-Ray Tomography and Carbon Binder Modeling: Reconstructing the Three Phases of LiCoO₂ Li-Ion Battery Cathodes. *Adv. Energy Mater.* **2014**, *4*, 1301617.

(400) Eastwood, D. S.; Bayley, P. M.; Chang, H. J.; Taiwo, O. O.; Vila-Comamala, J.; Brett, D. J. L.; Rau, C.; Withers, P. J.; Shearing, P. R.; Grey, C. P.; et al. Three-Dimensional Characterization of Electrodeposited Lithium Microstructures Using Synchrotron X-Ray Phase Contrast Imaging. *Chem. Commun.* **2015**, *51*, 266−268.

(401) Ebner, M.; Marone, F.; Stampanoni, M.; Wood, V. Visualization and Quantification of Electrochemical and Mechanical Degradation in Li Ion Batteries. *Science* **2013**, *342*, 716−720.

(402) Ren, Y. Y.; Shen, Y.; Lin, Y. H.; Nan, C. W. Direct Observation of Lithium Dendrites inside Garnet-Type Lithium-Ion Solid Electrolyte. *Electrochem. Commun.* **2015**, *57*, 27−30.

(403) Buechele, A. C.; De Jonghe, L. C.; Hitchcock, D. Degradation of Sodium Beta″-Alumina - Effect of Microstructure. *J. Electrochem. Soc.* **1983**, *130*, 1042−1049.

(404) Harry, K. J.; Hallinan, D. T.; Parkinson, D. Y.; MacDowell, A. A.; Balsara, N. P. Detection of Subsurface Structures Underneath Dendrites Formed on Cycled Lithium Metal Electrodes. *Nat. Mater.* **2013**, *13*, 69−73.

(405) Meirer, F.; Cabana, J.; Liu, Y. J.; Mehta, A.; Andrews, J. C.; Pianetta, P. Three-Dimensional Imaging of Chemical Phase Transformations at the Nanoscale with Full-Field Transmission X-Ray Microscopy. *J. Synchrotron Radiat.* **2011**, *18*, 773−781.

(406) Obst, M.; Schmid, G. 3d Chemical Mapping: Application of Scanning Transmission (Soft) X-Ray Microscopy (Stxm) in Combination with Angle-Scan Tomography in Bio-, Geo-, and Environmental Sciences. *Methods Mol. Biol.* **2014**, *1117*, 757−781.

(407) Aramburo, L. R.; Liu, Y. J.; Tyliszczak, T.; de Groot, F. M. F.; Andrews, J. C.; Weckhuysen, B. M. 3d Nanoscale Chemical Imaging of the Distribution of Aluminum Coordination Environments in Zeolites with Soft X-Ray Microscopy. *ChemPhysChem* **2013**, *14*, 496−499.

(408) Wang, J. J.; Chen-Wiegart, Y.-C. K.; Wang, J. In Operando Tracking Phase Transformation Evolution of Lithium Iron Phosphate with Hard X-Ray Microscopy. *Nat. Commun.* **2014**, *5*, 4570.

(409) Xu, Y.; Hu, E.; Yang, F. F.; Corbett, J.; Sun, Z.; Lyu, Y.; Yu, X. Q.; Liu, Y.; Yang, X. Q.; Li, H. Structural Integrity-Searching the Key Factor to Suppress the Voltage Fade of Li-Rich Layered Cathode Materials through 3d X-Ray Imaging and Spectroscopy Techniques. *Nano Energy* **2016**, *28*, 164−171.

(410) Lin, F.; Nordlund, D.; Li, Y.; Quan, M. K.; Cheng, L.; Weng, T.-C.; Liu, Y.; Xin, H. L.; Doeff, M. M. Metal Segregation in Hierarchically Structured Cathode Materials for High-Energy Lithium batteries. *Nat. Energy* **2016**, *1*, 15004.

(411) Wang, J.; Karen Chen-Wiegart, Y. C.; Eng, C.; Shen, Q.; Wang, J. Visualization of Anisotropic-Isotropic Phase Transformation Dynamics in Battery Electrode Particles. *Nat. Commun.* **2016**, *7*, 12372.

(412) Liu, Y. J.; Meirer, F.; Williams, P. A.; Wang, J. Y.; Andrews, J. C.; Pianetta, P. Txm-Wizard: A Program for Advanced Data Collection and Evaluation in Full-Field Transmission X-Ray Microscopy. *J. Synchrotron Radiat.* **2012**, *19*, 281−287.

(413) Meirer, F.; Liu, Y. J.; Pouyet, E.; Fayard, B.; Cotte, M.; Sanchez, C.; Andrews, J. C.; Mehta, A.; Sciau, P. Full-Field Xanes Analysis of Roman Ceramics to Estimate Firing Conditions-a Novel Probe to Study Hierarchical Heterogeneous Materials. *J. Anal. At. Spectrom.* **2013**, *28*, 1870−1883.

(414) Duan, X. Y.; Yang, F. F.; Antono, E.; Yang, W. G.; Pianetta, P.; Ermon, S.; Mehta, A.; Liu, Y. J. Unsupervised Data Mining in Nanoscale X-Ray Spectro-Microscopic Study of Ndfeb Magnet. *Sci. Rep.* **2016**, *6*, 34406.

(415) Robinson, I.; Vartanyants, I.; Williams, G.; Pfeifer, M.; Pitney, J. Reconstruction of the Shapes of Gold Nanocrystals Using Coherent X-Ray Diffraction. *Phys. Rev. Lett.* **2001**, *87*, 195505.

(416) Williams, G. J.; Pfeifer, M. A.; Vartanyants, I. A.; Robinson, I. K. Three-Dimensional Imaging of Microstructure in Au Nanocrystals. *Phys. Rev. Lett.* **2003**, *90*, 175501.

(417) Pfeifer, M. A.; Williams, G. J.; Vartanyants, I. A.; Harder, R.; Robinson, I. K. Three-Dimensional Mapping of a Deformation Field inside a Nanocrystal. *Nature* **2006**, *442*, 63−66.

(418) Takahashi, Y.; Zettsu, N.; Nishino, Y.; Tsutsumi, R.; Matsubara, E.; Ishikawa, T.; Yamauchi, K. Three-Dimensional Electron Density Mapping of Shape-Controlled Nanoparticle by Focused Hard X-Ray Diffraction Microscopy. *Nano Lett.* **2010**, *10*, 1922−1926.

(419) Ulvestad, A. P.; Singer, A.; Cho, H.-M.; Clark, J. N.; Harder, R.; Maser, J.; Meng, Y. S.; Shpyrko, O. G. Single Particle Nanomechanics in Operando Batteries Via Lensless Strain Mapping. *Nano Lett.* **2014**, *14*, 5123−5127.

(420) Ulvestad, A.; Cho, H. M.; Harder, R.; Kim, J. W.; Dietze, S. H.; Fohtung, E.; Meng, Y. S.; Shpyrko, O. G. Nanoscale Strain Mapping in Battery Nanostructures. *Appl. Phys. Lett.* **2014**, *104*, 073108−073108.

(421) Ulvestad, A.; Clark, J. N.; Singer, A.; Vine, D.; Cho, H. M.; Harder, R.; Meng, Y. S.; Shpyrko, O. G. In Situ Strain Evolution During a Disconnection Event in a Battery Nanoparticle. *Phys. Chem. Chem. Phys.* **2015**, *17*, 10551−10555.

(422) Singer, A.; Ulvestad, A.; Cho, H.-M.; Kim, J. W.; Maser, J.; Harder, R.; Meng, Y. S.; Shpyrko, O. G. Nonequilibrium Structural Dynamics of Nanoparticles in Lini1/2mn3/2o4 Cathode under Operando Conditions. *Nano Lett.* **2014**, *14*, 5295−5300.

(423) Wang, D.; He, H.; Han, L.; Lin, R.; Wang, J.; Wu, Z.; Liu, H.; Xin, H. L. Three-Dimensional Hollow-Structured Binary Oxide Particles as an Advanced Anode Material for High-Rate and Long Cycle Life Lithium-Ion Batteries. *Nano Energy* **2016**, *20*, 212−220.

(424) Muller, D. A. Structure and Bonding at the Atomic Scale by Scanning Transmission Electron Microscopy. *Nat. Mater.* **2009**, *8*, 263−270.

(425) Muller, D. A.; Kourkoutis, L. F.; Murfitt, M.; Song, J. H.; Hwang, H. Y.; Silcox, J.; Dellby, N.; Krivanek, O. L. Atomic-Scale Chemical Imaging of Composition and Bonding by Aberration-Corrected Microscopy. *Science* **2008**, *319*, 1073−1076.

(426) Yankovich, A. B.; Berkels, B.; Dahmen, W.; Binev, P.; Sanchez, S. I.; Bradley, S. A.; Li, A.; Szlufarska, I.; Voyles, P. M. Picometre-Precision Analysis of Scanning Transmission Electron Microscopy Images of Platinum Nanocatalysts. *Nat. Commun.* **2014**, *5*, 4155.

(427) Zhou, W.; Kapetanakis, M. D.; Prange, M. P.; Pantelides, S. T.; Pennycook, S. J.; Idrobo, J.-C. Direct Determination of the Chemical Bonding of Individual Impurities in Graphene. *Phys. Rev. Lett.* **2012**, *109*, 206803.

(428) Ramasse, Q. M.; Seabourne, C. R.; Kepaptsoglou, D.-M.; Zan, R.; Bangert, U.; Scott, A. J. Probing the Bonding and Electronic Structure of Single Atom Dopants in Graphene with Electron Energy Loss Spectroscopy. *Nano Lett.* **2013**, *13*, 4989−4995.

(429) Gu, M.; Belharouak, I.; Zheng, J.; Wu, H.; Xiao, J.; Genc, A.; Amine, K.; Thevuthasan, S.; Baer, D. R.; Zhang, J.-G.; et al. Formation of the Spinel Phase in the Layered Composite Cathode Used in Li-Ion Batteries. *ACS Nano* **2013**, *7*, 760−767.

(430) Gu, M.; Belharouak, I.; Genc, A.; Wang, Z.; Wang, D.; Amine, K.; Gao, F.; Zhou, G.; Thevuthasan, S.; Baer, D. R.; et al. Conflicting Roles of Nickel in Controlling Cathode Performance in Lithium Ion Batteries. *Nano Lett.* **2012**, *12*, 5186−5191.

(431) Qian, D.; Xu, B.; Chi, M.; Meng, Y. S. Uncovering the Roles of Oxygen Vacancies in Cation Migration in Lithium Excess Layered Oxides. *Phys. Chem. Chem. Phys.* **2014**, *16*, 14665−14668.

(432) Muller, D. A.; Nakagawa, N.; Ohtomo, A.; Grazul, J. L.; Hwang, H. Y. Atomic-Scale Imaging of Nanoengineered Oxygen Vacancy Profiles in Srtio3. *Nature* **2004**, *430*, 657−661.

(433) Zhu, Y.; Withers, R. L.; Bourgeois, L.; Dwyer, C.; Etheridge, J. Direct Mapping of Li-Enabled Octahedral Tilt Ordering and Associated Strain in Nanostructured Perovskites. *Nat. Mater.* **2015**, *14*, 1142−1149.

(434) Ishikawa, R.; Okunishi, E.; Sawada, H.; Kondo, Y.; Hosokawa, F.; Abe, E. Direct Imaging of Hydrogen-Atom Columns in a Crystal by

Annular Bright-Field Electron Microscopy. *Nat. Mater.* **2011**, *10*, 278−281.

(435) Sun, Y.; Zhao, L.; Pan, H.; Lu, X.; Gu, L.; Hu, Y.-S.; Li, H.; Armand, M.; Ikuhara, Y.; Chen, L.; et al. Direct Atomic-Scale Confirmation of Three-Phase Storage Mechanism in $Li_4Ti_5O_{12}$ Anodes for Room-Temperature Sodium-Ion Batteries. *Nat. Commun.* **2013**, *4*, 1870.

(436) He, Q.; Ishikawa, R.; Lupini, A. R.; Qiao, L.; Moon, E. J.; Ovchinnikov, O.; May, S. J.; Biegalski, M. D.; Borisevich, A. Y. Towards 3d Mapping of BO_6 Octahedron Rotations at Perovskite Heterointerfaces, Unit Cell by Unit Cell. *ACS Nano* **2015**, *9*, 8412−8419.

(437) Yan, P.; Zheng, J.; Lv, D.; Wei, Y.; Zheng, J.; Wang, Z.; Kuppan, S.; Yu, J.; Luo, L.; Edwards, D.; et al. Atomic-Resolution Visualization of Distinctive Chemical Mixing Behavior of Ni, Co, and Mn with Li in Layered Lithium Transition-Metal Oxide Cathode Materials. *Chem. Mater.* **2015**, *27*, 5393−5401.

(438) Krivanek, O. L.; Lovejoy, T. C.; Dellby, N.; Aoki, T.; Carpenter, R. W.; Rez, P.; Soignard, E.; Zhu, J.; Batson, P. E.; Lagos, M. J.; et al. Vibrational Spectroscopy in the Electron Microscope. *Nature* **2014**, *514*, 209−212.

(439) Holtz, M. E.; Yu, Y.; Gunceler, D.; Gao, J.; Sundararaman, R.; Schwarz, K. A.; Arias, T. A.; Abruña, H. D.; Muller, D. A. Nanoscale Imaging of Lithium Ion Distribution During in Situ Operation of Battery Electrode and Electrolyte. *Nano Lett.* **2014**, *14*, 1453−1459.

(440) Lin, F.; Markus, I. M.; Doeff, M. M.; Xin, H. L. Chemical and Structural Stability of Lithium-Ion Battery Electrode Materials under Electron Beam. *Sci. Rep.* **2014**, *4*, 5694.

(441) Sina, M.; Nam, K. W.; Su, D.; Pereira, N.; Yang, X. Q.; Amatucci, G. G.; Cosandey, F. Structural Phase Transformation and Fe Valence Evolution in FeO_xF_{2-x}/C Nanocomposite Electrodes During Lithiation and De-Lithiation Processes. *J. Mater. Chem. A* **2013**, *1*, 11629−11640.

(442) Zhang, H.; Karki, K.; Huang, Y.; Whittingham, M. S.; Stach, E. A.; Zhou, G. Atomic Insight into the Layered/Spinel Phase Transformation in Charged $LiNi_{0.80}Co_{0.15}Al_{0.05}O_2$ Cathode Particles. *J. Phys. Chem. C* **2017**, *121*, 1421−1430.

(443) Hwang, S.; Kim, S. M.; Bak, S.-M.; Kim, S. Y.; Cho, B.-W.; Chung, K. Y.; Lee, J. Y.; Stach, E. A.; Chang, W. Using Real-Time Electron Microscopy to Explore the Effects of Transition-Metal Composition on the Local Thermal Stability in Charged $Li_xNi_yMn_zCo_{1-y-z}O_2$ Cathode Materials. *Chem. Mater.* **2015**, *27*, 3927−3935.

(444) Huang, J. Y.; Zhong, L.; Wang, C. M.; Sullivan, J. P.; Xu, W.; Zhang, L. Q.; Mao, S. X.; Hudak, N. S.; Liu, X. H.; Subramanian, A.; et al. In Situ Observation of the Electrochemical Lithiation of a Single SnO_2 Nanowire Electrode. *Science* **2010**, *330*, 1515−1520.

(445) Liu, X.; Zheng, H.; Zhong, L.; Huang, S.; Karki, K.; Zhang, L. Q.; Liu, Y.; Kushima, A.; Liang, W. T.; Wang, J. W.; et al. Anisotropic Swelling and Fracture of Silicon Nanowires During Lithiation. *Nano Lett.* **2011**, *11*, 3312−3318.

(446) Wen, Y.; He, K.; Zhu, Y.; Han, F.; Xu, Y.; Matsuda, I.; Ishii, Y.; Cumings, J.; Wang, C. Expanded Graphite as Superior Anode for Sodium-Ion Batteries. *Nat. Commun.* **2014**, *5*, 4033.

(447) Wang, Z.; Santhanagopalan, D.; Zhang, W.; Wang, F.; Xin, H. L.; He, K.; Li, J.; Dudney, N.; Meng, Y. S. In Situ Stem-Eels Observation of Nanoscale Interfacial Phenomena in All-Solid-State Batteries. *Nano Lett.* **2016**, *16*, 3760−3767.

(448) Zeng, Z.; Liang, W.-I.; Liao, H.-G.; Xin, H. L.; Chu, Y.-H.; Zheng, H. Visualization of Electrode-Electrolyte Interfaces in $LiPF_6$/EC/DEC Electrolyte for Lithium Ion Batteries Via in Situ Tem. *Nano Lett.* **2014**, *14*, 1745−1750.

(449) Zeng, Z.; Zhang, X.; Bustillo, K.; Niu, K.; Gammer, C.; Xu, J.; Zheng, H. In Situ Study of Lithiation and Delithiation of MoS_2 Nanosheets Using Electrochemical Liquid Cell Transmission Electron Microscopy. *Nano Lett.* **2015**, *15*, 5214−5220.

(450) Gu, M.; Parent, L. R.; Mehdi, B. L.; Unocic, R. R.; McDowell, M. T.; Sacci, R. L.; Xu, W.; Connell, J. G.; Xu, P.; Abellan, P.; et al. Demonstration of an Electrochemical Liquid Cell for Operando

Transmission Electron Microscopy Observation of the Lithiation/Delithiation Behavior of Si Nanowire Battery Anodes. *Nano Lett.* **2013**, *13*, 6106−6112.

(451) Kourkoutis, L. F.; Xin, H.; Higuchi, T.; Hotta, Y.; Lee, J.; Hikita, Y.; Schlom, D.; Hwang, H.; Muller, D. Atomic-Resolution Spectroscopic Imaging of Oxide Interfaces. *Philos. Mag.* **2010**, *90*, 4731−4749.

(452) Zhou, Y. N.; Yue, J. L.; Hu, E. Y.; Li, H.; Gu, L.; Nam, K. W.; Bak, S. M.; Yu, X. Q.; Liu, J.; Bai, J. M.; et al. High-Rate Charging Induced Intermediate Phases and Structural Changes of Layer-Structured Cathode for Lithium-Ion Batteries. *Adv. Energy Mater.* **2016**, *6*, 1600597.

(453) Key, B.; Bhattacharyya, R.; Morcrette, M.; Seznec, V.; Tarascon, J. M.; Grey, C. P. Real-Time Nmr Investigations of Structural Changes in Silicon Electrodes for Lithium-Ion Batteries. *J. Am. Chem. Soc.* **2009**, *131*, 9239−9249.

(454) Borkiewicz, O. J.; Shyam, B.; Wiaderek, K. M.; Kurtz, C.; Chupas, P. J.; Chapman, K. W. The Ampix Electrochemical Cell: A Versatile Apparatus for in Situ X-Ray Scattering and Spectroscopic Measurements. *J. Appl. Crystallogr.* **2012**, *45*, 1261−1269.

(455) Nam, K. W.; Bak, S. M.; Hu, E. Y.; Yu, X. Q.; Zhou, Y. N.; Wang, X. J.; Wu, L. J.; Zhu, Y. M.; Chung, K. Y.; Yang, X. Q. Combining in Situ Synchrotron X-Ray Diffraction and Absorption Techniques with Transmission Electron Microscopy to Study the Origin of Thermal Instability in Overcharged Cathode Materials for Lithium-Ion Batteries. *Adv. Funct. Mater.* **2013**, *23*, 1047−1063.

(456) Yang, Z. Z.; Trahey, L.; Ren, Y.; Chan, M. K. Y.; Lin, C. K.; Okasinski, J.; Thackeray, M. M. In Situ High-Energy Synchrotron X-Ray Diffraction Studies and First Principles Modeling of Alpha-MnO_2 Electrodes in LiO_2 and Li-Ion Coin Cells. *J. Mater. Chem. A* **2015**, *3*, 7389−7398.

(457) Storm, M. M.; Johnsen, R. E.; Younesi, R.; Norby, P. Capillary Based Li-Air Batteries for in Situ Synchrotron X-Ray Powder Diffraction Studies. *J. Mater. Chem. A* **2015**, *3*, 3113−3119.

(458) Weker, J. N.; Liu, N.; Misra, S.; Andrews, J. C.; Cui, Y.; Toney, M. F. In Situ Nanotomography and Operando Transmission X-Ray Microscopy of Micron-Sized Ge Particles. *Energy Environ. Sci.* **2014**, *7*, 2771−2777.

(459) Feng, Z. X.; Chen, X.; Qiao, L.; Lipson, A. L.; Fister, T. T.; Zeng, L.; Kim, C.; Yi, T. H.; Sa, N.; Proffit, D. L.; et al. Phase-Controlled Electrochemical Activity of Epitaxial Mg-Spinel Thin Films. *ACS Appl. Mater. Interfaces* **2015**, *7*, 28438−28443.

(460) Fister, T. T.; Esbenshade, J.; Chen, X.; Long, B. R.; Shi, B.; Schleputz, C. M.; Gewirth, A. A.; Bedzyk, M. J.; Fenter, P. Lithium Intercalation Behavior in Multilayer Silicon Electrodes. *Adv. Energy Mater.* **2014**, *4*, 1301494.

(461) Fister, T. T.; Hu, X. Y.; Esbenshade, J.; Chen, X.; Wu, J. S.; Dravid, V.; Bedzyk, M.; Long, B.; Gewirth, A. A.; Shi, B.; et al. Dimensionally Controlled Lithiation of Chromium Oxide. *Chem. Mater.* **2016**, *28*, 47−54.

(462) Fister, T. T.; Long, B. R.; Gewirth, A. A.; Shi, B.; Assoufid, L.; Lee, S. S.; Fenter, P. Real-Time Observations of Interfacial Lithiation in a Metal Silicide Thin Film. *J. Phys. Chem. C* **2012**, *116*, 22341−22345.

(463) Meng, X.; Libera, J. A.; Fister, T. T.; Zhou, H.; Hedlund, J. K.; Fenter, P.; Elam, J. W. Atomic Layer Deposition of Gallium Sulfide Films Using Hexakis(Dimethylamido)Digallium and Hydrogen Sulfide. *Chem. Mater.* **2014**, *26*, 1029−1039.

(464) Borkiewicz, O. J.; Wiaderek, K. M.; Chupas, P. J.; Chapman, K. W. Best Practices for Operando Battery Experiments: Influences of X-Ray Experiment Design on Observed Electrochemical Reactivity. *J. Phys. Chem. Lett.* **2015**, *6*, 2081−2085.

(465) Kuppan, S.; Xu, Y. H.; Liu, Y. J.; Chen, G. Y. Phase Transformation Mechanism in Lithium Manganese Nickel Oxide Revealed by Single-Crystal Hard X-Ray Microscopy. *Nat. Commun.* **2017**, *8*, 14309.

(466) Li, Q.; Qiao, R. M.; Wray, L. A.; Chen, J.; Zhuo, Z.; Chen, Y.; Yan, S.; Pan, F.; Hussain, Z.; Yang, W. Quantitative Probe of the Transition Metal Redox in Battery Electrodes through Soft X-Ray

Absorption Spectroscopy. *J. Phys. D: Appl. Phys.* **2016**, *49* (41), 413003.